

---

# Remote Sensing Based Retrieval of High Spatio-Temporal Soil Moisture for Agriculture

Thomas Josef Weiß

---



München 2025



---

# **Remote Sensing Based Retrieval of High Spatio-Temporal Soil Moisture for Agriculture**

**Thomas Josef Weiß**

---

Dissertation zur Erlangung des Doktorgrades  
an Fakultät für Geowissenschaften  
der Ludwig-Maximilians-Universität München

vorgelegt von  
Thomas Josef Weiß

München, den 15.10.2024

First Reviewer: Prof. Dr. Ralf Ludwig,  
Department of Geography,  
Ludwig-Maximilians-Universität München

Second Reviewer: Prof. Dr. Philip Marzahn,  
Faculty of Agricultural and Environmental Sciences,  
University of Rostock

Date of Submission: 15.10.2024

Date of Defense: 22.04.2025

*"The best time to plant a tree is 20 years ago.  
The second best time is now."  
(Unknown)*

# Acknowledgments

As I am writing these lines, my PhD journey comes to an end. I want to begin with two poem lines from Ludwig Jacobowski's - Leuchtende Tage. "Nicht weinen, weil sie vorüber! Lächeln, weil sie gewesen" ("Don't cry because it's over! Smile because they have been!").

During this unforgettable journey, I have met some special people who I want to thank. First, I want to express my enormous gratitude to Alexander Löw for giving me the opportunity to start my PhD journey. Although you tragically passed away, your vision, expertise, and guidance were enormously important to me during the entire PhD. Thus, in some way, your spirit lives on. After your passing, I was lucky to find two people who lent me not only their professional expertise but also helped me to grow in other aspects of life as well. Thus, special thanks go to Philip Marzahn and Thomas Jagdhuber. Philip, I met you already during my bachelor studies, continued my scientific journey at some point with Alex, but in the end, I ended up with you again. Thank you for everything. Thomas, it was actually Philip who suggested that I apply for the internship that led to my master's thesis, which you were so kind to supervise. You have enriched and pushed my scientific and personal journey since day one. I also want to thank Ralf Ludwig for your kind ear and the official takeover as my supervisor.

I want to thank my office mates Ben and Gome, for the countless discussions and thought-sharing about science, coding, and personal matters. Without help from Andrea and Vera, the administrative stuff would have been a mess. Thank you for all the help with my contract, travel expenses, and all the other little details that matter. I further want to thank all the other colleagues, especially Flo, Raul, and Andrea for their countless balcony and basement beer and non-beer discussions. Furthermore, I want to thank Matthias and all the Hiwis for helping me collect all the necessary in-situ measurements for my studies. Special thanks go to Vicky and Janja for university and especially all non-university-related activities. All our joint adventures (Gammeltage, travel experiences, ...) kept me going. I would not miss those days for the world.

At the end, I want to thank my family and especially my parents for their unwavering support not only during my studies but since I was born.

# Summary

Soil moisture is a critical variable across several domains, including agriculture, hydrology, meteorology, and climatology. The required temporal and spatial resolutions for soil moisture information vary depending on the application, ranging from sub-daily to monthly, and from meters to tens of kilometers. Current operational soil moisture estimates at regional to global scales are typically provided at coarse to medium spatial resolutions (greater than 1 km). Due to the complexity of influencing factors and the high spatial and temporal variability of soil moisture, accurate estimation becomes increasingly challenging as the spatial resolution requirement increases. As a result, satellite remote sensing of soil moisture at sub-field scales (10–100 m) is generally confined to specific research sites, often limited in temporal resolution and available for only short periods, typically less than a year. However, with the launch of the Sentinel-1 satellites, which offer both high temporal and spatial resolutions, new opportunities arise to enhance the estimation of soil moisture. These advances open doors to more detailed, accurate, and temporally frequent observations, expanding the potential for broader applications beyond limited research sites.

This dissertation focuses on addressing these limitations by developing methods to estimate high spatio-temporal soil moisture values, which are essential for advancing precision and smart farming applications. The work covers the complete scientific process, from acquiring in-situ measurements for validation purposes, preprocessing and analyzing remote sensing data, to conducting a detailed analysis of the strengths and weaknesses of various Radiative Transfer (RT) model combinations used in soil moisture estimation. The primary objective is to generate high spatio-temporal distributed soil moisture maps. Emphasis is placed on minimizing the number of input variables, ensuring that all required data can be operationally retrieved from remote sensing sensors, which facilitates the transferability of the approach to other regions, with potential applications from regional to global scales.

Over decades, numerous empirical and physically-based RT models have been developed to calculate radar backscatter - a key parameter estimated by Sentinel-1 - based on soil surface and vegetation canopy characteristics. A comparison of various empirical and physically-based surface and canopy RT model combinations (Publication I) identified a semi-empirical surface model (Oh04) combined with a heuristic single scattering model for vegetation (SSRT) as an optimal compromise between model sophistication (which affects transferability) and the availability of required input parameters. The Oh04 model requires surface roughness and soil moisture but does not rely on soil texture information, which is often unavailable on a large scale and can restrict transferability. The SSRT model accounts not only for the canopy backscatter but also for combined bistatic scattering contributions from the ground and vegetation. Required input parameters can be either parameterized or retrieved from optical remote sensing satellites such as Sentinel-2.

The Sentinel-1 A/B satellites provide a temporal resolution with identical observation geometry every 6 days. However, by incorporating all available Sentinel-1 data - regardless

of observation geometry - a temporal resolution of 1.5 days can be achieved across most of Europe. The inclusion of Sentinel-1 time series with different observation geometries presents a challenge, as varying geometries produce changes in backscatter values that complicate the analysis. A detailed study of azimuth and incidence angle variations revealed that incidence angle changes significantly affect backscatter, while azimuth angle changes are largely negligible. Despite being accounted for in RT model equations, existing models are often unable to fully reproduce the observed changes in Sentinel-1 backscatter. Therefore, modifications to the original RT models were necessary to accommodate a dense time series of images with varying incidence angles, enabling the use of a 1.5 day temporal resolution (Publication II).

Building on the insights from Publications I and II, a retrieval scheme was developed using a minimal set of input parameters for high spatio-temporal soil moisture estimation (Publication III). This data assimilation approach estimates soil moisture by inverting the RT model, utilizing radar backscatter (Sentinel-1), Vegetation Water Content (VWC) (Sentinel-2), and parameterizations for surface roughness, single scattering albedo, and an empirical parameter  $b$ . To address the equifinality problem commonly encountered in remote sensing data assimilation, a medium-resolution (1 km) soil moisture dataset based on RADar-ONLine-ANeichung (RADOLAN) data is used as prior information to guide model outputs. High spatial (10 m) and temporal (1.5 day) soil moisture maps generated for the Munich North Isar (MNI) test site were validated against in-situ measurements from maize and winter wheat fields, producing mean unbiased root mean square error (ubRMSE) values of  $0.045 \text{ m}^3/\text{m}^3$  for 2017 and  $0.037 \text{ m}^3/\text{m}^3$  for 2018. These estimates align with the accepted accuracy range for operational coarse-resolution soil moisture products and successfully capture spatial patterns and wetting and drying dynamics associated with localized rainfall events.

To support the scientific output in Publications I, II, and III, two Python packages were developed (Publications IV and V). These packages are designed to serve both the scientific community and non-experts working with microwave remote sensing data. Freely available microwave remote sensing data typically require extensive preprocessing by experts, which limits their usability. The Python package in Publication IV provides a default preprocessing workflow to generate radiometrically and geometrically corrected sigma naught backscatter values, allowing non-experts to use microwave data with minimal preprocessing knowledge. At the same time, experts can leverage this package to streamline the creation and implementation of their own automated processing pipelines for time series data. The package described in Publication V implements various widely-used surface and canopy RT models. Its modular design allows users to easily combine different models, facilitating straightforward comparison and analysis of RT model outputs. This functionality offers significant value to the scientific community by making advanced remote sensing models more accessible and flexible.

In summary, the key scientific advancements of this dissertation are:

- An improved and enhanced understanding of the comparative performance of various surface and canopy radiative transfer (RT) models, highlighting the strengths and weaknesses of different model combinations. This comprehensive analysis facilitates the selection of appropriate models for specific remote sensing applications.
- A sensitivity analysis that systematically examines how variations in input parameters impact soil moisture estimates. This analysis assesses the models' robustness which significantly influence the accuracy of soil moisture retrieval, informing better model calibration and application.
- An exploration of the factors driving variations in Synthetic Aperture Radar (SAR) images, focusing on the effects of differing acquisition geometries, including azimuth and incidence angle changes. This insight contributes to a more detailed interpretation of SAR data, essential for accurate remote sensing analysis.
- An advancement in the understanding of scattering mechanisms through dual polarimetric decomposition techniques, which enhances the capability to analyze and interpret SAR signals related to changes in vegetation structure, moisture content, and varying acquisition geometries, such as incidence angle changes. This contribution provides deeper insights into how radar waves interact with different scattering surfaces, facilitating improved applications in agricultural monitoring and environmental assessments by accounting for these geometrical variations.
- The development of a novel approach to derive high spatio-temporal soil moisture estimates over agricultural fields, leveraging operational and freely available microwave and optical remote sensing data. This methodology enhances the accessibility and applicability of soil moisture data for agricultural monitoring and management.
- The utilization of a higher temporal resolution time series, allowing for a more comprehensive analysis of soil moisture dynamics. This increased frequency of observations significantly improves the detection of temporal variations and enhances the reliability of soil moisture estimates, ultimately supporting better decision-making in agricultural practices.
- The development of a Python-based automated preprocessing pipeline for microwave remote sensing data, enabling efficient and standardized preparation of data for analysis. This tool lowers the barrier for entry for researchers and practitioners in the field, allowing for broader utilization of microwave remote sensing technologies.
- The creation of a user-friendly Python tool designed to facilitate the integration and combination of different microwave RT models, incorporating both surface and vegetation components. This tool empowers researchers to customize their model configurations easily, promoting innovation in remote sensing studies.

# Zusammenfassung

Die Bodenfeuchte ist ein wichtiger Einflussfaktor in der Landwirtschaft, der Hydrologie, der Meteorologie und der Klimatologie. Die erforderlichen zeitlichen und räumlichen Auflösungen für Bodenfeuchteinformationen variieren je nach Anwendung und reichen von Tagesaktuellen bis hin zu monatlichen Werten sowie von Meter- bis zu mehreren Zehnkilometernaufösungen. Derzeit sind aus Satellitendaten abgeleitete Bodenfeuchtwerte auf regionalen bis globalen Skalen typischerweise mit grober (über 25 km) bis mittlerer räumlicher Auflösung (über 1 km) verfügbar. Aufgrund der Komplexität der Einflussfaktoren und der hohen räumlichen sowie zeitlichen Variabilität der Bodenfeuchte ist ihre Ableitung mit hohen Unsicherheiten behaftet. Zudem führen höhere räumliche Auflösungsanforderungen zu höherer Komplexität und höheren Unsicherheiten. Die satellitengestützte Ableitung der Bodenfeuchte auf sub-feldmaßstäblichen Skalen (10–100 m) befindet sich immer noch im Stadium der wissenschaftlichen Untersuchungen. Mit dem Start der Sentinel-1-Satelliten, die sowohl hohe zeitliche als auch räumliche Auflösungen bieten, ergeben sich jedoch neue Möglichkeiten zur Verbesserung der großflächigen Bodenfeuchteableitung.

Das Ziel dieser Dissertation ist die Weiterentwicklung von Methoden zur Ableitung von zeitlich und räumlich hochaufgelösten Bodenfeuchtwerten aus Satellitendaten, um Anwendungen im Bereich des Smart Farmings zu unterstützen. Die Arbeit umfasst den gesamten wissenschaftlichen Prozess, von der Erfassung von In-situ-Messungen zur Validierung über die Vorprozessierung und Analyse von Fernerkundungsdaten bis hin zu einer detaillierten Analyse der Stärken und Schwächen verschiedener Modellkombinationen. Der Fokus liegt auf der Minimierung der benötigten Eingangsvariablen, um eine hohe Übertragbarkeit des entwickelten Ansatzes auf andere Gebiete zu ermöglichen. Zudem sollen alle Eingangsvariablen aus bereits frei verfügbaren Fernerkundungsdaten bereitgestellt werden.

Die vom Sentinel-1-Satelliten gemessenen Radar-Backscatterwerte können mithilfe von empirisch und physikalisch basierte Strahlungstransfermodelle modelliert werden. Ein Vergleich verschiedener empirischer und physikalisch basierter Modellkombinationen (Veröffentlichung I) identifizierte ein semi-empirisches Strahlungstransfermodell (Oh04), das mit einem heuristischen Strahlungstransfermodell für Vegetation (SSRT) kombiniert wurde, als optimalen Kompromiss zwischen Modellkomplexität und der Verfügbarkeit der erforderlichen Eingangsparameter. Die Eingangsvariablen des Oh04-Modells umfassen die Bodenrauhigkeit und die Bodenfeuchte. Informationen über die Bodenart, die oft nicht in ausreichendem Maß verfügbar sind, werden nicht benötigt. Die erforderlichen Eingangsparameter des SSRT-Modells können entweder parametrisiert oder von optischen Fernerkundungssatelliten wie Sentinel-2 abgeleitet werden. Das SSRT-Modell berücksichtigt sowohl die Rückstreuung der Vegetation als auch die Rückstreuung durch die Wechselwirkungen zwischen Vegetation und Boden mit der ausgesendeten elektromagnetischen Welle.

Die Sentinel-1-Satelliten bieten eine zeitliche Auflösung mit identischer Beobachtungsgeometrie alle sechs Tage. Durch die Nutzung aller verfügbaren Sentinel-1-Überflüge –

unabhängig von der Aufnahmegeometrie – kann jedoch eine zeitliche Auflösung von 1.5 Tagen für weite Teile Europas erreicht werden. Die Verwendung von Zeitserien mit unterschiedlichen Aufnahmegeometrien stellt allerdings eine Herausforderung dar, da unterschiedliche Aufnahmegeometrien zu Veränderungen der Rückstreuung führen und somit die Ableitung der Bodenfeuchte erschweren. Eine detaillierte Untersuchung von verschiedenen Azimut- und Einfallswinkeln zeigt, dass Veränderungen des Einfallswinkels den Backscatter erheblich beeinflussen, während Änderungen im Azimutwinkel weitgehend vernachlässigbar sind. Obwohl die Modelle den Einfallswinkel berücksichtigen, sind sie oft nicht in der Lage, die beobachteten Änderungen im Sentinel-1-Backscatter vollständig zu reproduzieren. Daher sind Anpassungen an der ursprünglichen Modellkonzeption notwendig, um eine zeitlich hochaufgelöste Zeitreihe (Auflösung von 1.5 Tagen) mit Szenen bestehend aus unterschiedlichen Einfallswinkeln nutzbar zu machen (Veröffentlichung II).

Veröffentlichungen I und II bilden die Grundlage für einen Datenassimilationsansatz, der mit minimalen Anforderungen an die Eingangsparameter, zeitlich und räumlich hochaufgelöste Bodenfeuchte aus Satellitendaten ableitet (Veröffentlichung III). Durch eine inverse Modellierung des Strahlungstransfermodells unter Verwendung des Radar-Backscatters (Sentinel-1), des Vegetationswassergehaltes (Sentinel-2) sowie einer Parametrisierung der Bodenrauhigkeit, der Reflexionsstrahlung und eines empirischen Parameters  $b$ , wird die Bodenfeuchte ermittelt. Um das häufig auftretende Problem der Äquifinalität in der Datenassimilation von Fernerkundungsdaten zu minimieren, wird zusätzlich ein 1 km aufgelöstes Bodenfeuchteprodukt, welches auf den RADOLAN-Daten des Deutschen Wetterdienstes basiert, als Zusatzinformation genutzt. Die modellierten Bodenfeuchtekarten für das Münchner Nord-Isar-Testgebiet mit 10 m räumlicher und 1.5 Tagen zeitlicher Auflösung wurden anhand von In-situ-Messungen von Mais- und Winterweizenfeldern validiert. Die modellierten Bodenfeuchtwerte liegen mit einem unbiased RMSE von  $0.045 \text{ m}^3/\text{m}^3$  für 2017 und  $0.037 \text{ m}^3/\text{m}^3$  für 2018 im angestrebten Genauigkeitsbereich für satellitengestützte Bodenfeuchteinformationen. Außerdem konnten Räumliche Muster bezüglich Vernässung- und Abtrocknungsdynamiken, die mit lokalisierten Niederschlagsereignissen verbunden sind, mit hoher Genauigkeit reproduziert werden.

Zur Erstellung der wissenschaftlichen Ergebnisse der Veröffentlichungen I, II und III wurden zwei Python-Bibliotheken entwickelt. Frei verfügbare Mikrowellenfernerkundungsdaten sind in der Regel nicht ohne weiteres nutzbar und erfordern zunächst eine umfangreiche Vorprozessierung, was ihre Anwendbarkeit stark limitiert. Die in Veröffentlichung IV beschriebene Python-Bibliothek bietet eine automatisierte Vorprozessierungskette, um radiometrisch und geometrisch korrigierte Sentinel-1-Sigma-Naught-Backscatter-Werte zu generieren. Durch diesen Python-Code können auch Personen mit Programmierkenntnissen und minimalem Vorwissen im Bereich der Fernerkundung Sentinel-1-Daten nutzen. Zudem können Fernerkundungsexperten mit Programmierkenntnissen dieses Paket verwenden, um eine angepasste oder komplett neue Prozessierungskette für Sentinel-1-Zeitreihendaten zu erstellen. Die in Veröffentlichung V beschriebene Python-Bibliothek umfasst verschiedene gängig verwendete Strahlungstransfermodelle. Das modulare Design ermöglicht den Nutzern, verschiedene Modelle einfach zu kombinieren, wodurch eine schnelle und einfache Analyse verschiedener Modellergebnisse ermöglicht wird.

Die wichtigsten wissenschaftlichen Fortschritte dieser Doktorarbeit sind:

- Ein verbessertes und erweitertes Verständnis der meistverwendeten Mikrowellen Strahlungstransfermodellen. Die durchgeführte umfassende Analyse erleichtert die Auswahl geeigneter Modelle für spezifische Anwendungen der Fernerkundung.
- Eine Sensitivitätsanalyse, die systematisch untersucht, wie Variationen der Eingangsvariablen die Ableitungsqualität von Bodenfeuchtwerten beeinflussen. Diese Analyse bewertet die Robustheit der Modelle und Eingangsparameter, welche die Genauigkeit der Bodenfeuchteretrievals erheblich beeinflussen und somit eine bessere Modellkalibrierung und Anwendung ermöglichen.
- Eine Analyse der Auswirkungen von unterschiedlichen Sentinel-1 Aufnahmegeometrien auf den Radar-Backscatter. Diese Erkenntnisse im Bereich des Azimut- und Einfallswinkels tragen zu einer verbesserten Interpretation der Sentinel-1 Zeitreihen bei.
- Ein Fortschritt im Verständnis der Streumechanismen durch duale polarimetrische Dekomposition, der die Fähigkeit zur Analyse und Interpretation von Radarsystemen mit synthetischer Aperatur in Bezug auf Veränderungen in der Vegetationsstruktur, dem Feuchtigkeitsgehalt und variierenden Aufnahmegeometrien, verbessert. Dieser Beitrag liefert tiefere Einblicke in die Wechselwirkungen von Radarwellen mit unterschiedlichen Oberflächen, wodurch verbesserte Anwendungen in der landwirtschaftlichen Überwachung und der Umweltbewertung ermöglicht werden.
- Die Entwicklung eines neuartigen Ansatzes zur Ableitung räumlich und zeitlich hochaufgelöster Bodenfeuchteinformationen von landwirtschaftliche Flächen, welcher auf frei verfügbaren Mikrowellen- und optischen Fernerkundungsdaten basiert. Diese Methodik verbessert die Ableitung von der Bodenfeuchte für Smart-Farming Anwendungen.
- Die Nutzung einer Zeitreihe mit erhöhter zeitlicher Auflösung, die eine umfassendere Analyse der Dynamik der Bodenfeuchte ermöglicht. Die erhöhte Beobachtungsfrequenz verbessert die Erkennung zeitlicher Variationen und erhöht die Zuverlässigkeit der Bodenfeuchteableitung, was letztendlich bessere Entscheidungsfindungen in landwirtschaftlichen Praktiken unterstützt.
- Die Entwicklung einer Python-Bibliothek zur automatisierten Vorprozessierung von Mikrowellenfernerkundungsdaten. Dieses Tool senkt die Eintrittsbarrieren für Forscher und Praktiker in diesem Bereich und ermöglicht eine breitere Nutzung der Technologien der Mikrowellenfernerkundung.
- Die Erstellung einer Python-Bibliothek, das darauf ausgelegt ist, die Integration und Kombination verschiedener Mikrowellenstrahlungstransfermodellen zu vereinfachen. Dieses Tool ermöglicht es Forschern, verschiedene Modellkombinationen schnell und einfach zu analysieren.

# Contents

<b>Acknowledgments</b>	<b>i</b>
<b>Summary</b>	<b>ii</b>
<b>Zusammenfassung</b>	<b>v</b>
<b>List of Figures</b>	<b>ix</b>
<b>Abbreviations</b>	<b>x</b>
<b>1 Introduction</b>	<b>1</b>
1.1 Motivation . . . . .	1
1.2 Definition of Soil Moisture . . . . .	5
1.3 Soil Moisture in Agriculture . . . . .	6
1.4 Soil Moisture Monitoring with Microwave Remote Sensing Techniques . . . . .	9
1.5 Demands, Benefits, and Current Limitations of Soil Moisture Estimates from Remote Sensing Data . . . . .	12
<b>2 Research Questions</b>	<b>17</b>
<b>3 Publications</b>	<b>18</b>
3.1 Publication I: Evaluation of Different Radiative Transfer Models for Microwave Estimation of Wheat Fields . . . . .	20
3.2 Transition to Publication II . . . . .	47
3.3 Publication II: Sentinel-1 Backscatter Analysis and Radiative Transfer Modeling of Dense Winter Wheat Time Series . . . . .	48
3.4 Transition to Publication III . . . . .	74
3.5 Publication III: RTM-based Downscaling of Medium Resolution Soil Moisture using Sentinel-1 Data over Agricultural Fields . . . . .	75
3.6 Usage of Publication IV and V (Python software packages) within Publication I, II and III . . . . .	93
3.7 Publication IV: SenSARP - A pipeline to pre-process Sentinel-1 SLC data by using ESA SNAP Sentinel-1 Toolbox . . . . .	94
3.8 Publication V: SenSE - Community SAR ScattEring model . . . . .	99
<b>4 Conclusion</b>	<b>103</b>
4.1 Answers of Research Questions . . . . .	103
4.2 Research Usage and Application . . . . .	108
<b>References</b>	<b>109</b>

# List of Figures

<b>Figure 1:</b> Schematic diagram of the unsaturated and saturated soil zones. . . .	6
<b>Figure 2:</b> Categorization of parameters that define crop development and important applications in agriculture, based on their required temporal and spatial resolutions. . . . .	7
<b>Figure 3:</b> Electromagnetic spectrum with active and passive remote sensor information. . . . .	9
<b>Figure 4:</b> Timeline of spaceborne active and passive microwave sensors for soil moisture retrieval. . . . .	11
<b>Figure 5:</b> Schematic overview of backscatter changes based on incidence angle, soil moisture, and vegetation status. . . . .	12
<b>Figure 6:</b> Classification of application areas based on soil moisture information, categorized by their temporal and spatial resolution requirements, and allocated to microwave remote sensing missions. . . . .	14
<b>Figure 7:</b> Schematic overview of the dissertation. . . . .	19

# Abbreviations

**AMS** American Meteorological Society  
**AMSR-2** Advanced Microwave Scanning Radiometer 2  
**AMSR-E** Advanced Microwave Scanning Radiometer for EOS  
**ASCAT** Advanced SCATterometer  
**BEC** Barcelona Expert Center  
**CESBIO** Centre d'Études Spatiales de la BIOSphère  
**CNR** Consiglio Nazionale delle Ricerche  
**EO** Earth Observation  
**ERS-2** European Remote Sensing satellite 2  
**ESA** European Space Agency  
**ESA CCI** ESA Climate Change Initiative  
**EUMETSAT** European Organisation for the Exploitation of Meteorological Satellites  
**JAXA** Japan Aerospace Exploration Agency  
**LAI** Leaf Area Index  
**LMU** Ludwig-Maximilians-Universität  
**MNI** Munich North Isar  
**MODIS** Moderate Resolution Imaging Spectroradiometer  
**NASA** National Aeronautics and Space Administration  
**NISAR** NASA-ISRO Synthetic Aperture Radar  
**NOAA** National Oceanic and Atmospheric Administration  
**RADOLAN** RADar-ONLine-ANeichung  
**RT** Radiative Transfer  
**SAOCOM** Satelite Argentino de Observacion COn Microondas  
**SAR** Synthetic Aperture Radar  
**SEC** Scientific Expertise Centre  
**SMAP** Soil Moisture Active Passive  
**SMMR** Scanning Multi-channel Microwave Radiometer  
**SMOPS** Soil Moisture Operational Products System  
**SMOS** Soil Moisture and Ocean Salinity  
**SSM/I** Special Sensor Microwave Imager  
**TPDC** Tibetan Plateau Data Center  
**TRMM-TMI** Tropical Rainfall Measuring Mission's - Microwave Imager  
**VWC** Vegetation Water Content

# Chapter 1

## Introduction

This introductory chapter provides a general overview of the research topic - soil moisture - and guides the reader to the research questions (Chapter 2) and scientific publications (Chapter 3). First, the motivation for the research topics is described (Section 1.1). Afterwards, a definition of soil moisture is provided (Section 1.2). Next, the importance of soil moisture knowledge for agricultural purposes, as well as the required spatial and temporal resolutions, are demonstrated (Section 1.3). This is followed by an overview of the state-of-the-art microwave remote sensing soil moisture monitoring methods, along with their respective spatial and temporal limitations (Section 1.4). Finally, as a lead-up to the scientific contribution and research questions, the demands, benefits, and current limitations of high spatio-temporal soil moisture estimates from remote sensing data are discussed (Section 1.5).

### 1.1 Motivation

The motivation for the research presented in this dissertation is based on the need for sustainable change, the growing availability of data to be analyzed, and the focus on one important aspect/parameter that influences all life on our planet. The need for change is driven by the increasing impacts of climate change and the need for greater sustainability. The growing availability of data to be analyzed is both a challenge and an opportunity for new innovations. Innovations are important to ensure the current quality of life while simultaneously increasing sustainability. Finally, the focus on **soil moisture** is based on the importance of fresh water, which is often referred to as the basis of all life on Earth (United Nations World Water Assessment Programme, 2018).

### Need for Sustainability and Increasing Climate Change Impacts

Our world has been changing at an unprecedented rate on both regional and global scales over the past few decades. Political events (Brexit, conflict in Ukraine) (Martill, 2023; Vu et al., 2023), social changes (generation Z entering the labor market, interactions during the covid pandemic due to masks) (Larsen et al., 2018; Freud et al., 2020), technological advancements (artificial intelligence, blockchain) (Hussain and Al-Turjman, 2021), economic issues (trade wars, energy crises, inflation) (Fajgelbaum and Khandelwal, 2022; Carrière-Swallow et al., 2023), and environmental challenges (climate change) (Intergovernmental Panel on Climate Change (IPCC), 2022) influence our daily lives in various ways. As a society, we thus face enormous challenges in achieving self-set goals such as food security,

clean water provision, energy decarbonization, and mitigating and adapting to climate change impacts (Sachs et al., 2019).

In 2015, the United Nations General Assembly formulated 17 Sustainable Development Goals to help transform our world into a better living place and a more sustainable future (United Nation General Assembly, 2015). An initial effort to quantify the sustainability of human lifestyles was made in 1972 by a small group of researchers at Massachusetts Institute of Technology (Meadows et al., 1972). They analyzed growing trends in the world population, industrialization, pollution, food production, and the consumption of non-sustainable natural resources, reaching the at the time controversial conclusion that humanity would reach the limits of our planet within the next hundred years (Meadows and Meadows, 2007; Bardi, 2011).

In 1992, William Rees introduced a new calculation method to measure the ecological footprint in an effort to visualize the planet's limits and the current demands of humanity (Rees, 1992). Today's estimates by Wackernagel and Beyers (2019) indicate that we already reached the Earth's annual biological capacity to regenerate (one Earth's worth of resources) in 1970. The estimates for 2022 suggest that today 1.75 Earths are required to sustainably provide the consumed resources and absorb the waste produced by humanity (Lin et al., 2022). This means that the ecological footprint has increased by 75% since 1970 and by 1.2% from 2021 to 2022 (Lin et al., 2022). Under a business-as-usual scenario (population and consumption growth), the Global Footprint Network projects that by 2030, two planets would be necessary to sustain humanity's needs (Global Footprint Network, 2015).

Furthermore, on basis of calculations for the special Intergovernmental Panel on Climate Change (IPCC) (2018) report on 1.5°C from 2018, the United Nations believe that we have only until 2030 to prevent irreversible damage from climate change impacts. Although the estimated numbers and methods have been controversial since the 1970s, the majority of researchers now agree that we overuse our planet's resources (Intergovernmental Panel on Climate Change (IPCC), 2021). Despite decades of warnings from scientists about the overuse of our planet's resources, a broad public discussion of sustainable development (meeting the needs of the present without jeopardizing the prosperity of future generations (Mitra, 2016)) has emerged only in recent years.

The initiation of adaptation strategies and changes to our predominantly Western lifestyle to create a more sustainable society (considering social, environmental, and economic resources) was delayed by decades. As a result of our consumption and lifestyle, we are now experiencing severe environmental changes due to climate change impacts (Intergovernmental Panel on Climate Change (IPCC), 2019). Given the negative consequences experienced around the world, it is unsurprising that a broad range of researchers, politicians, economists, and the general public believe that adapting to climate change and transitioning to a more sustainable society might be the greatest challenge our generation faces.

## Growth and Benefit of Earth Observation Data

An insight report from 2024 by the World Economic Forum estimates the economic benefit from Earth Observation (EO) data at \$266 billion in 2023 (World Economic Forum and Deloitte, 2024). This amount is expected to increase to more than \$700 billion by 2030. Thus, EO offers a potential cumulative economic benefit of \$3.8 trillion to the global gross domestic product from 2023 to 2030 while simultaneously having positive impacts on climate and nature (World Economic Forum and Deloitte, 2024). By far, the largest sector for EO's potential global economic value is agriculture, followed by mining (oil and gas), government (public and emergency services), electricity and utilities, supply chain and transport, and insurance. Agriculture alone accounts for \$399 billion, which correspond to over 50% of the projected global economic value (World Economic Forum and Deloitte, 2024). Moreover, the agricultural sector has the potential to reduce annual greenhouse gas emissions by 27 million tonnes of  $CO_2$  equivalent. Counting only the five leading EO applications with direct climate benefits (early warning, environmental impact monitoring, route optimization, precision farming, and supply chain monitoring) EO applications has the potential to reduce more than 2 gigatons (Gt) of  $CO_2$  equivalent annually by 2030. Furthermore, the reduction in greenhouse gas emissions might be underestimated, as indirect effects are not accounted for. However, the modeled emission reduction of 2 Gt  $CO_2$  is equivalent to approximately 3.6% of the global emissions in 2024 (World Economic Forum and Deloitte, 2024).

If we look at only the global satellite imaging market, a value of \$3.27 billion in 2022 and \$4.16 billion in 2023 are estimated. Furthermore, the satellite imaging market is expected to increase to \$14.18 billion by 2030, which corresponds to a compound annual growth rate of 19% (Fortune Business Insights, 2023). Currently, considering only the top two commercial imaging companies, the amount of data from satellites exceeds 100 terabytes (TBs) per day for 365 days per year (Fortune Business Insights, 2023). Thus, it is not surprising that a report from Analysis Mason, the global leader in satellite and space market research, estimates EO-introduced satellite and space application traffic at 787 petabytes (PBs) in 2022. A forecast predicts the generation of more than 2 exabytes (EB) by 2032, which corresponds to a compound annual growth rate of 11% (Oni, 2024). On the basis of these growth rates and the enormous numbers, it is highly likely that EO data will become increasingly important to life on Earth.

Given the expected amount of data volume, issues such as storage and EO data provision to users are highly important. Thus, in 2023, the European Union launched the Copernicus Data Space Ecosystem, a new initiative to create one of the world's largest EO offerings. The Copernicus Data Space Ecosystem aims not only to provide open access data download capabilities but also to offer possibilities for cloud-based EO data processing to enhance the usage of freely available EO. Currently, the Copernicus Data Space Ecosystem grants access to over 50 PBs of EO data (new and historical Sentinel, Landsat, Soil Moisture and Ocean Salinity (SMOS), and other Copernicus Contribution Mission data) and is expected to grow to over 100 PBs within the next six years (CloudFerro S.A., 2024).

In summary, based on these numbers, the immense potential of EO applications is evident, but it might be surprising that a study of World Economic Forum and Deloitte (2024) conclude that the potential has not yet been fully realized.

## **Water/Soil Moisture as One of the Most Important Variables in the Earth's System**

Climate change will have a considerable impact on the availability and usage of the most precious resource we have on our planet "water", or more precisely, "freshwater" (Mishra, 2023). Different studies have concluded that, owing the increasing demand for our freshwater resources, the socio-economic impacts might be as large as the impacts of climate change (Fischer et al., 2007; den Besten et al., 2021). Furthermore, with expected population growth to approximately 9.7 billion by 2050 (United Nations Department of Economic and Social Affairs, 2022), the demand for freshwater will increase. The global water demand for industry, domestic, and agriculture is projected to increase by 20% to 30% by 2050 (Burek et al., 2016). Moreover, projections for 2050 estimate an increase in food demand of 60% (United Nations World Water Assessment Programme, 2018).

As agriculture alone already accounts for 70% of global water usage (Boretti and Rosa, 2019), the importance of sufficient water availability cannot be emphasized enough. Although enough freshwater for agriculture and other human needs is available globally and annually, spatial and temporal variations in water accessibility and demand lead to water scarcity in some regions (Mekonnen and Hoekstra, 2016). Thus, mainly due to geographic and temporal mismatches between freshwater demand and availability approximately four billion people live with (temporary) water scarcity worldwide (Mekonnen and Hoekstra, 2016). Hence, it is not surprising that the World Meteorological Organization has added soil moisture to the list of 50 Essential Climatic Variables recommended for systematic observation (World Meteorological Organization, 2010).

However, the actual mapping of high-resolution soil moisture from space is challenging because of its high spatial and temporal variability and the complexity of the derivation procedure. In agricultural regions, soil and crop conditions fluctuate throughout the day, on a daily basis, and across different seasons. Furthermore, challenges due to temporal changes and spatial variations (field-to-field and intra-field variances) present difficulties in mapping and monitoring soil moisture and other soil and crop characteristics. Nevertheless, reliable large-scale high-resolution soil moisture information is a key factor in determining if and how much food can be produced.

As water can often be a scarce resource and agriculture requires much water at the right moment, knowledge about daily soil moisture changes is essential. Thus, to reduce water consumption, soil moisture information is vital for enabling highly efficient irrigation and smarter decision-making in agriculture. Furthermore, knowledge about spatially and temporally distributed soil moisture is especially needed as climate change impacts change the availability of water on temporal and spatial scales (United Nations World Water Assessment Programme, 2018; Intergovernmental Panel on Climate Change (IPCC), 2019).

Moreover, changes in precipitation patterns due to climate change effects require adaptation strategies worldwide (Dai et al., 2018).

In summary, with a rapidly changing world (climate change), the importance of high-resolution soil moisture information and the possibility of enhancing soil moisture estimates by analyzing a large amount of (upcoming) EO data, research to provide high spatial and temporal distributed soil moisture maps is necessary and has significant impact potential.

## 1.2 Definition of Soil Moisture

In general, soil moisture is defined as the amount of water within a soil sample. However, different disciplines (agriculture, meteorology, or hydrology) use the term soil moisture in slightly different ways. For example, the American Meteorological Society (AMS) defines soil moisture as the total amount of water in unsaturated soil (Seneviratne et al., 2010). In simple hydrological models, soil moisture is often defined similarly to the definition provided by the AMS. However, more complex hydrological models, such as Water balance Simulation Model (WaSiM) (Schulla and Jasper, 2015), may differentiate between soil moisture in the root zone and soil moisture in the unsaturated zone. Regardless, the relevant water for agricultural purposes is the soil moisture of the root zone, as this water is available for plants (Iqbal et al., 2020). In terms of soil moisture estimates from remote sensing data, the term soil moisture generally refers to the water within the upper 5 cm to 10 cm of the soil (Lakhankar et al., 2009). Nevertheless, sometimes more precise terminology, such as surface soil moisture, is used within the remote sensing community (Loew et al., 2006). Hence, if not specified with terms such as surface, root zone, or unsaturated soil, the commonly used term soil moisture might lead to misunderstandings. Therefore, for clarification, if the term "soil moisture" is used here, it refers to the water within the upper 5 cm to 10 cm of the soil, as the primarily used remote sensing data (Sentinel-1) can only detect surface soil moisture. A summary and graphical overview of the different layers of the soil are shown in Figure 1.

Mathematically speaking, soil moisture is described on either a volumetric ( $m_v$ ) or gravimetric ( $m_g$ ) basis as:

$$m_v = \frac{v_w}{v_t} \quad (1.1)$$

$$m_g = \frac{m_{wet} - m_{dry}}{m_{dry}} \quad (1.2)$$

$$m_v = m_g * \frac{\sigma_{soil}}{\sigma_{water}} \quad (1.3)$$

where  $v_w$  is the water volume,  $v_t$  is the total volume,  $m_{wet}$  is the mass of the wet soil sample,  $m_{dry}$  is the mass of the dry soil sample,  $\sigma_{soil}$  is the dry bulk density of the soil, and  $\sigma_{water}$  is the density of water (Shukla et al., 2014; Kashyap and Kumar, 2021). Although soil moisture is dimensionless, it is often expressed in units of  $[g/g]$ ,  $[m^3/m^3]$ ,  $[g/m^3]$ , or, if multiplied by 100, as a volume percentage. Although soil moisture accounts for only 0.05%

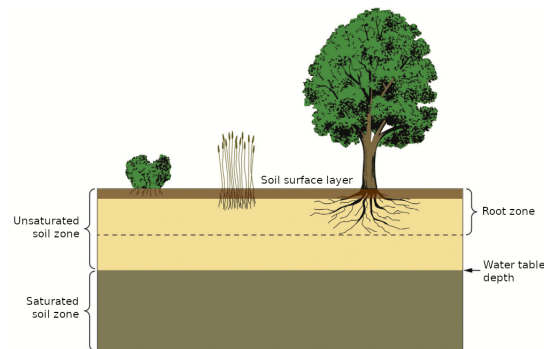


Figure 1: Schematic diagram of the unsaturated and saturated soil zones (adapted from Petropoulos et al. (2015)).

of the freshwater within the hydrological cycle, its importance is undisputed (Dingman, 2008). The upper 5 cm to 10 cm of soil and the proportion of water in it (0.0012% of the total Earth's water (Brogi et al., 2023)) might seem insignificant, but it is vital for agricultural plant growth and thus for our survival (Sutanto et al., 2022). Furthermore, the small amount of water in this thin layer is a key factor in the entire water cycle and thus influences and is highly intertwined with rainfall distributions, surface water, groundwater, vegetation growth, ecosystem health, and climate conditions (Zhang et al., 2020).

### 1.3 Soil Moisture in Agriculture

By nature, water and agriculture are intertwined. Water is a determinant factor for agricultural production, and several agriculture related processes affect the hydrological cycle in terms of evapotranspiration, precipitation, groundwater recharge, and runoff (Kashyap and Kumar, 2021). In agriculture, the optimum availability of moisture in the soil is vital for processes such as seed germination, plant growth, and nutrient cycling (Hou et al., 2022; Bauke et al., 2022). Thus, to reduce dependence on natural rainfall, large areas (approximately 20% of croplands) are irrigated (Brocca et al., 2018). The area equipped with irrigation nearly doubled within the last 50 years and is responsible for around 40% of food production (Scheierling and Treguer, 2016). Currently, approximately 70% of freshwater withdrawals are used for irrigation, making the agricultural sector the world's largest water user (Fischer et al., 2007; Campbell et al., 2017). Nevertheless, the large amount of irrigation used poses a major threat to water resources in many parts of the world.

Furthermore, changing conditions in terms of temporal and spatial water availability due to climate change can be observed. Thus, adaptation strategies (change in crop type and irrigation efficiency) need to be evaluated (Loboguerrero et al., 2019). Additionally, with expected population growth from 8 billion (in 2022) to approximately 9.7 billion by 2050 and 10.4 billion by 2100 (United Nations Department of Economic and Social Affairs, 2022), the demand of freshwater for electricity, industry, households, and especially

agriculture will further increase. For the development of adaptation strategies and the efficient use of available water resources, systematic large-scale observations of soil moisture are essential.

However, soil moisture changes are highly affected by land topography, inhomogeneity of soil properties, and non-uniformity of rainfall and evapotranspiration (Weng, 2016). Thus, the systematic observation of soil moisture, especially for agricultural purposes, is challenging because of the interaction of high-resolution demands and the high natural variability of soil moisture in space and time. An overview of different soil moisture dependent agricultural areas/processes and their respective spatial and temporal resolution demands is given in Figure 2. As indicated in Figure 2, information about crop phenology and crop yield is relevant mostly from weekly (change in phenology) to seasonal and annual (crop yield) time intervals. On a spatial scale, field to sub-field resolutions are required to provide phenology and crop yield information at the farmer level.

Nevertheless, since there is a global wheat market (production, demand, and price have a global effect), crop yield information and predictions at regional to global scales are important for food security reasons (Iizumi et al., 2018; Abbas et al., 2020). Information about the mortality of plants is usually required at a higher resolution (sub-field) than phenology, but the temporal resolution spans from weekly to almost annual. On the other hand, irrigation has a large span in terms of spatial and temporal resolution. Irrigation management starts at the sub-field scale for individual farmers but can reach regional dimensions. For example, the largest combined irrigation area is the Indus Basin Irrigation System, with 26.02 million hectares (mha) in India and Pakistan (Khan and Adams, 2019). Additionally, the time constraint of irrigation spans due to climate and individual seasonal soil moisture dynamics from sub-daily (irrigation of fields) to seasonal (water allocation and usage at a later time) (Salman et al., 2001; Phung et al., 2022). Individual farmers require the highest spatial resolution for their fieldwork (e.g., precision farming applications).

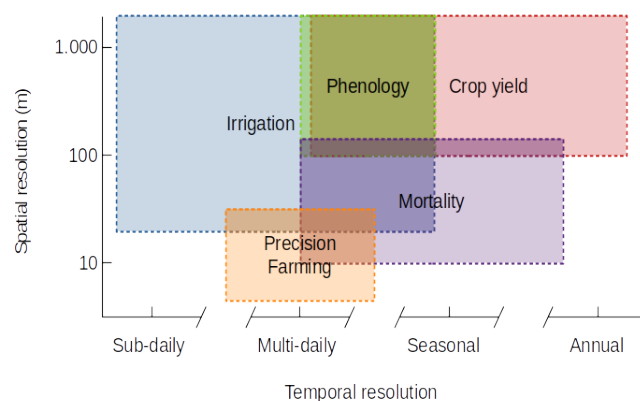


Figure 2: Categorization of parameters that define crop development and important applications in agriculture, based on their required temporal and spatial resolutions (adapted from Konings et al. (2019)).

Precision farming can be applied only if sub-field to meter resolution is available.

Moreover, information about soil and crop status must be available at the right time (daily to weekly basis) (Finger et al., 2019). The benefit of high-resolution soil moisture information for farmers is the easy and quick determination of whether the use of heavy machinery is possible under certain moisture conditions or to find the perfect time (in terms of soil moisture) for seed sowing or fertilization. Efficient nitrogen fertilization, including nitrogen uptake by plants and reducing nitrogen-related greenhouse gas emissions, is highly dependent on soil moisture conditions (Liang, 2022; Gao and Cabrera Serrenho, 2023).

Furthermore, information from soil moisture monitoring systems can help farmers with optimal decision-making in terms of crop selection or if activities such as drainage are needed (den Besten et al., 2021). The monitoring of soil moisture not only helps to effectively plan and manage agricultural processes but also provides information about crop health and moisture retention, which are important indicators of sustainable agroecosystems (Kashyap and Kumar, 2021). A previous study by Vanino et al. (2018) revealed that, especially in drought situations, farmers tend to overirrigate and misuse water resources. Thus, in areas where water is often a scarce resource, reliable soil moisture and crop status information will help farmers reduce water consumption and optimize their irrigation practices on the basis of soil matric potential (Thompson et al., 2007).

Nevertheless, as irrigation or other agricultural practices are mostly time sensitive, the provision of continuous (e.g., daily) information is vital (Shannon et al., 2018). Additionally, the use of soil moisture information by farmers is highly affected by product costs, accessibility, reliability, and usage simplicity. Furthermore, without expected efficiency improvements and thus economic savings potential and seamless integration of the information into easy decision-making processes for farmers, a soil moisture product will not be used (Tebbs et al., 2016). Even though soil moisture is an important parameter and might serve as an indicator, additional information about the crops (biomass, phenology stages, etc.) is often needed to determine a full picture of agricultural fields (Hosseini and McNairn, 2017).

Thus, the development of a usable soil moisture product for farmers or an even more advanced platform with additional field information will likely require contributions from the scientific community and the private sector (Tebbs et al., 2016). Additionally, building historical data will help farmers determine if a change in crop type might be favorable. In addition to farmers, on a larger scale, policy and other decision-makers rely on soil moisture information for agricultural regions (Zhang et al., 2021). Droughts and flooding, as examples of events that can cause harvest failures, might change the global crop price, thus, national economic security might require a change in import-export strategies (Tebbs et al., 2016).

## 1.4 Soil Moisture Monitoring with Microwave Remote Sensing Techniques

As traditional in-situ soil moisture measurements are expensive and usually involve point measurements, they fall short of providing large-scale information. However, with advances in technology, especially in the field of remote sensing, it is possible to monitor changes at regional to global scales from space. Today, a variety of different airborne and satellite systems (optical, microwave, and thermal) provide the opportunity to improve Earth observations in terms of ground coverage and spatio-temporal resolution.

In terms of soil moisture, microwave remote sensing images were found to be highly suitable (Engman, 1991). Compared with optical remote sensing applications (aerial photography has been used since the late 1800s), microwave remote sensing is a fairly new profession, with civilian use starting in the early 1960s (Ulaby and Long, 2014). As optical and microwave radiation are located in different wavelength ranges of the electromagnetic spectrum (Figure 3), each of them offers a unique view of the Earth's environment. In contrast to optical remote sensing, microwave remote sensing has certain advantages. First, especially active microwave signals are independent of sun illumination, and they are able to penetrate clouds (Dwivedi et al., 2000). Therefore, microwave remote sensing data can be recorded at any time of day and under almost all weather conditions (Woodhouse, 2006). Furthermore, microwave signals are not only able to penetrate clouds but can also penetrate vegetation and, to some extent, even the upper soil layer (Beale et al., 2021). The actual penetration depths of vegetation and soil depend on several factors such as the wavelength or the amount of water in the plants and the soil (Baur et al., 2018).

In general, microwave remote sensing can be separated into active (radar, SAR) and passive (radiometry) sensors. Whereas active radar measures the reflected energy of a

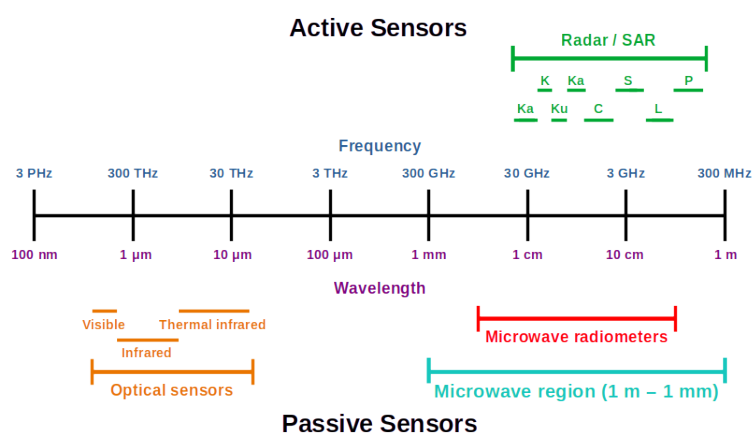


Figure 3: Electromagnetic spectrum with active and passive remote sensor information.

self-emitted microwave, passive radiometers measure the natural energy emitted from the land surface (brightness temperature) (Richards, 2009). Passive remote sensing satellites provide coarse spatial resolutions (usually 10 to 50 km), whereas SAR as active sensor, is able to provide much higher spatial resolutions (Wagner et al., 2007). Passive radiometers are commonly used for monitoring climate and environmental parameters such as soil moisture, sea surface temperature, sea ice concentration, rainfall, and atmospheric water vapor. Owing to the higher possible resolution, SAR data are used in applications such as terrain mapping, disaster monitoring, agriculture (precision farming, crop monitoring, soil moisture estimation, and vegetation health assessment), forestry, glacier and ice monitoring, and urban planning (Ulaby and Long, 2014). A history of spaceborne active and passive microwave sensors for soil moisture estimation is given in Figure 4.

The reason for the use of microwave remote sensing to determine soil moisture is the high dependency of electromagnetic radiation on the dielectric properties of the soil-water mixture (Ulaby and Long, 2014). Thus, changes in soil moisture can be related to measured soil scattering and emission changes from remote sensing sensors (Engman, 1991). In general, an increase in the dielectric constant of the soil results in a radar backscatter increase, thus, backscatter and soil moisture are positively correlated (Champion, 1996). The remote sensing information in terms of brightness temperature (passive) and radar backscatter (active), depends not only on soil moisture but also on other radar system parameters (wavelength, incidence angle, azimuth angle, and polarization). More detailed information on incidence and azimuth angle changes in regard to RT model estimation of soil moisture from Sentinel-1 can be found in Publication II.

Earth surface characteristics (surface roughness, soil texture, topography, vegetation structure, and water content) also influence radar signals (Bousbih et al., 2018). Moreover, the parameters themselves and their sensitivity to the radar signal are influenced by each other. For example, studies have shown that the sensitivity of the radar signal to surface roughness increases with increasing incidence angle (Mattia et al., 2003). Additionally, the influence of different moisture conditions (wet soil, dry soil), vegetation conditions (fully grown, dormant), and incidence angle changes on radar backscattering changes non-linearly (Wagner et al., 1999a). The effects of the various dependencies are shown in Figure 5. Moreover, variables such as the soil bulk density and soil texture affect the dielectric properties of the soil as well. The water-holding capacity of the soil changes based on the soil texture. It was found that the higher amount of free water in sandy soil compared to clay soils results in a higher Pearson correlation of soil moisture and radar backscatter (Kong and Dorling, 2008; Srivastava et al., 2006). Additionally, the presence of vegetation cover reduces the backscatter sensitivity to the soil and thus the soil moisture. In general, the soil moisture sensitivity decreases with increasing density and height of the vegetation layer. However, various factors such as vegetation biomass, canopy type, and crop conditions (especially VWC), influence the effect of vegetation (Kornelsen and Coulibaly, 2013; Petropoulos et al., 2015). Studies have shown that the sensitivity of a C-band radar to soil moisture conditions within a wheat field highly increases during the ripening of wheat plants, thus the vegetation cover (approximately 1 m in height) was found to be almost invisible for C-band microwaves with high incidence angles (Weiß et al.,

## 1.4 Soil Moisture Monitoring with Microwave Remote Sensing Techniques 11

2021). In summary, owing to the different dependencies and impacts of radar, soil, and vegetation characteristics, soil moisture retrievals are difficult without detailed knowledge of these parameters (Das and Paul, 2015).

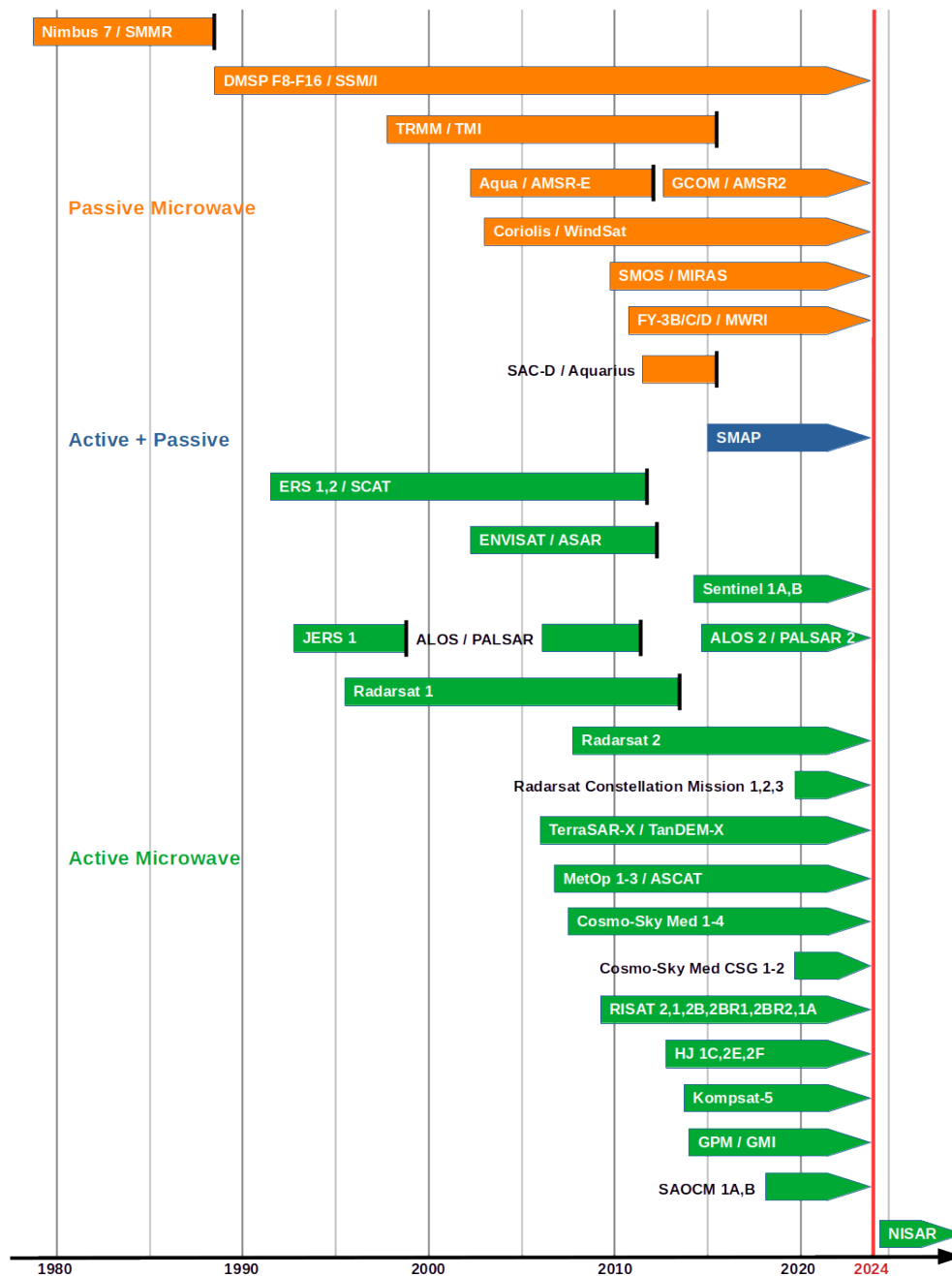


Figure 4: Timeline of spaceborne active and passive microwave sensors for soil moisture retrieval (adapted from Kim et al. (2019)).

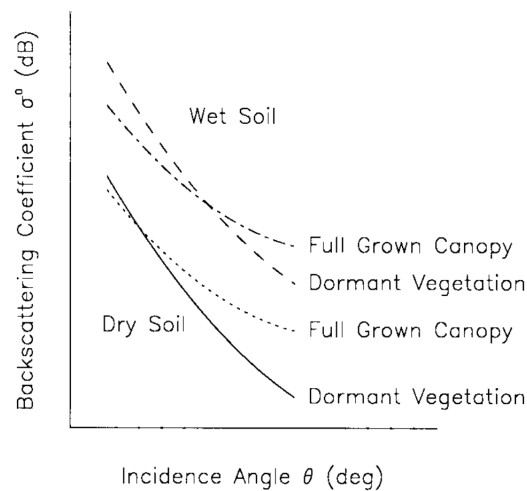


Figure 5: Schematic overview of backscatter changes based on incidence angle, soil moisture, and vegetation status (Wagner et al., 1999a).

In recent decades, the influences of radar, soil, and vegetation characteristics have been investigated through numerous experimental and theoretical studies in the active and passive microwave domains. This has led to the development and improvement of different sensor techniques and retrieval approaches (Ulaby and Long, 2014; Wagner et al., 2007). Given that the availability of detailed knowledge of soil and vegetation characteristics differs greatly, different methods for soil moisture estimation ranging from empirical/semi-empirical/theoretical RT models, change detection, polarimetric decomposition, statistical approaches, to data fusion and machine learning, have been developed. This dissertation focuses on the most commonly used RT models and their potential to estimate soil moisture from Sentinel-1 C-band.

## 1.5 Demands, Benefits, and Current Limitations of Soil Moisture Estimates from Remote Sensing Data

Despite the challenges and limitations in deriving accurate soil moisture estimates from microwave remote sensing satellites, various disciplines, including hydrology, ecology, meteorology, agriculture, and climate science, already benefit from existing coarse to medium-resolution soil moisture data products, as high-resolution products remain scarce (Seneviratne et al., 2010; Chaparro et al., 2016). Currently available global-scale soil moisture products typically feature coarse grid spacing and extensive temporal coverage, predominantly derived from passive sensors. In contrast, datasets with higher spatial resolutions usually originate from active SAR sensors, although they may have limited spatial coverage. A summary of publicly available satellite-derived soil moisture datasets from both

passive and active microwave sensors is presented in Table 1.

The demand for soil moisture products varies depending on the application and its spatial and temporal requirements. Figure 6 provides an overview of application areas and their specific temporal and spatial resolution requirements, along with associated remote sensing soil moisture missions. Soil moisture is crucial for determining land-atmosphere interactions; thus, hydrologists require accurate soil moisture information to enhance weather and climate forecasting models. Additionally, understanding soil moisture dynamics is essential for linking terrestrial water, energy, and carbon cycles, which significantly impact the climate system. Weather patterns and climate variability are also heavily influenced by soil moisture conditions. Furthermore, soil moisture serves as a key parameter in hydrological models, influencing surface runoff, streamflow, and water recharge. Its effects on land surface processes, atmospheric moisture content, precipitation patterns, and the hydrological cycle make soil moisture a crucial parameter in climate models, whose predictions assess

Table 1: Summary of publicly available satellite-derived soil moisture products, updated and extended from Peng et al. (2021a). The table entries are sorted by spatial coverage, grid spacing, and temporal coverage. Data links have been last accessed on Oct. 11, 2024.

Institution	Temporal coverage	Spatial coverage	Temporal resolution	Grid spacing	Sensor	Data link	Reference
Vrije Universiteit Amsterdam	1978-1987	global	2-3 days	0.25 deg	SMMR	<a href="https://www.geo.vu.nl/~jeur/lprm/">https://www.geo.vu.nl/~jeur/lprm/</a>	Owe et al. (2001); Holmes et al. (2009)
Vrije Universiteit Amsterdam	1987-1999	global	2-3 days	50 km	SSM/I	<a href="https://www.geo.vu.nl/~jeur/lprm/">https://www.geo.vu.nl/~jeur/lprm/</a>	Owe et al. (2008); Holmes et al. (2009)
ESA	1996-2001	global	1-2 days	25/50 km	ERS-2	<a href="https://earth.esa.int/eogateway/activities/scirocco">https://earth.esa.int/eogateway/activities/scirocco</a>	Wagner et al. (1999b); Crapolicchio et al. (2016)
Vrije Universiteit Amsterdam	1998-2015	global	2-3 days	50 km	TRMM-TMI	<a href="https://www.geo.vu.nl/~jeur/lprm/">https://www.geo.vu.nl/~jeur/lprm/</a>	Owe et al. (2008); Holmes et al. (2009)
Vrije Universiteit Amsterdam	2002-2011	global	1-3 days	25 km	AMSR-E	<a href="https://www.geo.vu.nl/~jeur/lprm/">https://www.geo.vu.nl/~jeur/lprm/</a>	Owe et al. (2008); Holmes et al. (2009)
NASA	2002-now	global	daily	25 km	AMSR-E, AMSR-2	<a href="https://nsidc.org/data/au_land/versions/1">https://nsidc.org/data/au_land/versions/1</a>	Kim et al. (2015)
CESBIO	2003-2011	global	daily	15/25 km	SMOS, aAMSR-E	<a href="https://www.catds.fr/Products/Products-over-Land/L4-Soil-Moisture-from-AMSR-E-SMOS-synergie-using-Neural-Networks">https://www.catds.fr/Products/Products-over-Land/L4-Soil-Moisture-from-AMSR-E-SMOS-synergie-using-Neural-Networks</a>	Rodríguez-Fernández et al. (2016)
EUMETSAT H-SAF	2007-now	global	1-2 days	12.5/25/50 km	ASCAT	<a href="https://hsaf.meteoam.it/Products/ProductsList?type=soil_moisture">https://hsaf.meteoam.it/Products/ProductsList?type=soil_moisture</a>	Bartalis et al. (2007); Wagner et al. (2013)
CESBIO	2010-now	global	1-2 days	25 km	SMOS	<a href="https://www.catds.fr/Products/Availabile-products-from-CEC-SM/SMOS-IC">https://www.catds.fr/Products/Availabile-products-from-CEC-SM/SMOS-IC</a>	Jacquette et al. (2010); Rodríguez-Fernández et al. (2016)
ESA	2010-now	global	1-2 days	15 km	SMOS	<a href="https://smos-dis.eo.esa.int/oads/access/">https://smos-dis.eo.esa.int/oads/access/</a>	Jacquette et al. (2010); Rodríguez-Fernández et al. (2016)
BEC	2010-now	global	daily	15/25 km	SMOS	<a href="https://bec.icm.csic.es/">https://bec.icm.csic.es/</a>	González-Zamora et al. (2015)
NASA	2011-2015	global	7 days	1 deg	Aquarius	<a href="https://nsidc.org/data/aquarius">https://nsidc.org/data/aquarius</a>	Bindlish et al. (2015)
JAXA	2012-now	global	2-3 days	50 km	AMSR-2	<a href="https://suzaku.eorc.jaxa.jp/GCOM_W/data/data_w_index.html">https://suzaku.eorc.jaxa.jp/GCOM_W/data/data_w_index.html</a>	Kim et al. (2015)
NASA	2015-now	global	1-2 days	3/9/36 km	SMAP	<a href="https://nsidc.org/data/smap/data">https://nsidc.org/data/smap/data</a>	Entekhabi et al. (2010)
NASA	2015-now	global	1-2 days	1/3 km	SMAP/Sentinel-1	<a href="https://nsidc.org/data/smap/data">https://nsidc.org/data/smap/data</a>	Das et al. (2019)
ESA	1978-2019	global	daily	0.25 deg	Merged Active+Passive Microwave Sensors (ESA CCI)	<a href="https://www.esa-soilmoisture-cci.org/">https://www.esa-soilmoisture-cci.org/</a>	Dorigo et al. (2017); Gruber et al. (2017, 2019)
NOAA	2012-now	global	6 hours	0.25 deg	Merged Active+Passive Microwave Sensors (SMOPS)	<a href="https://www.ospo.noaa.gov/Products/land/smops/">https://www.ospo.noaa.gov/Products/land/smops/</a>	Liu et al. (2016)
EUMETSAT H-SAF	2007-now	Europe	1-2 days	1 km	ASCAT	<a href="https://hsaf.meteoam.it/Products/Detail?prod=H08">https://hsaf.meteoam.it/Products/Detail?prod=H08</a>	Wagner et al. (2013); Brocca et al. (2017)
LMU	2015-2020	Germany	hourly	1 km	RADOLAN	<a href="https://zenodo.org/record/6489998">https://zenodo.org/record/6489998</a>	Ramsauer et al. (2021)
TPDC	2003-2019	China	daily	1 km	AMSR-E, AMSR-2, MODIS	<a href="https://data.tpdc.ac.cn/en/data/e1f24e35-6235-40b2-b3d7-677dfb249e39/">https://data.tpdc.ac.cn/en/data/e1f24e35-6235-40b2-b3d7-677dfb249e39/</a>	Song et al. (2022)
ESA	2015-now	Europe	1.5-4 days	1 km	Sentinel-1	<a href="https://land.copernicus.eu/global/products/ssm">https://land.copernicus.eu/global/products/ssm</a>	Bauer-Marschallinger et al. (2019)
CNR	2015-2018	Southern Italy	6-12 days	1 km	Sentinel-1	<a href="https://zenodo.org/record/5006307">https://zenodo.org/record/5006307</a>	Balenzano et al. (2021)
Theia	2016-2021	19 sites in Europe	6 days	1 km	Sentinel-1, Sentinel-2, Land Cover SEC	<a href="https://www.theia-land.fr/en/ceslist/soil-moisture-with-very-high-spatial-resolution-sec/">https://www.theia-land.fr/en/ceslist/soil-moisture-with-very-high-spatial-resolution-sec/</a>	El Hajj et al. (2017)

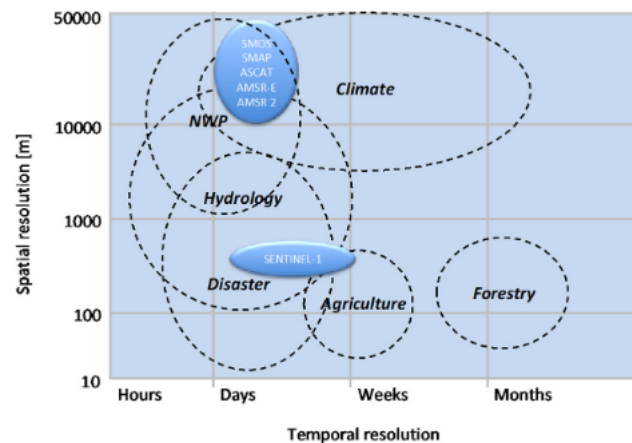


Figure 6: Classification of application areas based on soil moisture information, categorized by their temporal and spatial resolution requirements, and allocated to microwave remote sensing missions (Peng et al., 2021a).

climate change impacts on terrestrial ecosystems, water resources, and extreme weather events. Currently, high-resolution soil moisture estimates at regional to global scales are scarce or non-existent. Consequently, the soil moisture estimates derived from remote sensing, currently used for climate modeling, numerical weather prediction, and hydrological applications, typically exhibit coarse spatial resolutions. While soil moisture information with a spatial resolution of 1 km or coarser may suffice for some applications, disaster management (e.g., flooding, drought, and wildfire risk estimations), precision farming, and forest management necessitate higher spatial resolutions ( $<1$  km) (Gruber and Peng, 2023; Liu and Yang, 2022).

Although not yet utilized for climate models or numerical weather prediction, the availability of high-resolution soil moisture information has the potential to enhance model predictions (Nayak et al., 2018). Areas with diverse land surface characteristics would benefit significantly from such information due to the substantial impact of land surface conditions on model outcomes (Trier et al., 2004; Osuri et al., 2017). Moreover, high-resolution soil moisture data could improve the monitoring and forecasting of extreme hydrological events (O et al., 2022). The demand for soil moisture information, particularly high-resolution data, is further increasing in response to severe climate change impacts worldwide (Holsten et al., 2009).

As illustrated in Figure 6, sectors such as natural disaster management, agricultural activities (e.g., precision farming), and forest management require high spatial resolution at varying temporal scales. Changes in soil moisture within forested areas, even if seasonal, can stress specific tree types, reducing resilience to pests and diseases (Mina et al., 2022). Thus, modern forest management relies on current soil moisture information and future estimates to enhance biomass productivity and mitigate forest health risks by adjusting tree composition in response to changing climate conditions (Cholet et al., 2022). While

temporal resolution may not be as crucial for forests, spatial resolution is essential.

Conversely, disaster management and the assessment and prevention of flooding, drought, or wildfires are regionally diverse and heavily depend on high spatial and temporal resolution data (U.S. Global Change Research Program (USGCRP), 2017; Saco et al., 2021). Water resources are managed based on soil moisture information, especially in regions vulnerable to water scarcity or flooding. Operational flood monitoring and prediction models necessitate high temporal resolution soil moisture data, as flood forecasting relies on time-sensitive soil moisture values. For effective drought monitoring and early flood warning systems, high-resolution data and real-time or near-real-time information availability are essential (Liu and Yang, 2022). High-resolution soil moisture estimates can support mitigation strategies and are vital for decision-making in administrative and public services.

As detailed in Section 1.3, soil moisture information is invaluable for enhancing agricultural productivity. Remote sensing technologies can provide farmers with real-time soil moisture conditions, allowing them to optimize irrigation and fertilization practices. Given that soil moisture can vary significantly within fields due to factors such as soil texture, compaction, topography, vegetation cover, and management practices, high spatial resolution is crucial. Additionally, high temporal resolution and near-real-time processing are particularly important during specific growing stages.

In terms of soil moisture retrieval, higher spatial resolution presents unique challenges in mapping small-scale changes in vegetation, surface roughness, and water content and their effects on radar signals (Peng et al., 2021a). Unlike operationally derived coarse-to-medium resolution soil moisture products, operationally derived soil moisture information with high spatial resolution ( $<1$  km), comparable temporal coverage, and retrieval quality is not yet available (Sabaghy et al., 2018; Peng et al., 2021a). However, with the launch of the first Sentinel-1 satellite in 2014, the availability of high-resolution SAR data with global coverage has opened new possibilities for soil moisture retrieval at regional and continental scales (Balenzano et al., 2012; Alexakis et al., 2017). Based on Sentinel-1 images, the Copernicus Global Land Service launched an operational soil moisture product with 1 km resolution covering Europe (Bauer-Marschallinger et al., 2019). Other regional-scale prototypes for soil moisture retrieval with 1 km resolution using Sentinel-1 include datasets from Italy's Consiglio Nazionale delle Ricerche (CNR) covering southern Italy (Balenzano et al., 2021) and datasets from Theia (El Hajj et al., 2017) covering various test sites across Europe. Despite the European Space Agency (ESA) announcement in 2022 regarding issues with the Sentinel-1 B satellite, which is no longer operational, the twin satellite Sentinel-1 A remains functional. Furthermore, Sentinel-1 C (launch date 2024) and Sentinel-1 D (launch date  $\geq 2025$ ) are set to continue providing high-resolution SAR data for the next decade. Alongside the Sentinel-1 satellites, other partially commercial missions, such as Radarsat, the Advanced Land Observing Satellite-2 (ALOS-2), and Satellite Argentino de Observacion COm Microondas (SAOCOM), also provide high-resolution microwave data. Given the recognized importance of high-resolution SAR information for estimating land surface parameters and monitoring Earth changes (land, ocean, ice) (Hajnsek and Desnos, 2021), additional satellite missions such as NASA-ISRO Synthetic Aperture Radar (NISAR) (planned launch date 2025, S- and L-band), the Radar Observing System

for Europe L (ROSE-L, planned launch date 2028, L-band), and Tandem-L (considered launch  $\geq 2029$ ) are also in development.

Despite numerous studies, the availability of new satellite data, and other advancements in the field of soil moisture retrieval from space, significant challenges remain, particularly regarding high spatial and temporal resolutions (Zeng et al., 2023). These challenges include improving spatial coverage, acquiring data over longer consistent time spans, achieving higher temporal resolutions and shorter time lags (with the launch of more satellites such as Sentinel-1 C and D), and enhancing spatial resolution (new SAR systems) and frequency coverage (e.g., L-band data from NISAR). Moreover, substantial efforts are needed to improve model performance, soil moisture accuracy, and the understanding of radar scattering changes throughout the vegetation period, as well as the development of products that estimate soil moisture at multiple depths. Research is also necessary to determine how SAR images obtained with different observation geometries and/or from different sensors can be integrated within a single retrieval framework to enhance temporal resolution. Additionally, investigating the transferability of high-resolution retrieval approaches for regional to global applications, the provision of near-real-time information, and simplifying usability for end users (e.g., farmers) are crucial issues that must be addressed. Despite these challenges, the continuous data provided by Sentinel-1 imagery and upcoming missions present unprecedented opportunities to develop operational applications for estimating high-resolution soil moisture at a global scale (Balenzano et al., 2012; Pandey et al., 2021). Thus, the research questions and original research presented in the following Chapters 2 and 3 aim to advance the provision of high spatial and temporal soil moisture estimates for smart farming applications.

# Chapter 2

## Research Questions

In this dissertation, the primary focus is on the analysis and improvement of model performance (Research Questions (RQs) I and II) and the accuracy of soil moisture estimates (RQ VI) for high-resolution soil moisture retrievals. The use of synthetic aperture radar (SAR) images with varying observation geometries (RQs III and V), as well as the understanding of scattering changes throughout the vegetation period (RQ IV), are also key areas of investigation. Additionally, this dissertation explores retrieval approaches that promote high transferability from test areas, facilitating regional or even global applications. Ultimately, this research aims to contribute towards providing high spatial and temporal soil moisture estimates for smart farming applications.

Given the importance of high spatio-temporal soil moisture estimates, especially in agriculture, the following research questions were formulated.

- **RQ I:** Can existing microwave radiative transfer RT models accurately simulate high spatio-temporal Sentinel-1 VV-polarized radar backscatter throughout the entire wheat growing season?
- **RQ II:** To what extent do the simulated Sentinel-1 VV-polarized radar backscatter results differ among empirical, semi-empirical, and physically-based RT models?
- **RQ III:** What specific characteristics are observed in dense Sentinel-1 time series with varying acquisition geometries, and how do these geometries influence the simulated RT model outcomes?
- **RQ IV:** How do different incidence and azimuth angles in Sentinel-1 images affect the emergence of distinct scattering mechanisms?
- **RQ V:** Can a modified RT model effectively simulate a dense Sentinel-1 time series comprising images with varying observation geometries?
- **RQ VI:** Can high-resolution soil moisture estimates over agricultural fields be derived using microwave and optical remote sensing data in conjunction with microwave RT models?

RQs I, II, and VI serve as the initial questions, while RQs III, IV, and V are guided by the insights gained from the research conducted on RQs I and II.

# Chapter 3

## Publications

This dissertation comprises three peer-reviewed scientific publications (Publications I, II, and III) and two peer-reviewed research software packages (Publications IV and V). Publications I, II, III, and IV have already been published, whereas Publication V has been submitted to the Journal of Open Source Software. The scientific research presented in this dissertation aims to contribute to the development and enhancement of high spatio-temporal soil moisture estimates across agricultural regions. For potential global applicability, the methods investigated are based on data that can be operationally derived from various remote sensing sensors.

The evaluation of different RT models (Publication I) and an analysis of the potential applications of a dense Sentinel-1 time series (Publication II) serve as foundational work for Publication III, which ultimately produces and validates a high spatio-temporal soil moisture time series over an agricultural area using two years of in-situ measurements. Research questions (RQs) I and II are addressed in Publication I. RQs III, IV, and V are explored in Publication II. Finally, RQ VI constitutes the main objective of Publication III. In addition to the scientific insights gained from Publications I, II, and III, the production and provision of open-source software (Publications IV and V), which were essential for conducting this research, represent a significant contribution of this thesis. Publication IV details the development of an automated pipeline for preprocessing Sentinel-1 SLC data using the ESA SNAP Sentinel-1 Toolbox, designed for use by other researchers (ReadTheDocs documentation: <https://multiply-sar-pre-processing.readthedocs.io/en/latest/>). Publication V summarizes various microwave RT models (ReadTheDocs documentation: <https://sense-community-sar-scattering-model.readthedocs.io/en/latest/>) and provides a Python package that allows researchers to easily implement different surface and canopy RT models for their own applications. A graphical summary of the dissertation, illustrating the connections between the publications and research questions, is presented in Figure 7.

The following sections include a brief introduction, detailed author contributions, and information about the scientific journals for each publication. Additionally, short transitions between publications will weave a storyline and describe the significance and impact of each research publication. Prior to Publications IV and V (open-source Python software), an overview of the software and its importance for the execution of scientific research will be provided.

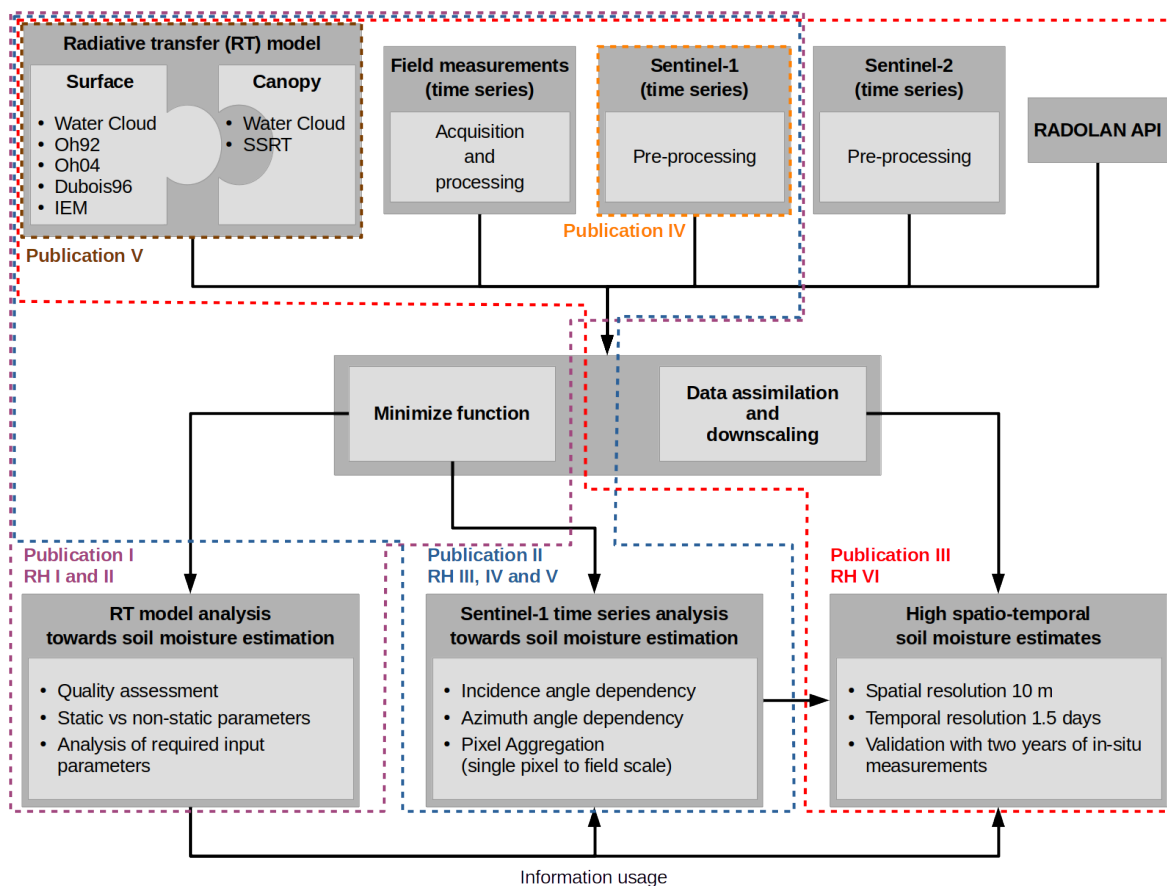


Figure 7: Schematic overview of the dissertation. The dashed line indicates the subject as well as the input data and method used for each publication.

## 3.1 Publication I: Evaluation of Different Radiative Transfer Models for Microwave Estimation of Wheat Fields

**Reference:** Weiß, T., Ramsauer, T., Löw, A., Marzahn, P., 2020. Evaluation of Different Radiative Transfer Models for Microwave Backscatter Estimation of Wheat Fields. *Remote Sensing* 12, 3037. doi:10.3390/rs12183037

**Status:** published

**Plain language summary:** Over the past half-century, various microwave RT models, which link radar backscatter to soil moisture, have been developed and extensively analyzed. A key purpose of RT models is to simulate the interaction between radar waves and soil or vegetation, facilitating the retrieval of biophysical land surface parameters. The complexity of these models varies, ranging from simple empirical models to semi-empirical and physically-based approaches.

This study reviews and evaluates six commonly used RT models, focusing on their ability to simulate radar backscatter from a dense Sentinel-1 C-band time series at field scale (100 m), with a revisit time of 1.5 days. In addition to comparing the models, the study examines backscatter trends throughout the entire wheat growing season. The findings indicate that when using soil moisture, the Leaf Area Index (LAI) as a vegetation descriptor, and a static empirical parameter, all models fail to accurately simulate the observed increase in backscatter during the latter half of the growing season. The observed increase in backscatter is driven by changes in VWC, which alters the canopy's transmissivity. As a result, the transmissivity calculations within the models were adjusted to incorporate a temporally dynamic empirical parameter, replacing the static one. The dense time series analyzed includes images with varying satellite acquisition geometries (e.i., different azimuth and incidence angles). Despite the overall improvement in modeling the backscatter increase, a persistent trend mismatch remains between the modeled and observed backscatter at consecutive time points with differing acquisition geometries.

**Author contributions:** Conceptualization, T.W. and A.L.; Methodology and formal analysis, T.W.; Software, T.W. and A.L.; Writing-original draft preparation, T.W., Writing-review and editing, T.W., T.R. and P.M.; Resources, T.W. and T.R.; Visualization, T.W.; Supervision, A.L and P.M.; Project administration, A.L. and P.M.; Funding acquisition, A.L.

**Journal:** *Remote Sensing* - MDPI (Special Issue: Remote Sensing of Regional Soil Moisture)

**Impact factor:** 4.848

**CiteScore:** 6.6

Article

# Evaluation of Different Radiative Transfer Models for Microwave Backscatter Estimation of Wheat Fields

Thomas Weiß <sup>\*</sup> , Thomas Ramsauer , Alexander Löw  and Philip Marzahn 

Department of Geography, Ludwig-Maximilians-Universität München, Luisenstraße 37, 80333 Munich, Germany; t.ramsauer@iggf.geo.uni-muenchen.de (T.R.); alexander.loew@lmu.de (A.L.); p.marzahn@iggf.geo.uni-muenchen.de (P.M.)

\* Correspondence: weiss.thomas@lmu.de

Received: 28 July 2020; Accepted: 10 September 2020; Published: 17 September 2020

**Abstract:** This study aimed to analyze existing microwave surface (Oh, Dubois, Water Cloud Model “WCM”, Integral Equation Model “IEM”) and canopy (Water Cloud Model “WCM”, Single Scattering Radiative Transfer “SSRT”) Radiative Transfer (RT) models and assess advantages and disadvantages of different model combinations in terms of VV polarized radar backscatter simulation of wheat fields. The models are driven with field measurements acquired in 2017 at a test site near Munich, Germany. As vegetation descriptor for the canopy models Leaf Area Index (LAI) was used. The effect of empirical model parameters is evaluated in two different ways: (a) empirical model parameters are set as static throughout the whole time series of one growing season and (b) empirical model parameters describing the backscatter attenuation by the canopy are treated as non-static in time. The model results are compared to a dense Sentinel-1 C-band time series with observations every 1.5 days. The utilized Sentinel-1 time series comprises images acquired with different satellite acquisition geometries (different incidence and azimuth angles), which allows us to evaluate the model performance for different acquisition geometries. Results show that total LAI as vegetation descriptor in combination with static empirical parameters fit Sentinel-1 radar backscatter of wheat fields only sufficient within the first half of the vegetation period. With the saturation of LAI and/or canopy height of the wheat fields, the observed increase in Sentinel-1 radar backscatter cannot be modeled. Probable cause are effects of changes within the grains (both structure and water content per leaf area) and their influence on the backscatter. However, model results with LAI and non-static empirical parameters fit the Sentinel-1 data well for the entire vegetation period. Limitations regarding different satellite acquisition geometries become apparent for the second half of the vegetation period. The observed overall increase in backscatter can be modeled, but a trend mismatch between modeled and observed backscatter values of adjacent time points with different acquisition geometries is observed.

**Keywords:** Oh; Dubois; IEM; WCM; SSRT; SAR; soil moisture; LAI; wheat; Sentinel-1

## 1. Introduction

Soil moisture plays an important role in land surface processes, such as water and energy fluxes. Therefore, soil moisture is a key variable in scientific fields like climatology, hydrology, meteorology, or agriculture [1,2]. In recent decades, microwave data has proven to be a suitable tool for long-term soil moisture derivation of large areas and different land cover types [3–9]. The retrieved soil moisture information is widely used in applications, like climate modeling, precision farming, water management, flood forecast, and drought monitoring [10–14]. With different available Synthetic Aperture Radar (SAR) data from different sensors and for different usage in terms of absolute accuracy and spatial scale, various soil moisture retrieval approaches, like change detection, microwave data fusion (active and passive), differential Synthetic Aperture Radar (SAR) interferometry, or

SAR polarimetry, are available [15]. Furthermore, land surface parameters, like soil moisture, can be also derived by using Radiative Transfer (RT) models. Starting in 1974 [16], with the first publication examining radar response and soil moisture [17], hundreds of different studies developing and/or analyzing new or existing RT models have been conducted. RT models try to simulate the interaction of the radar wave with the soil and the vegetation to derive different soil and vegetation parameters [18]. Complexities in RT models for surface backscatter calculations range from simple empirical regression-based models [18–21] and different empirical models based on the Water Cloud approach (WCM surface part) [22–25], over semi-empirical models from Oh (Oh92, Oh04) [26,27] or Dubois (Dubois95), [28] to physical-based models, like the Integral Equation Model (IEM) in its original form [29] or refined versions [30–32]. Common RT models for canopy backscatter calculations range from empirical models, like Water Cloud Model (WCM canopy part) [22], to more sophisticated and multi-layered models, like the Michigan Canopy Scattering Model (MIMICS) [33], Tor Vergata model [34], Single Scattering Radiative Transfer (SSRT) models described by De Roo [35] or Ulaby [17], or a first order scattering model from Quast [36,37]. Despite the large numbers of existing models, there is still the need of an algorithm generating soil moisture maps with acceptable accuracy of 3–4% [17].

So far, several studies have been carried out to test and compare pure surface RT models [15,38–42]. Research analyzing radar backscatter calculations and soil moisture retrieval approaches of combined surface and canopy RT models has been performed. For these studies different test sites, land cover types, and vegetation descriptors were used [25,43–55]. Investigations on how different vegetation descriptors, like Leaf Area Index (LAI), Vegetation Water Content (VWC), Leaf Water Area Index (LWAI), normalized Plant Water Index (PWI), or Normalized Different Water Index (NDWI), affect soil moisture retrievals have been carried out, as well [25,48,53,54]. In this context, synergistic retrieval approaches by using vegetation descriptors derived from optical sensors as input data for microwave RT models have been published more and more in recent years [45,52,56–61].

Despite the existing analyses, a study testing and comparing different surface and canopy RT model combinations with focus on the interaction between surface and canopy part and advantages or disadvantages of the model combinations is missing. The launch of Sentinel-1A/B, and, therefore, the availability of free SAR data with high temporal and spatial coverage, constitutes a suitable basis for such an analysis. Investigations of the usage of dense Sentinel-1 time series with observations up to every 1.5 days in terms of future synergistic retrieval approaches of SAR and optical data are needed. The models and the knowledge gained from this paper shall be used within a newly developed platform called MULTIPLY, which combines data from different optical and microwave satellites by using state-of-the-art RT models within a data assimilation framework to consistently acquire and interpret different land surface parameters.

This study was performed on time series data with high temporal and spatial (field scale) resolution. The surface RT models WCM, Oh92, Oh04, Dubois95, and IEM were coupled with canopy models WCM or SSRT. With these model combinations, VV polarized backscatter values for an entire vegetation period of different wheat fields was calculated. The different input variables for the model combinations, such as soil moisture, canopy height, LAI, or soil properties, were provided by field measurements. For other parameters, like surface roughness or single scattering albedo, suitable literature values were chosen. LAI was used as vegetation descriptor because of available field measurements and its straight forward derivation from optical sensors [62–64]. The remaining empirical parameters were calibrated by comparing modeled backscatter with Sentinel-1 backscatter values. In summary, this paper aimed to

- investigate different RT model combinations and assess their advantages and disadvantages;
- evaluate if different radar acquisition geometries are modeled adequately with the used RT models; and
- serve as preliminary work for future synergistic retrieval approaches of SAR and optical sensors with a focus on high spatial and temporal resolutions.

Section 2 presents the used dataset. Section 3 summarizes the used RT models. In Section 4, calibration and validation results are shown and discussed. Finally, the main conclusions are drawn in Section 5.

## 2. Datasets

### 2.1. Study Area

The study area, Munich North Isar (MNI), is located in southern Germany (Bavaria), near Munich ( $48^{\circ}13'N$ – $48^{\circ}20'N$ ,  $11^{\circ}39'E$ – $11^{\circ}45'E$ , Figure 1). Since 2014, almost every year from spring until autumn, different field campaigns targeting agricultural purposes were carried out [65–68]. From March to September 2017, an intensive field campaign focusing on maize and wheat fields for validation of soil and vegetation parameter retrievals from Sentinel-1, Sentinel-2 and the future EnMAP satellite was conducted. MNI is characterized by intensive agriculture with wheat, maize, and grassland as main crop types. In close vicinity ( $<10$  km) to the test site two meteorological stations, Freising (470 m a.s.l.) and Eichenried (475 m a.s.l.) managed by the Bavarian State Research Institute (LFL) and one meteorological station Munich-airport (446 m a.s.l.) managed by the German Meteorological Service (DWD) are situated. The annual measured mean temperature for 2017 ranges between  $9^{\circ}C$  (Freising) and  $9.3^{\circ}C$  (Eichenried). The average annual precipitation for 2017 reached 753 mm (Munich-airport) to 853 mm (Eichenried). The used data for this study includes field campaign data of wheat fields from 2017 (Section 2.2) and Sentinel-1 satellite data (Section 2.3).

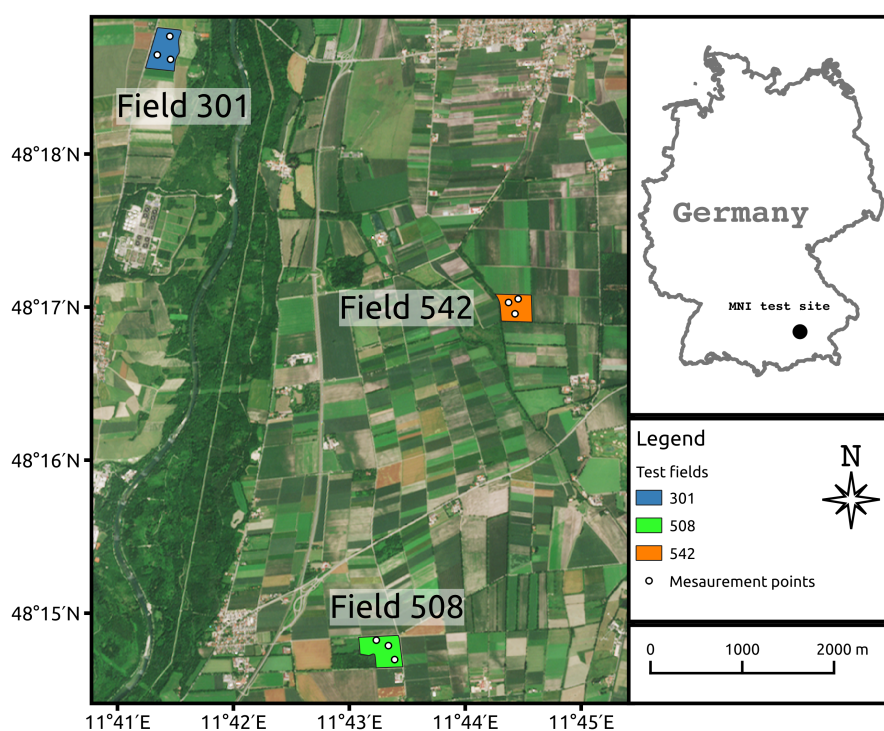


**Figure 1.** Overview of study area Munich-North-Isar (MNI) located in southern Germany (Bavaria). Three wheat test fields—508 (green), 542 (orange), and 301 (blue)—with three measurement points each of the field campaign in 2017 are highlighted. Reference system: WGS84 (EPSG:4326)

### 2.2. Field Data

During the MNI field campaign of 2017, weekly field measurements of different biophysical parameters (Table 1) were conducted. The total LAI was measured with a LI-COR Biosciences LAI-2200C device (LI-COR Biosciences Inc., Lincoln, NE, USA) as an average of 14 measurements

from the same area. The measurements were taken within each test field at three different locations (Figure 1). The accuracy of LAI in terms of mean standard deviation of repeated measurements ranges within the fields between 0.45 and 0.52. The monitoring period started end of March and ended shortly before the fields were almost simultaneously harvested in mid of July. Additionally, Decagon TM5 soil moisture sensors using the capacity method were installed permanently within the first five centimeters of the soil surface. Soil moisture changes were monitored with a time interval of 10 min. Information about the soil was provided by earlier campaigns when soil samples were taken from the fields, and the soil properties were analyzed in the laboratory (Table 2). The soils bulk density with  $1.45 \pm 0.13 \text{ g/cm}^3$ , and the clay content with  $7.38 \pm 1.8\%$ , show no high variability between the different fields. The sand content, on the other hand, shows higher variability, with  $24.08 \pm 10.46\%$ .

**Table 1.** Acquisition time, time interval, and range of dynamic in-situ measurements.

Variable	Acquisition Time	Time Interval	Range
Canopy height [cm]	03/24–07/17/2017	weekly	7–105
LAI	03/24–07/17/2017	weekly	0.35–6.25
Soil moisture [ $\text{m}^3/\text{m}^3$ ]	03/24–07/17/2017	continues	0.09–0.38

**Table 2.** Laboratory results for sand, clay, and bulk content of soil surface samples.

Variable	Time Interval	Mean	Std
Soil sand content [%]	once (several locations)	24.08	10.46
Soil clay content [%]	once (several locations)	7.38	1.80
Bulk density [ $\text{g/cm}^3$ ]	once (several locations)	1.45	0.13

### 2.3. Satellite Data

For this study, C-band Sentinel-1 SLC data of Sentinel-1A/B was used. The Sentinel data was pre-processed with ESA's SNAP Toolbox Version 7.0.3. An overview of all applied pre-processing steps is given in Figure 2. For the geometric correction, SRTM data with 1 arc-second resolution was chosen as digital elevation model input. Afterward, the radiometric correction method of Kellndorfer et al. [69] was applied. In a second pre-processing step, a multi-temporal Lee-sigma filter was used for speckle reduction. The temporal filter was applied on each image with information of 6 other images (three before the target and three after) with a spatial window size of  $5 \times 5$  pixels, a sigma of 0.9, and a target window size of  $3 \times 3$  pixels. For the period of the field campaign in 2017 (March to July), in total, 78 Sentinel images covering the study area are available. Considering images with different orbit directions (ascending and descending) and different incidence angles (ranges from  $35^\circ$  to  $45^\circ$ ) a revisit time of 1.5 days was archived. The spatial resolution of the processed data was  $10 \times 10 \text{ m}$ . A more detailed overview of the used Sentinel-1 dataset and the image properties is given in Table 3. The primary acquisition mode of Sentinel-1 provides data with polarization VV and VH. For our study, the focus was set on polarization VV due to findings that, for retrieving soil moisture, the usage of VH alone or in addition to VV is not suitable for well-developed vegetation [45,70].

**Table 3.** Available Sentinel-1A/B satellite data for MNI field campaign period in 2017 (03/23–07/17/2017).

Asc./Desc.	Incidence Angle [°]	Relative Orbit	Amount	Revisit Time [Days]	Acquisition Time
Ascending	36	44	19	6	4:58 p.m.
	45	117	19	6	5:06 p.m.
Descending	43	95	20	6	5:17 a.m.
	35	168	20	6	5:25 a.m.

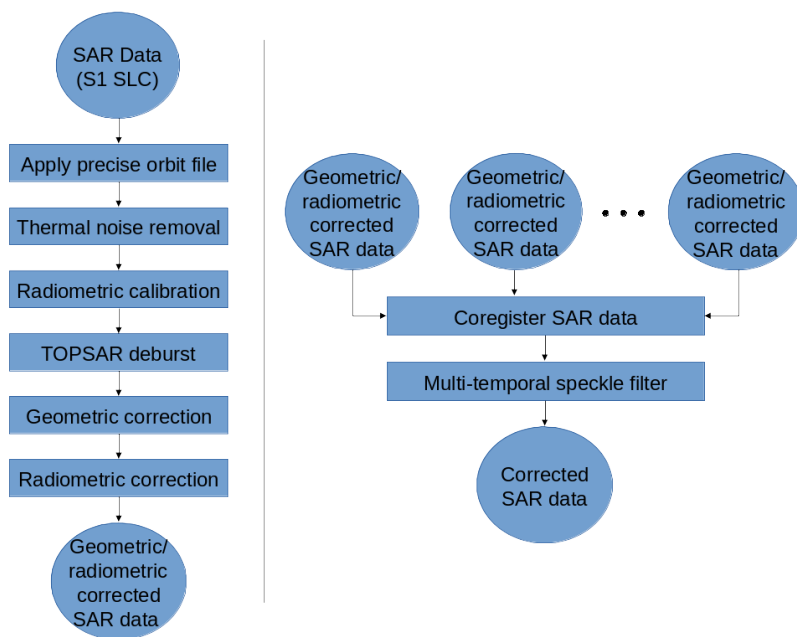


**Figure 2.** Schematic overview of SNAP pre-processing steps to retrieve geometric and radiometric corrected images from Sentinel-1 SLC data (left). Pre-processing steps for speckle reduction using a multi-temporal speckle filter (right).

### 3. Microwave Radiative Transfer Models

#### 3.1. Surface RT Models

##### 3.1.1. Empirical Water Cloud Model (WCM Surface Part)

The WCM, often referred to as the tau-omega model, was developed by Attema and Ulaby in 1978 [22]. For a given polarization  $pq$  ( $pq = HH, VV, \text{ or } HV$ ), the surface contribution  $\sigma_{spq}^0$  of WCM to the backscattered radar signal in dB scale is defined as

$$\sigma_{spq}^0 = C_{pq} + D_{pq} \cdot mv, \quad (1)$$

with empirical fitted soil parameters  $C_{pq}$  and  $D_{pq}$  and soil moisture content  $mv$ .  $C_{pq}$  is an empirical calibration constant, whereas  $D_{pq}$ , as a calibration factor, indicates the sensitivity of soil moisture on the received radar signal. The WCM surface part is a purely empirical model thus no additional information about surface roughness or incidence angle is needed. Therefore, the empirical parameters have to be calibrated for each test site separately.

##### 3.1.2. Semi-Empirical Oh Model 1992 (Oh92)

In 1992, Oh et al. [26] developed an approach for the retrieval of soil moisture and soil surface roughness by empirical determined functions. Based on scatterometer measurements and various ground measurements of soil moisture and surface roughness, two functions for the co- ( $p = \frac{\sigma_{sHH}^0}{\sigma_{sVV}^0}$ ) and cross-polarized ( $q = \frac{\sigma_{sHV}^0}{\sigma_{sVV}^0}$ ) backscatter ratios were fitted. Consequently,  $p$  and  $q$  are defined as

$$p = \frac{\sigma_{sHH}^0}{\sigma_{sVV}^0} = \left[ 1 - \left( \frac{2\theta}{\pi} \right)^{\frac{1}{3R_0}} \cdot e^{-ks} \right]^2 \quad (2)$$

and

$$q = \frac{\sigma_{sHV}^0}{\sigma_{sVV}^0} = 0.23 \sqrt{R_0} (1 - e^{-ks}), \quad (3)$$

with  $\theta$  as local incidence angle,  $k$  as radar wave number ( $k = 2\pi/\lambda$ ), where  $\lambda$  is the wavelength, and  $s$  as rms height.  $R_0$  is the Fresnel reflectivity coefficient at nadir given by

$$R_0 = \left| \frac{1 - \sqrt{\epsilon_r}}{1 + \sqrt{\epsilon_r}} \right|^2, \quad (4)$$

where  $\epsilon_r$  is the relative dielectric constant. The  $VV$  polarized backscatter coefficient  $\sigma_{sVV}^0$  is further defined as

$$\sigma_{sVV}^0 = 0.7 \left[ 1 - e^{-0.65(ks)^{1.8}} \right] \frac{\cos^3\theta}{\sqrt{p}} \left[ R_v(\theta) + R_h(\theta) \right], \quad (5)$$

with the Fresnel coefficients for horizontal  $R_h$  and vertical  $R_v$  polarization

$$R_h = \frac{\mu_r \cos\theta - \sqrt{\mu_r \epsilon_r - \sin^2\theta}}{\mu_r \cos\theta + \sqrt{\mu_r \epsilon_r - \sin^2\theta}}, \quad (6)$$

$$R_v = \frac{\epsilon_r \cos\theta - \sqrt{\mu_r \epsilon_r - \sin^2\theta}}{\epsilon_r \cos\theta + \sqrt{\mu_r \epsilon_r - \sin^2\theta}}, \quad (7)$$

where  $\mu_r$  is the relative permittivity. Furthermore, the backscatter coefficients  $\sigma_{sHH}^0$  and  $\sigma_{sHV}^0$  are given with respect to  $\sigma_{sVV}^0$ ,  $p$ , and  $q$  by

$$\sigma_{sHH}^0 = p \sigma_{sVV}^0, \quad (8)$$

$$\sigma_{sHV}^0 = q \sigma_{sVV}^0. \quad (9)$$

The model in its original form can be applied for the retrieval of soil moisture or soil surface roughness for bare soil conditions at several frequencies (X- to L-Band) and a broad range of incidence angles (10–70°). Because it is a semi-empirical model, the validity range of the model in terms of soil moisture and soil surface roughness is defined with  $0.1 < ks < 6$ , and  $9 \text{ Vol.\%} < mv < 31 \text{ Vol.\%}$ .

### 3.1.3. Semi-Empirical Oh Model 2004 (Oh04)

In 2004, Oh [27] revised and simplified his original approach to use only soil moisture ( $mv$ ) as an independent variable rather than  $R_0$  and  $\epsilon_r$  (Section 3.1.2). Thus, if using  $mv$  as input variable, no additional information about the soil properties (bulk density, sand and clay content) is needed. The model is defined by

$$p = \frac{\sigma_{sHH}^0}{\sigma_{sVV}^0} = 1 - \left( \frac{2\theta}{\pi} \right)^{0.35} mv^{-0.63} \cdot e^{-0.4 (ks)^{1.4}}, \quad (10)$$

$$q = \frac{\sigma_{sHV}^0}{\sigma_{sVV}^0} = 0.095 (0.13 + \sin^{1.5}\theta)^{1.4} [1 - e^{-1.3 (ks)^{0.9}}], \quad (11)$$

$$\sigma_{sHV}^0 = 0.11 mv^{0.7} (\cos\theta)^{2.2} [1 - e^{-0.32 (ks)^{1.8}}]. \quad (12)$$

Oh04 is optimized for bare soils with  $0.13 < ks < 6.98$ ,  $4 \text{ Vol.\%} < mv < 29.1 \text{ Vol.\%}$  and  $10^\circ < \theta < 70^\circ$ .

### 3.1.4. Semi-Empirical Dubois Model (Dubois95)

Dubois et al. [28] proposed, in 1995, an empirical approach to determine backscatter values for  $HH$  and  $VV$  polarizations based on soil moisture, soil surface roughness, and system parameters, like local

incidence angle, wavelength, and frequency. Two non-linear equations were fitted to measured backscatter values obtained by a scatterometer for a broad range of frequencies ranging from 2.5 GHz to 11 GHz and incidence angles ranging from 30° to 60°. The backscatter values can be calculated by

$$\sigma_{sHH}^0 = 10^{-2.75} \frac{\cos^{1.5}\theta}{\sin^5\theta} 10^{0.028 \epsilon_r \tan\theta} (ks \cdot \sin\theta)^{1.4} \lambda^{0.7}, \quad (13)$$

$$\sigma_{sVV}^0 = 10^{-2.37} \frac{\cos^3\theta}{\sin^3\theta} 10^{0.046 \epsilon_r \tan\theta} (ks \cdot \sin\theta)^{1.1} \lambda^{0.7}. \quad (14)$$

The Dubois model was optimized for bare soil conditions and has a validity range for soil moisture of  $mv \leq 35$  Vol.% and soil surface roughness of  $ks \leq 2.5$ .

### 3.1.5. Physical Integral Equation Model (IEM)

The IEM is a theoretical backscattering model and was developed by Fung et al. [29] in 1992. Since then, Fung and colleagues extended the IEM to bistatic scattering [71]. The general co-polarized backscatter coefficient  $\sigma_{pp}^0$  for  $pp = VV$  or  $HH$  is defined as

$$\sigma_{spp}^0 = \frac{k^2}{4\pi} e^{k^2 s^2 \cos^2\theta} \sum_{n=1}^{\infty} |I_{pp}^n|^2 \frac{W^n(2k \sin\theta, 0)}{n!}, \quad (15)$$

where  $I_{pp}^n$  is

$$I_{pp}^n = (2ks \cos\theta)^n f_{pp} e^{-k^2 s^2 \cos^2\theta} + (ks \cos\theta)^n F_{pp}, \quad (16)$$

with  $W^n$  as the Fourier transform of the  $n$ th power of the surface correlation function  $p(x, y)$ . Furthermore, the backscatter at cross polarization  $\sigma_{sHV}^0$  is calculated as

$$\sigma_{sHV}^0 = \frac{k^2}{16\pi} e^{-2k^2 s^2 \cos^2\theta} \sum_{n=1}^{\infty} \sum_{m=1}^{\infty} \frac{(k^2 s^2 \cos^2\theta)^{n+m}}{n!m!} \int [|F_{HV}(u, v)|^2 + F_{HV}(u, v) F_{HV}^*(-u, -v)] W^n(u - k \sin\theta, v) W^m(u + k \sin\theta) dudv. \quad (17)$$

The Kirchhoff coefficients  $f_{HH}$ ,  $f_{VV}$  and complementary field coefficients  $F_{HH}$ ,  $F_{VV}$ ,  $F_{HV}$  are given as

$$f_{HH} = \frac{2R_h}{\cos\theta}, \quad (18)$$

$$f_{VV} = \frac{2R_v}{\cos\theta}, \quad (19)$$

$$F_{HH} = 2 \frac{\sin^2\theta}{\cos\theta} [4R_h - (1 - \frac{1}{\epsilon_r}(1 + R_h)^2)], \quad (20)$$

$$F_{VV} = 2 \frac{\sin^2\theta}{\cos\theta} [(1 - \frac{\epsilon \cos^2\theta}{\mu_r \epsilon_r - \sin^2\theta})(1 - R_v)^2 + (1 - \frac{1}{\epsilon_r})(1 + R_v)^2], \quad (21)$$

$$F_{HV}(u, c) = \frac{Uv}{k \cos\theta} [\frac{8R^2}{\sqrt{k^2 - u^2 - v^2}} + \frac{-2 + 6R^2 + \frac{(1+R)^2}{\epsilon_r} + \epsilon_r(1 - R)^2}{\sqrt{\epsilon_r k^2 - u^2 - v^2}}], \quad (22)$$

with Fresnel coefficient at horizontal  $R_h$  (Equation (6)) and vertical  $R_v$  (Equation (7)) polarization thus  $R$  is described by

$$R = \frac{R_v - R_h}{2}. \quad (23)$$

The Fourier transform of the  $n$ th power of the surface correlation coefficient  $W^n(a, b)$  is calculated by

$$W^n(a, b) = \frac{1}{2\pi} \int \int p^n(x, y) e^{-i(ax+by)} dx dy. \quad (24)$$

The distribution of surface correlation function  $p(x, y)$  can be described for low surface roughness as exponential and high surface roughness values as Gaussian by

$$p(x, y) = e^{-\left(\frac{|x|+|y|}{L}\right)} \text{ (exponential),} \quad (25)$$

$$p(x, y) = e^{-\left(\frac{x^2+y^2}{L^2}\right)} \text{ (Gaussian),} \quad (26)$$

with  $L$  as correlation length.

### 3.2. Surface and Canopy RT Models

#### 3.2.1. Empirical Water Cloud Model (WCM)

The WCM [22] with respect to surface  $\sigma_{spq}^0$  and canopy  $\sigma_{cpq}^0$  contribution, as well as two-way attenuation  $T_{pq}^2$ , is defined as

$$\sigma_{pq}^0 = \sigma_{cpq}^0 + T^2 \sigma_{spq}^0, \quad (27)$$

whereas the canopy part  $\sigma_{cpq}^0$  in linear scale and the two-way attenuation  $T_{pq}^2$  are written as

$$\sigma_{cpq}^0 = A_{pq} V_1 \cos\theta (1 - T_{pq}^2), \quad (28)$$

$$T_{pq}^2 = e^{-2 B_{pq} V_2 \sec\theta}, \quad (29)$$

where  $\theta$  is the local incidence angle,  $V_1$  and  $V_2$  are empirical vegetation descriptors, and  $A_{pq}$ , as well as  $B_{pq}$ , are fitted parameters of the model which depend on the vegetation properties and the radar configuration. For  $\sigma_{spq}^0$  in Equation (27), each of the described surface models in Section 3.1 can be used.

#### 3.2.2. Semi-Empirical Single Scattering Radiative Transfer (SSRT) Model

The SSRT model used by De Roo [35] and Ulaby [17] is a semi-empirical first-order scattering model. The model is defined as

$$\sigma_{pq}^0 = \sigma_{g_{pq}}^0 + \sigma_{cpq}^0 + \sigma_{cgt_{pq}}^0 + \sigma_{gc_{g_{pq}}}^0, \quad (30)$$

where

$$\sigma_{g_{pq}}^0 = T_p T_q \sigma_{spq}^0, \quad (31)$$

with  $T_p$  and  $T_q$  as attenuation of the canopy for different polarizations and  $\sigma_{spq}^0$  describing the pure surface scattering mechanism. Similar to the definition of WCM in Section 3.2.1, all surface models described in Section 3.1 can be used for calculating the surface contribution  $\sigma_{spq}^0$  within SSRT. Furthermore, the  $p$  polarized one way transmittivity of the canopy  $T_p$  is defined as

$$T_p = e^{-\tau_p}, \quad (32)$$

with  $\tau_p$  as the  $p$  polarized attenuation of the canopy given by

$$\tau_p = k_e^p H \sec\theta, \quad (33)$$

whereas  $H$  represents the canopy height. The extinction coefficient  $k_e^p$  which accounts for the absorption and scattering losses of the electromagnetic wave through the canopy is defined as

$$k_e^p = k_a^p + k_s^p. \quad (34)$$

In general, a canopy consists of leaves, stalks, and branches with different shapes and orientations, which do not show a linear distribution in the vertical. However, in the applied SSRT, it is assumed

that  $k_e^p$ ,  $k_a^p$ , and  $k_s^p$  follow a uniform distribution in the vertical as a function of  $z$  within the canopy layer. In addition to the extinction coefficient, the scattering part  $k_s^p$  of  $k_e^p$  can be derived by

$$k_s^p = k_e^p \omega, \quad (35)$$

where  $\omega$  represents the single scattering albedo. For the direct backscattering contribution of the canopy  $\sigma_{c_{pq}}^0$ , Attema and Ulaby's [22] water cloud approach of identical scatterers, which are uniformly distributed within the volume, is used. Thus, multiple scattering effects are ignored. As a consequence, the volume backscattering coefficient  $\sigma_{V_{pq}}^{back}$  of the vegetation medium is defined as

$$\sigma_{V_{pq}}^{back} = N_v \sigma_{pq}^{back}, \quad (36)$$

with  $N_v$  as the number of scattering particles per unit volume and  $\sigma_{pq}^{back}$  as the  $pq$  polarized backscattering cross section of a single particle. Finally, the  $pq$  polarized canopy backscattering coefficient  $\sigma_{c_{pq}}^0$  within Equation (30) can be obtained from

$$\sigma_{c_{pq}}^0 = \frac{\sigma_{V_{pq}}^{back} \cos\theta}{k_e^p + k_e^q} (1 - T_p T_q). \quad (37)$$

Furthermore, ground/canopy ( $\sigma_{gc_{pq}}^0$ ) and canopy/ground ( $\sigma_{cg_{pq}}^0$ ) scattering contributions are defined as

$$\sigma_{gc_{pq}}^0 = \sigma_{v_{pq}}^{bist} H R_q T_p T_q, \quad (38)$$

$$\sigma_{cg_{pq}}^0 = \sigma_{v_{pq}}^{bist} H R_p T_p T_q, \quad (39)$$

where  $H$  is the canopy height,  $\sigma_{v_{pq}}^{bist}$  is the bi-static scattering cross section of a single leaf or stalk, and  $R_p$  describes the  $p$  polarized Fresnel reflectivity (Equations (6) and (7)). Thus, the total canopy ground contribution  $\sigma_{cgt_{pq}}^0$  within Equation (30) as the sum of  $\sigma_{gc_{pq}}^0$  and  $\sigma_{cg_{pq}}^0$  can be written as

$$\sigma_{cgt_{pq}}^0 = \sigma_{v_{pq}}^{bist} H [R_p + R_q] T_p T_q. \quad (40)$$

Furthermore, ground canopy ground contribution ( $\sigma_{gcg_{pq}}^0$ ) within Equation (30) is defined as

$$\sigma_{gcg_{pq}}^0 = \frac{\sigma_{V_{pq}}^{back} \cos\theta}{k_e^p + k_e^q} (R_p R_q - T_p T_q). \quad (41)$$

### 3.3. Practical Considerations

Each described model requires a different set of input parameters. A summary for the different RT models is given in Table 4. For some parameters, field measurements (Section 2.2) or literature values ( $s$  and  $\omega$ , Table 5) are used, and other site dependent parameters have to be fitted. The analyzed wheat fields were sown in autumn of 2016. By the starting point of the observation period (end of March 2017), the soil surface was already smoothed out by rain and the ground was covered by wheat plants (height > 10 cm). Marzahn et al. [72] showed that, for wheat fields with the above mentioned state, only minor changes in terms of roughness throughout the vegetation period are observable. Previous studies regarding periodic features and roughness changes [73,74] found out that changes in surface roughness due to soil rows as periodic feature within wheat fields are essential if the viewing angle is nearly perpendicular to the row orientation, but, for other viewing angles, the changes within surface roughness are negligible. The viewing angle and the row orientation of the wheat fields in our study are always  $<75^\circ$ . Therefore, changes due to periodic soil rows are assumed to be negligible. Typical roughness measurements of various winter wheat fields suggest rms values between 1.0 and

1.3 [72,73,75–78]. With the assumption of only minor roughness changes throughout the vegetation period, a literature value for surface height  $s$  of 1.2 cm was chosen. The value of 1.2 cm was used due to former field campaign measurements of wheat fields in Germany [72,73]. For single scattering albedo  $\omega$ , a common literature value of 0.03 [79] was set. The conversion from soil moisture field measurements to the required model input of dielectric constant  $\epsilon$  for models Oh92, Dubois95, and IEM was performed by using a dielectric mixing model for soils after Dobson et al. [80]. The required soil information about sand and clay content, bulk density (Table 2), and soil moisture (Table 1) were provided by field measurements and laboratory results. Additionally, for some parameters, in their original form, adjustments were made within this study. In particular, DeRoo et al. [35] used for parameterizing of the extinction coefficient  $k_e^p$  a combination of an empirical parameter, vegetation water mass and vegetation height. In our study, the vegetation water mass, and the vegetation height were replaced by total LAI. Therefore,  $k_e^p$  is defined by

$$k_e^p = coef * \sqrt{LAI}, \quad (42)$$

with  $coef$  as an empirical parameter. To reduce the required parameters for model IEM, a well-established approach of Baghdadi et al. [31,45] was used. The correlation length  $L$  was replaced by a fitted parameter  $Lopt$  which is dependent on  $s$ ,  $\theta$ , and the polarization.  $Lopt$  for C-band VV polarization data and the Gaussian correlation function after Baghdadi et al. [45] is defined as

$$Lopt(s, \theta, VV) = 1.281 + 0.134(\sin 0.19\theta)^{-1.59s}. \quad (43)$$

The refined version of Baghdadi is hereinafter referred to as IEM\_B. A schematic illustration of the RT model calibration approach is shown in Figure 3. All RT model combinations (surface + canopy) are driven by field measurements and the required empirical parameters (Table 4). The fitting of the empirical parameters was carried out by minimizing the sum of the squared error between modeled and measured (Sentinel-1) radar backscatter values. For the measured Sentinel-1 backscatter value of each measurement point shown in Figure 1, the mean backscatter of  $5 \times 5$  pixel ( $50 \times 50$  m) around the measurement location was chosen. In a first fitting approach, all parameters shown in Table 4 were defined to be static for the entire vegetation period. In a second fitting approach, WCM parameters  $C$ ,  $D$ , and  $A$  were set to be static; therefore, the mean (Table 5) of all model results of the static approach was used. The used values for the different parameters for validation are shown in Table 5. Additionally, the attenuation of the backscatter through the canopy was defined to be variable throughout the time series. More specifically, parameters  $coef$  within SSRT and  $B$  within WCM were fitted for each time step individually by taking three observations before and after into account. By making only  $coef$  or  $B$  variable, changes within the results can then clearly related to changes of the attenuation of the radar backscatter signal by the canopy. Field measurements used as model input parameters show multidimensionally unstructured inter- and intra-field correlations. Therefore, measurement point independency is assumed, and a validation of the parametrized RT models is performed using a leave-one-out cross-validation approach. Hereby, the parameter mean of the calibration results of eight measurement points is validated with the remaining measurement point.

**Table 4.** Overview of differences of surface models Water Cloud Model (WCM surface), Oh models Oh92 and Oh04, Dubois95, and Integral Equation Model refined version of Baghdadi (IEM\_B), as well as canopy models Single Scattering Radiative Transfer (SSRT) and WCM canopy, in terms of type, validity range, site dependency, required input parameters, and polarization. Separation of used input parameter of the analyzed Radiative Transfer (RT) models in fitted parameters and parameters where field measurements or literature values were used as input data.

	Type	Validity Range	Site Dependent	Required Parameters		Pol.
				Fitted	Field Measurements or Literature Values	
WCM surface	empi.	$10^\circ < \theta < 70^\circ$	Yes	<i>C, D</i>	$\theta, mv$	HH, VV VH
Oh92	semi-empi.	$10^\circ < \theta < 70^\circ$ $0.1 < ks < 6$ $9 < mv < 31Vol.%$	No		$s, k, \theta, \epsilon$ ( <i>clay, sand, bulk, mv</i> )	HH, VV VH
Oh04	semi-empi.	$10^\circ < \theta < 70^\circ$ $0.13 < ks < 6.98$ $4 < mv < 29.1Vol.%$	No		$s, k, \theta, mv$	HH, VV VH
Dubois95	semi-empi.	$30^\circ < \theta < 60^\circ$ $ks \leq 2.5$ $mv \leq 35Vol.%$	No		$s, k, \theta, \epsilon$ ( <i>clay, sand, bulk, mv</i> )	HH, VV
IEM_B	theoretical	$10^\circ < \theta < 70^\circ$ $ks \leq 3$	No		$s, k, l, \theta, \epsilon$ ( <i>clay, sand, bulk, mv</i> )	HH, VV VH
SSRT	semi-empi.		Yes	<i>ke (coef)</i>	$H, LAI, \theta, \omega$	HH, VV VH
WCM canopy	empi.		Yes	<i>A, B</i>	$V1 (LAI), V2 (LAI), \theta$	HH, VV VH

**Table 5.** Used model input parameters for validation.

<i>k</i> [cm <sup>-1</sup> ]	<i>s</i> [cm]	$\omega$	<i>C</i> [dB]	<i>D</i> [dB]	<i>A</i>
1.13	1.2	0.03	-14.61	12.88	0.0029

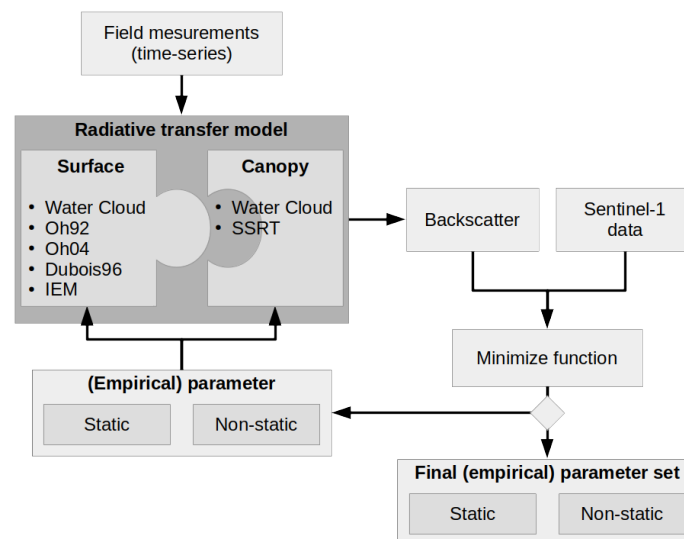


**Figure 3.** Schematic illustration of RT model calibration approach.

### 3.4. Differences Between Applied Models

WCM is a purely empirical model and depends, therefore, only on the calibrated empirical coefficients. It is applicable under almost all surface/vegetation conditions, but it has to be calibrated

for different test sites separately. The transferability to other test sites and or other surface/vegetation conditions is not possible. Surface models, like Oh92, Oh04, Dubois95, and IEM, were originally only developed for bare soil and or sparse vegetation conditions. Nevertheless, different studies replaced the surface component within WCM and SSRT with Oh [17,35,43,47], Dubois95 [51,54,55], or IEM/IEM\_B [17,45,53] models. One key advantage of the semi-empirical-based (Oh92, Oh04, Dubois95) or theoretical-based (IEM/IEM\_B) surface models in comparison to WCM is their better transferability to other test sites and surface/vegetation conditions. Models, like Oh92, Oh04, or Dubois95, are based on a hybrid construction with experimental data guided by trends predicted by theoretical models [17]. Theoretical models, like IEM/IEM\_B, on the other hand, have a theoretical foundation, whereas, for used mathematical approximations within the model, various assumptions to retrieve an analytical solution are made [17]. The Oh model of 1992 was developed based on a single experiment with information about only four different soil surfaces [26]. For the model version of 2004, Oh used information of approximately 40 bare soil fields conducted over seven experiments [27]. Furthermore, the usage of  $\epsilon$  and  $R$  in model Oh92 was refined to the usage of  $mv$  in model Oh04. Model Dubois95 is the only model which was developed only for co-polarized backscatter data (HH or VV), whereas the other models can calculate co- and cross-polarized backscatter values (HH, VH, VV). Differences between vegetation models WCM and SSRT exist in the form of their simplicity. WCM calculates only the volume backscattering component, whereas, within SSRT, additional backscatter components, such as plant-ground and ground-plant interaction, as well as ground-plant-ground scattering contributions, are considered. In our implementation, the vegetation descriptor of WCM is LAI, whereas the vegetation descriptor of SSRT consists of LAI and canopy height. In general, the computational time and the required additional input parameters are increasing from empirical to semi-empirical and theoretical models. A summary of the different models with information about type, validity range, site dependency, required parameters, and used polarization are given in Table 4.

## 4. Results and Discussion

### 4.1. Model Calibration Results

#### 4.1.1. Static Empirical Parameters

In a first calibration approach, the empirical parameters for the different models were treated as static throughout the entire time series. The modeled backscatter was then compared to the measured backscatter from Sentinel-1. Table 6 shows the mean of RMSE and  $R^2$  of all analyzed sample points (Figure 1) for different surface and canopy model combinations. The retrieved RMSE of the calibration results ranges from 1.92 to 2.25 dB with  $R^2$  of 0.08 to 0.34, respectively. A more detailed picture regarding differences between modeled and Sentinel-1 backscatter during the time series is shown for field 508 in Figure 4. While, for the first half of the vegetation period, all model combinations show a relatively good fit to Sentinel-1 backscatter data, in the second half, deviations are obvious. Furthermore, from the beginning of June where LAI reaches its saturation point and the maximum plant height is almost reached, no significant change over time within the modeled backscatter can be observed. The analyzed soil models (different colors) show small differences, whereas a clear separation between analyzed canopy models (solid vs dashed lines), especially for later vegetation stages, is noticeable. As described in Section 2.3, Sentinel-1 data of four different overpasses, and therefore with different incidence and azimuth angles, were used for this analysis. In Figure 4, every fourth point (same icon) of the Sentinel-1 backscatter time series represents the same satellite acquisition geometry (same incidence and azimuth angle). The incidence angle is implemented within the used RT models, whereas the models do not account for difference azimuth angles. The black line (Sentinel-1 backscatter) in Figure 4 shows that the observed backscatter values differ with varying incidence angles and changes in soil moisture. The model predictions (different colors) illustrate that the models can account for varying incidence angles and changes in soil moisture only until the end of May. Furthermore, the good correlation of modeled and Sentinel-1 backscatter values suggests

that the effect of different azimuth angles on backscatter values seems to be negligible until the end of May. The main change within the wheat fields in June and July in terms of phenology are the flowering, the development of the fruit, and, later on, the ripening [75,81]. For these phenology stages, the increase in backscatter is caused by higher sensitivity of the radar signal to the ground contribution due to water loss within the vegetation [81]. Mattia et al. [76] identified the heading period as turning point where the sensitivity of the radar backscatter to above-ground biomass decreases, whereas the sensitivity to soil surface increases. The temporal evolution of modeled ground contribution to the total backscatter for different model combinations (different colors) with the observed Sentinel-1 total backscatter (black line) is shown in Figure 5 (top part). Until the increase in canopy height at the beginning of May (Table 4), the modeled ground scattering part seems to be the main contributor to the total backscatter, whereas the canopy part is negligible. With increase, especially in canopy height, the ground contribution drops significantly. The expected decrease in backscatter of the ground contribution due to a bigger canopy layer (increase of canopy height and LAI) can be more clearly observed for SSRT than WCM. The differences between SSRT and WCM might be found by using different canopy descriptors (SSRT: LAI and canopy height; WCM: LAI). Differences in ground contributions between Dubois95 and the other surface models are related to differences in the modeled attenuation through the canopy  $T$  (Figure 4, bottom part).  $T$  is regulating the contribution intensity of the ground and canopy part for the total backscatter calculation. The temporal evolution of  $T$  with a value range from 0 (dominant canopy contribution) to 1 (dominant ground contribution) is shown in Figure 5 (bottom part). All model combinations show a similar temporal shape with slightly higher values for model Dubois95.  $T$  decreases from April (dominant ground contribution) to mid-May (dominant canopy contribution) and stays at its minimum after mid-May. The expected increase [76,81] of the modeled ground contribution due to higher ground sensitivity in June and July (phenology: flowering, development of the fruit, and ripening) is not observed within the modeled data. In our case,  $T$  is mainly driven by static empirical parameter  $B$  (WCM) and  $coef$  (SSRT), as well as non-static vegetation descriptors LAI and/or canopy height. Therefore, with almost no changes in LAI and canopy height in June and July (Figure 4, middle part), the two-way attenuation  $T$  stays near zero, which indicates a dominant canopy model contribution to the total backscatter calculation. By definition, LAI is defined as the one-sided leaf area per measured ground unit [82]. By the time wheat plants reach their maximum height, the leaves are fully developed. Changes within the wheat plants, especially during vegetation stages of flowering, fruit development, or ripening (Figure 4), are based mainly on increasing biomass within grains and stems, as well as changes of the vegetation water content. However, biomass changes in grains and stems, as well as vegetation water content loss, especially during the ripening stage, are not reflected within the LAI. Therefore, almost no information about the increased biomass and the water loss due to ripening of the plants is given within this model configuration. Plant moisture reduction affects the attenuation of the radar signal by the canopy in a way that the canopy is more transparent for the radar wave [83]. Therefore, the sensitivity of the radar signal to the canopy should decrease, whereas the sensitivity to the surface increases. The almost non-existent deviation between Sentinel-1 and modeled backscatter in early vegetation stages suggests that the interaction between surface and canopy model, and therefore the attenuation of the backscatter signal by the canopy, described by static empirical parameters and LAI, can be modeled sufficiently only in early vegetation stages. For good backscatter model results during later vegetation stages, the backscatter changes due to water loss within the plants have to be considered. The effects of utilizing non-static empirical parameters to account for these shortcomings are discussed in the next sections.

**Table 6.** Calibration results of different model combinations with static empirical parameters. Mean RMSE, ubRMSE, and R<sup>2</sup> of all analyzed field measurement points.

Model Surface + Canopy	Calibration	
	RMSE [dB]	R <sup>2</sup>
Oh92 + SSRT	2.11	0.20
Oh92 + WCM	1.97	0.26
Oh04 + SSRT	2.02	0.18
Oh04 + WCM	1.92	0.23
Dubois95 + SSRT	2.09	0.08
Dubois95 + WCM	2.03	0.08
WCM + SSRT	2.25	0.22
WCM + WCM	2.08	0.34
IEM_B + SSRT	2.24	0.15
IEM_B + WCM	2.13	0.24

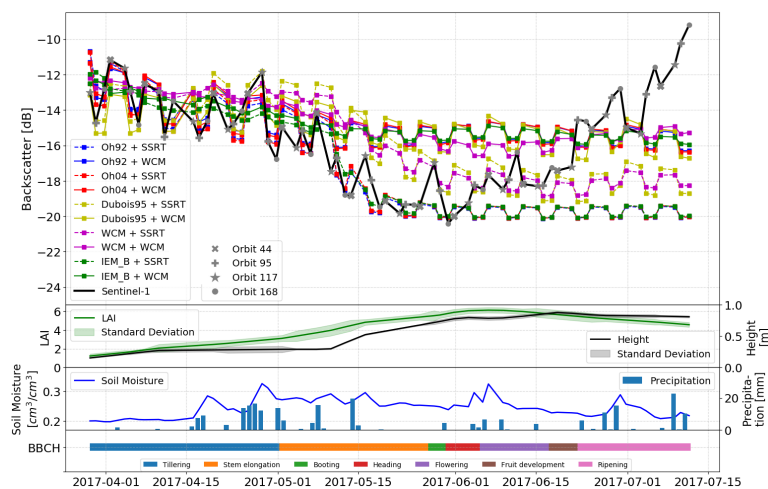


**Figure 4.** Measured and modeled data (static parameters) of wheat field 508 for vegetation period 2017. VV-polarized backscatter comparison of different model combinations (surface + canopy) with static empirical parameters and Sentinel-1 data. Different icons represent different acquisition geometries of Sentinel-1 (top). Field measurements of Leaf Area Index (LAI), canopy height, and soil moisture, as well as precipitation data from meteorological station Freising (middle). Observed vegetation phenology according to BBCH scale [84] (bottom).

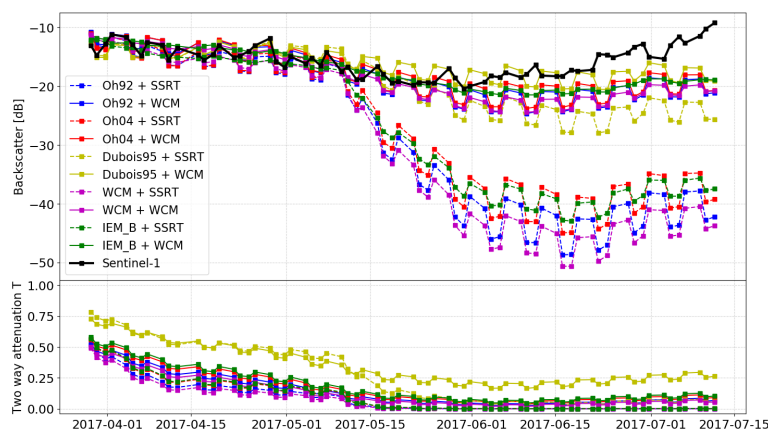


**Figure 5.** Model results (wheat field 508, static parameter) of ground contribution to total backscatter for different model combinations (different colors) with Sentinel-1 VV polarized total backscatter (black line) as reference (top). Temporal evolution of model component two way attenuation by the canopy *T* (bottom).

#### 4.1.2. Non-Static Empirical Parameters

Due to the results in Section 4.1.1, which showed that LAI and height cannot account for the observed backscatter changes in June and July (increase of Sentinel-1 backscatter), a second calibration approach with non-static empirical parameter where chosen. As already mentioned, the observed increase in backscatter is caused by a higher sensitivity of the radar signal to the ground contribution. The attenuation of the backscatter  $T$ , more precisely  $B$ , for WCM and  $coef$  for SSRT were identified as the main drivers for the increase or decrease of the ground contribution; therefore, a non-static approach for these parameters was tried. The other empirical parameters of WCM (surface: C, D; canopy: A) were set as static values (mean of the retrieved static values during the calibration approach shown in Section 4.1.1) to clearly relate the observed changes to the attenuation of the backscatter. The modeled backscatter was compared to Sentinel-1 observations and the statistics for different model combinations are shown in form of mean RMSE and  $R^2$  of all analyzed field measurement points in Table 7. The retrieved RMSE ranges from 1.13 to 1.60dB with  $R^2$  of 0.45 to 0.82, respectively. By comparing different model combinations, almost no differences between the two analyzed canopy models can be observed. A different picture is shown by comparing surface models only. WCM seems to outperform all others, whereas differences between WCM and Oh92, Oh04, and IEM\_B are smaller than differences of these models to Dubois95. Similar to the approach with static empirical parameters, the evolution over time of modeled and Sentinel-1 backscatter is shown in Figure 6 for one measurement point of field 508. Like the results in Section 4.1.1, modeled backscatter results of the first half of the vegetation period fit well to the observed Sentinel-1 backscatter data. Contrary to the static parameter approach, the second half of the vegetation period shows high correlations between Sentinel-1 and modeled backscatter. Unlike the results of the static approach (Figure 5, top part), the expected increase of the ground contribution at the end of the vegetation period can be observed in Figure 7 (top part). The increase of the ground contribution to the total backscatter is also reflected within the two-way attenuation by the canopy  $T$  shown in Figure 7 (bottom part). Compared to the static approach (Figure 5, bottom part), the values of  $T$  from April to the beginning of June are very similar for all model combinations, except Dubois95. The temporal changes of non-static parameters  $B$  and  $coef$  are shown for the validation results in Figures 8 and 9 and will be further discussed in the validation Section 4.2. Besides the modeled backscatter increase for the second half of the vegetation period, different trends between Sentinel-1 and modeled backscatter for individual time steps are observed. This mismatch might occur for several reasons. As already mentioned in Section 4.1.1, Sentinel-1 data with different incidence and azimuth angles were used. A closer look at every fourth modeled point (same incidence and azimuth angle) in Figure 6 (same icon) shows a steady increase of modeled backscatter values at the end of the vegetation period. Therefore, an overall trend of an increasing backscatter can be seen for Sentinel-1 and modeled data. Due to non contradictory trends during the first half of the vegetation period, it seems that the influence on backscatter due to incidence and azimuth angles increases for the second half of the vegetation period. Thus, higher canopy heights and LAI values may also increase the impact of different incidence and azimuth angles on the backscatter behavior. In addition, the acquisition time (Table 3) of the Sentinel-1 images might play another role for different attenuation effects by the canopy [81]. The acquisition time of the satellite differs for different overpasses. For the MNI test site, Sentinel-1 data was acquired during early morning or late afternoon (Table 3). This might lead to differences in the observations due to dew [85,86] or different plant alignments towards the sun which, in theory, leads to different backscatter attenuations through the canopy [87–89], which are not accounted for within the models. Despite the different trends during the temporal evolution of modeled and Sentinel-1 backscatter for the second half of the vegetation period, the observed overall increase in backscatter at the end of the vegetation period can be modeled well.

**Table 7.** Calibration and validation results of different model combinations with non-static empirical parameters. Mean RMSE, ubRMSE, and R<sup>2</sup> of all analyzed field measurement points.

Model Surface + Canopy	Calibration		Validation		
	RMSE [dB]	R <sup>2</sup>	RMSE [dB]	ubRMSE [dB]	R <sup>2</sup>
Oh92 + SSRT	1.24	0.73	2.82	2.10	0.59
Oh92 + WCM	1.22	0.73	2.75	2.21	0.57
Oh04 + SSRT	1.33	0.69	2.87	2.14	0.57
Oh04 + WCM	1.32	0.68	2.81	2.22	0.57
Dubois95 + SSRT	1.55	0.49	3.06	2.11	0.49
Dubois95 + WCM	1.60	0.45	3.06	2.18	0.48
WCM + SSRT	1.16	0.82	2.65	1.93	0.63
WCM + WCM	1.13	0.81	2.57	2.08	0.60
IEM_B + SSRT	1.32	0.78	2.62	1.82	0.64
IEM_B + WCM	1.34	0.77	2.54	1.92	0.62

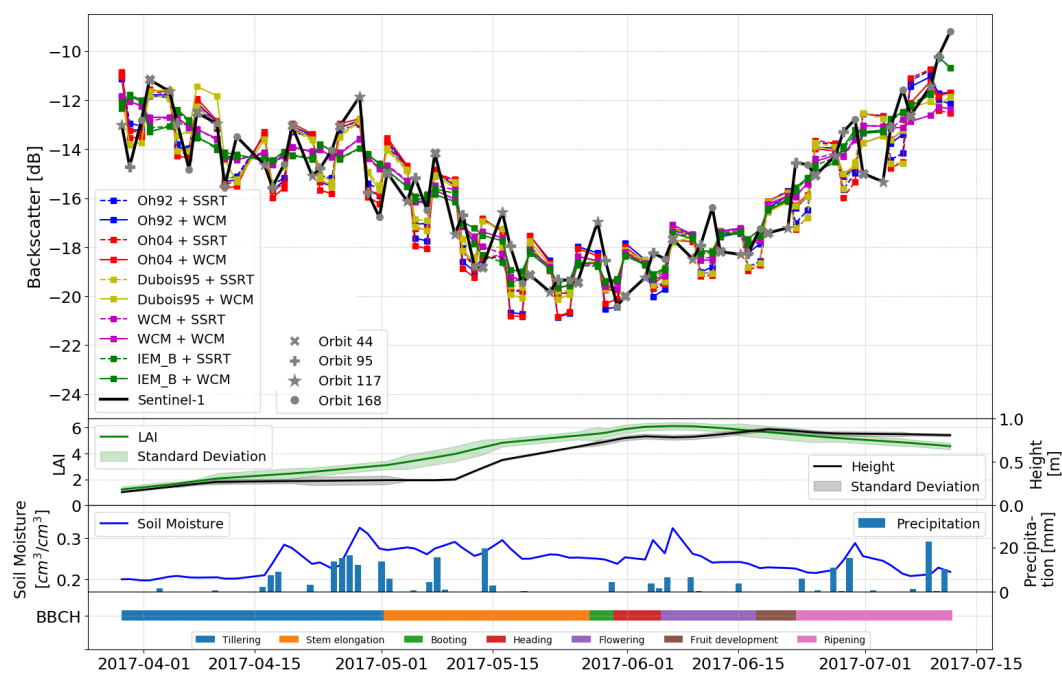


**Figure 6.** Measured and modeled data (non-static parameters) of wheat field 508 for vegetation period 2017. VV-polarized backscatter comparison of different model combinations (surface + canopy) with non-static empirical parameters and Sentinel-1 data. Different icons represent different acquisition geometries of Sentinel-1 (**top**). Field measurements of LAI, canopy height, and soil moisture, as well as precipitation data from meteorological station Freising (**middle**). Observed vegetation phenology according to BBCH scale [84] (**bottom**).

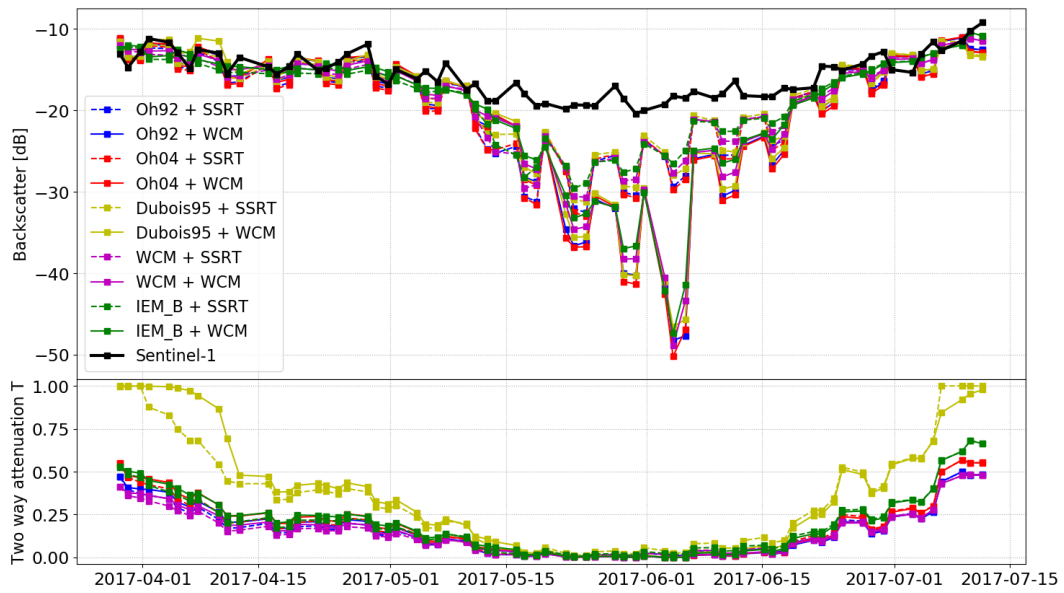


**Figure 7.** Model results (wheat field 508, non-static parameter) of ground contribution to total backscatter for different model combinations (different colors) with Sentinel-1 VV polarized total backscatter (black line) as reference (**top**). Temporal evolution of model component two way attenuation by the canopy  $T$  (**bottom**).

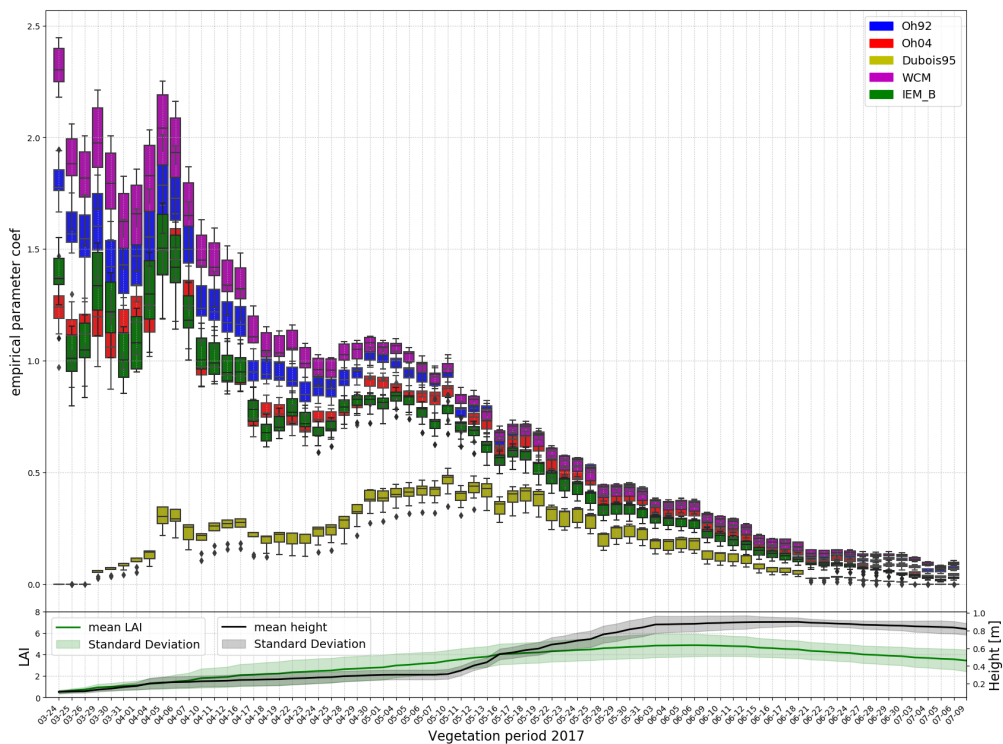


**Figure 8.** Evolution over time of non-static parameter  $coef$  separated by different surface models (colors) for each Sentinel-1 acquisition date during vegetation period 2017. The box plots show the range of  $coef$  used during the validation approach for different fields point (**top**). Mean and standard deviation of all measurement points for LAI and canopy height (**bottom**).

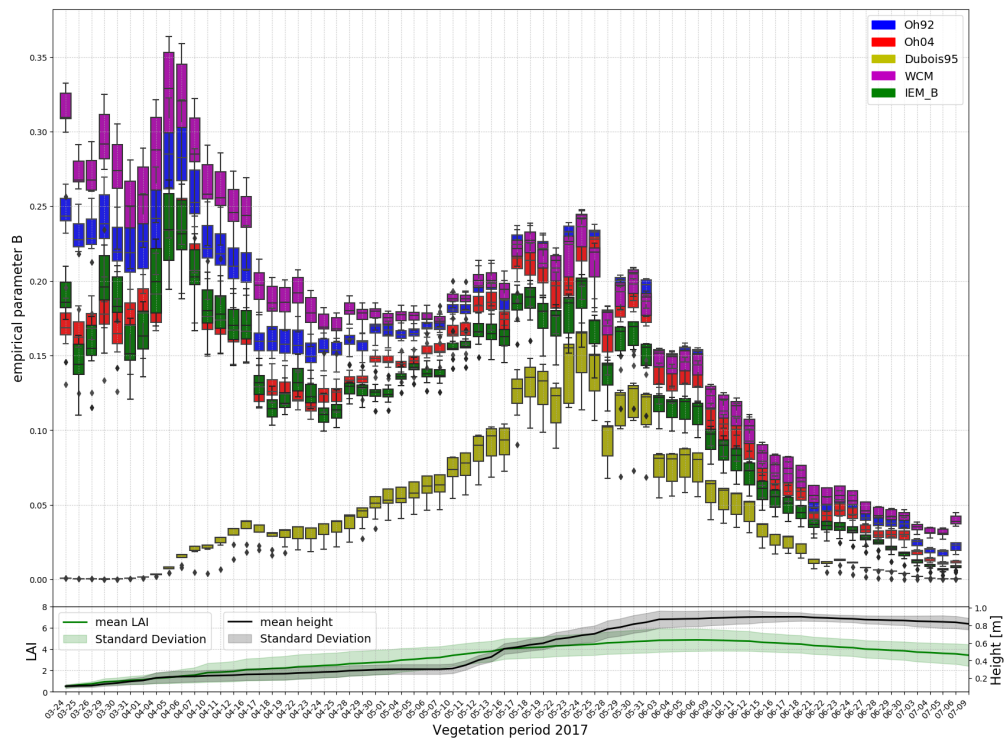


**Figure 9.** Evolution over time of non-static parameter  $B$  separated by different surface models (colors) for each Sentinel-1 acquisition date during vegetation period 2017. The box plots show the range of  $B$  used during the validation approach for different fields point (top). Mean and standard deviation of all measurement points for LAI and canopy height (bottom).

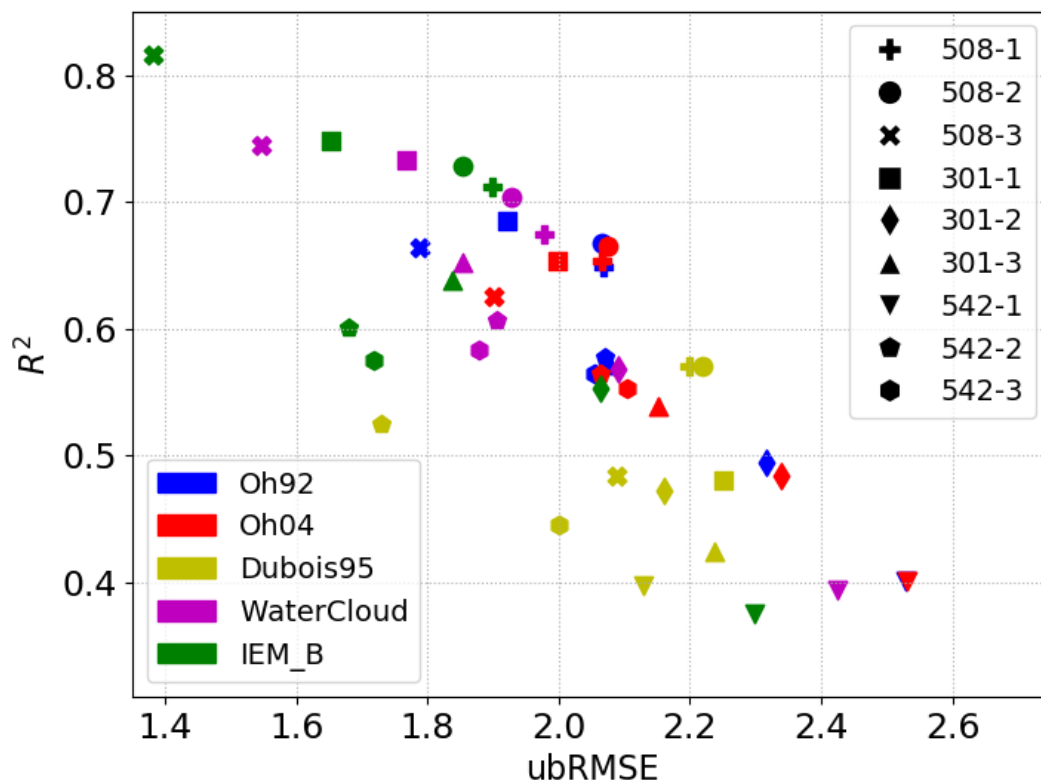


**Figure 10.** Scatter plot showing statistical validation results (correlation coefficient  $R^2$  and ubRMSE) for canopy model SSRT separated by different surface models (colors) and different field points (icons).

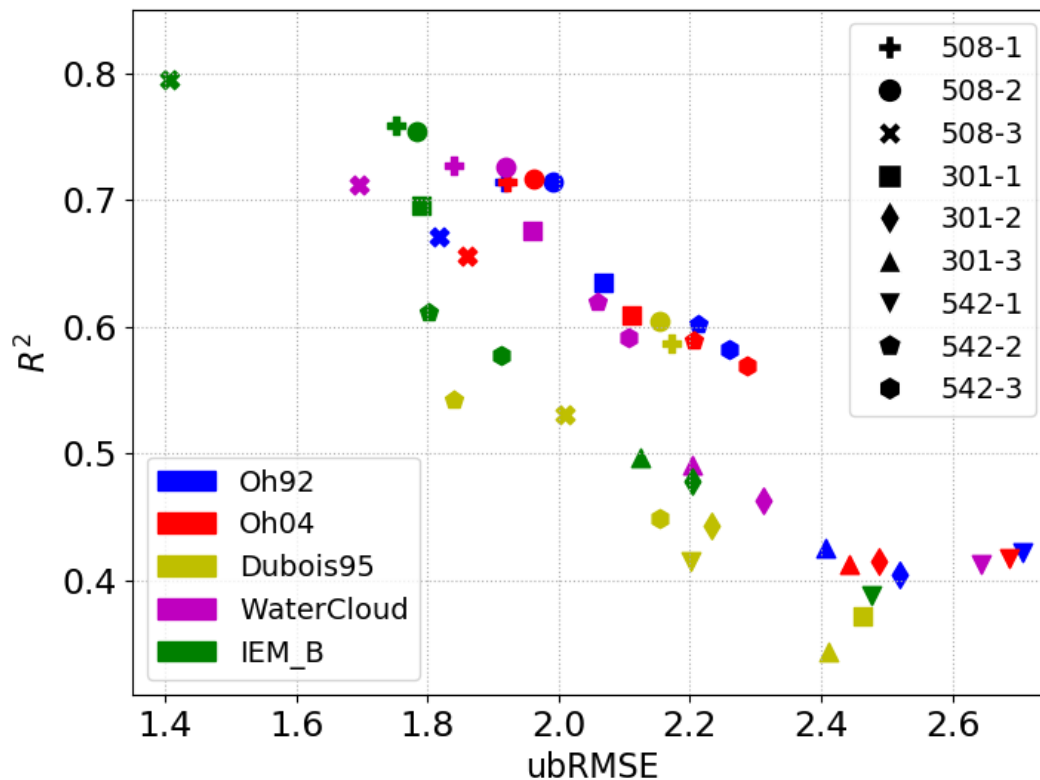


**Figure 11.** Scatter plot showing statistical validation results (correlation coefficient  $R^2$  and ubRMSE) for canopy model WCM separated by different surface models (colors) and different field points (icons).

#### 4.2. Model Validation Results

The validation for the non-static approach was performed by a leave-one-out cross-validation method. Means of RMSE, ubRMSE, and  $R^2$  are shown in Table 7. The results for the non-static approach show ubRMSE values between 1.92 and 2.22dB. All validation (ubRMSE) results are in a range of 0.65 to 0.95dB poorer than the calibration (RMSE) results. Furthermore, for the validation results  $R^2$  ranges between 0.49 and 0.64, whereas the poorest results are archived with surface model Dubois95. A comparison of ubRMSE for canopy model SSRT and WCM yields for all surface models slightly better results for canopy model SSRT. A more detailed overview of the validation results separated by models and measurement points is given in Figure 10 for canopy model SSRT and in Figure 11 for canopy model WCM. Comparing different fields, as well as field measurement points, a diverse picture is drawn. In general, field 508, especially 508-1, shows the best results, with  $R^2$  values mainly higher than 0.6 and ubRMSE lower than 2.2. Field 542, and especially 542-1, show the worst results, with  $R^2$  around 0.4 and ubRMSE higher than 2.2. Comparing different surface model combinations, IEM\_B and WCM show, for both canopy models, slightly better results than the others. It is noticeable that the results of Dubois95 are, in general, poorer than the results of the other surface models, with the exception of point 542-1 (measurement point with the poorest overall results) and partly 301-2. Differences between Oh92 and Oh04 for the different measurement points are present but, compared to the other models, very low. A closer look into each model combination, and especially at the used non-static empirical parameters  $coef$  and  $B$ , and thus at the change of the attenuation of the canopy in time, are given with Figures 8 and 9. The figures show the development of  $coef$  and  $B$  over the vegetation period and the parameter calibration spread, which is defined by the used leave-one-out cross-validation results. Comparing different surface models, the same evolution over time (except Dubois95 for the first half of the vegetation period), with some differences in the absolute values, can be observed. The low values of  $coef$  and  $B$  for model Dubois95 in the first half of the vegetation period can explain the differences in absolute values of  $T$  (Figure 7, bottom part) between Dubois95

and the other model combinations. A comparison of canopy model SSRT (parameter *coef*) and WCM (parameter *B*) show, for all surface models (except Dubois95), for parameter *coef*, a almost steady decrease from the beginning to the end of the vegetation period and a similar evolution for parameter *B*, except for a short period of increasing values to a relative maximum from mid-May to the end of May. The differences in shape between *coef* and *B* might be explained due to different model input data. SSRT uses the canopy height and LAI for the description of the canopy, whereas WCM only uses LAI. The increase of parameter *B* correlates very well with the measured increase of the canopy height. This suggests that parameter *B* compensates for possible shortcomings of WCM due to missing information about the canopy height. Furthermore, not only the absolute values but also the spread of *coef* and *B* for different models are higher at the beginning of the vegetation period and strongly decrease over time. This means that *coef* and *B* show higher differences between fields and field measurement points at the beginning of the vegetation period. This is in line with observations made during the field campaign, where higher differences within one field and between fields could be observed more easily at early vegetation stages. At the end of the vegetation period, such differences were not detectable anymore. Another indicator of low field differences regarding the ripening stage of the wheat plants was the almost simultaneous harvesting date. Another factor to be considered if looking at higher variability of *coef* and *B* at the beginning of the vegetation season is the model implementation itself. *B* and *coef* are influencing the attenuation of the backscatter by the canopy and therefore how strong each model compartment (surface or canopy) contributes to the total backscatter calculation. At the beginning of the growing season, LAI and canopy height are low; therefore, notable differences within *coef* and *B* might have not such a high impact on total backscatter predictions. Differences in the range of *coef* (0 to 2.5) and *B* (from 0 to 0.35) are most likely based on differences between the model definitions and the required input parameters.

## 5. Conclusions

Modeled backscatter results of wheat field time series data using different RT model combinations (surface: Oh92, Oh04, Dubois95, IEM\_B, WCM; canopy: WCM, SSRT) were compared to observed C-band data from Sentinel-1. Differences between the models were analyzed. The used dataset was acquired by an intense field campaign throughout one vegetation period in 2017. The analysis focused on coupled performance of surface and canopy models and especially on how changes of backscatter attenuation through the canopy influence the total backscatter calculation for different vegetation stages. The two novelties of this study are the evaluation of different combinations of widely used surface and canopy RT models on one test site and the analysis over time of empirical model parameters *coef* (SSRT) and *B* (WCM) describing the backscatter attenuation through the canopy *T*.

Results show that, for total LAI, as vegetation descriptor, a static parameter influencing the backscatter attenuation through the canopy is suitable for the first half but not for the second half of the vegetation period. By using a non-static parameter approach, the backscatter increase at the end of the vegetation period can be modeled. The static calibration performance results in the form of RMSE improved from 1.92–2.25dB to 1.13–1.60dB for the non-static approach. The validation accuracy for the non-static parameter approach was evaluated with ubRMSE and ranges for all model combinations between 1.82 and 2.22dB. Validation results with SSRT as canopy model show better results in combination with all surface models when compared to respective combinations using WCM for the canopy part. Furthermore, it has been shown that the modeled backscatter results highly depend on the non-static empirical parameter. The evolution of the empirical parameter is similar for all surface models except Dubois95. At the beginning of the vegetation period, high values are observed, which decrease during the vegetation season to a minimum shortly before harvesting. Differences between the canopy model SSRT and WCM are noticeable in the form of higher variability (more outliers) of the empirical parameter from canopy model WCM. Furthermore, the empirical parameter for canopy model WCM has a relative maximum at the end of June. This increase of WCM's empirical parameter *B* can most likely be explained by not including information about the canopy

height. Overall, the results of this study indicate that more complex models, like IEM\_B as surface and SSRT as canopy model, provide the best results in our setup regarding ubRMSE and  $R^2$ . It should be mentioned that the disadvantage of more complex models, by requiring more input parameters, were set to a minimum because of model parameter reduction by model adjustments and the use of literature values for rms height and single scattering albedo. Therefore, based on this study, we suggest using surface model IEM\_B in combination with canopy model SSRT.

To accomplish a very dense time series of satellite acquisitions with a revisit time of 1.5 days, Sentinel-1 images with different incidence and azimuth angles were used. The models can account for backscatter changes due to different acquisition geometries only during the first half of the vegetation period. During the second half, a trend mismatch between Sentinel-1 and modeled backscatter is apparent in all model results. Therefore, it has to be stated that the used models in this study are only partially able to handle differences due to changes in radar acquisition geometries.

To take full advantage of dense time series provided, e.g., by incorporating different sensors on top of varying radar acquisition geometries, extended research on the suitability of certain RT models is required. Respectively, arising radiometric differences added to the disparity in radar acquisition geometries must be investigated, for that matter. To advance synergistic retrieval methods of SAR and optical data for soil moisture estimation, further research on incorporating non-static empirical parameter sets retrieved from optical sensors, to account for vegetation phenological states, is needed.

**Author Contributions:** Conceptualization, T.W. and A.L.; Methodology and Formal Analysis, T.W.; Software, T.W. and A.L.; Writing—Original Draft Preparation, T.W., Writing—Review & Editing, T.W., T.R. and P.M.; Resources, T.W. and T.R.; Visualization, T.W.; Supervision, A.L. and P.M.; Project administration, A.L. and P.M.; Funding acquisition, A.L. All authors have read and agreed to the published version of the manuscript.

**Funding:** The project leading to this application has received funding from the European Union’s Horizon 2020 research and innovation program under Grant Agreement No. 687320.

**Acknowledgments:** Thomas Weiß is truly thankful for the inspiration, ideas, and support that Alexander Löw († 2. July 2017) has given him.

**Conflicts of Interest:** The authors declare no conflict of interest.

## References

- Hollmann, R.; Merchant, C.J.; Saunders, R.; Downy, C.; Buchwitz, M.; Cazenave, A.; Chuvieco, E.; Defourny, P.; de Leeuw, G.; Forsberg, R.; et al. The ESA Climate Change Initiative: Satellite Data Records for Essential Climate Variables. *Bull. Am. Meteorol. Soc.* **2013**, *94*, 1541–1552. [[CrossRef](#)]
- Brocca, L.; Ciabatta, L.; Massari, C.; Camici, S.; Tarpanelli, A. Soil Moisture for Hydrological Applications: Open Questions and New Opportunities. *Water* **2017**, *9*, 140. [[CrossRef](#)]
- Hochschild, V.; Thiel, C.; Grünler, S. Derivation of Land Cover and Soil Moisture from Airborne Polarimetric SAR-Data. *Sao/NASA Astrophys. Data Syst.* **2001**, *475*, 355–358.
- Zribi, M.; Muddu, S.; Bousbih, S.; Al Bitar, A.; Tomer, S.K.; Baghdadi, N.; Bandyopadhyay, S. Analysis of L-Band SAR Data for Soil Moisture Estimations over Agricultural Areas in the Tropics. *Remote Sens.* **2019**, *11*, 1122. [[CrossRef](#)]
- Oldak, A.; Jackson, T.J.; Starks, P.; Elliott, R. Mapping Near-Surface Soil Moisture on Regional Scale Using ERS-2 SAR Data. *Int. J. Remote Sens.* **2003**, *24*, 4579–4598. [[CrossRef](#)]
- Baghdadi, N.; Aubert, M.; Cerdan, O.; Franchistéguy, L.; Viel, C.; Martin, E.; Zribi, M.; Desprats, J.F. Operational Mapping of Soil Moisture Using Synthetic Aperture Radar Data: Application to the Touch Basin (France). *Sensors* **2007**, *7*, 2458–2483. [[CrossRef](#)]
- Kornelsen, K.C.; Coulibaly, P. Advances in Soil Moisture Retrieval from Synthetic Aperture Radar and Hydrological Applications. *J. Hydrol.* **2013**, *476*, 460–489. [[CrossRef](#)]
- Engman, E. The Potential of SAR in Hydrology. In Proceedings of the IGARSS '94-1994 IEEE International Geoscience and Remote Sensing Symposium, Pasadena, CA, USA, 8–12 August 1994; Volume 1, pp. 283–285. [[CrossRef](#)]

9. Le Hegarat-Masclé, S.; Zribi, M.; Alem, F.; Weisse, A.; Loumagne, C. Soil Moisture Estimation from ERS/SAR Data: Toward an Operational Methodology. *IEEE Trans. Geosci. Remote Sens.* **2002**, *40*, 2647–2658. [[CrossRef](#)]
10. Dorigo, W.; Wagner, W.; Albergel, C.; Albrecht, F.; Balsamo, G.; Brocca, L.; Chung, D.; Ertl, M.; Forkel, M.; Gruber, A.; et al. ESA CCI Soil Moisture for Improved Earth System Understanding: State-of-the Art and Future Directions. *Remote Sens. Environ.* **2017**, *203*, 185–215. [[CrossRef](#)]
11. Amitrano, D.; Martino, G.D.; Iodice, A.; Riccio, D.; Ruello, G.; Ciervo, F.; Papa, M.N.; Koussoubé, Y. Effectiveness of High-Resolution SAR for Water Resource Management in Low-Income Semi-Arid Countries. *Int. J. Remote Sens.* **2014**, *35*, 70–88. [[CrossRef](#)]
12. Holtgrave, A.K.; Förster, M.; Greifeneder, F.; Notarnicola, C.; Kleinschmit, B. Estimation of Soil Moisture in Vegetation-Covered Floodplains with Sentinel-1 SAR Data Using Support Vector Regression. *Photogramm. Remote. Sens. Geoinf. Sci.* **2018**, *86*, 85–101. [[CrossRef](#)]
13. Urban, M.; Berger, C.; Mudau, T.E.; Heckel, K.; Truckenbrodt, J.; Onyango Odipo, V.; Smit, I.P.J.; Schmillius, C. Surface Moisture and Vegetation Cover Analysis for Drought Monitoring in the Southern Kruger National Park Using Sentinel-1, Sentinel-2, and Landsat-8. *Remote Sens.* **2018**, *10*, 1482. [[CrossRef](#)]
14. Bousbih, S.; Zribi, M.; El Hajj, M.; Baghdadi, N.; Lili-Chabaane, Z.; Gao, Q.; Fanise, P. Soil Moisture and Irrigation Mapping in A Semi-Arid Region, Based on the Synergetic Use of Sentinel-1 and Sentinel-2 Data. *Remote Sens.* **2018**, *10*, 1953. [[CrossRef](#)]
15. Barrett, B.W.; Dwyer, E.; Whelan, P. Soil Moisture Retrieval from Active Spaceborne Microwave Observations: An Evaluation of Current Techniques. *Remote Sens.* **2009**, *1*, 210–242. [[CrossRef](#)]
16. Ulaby, F. Radar Measurement of Soil Moisture Content. *IEEE Trans. Antennas Propag.* **1974**, *22*, 257–265. [[CrossRef](#)]
17. Ulaby, F.; Long, D.; Blackwell, W.; Elachi, C.; Fung, A.; Ruf, C.; Sarabandi, K.; Zyl, J.; Zebker, H. *Microwave Radar and Radiometric Remote Sensing*; University of Michigan Press: Ann Arbor, MI, USA, **2014**.
18. Baghdadi, N.; King, C.; Bourguignon, A.; Remond, A. Potential of ERS and Radarsat Data for Surface Roughness Monitoring over Bare Agricultural Fields: Application to Catchments in Northern France. *Int. J. Remote Sens.* **2002**, *23*, 3427–3442. [[CrossRef](#)]
19. Holah, N.; Baghdadi, N.; Zribi, M.; Bruand, A.; King, C. Potential of ASAR/ENVISAT for the Characterization of Soil Surface Parameters over Bare Agricultural Fields. *Remote Sens. Environ.* **2005**, *96*, 78–86. [[CrossRef](#)]
20. Wickel, A.J.; Jackson, T.J.; Wood, E.F. Multitemporal Monitoring of Soil Moisture with RADARSAT SAR during the 1997 Southern Great Plains Hydrology Experiment. *Int. J. Remote Sens.* **2001**, *22*, 1571–1583. [[CrossRef](#)]
21. Mathieu, R.; Sbih, M.; Viau, A.A.; Anctil, F.; Parent, L.E.; Boisvert, J. Relationships between Radarsat SAR Data and Surface Moisture Content of Agricultural Organic Soils. *Int. J. Remote Sens.* **2003**, *24*, 5265–5281. [[CrossRef](#)]
22. Attema, E.P.W.; Ulaby, F.T. Vegetation Modeled as a Water Cloud. *Radio Sci.* **1978**, *13*, 357–364. [[CrossRef](#)]
23. Prévot, L.; Champion, I.; Guyot, G. Estimating Surface Soil Moisture and Leaf Area Index of a Wheat Canopy Using a Dual-Frequency (C and X Bands) Scatterometer. *Remote Sens. Environ.* **1993**, *46*, 331–339. [[CrossRef](#)]
24. Champion, I.; Prévot, L.; Guyot, G. Generalized Semi-Empirical Modelling of Wheat Radar Response. *Int. J. Remote Sens.* **2000**, *21*, 1945–1951. [[CrossRef](#)]
25. Dabrowska-Zielinska, K.; Inoue, Y.; Kowalik, W.; Gruszczynska, M. Inferring the Effect of Plant and Soil Variables on C- and L-Band SAR Backscatter over Agricultural Fields, Based on Model Analysis. *Adv. Space Res.* **2007**, *39*, 139–148. [[CrossRef](#)]
26. Oh, Y.; Sarabandi, K.; Ulaby, F. An Empirical Model and an Inversion Technique for Radar Scattering from Bare Soil Surfaces. *IEEE Trans. Geosci. Remote Sens.* **1992**, *30*, 370–381. [[CrossRef](#)]
27. Oh, Y. Quantitative Retrieval of Soil Moisture Content and Surface Roughness from Multipolarized Radar Observations of Bare Soil Surfaces. *IEEE Trans. Geosci. Remote Sens.* **2004**, *42*, 596–601. [[CrossRef](#)]
28. Dubois, P.; van Zyl, J.; Engman, T. Measuring Soil Moisture with Imaging Radars. *IEEE Trans. Geosci. Remote Sens.* **1995**, *33*, 915–926. [[CrossRef](#)]
29. Fung, A.; Li, Z.; Chen, K. Backscattering from a Randomly Rough Dielectric Surface. *IEEE Trans. Geosci. Remote Sens.* **1992**, *30*, 356–369. [[CrossRef](#)]

30. Baghdadi, N.; King, C.; Chanzy, A.; Wigneron, J.P. An Empirical Calibration of the Integral Equation Model Based on SAR Data, Soil Moisture and Surface Roughness Measurement over Bare Soils. *Int. J. Remote Sens.* **2002**, *23*, 4325–4340. [[CrossRef](#)]
31. Baghdadi, N.; Abou Chaaya, J.; Zribi, M. Semiempirical Calibration of the Integral Equation Model for SAR Data in C-Band and Cross Polarization Using Radar Images and Field Measurements. *IEEE Geosci. Remote Sens. Lett.* **2011**, *8*, 14–18. [[CrossRef](#)]
32. Chen, K.; Wu, T.D.; Tsang, L.; Li, Q.; Shi, J.; Fung, A. Emission of Rough Surfaces Calculated by the Integral Equation Method with Comparison to Three-Dimensional Moment Method Simulations. *IEEE Trans. Geosci. Remote Sens.* **2003**, *41*, 90–101. [[CrossRef](#)]
33. Ulaby, F.T.; Sarabandi, K.; McDonald, K.; Whitt, M.; Dobson, M.C. Michigan Microwave Canopy Scattering Model. *Int. J. Remote Sens.* **1990**, *11*, 1223–1253. [[CrossRef](#)]
34. Ferrazzoli, P.; Guerriero, L. Radar Sensitivity to Tree Geometry and Woody Volume: A Model Analysis. *IEEE Trans. Geosci. Remote Sens.* **1995**, *33*, 360–371. [[CrossRef](#)]
35. De Roo, R.; Du, Y.; Ulaby, F.; Dobson, M. A Semi-Empirical Backscattering Model at L-Band and C-Band for a Soybean Canopy with Soil Moisture Inversion. *IEEE Trans. Geosci. Remote Sens.* **2001**, *39*, 864–872. [[CrossRef](#)]
36. Quast, R.; Wagner, W. Analytical Solution for First-Order Scattering in Bistatic Radiative Transfer Interaction Problems of Layered Media. *Appl. Opt.* **2016**, *55*, 5379–5386. [[CrossRef](#)] [[PubMed](#)]
37. Quast, R.; Albergel, C.; Calvet, J.C.; Wagner, W. A Generic First-Order Radiative Transfer Modelling Approach for the Inversion of Soil and Vegetation Parameters from Scatterometer Observations. *Remote Sens.* **2019**, *11*, 285. [[CrossRef](#)]
38. Zribi, M.; Taconet, O.; Le Hégarat-Masclé, S.; Vidal-Madjar, D.; Emblanch, C.; Loumagne, C.; Normand, M. Backscattering Behavior and Simulation Comparison over Bare Soils Using SIR-C/X-SAR and ERASME 1994 Data over Orgeval. *Remote Sens. Environ.* **1997**, *59*, 256–266. [[CrossRef](#)]
39. Baghdadi, N.; Zribi, M. Evaluation of Radar Backscatter Models IEM, OH and Dubois Using Experimental Observations. *Int. J. Remote Sens.* **2006**, *27*, 3831–3852. [[CrossRef](#)]
40. Khabazan, S.; Motagh, M.; Hosseini, M. Evaluation of Radar Backscattering Models IEM, OH, and Dubois Using L and C-Bands SAR Data over Different Vegetation Canopy Covers and Soil Depths. In *ISPRS-International Archives of the Photogrammetry, Remote Sensing and Spatial Information Sciences; Copernicus GmbH: Göttingen, Germany, 2013; Volume XL-1-W3*, pp. 225–230. [[CrossRef](#)]
41. Choker, M.; Baghdadi, N.; Zribi, M.; El Hajj, M.; Paloscia, S.; Verhoest, N.E.C.; Lievens, H.; Mattia, F. Evaluation of the Oh, Dubois and IEM Backscatter Models Using a Large Dataset of SAR Data and Experimental Soil Measurements. *Water* **2017**, *9*, 38. [[CrossRef](#)]
42. Ezzahar, J.; Ouaadi, N.; Zribi, M.; Elfarkh, J.; Aouade, G.; Khabba, S.; Er-Raki, S.; Chehbouni, A.; Jarlan, L. Evaluation of Backscattering Models and Support Vector Machine for the Retrieval of Bare Soil Moisture from Sentinel-1 Data. *Remote Sens.* **2020**, *12*, 72. [[CrossRef](#)]
43. Kweon, S.K.; Oh, Y. A Modified Water-Cloud Model With Leaf Angle Parameters for Microwave Backscattering From Agricultural Fields. *IEEE Trans. Geosci. Remote Sens.* **2015**, *53*, 2802–2809. [[CrossRef](#)]
44. Pierdicca, N.; Pulvirenti, L.; Pace, G. A Prototype Software Package to Retrieve Soil Moisture From Sentinel-1 Data by Using a Bayesian Multitemporal Algorithm. *IEEE J. Sel. Top. Appl. Earth Obs. Remote Sens.* **2014**, *7*, 153–166. [[CrossRef](#)]
45. Baghdadi, N.; El Hajj, M.; Zribi, M.; Bousbih, S. Calibration of the Water Cloud Model at C-Band for Winter Crop Fields and Grasslands. *Remote Sens.* **2017**, *9*, 969. [[CrossRef](#)]
46. Graham, A.J.; Harris, R. Estimating Crop and Waveband Specific Water Cloud Model Parameters Using a Theoretical Backscatter Model. *Int. J. Remote Sens.* **2002**, *23*, 5129–5133. [[CrossRef](#)]
47. Liu, C.; Shi, J. Estimation of Vegetation Parameters of Water Cloud Model for Global Soil Moisture Retrieval Using Time-Series L-Band Aquarius Observations. *IEEE J. Sel. Top. Appl. Earth Obs. Remote Sens.* **2016**, *9*, 5621–5633. [[CrossRef](#)]
48. Kumar, K.; Prasad, K.S.H.; Arora, M.K. Estimation of Water Cloud Model Vegetation Parameters Using a Genetic Algorithm. *Hydrol. Sci. J.* **2012**, *57*, 776–789. [[CrossRef](#)]
49. Kumar, K.; Rao, H.P.S.; Arora, M.K. Study of Water Cloud Model Vegetation Descriptors in Estimating Soil Moisture in Solani Catchment. *Hydrol. Process.* **2015**, *29*, 2137–2148. [[CrossRef](#)]

50. Song, X.; Ma, J.; Li, X.; Leng, P.; Zhou, F.; Li, S. First Results of Estimating Surface Soil Moisture in the Vegetated Areas Using ASAR and Hyperion Data: The Chinese Heihe River Basin Case Study. *Remote Sens.* **2014**, *6*, 12055–12069. [[CrossRef](#)]
51. van Emmerik, T.; Steele-Dunne, S.C.; Judge, J.; van de Giesen, N. Impact of Diurnal Variation in Vegetation Water Content on Radar Backscatter From Maize During Water Stress. *IEEE Trans. Geosci. Remote Sens.* **2015**, *53*, 3855–3869. [[CrossRef](#)]
52. Xu, C.; Qu, J.J.; Hao, X.; Wu, D. Monitoring Surface Soil Moisture Content over the Vegetated Area by Integrating Optical and SAR Satellite Observations in the Permafrost Region of Tibetan Plateau. *Remote Sens.* **2020**, *12*, 183. [[CrossRef](#)]
53. Lievens, H.; Verhoest, N.E.C. On the Retrieval of Soil Moisture in Wheat Fields From L-Band SAR Based on Water Cloud Modeling, the IEM, and Effective Roughness Parameters. *IEEE Geosci. Remote Sens. Lett.* **2011**, *8*, 740–744. [[CrossRef](#)]
54. Bai, X.; He, B. Potential of Dubois Model for Soil Moisture Retrieval in Prairie Areas Using SAR and Optical Data. *Int. J. Remote Sens.* **2015**, *36*, 5737–5753. [[CrossRef](#)]
55. Xing, M.; He, B.; Ni, X.; Wang, J.; An, G.; Shang, J.; Huang, X. Retrieving Surface Soil Moisture over Wheat and Soybean Fields during Growing Season Using Modified Water Cloud Model from Radarsat-2 SAR Data. *Remote Sens.* **2019**, *11*, 1956. [[CrossRef](#)]
56. He, B.; Xing, M.; Bai, X. A Synergistic Methodology for Soil Moisture Estimation in an Alpine Prairie Using Radar and Optical Satellite Data. *Remote Sens.* **2014**, *6*, 10966–10985. [[CrossRef](#)]
57. Qiu, J.; Crow, W.T.; Wagner, W.; Zhao, T. Effect of Vegetation Index Choice on Soil Moisture Retrievals via the Synergistic Use of Synthetic Aperture Radar and Optical Remote Sensing. *Int. J. Appl. Earth Obs. Geoinf.* **2019**, *80*, 47–57. [[CrossRef](#)]
58. Tao, L.; Wang, G.; Chen, W.; Chen, X.; Li, J.; Cai, Q. Soil Moisture Retrieval From SAR and Optical Data Using a Combined Model. *IEEE J. Sel. Top. Appl. Earth Obs. Remote Sens.* **2019**, *12*, 637–647. [[CrossRef](#)]
59. Zhao, X.; Huang, N.; Niu, Z.; Raghavan, V.; Song, X. Soil Moisture Retrieval in Farmland Using C-Band SAR and Optical Data. *Spat. Inf. Res.* **2017**, *25*, 431–438. [[CrossRef](#)]
60. Attarzadeh, R.; Amini, J.; Notarnicola, C.; Greifeneder, F. Synergetic Use of Sentinel-1 and Sentinel-2 Data for Soil Moisture Mapping at Plot Scale. *Remote Sens.* **2018**, *10*, 1285. [[CrossRef](#)]
61. El Hajj, M.; Baghdadi, N.; Zribi, M.; Bazzi, H. Synergic Use of Sentinel-1 and Sentinel-2 Images for Operational Soil Moisture Mapping at High Spatial Resolution over Agricultural Areas. *Remote Sens.* **2017**, *9*, 1292. [[CrossRef](#)]
62. Gao, F.; Morisette, J.T.; Wolfe, R.E.; Ederer, G.; Pedelty, J.; Masuoka, E.; Myneni, R.; Tan, B.; Nightingale, J. An Algorithm to Produce Temporally and Spatially Continuous MODIS-LAI Time Series. *IEEE Geosci. Remote Sens. Lett.* **2008**, *5*, 60–64. [[CrossRef](#)]
63. Dhakar, R.; Sehgal, V.K.; Chakraborty, D.; Sahoo, R.N.; Mukherjee, J. Field Scale Wheat LAI Retrieval from Multispectral Sentinel 2A-MSI and LandSat 8-OLI Imagery: Effect of Atmospheric Correction, Image Resolutions and Inversion Techniques. *Geocarto Int.* **2019**, 1–21. [[CrossRef](#)]
64. Xie, Q.; Dash, J.; Huete, A.; Jiang, A.; Yin, G.; Ding, Y.; Peng, D.; Hall, C.C.; Brown, L.; Shi, Y.; et al. Retrieval of Crop Biophysical Parameters from Sentinel-2 Remote Sensing Imagery. *Int. J. Appl. Earth Obs. Geoinf.* **2019**, *80*, 187–195. [[CrossRef](#)]
65. Berger, K.; Atzberger, C.; Danner, M.; Wocher, M.; Mauser, W.; Hank, T. Modellbasierte Selektion Hyperspektraler EnMAP Kanäle Zur Optimalen Invertierung von Strahlungstransfermodellen Für Landwirtschaftliche Kulturen. *PFG J. Photogramm. Remote Sens. Geoinf. Sci.* **2018**, *86*, 263–272. [[CrossRef](#)]
66. Danner, M.; Berger, K.; Wocher, M.; Mauser, W.; Hank, T. Retrieval of Biophysical Crop Variables from Multi-Angular Canopy Spectroscopy. *Remote Sens.* **2017**, *9*, 726. [[CrossRef](#)]
67. Danner, M.; Berger, K.; Wocher, M.; Mauser, W.; Hank, T. Fitted PROSAIL Parameterization of Leaf Inclinations, Water Content and Brown Pigment Content for Winter Wheat and Maize Canopies. *Remote Sens.* **2019**, *11*, 1150. [[CrossRef](#)]
68. Wocher, M.; Berger, K.; Danner, M.; Mauser, W.; Hank, T. Physically-Based Retrieval of Canopy Equivalent Water Thickness Using Hyperspectral Data. *Remote Sens.* **2018**, *10*, 1924. [[CrossRef](#)]
69. Kellndorfer, J.; Pierce, L.; Dobson, M.; Ulaby, F. Toward Consistent Regional-to-Global-Scale Vegetation Characterization Using Orbital SAR Systems. *IEEE Trans. Geosci. Remote Sens.* **1998**, *36*, 1396–1411. [[CrossRef](#)]

70. El Hajj, M.; Baghdadi, N.; Zribi, M.; Belaud, G.; Cheviron, B.; Courault, D.; Charron, F. Soil Moisture Retrieval over Irrigated Grassland Using X-Band SAR Data. *Remote Sens. Environ.* **2016**, *176*, 202–218. [[CrossRef](#)]
71. Fung, A.; Liu, W.; Chen, K.; Tsay, M. An Improved Iem Model for Bistatic Scattering From Rough Surfaces. *J. Electromagn. Waves Appl.* **2002**, *16*, 689–702. [[CrossRef](#)]
72. Marzahn, P.; Ludwig, R. Using Multi-Dimensional Microwave Remote Sensing Information for the Retrieval of Soil Surface Roughness. *Int. Arch. Photogramm. Remote Sens. Spat. Inf. Sci.* **2016**, *41*, 1257–1262 [[CrossRef](#)]
73. Marzahn, P.; Rieke-Zapp, D.; Ludwig, R. Assessment of Soil Surface Roughness Statistics for Microwave Remote Sensing Applications Using a Simple Photogrammetric Acquisition System. *ISPRS J. Photogramm. Remote Sens.* **2012**, *72*, 80–89. [[CrossRef](#)]
74. Wegmüller, U.; Santoro, M.; Mattia, F.; Balenzano, A.; Satalino, G.; Marzahn, P.; Fischer, G.; Ludwig, R.; Floury, N. Progress in the Understanding of Narrow Directional Microwave Scattering of Agricultural Fields. *Remote Sens. Environ.* **2011**, *115*, 2423–2433. [[CrossRef](#)]
75. Jia, M.; Tong, L.; Zhang, Y.; Chen, Y. Multitemporal Radar Backscattering Measurement of Wheat Fields Using Multifrequency (L, S, C, and X) and Full-Polarization. *Radio Sci.* **2013**, *48*, 471–481. [[CrossRef](#)]
76. Mattia, F.; Le Toan, T.; Picard, G.; Posa, F.; D'Alessio, A.; Notarnicola, C.; Gatti, A.; Rinaldi, M.; Satalino, G.; Pasquariello, G. Multitemporal C-Band Radar Measurements on Wheat Fields. *IEEE Trans. Geosci. Remote Sens.* **2003**, *41*, 1551–1560. [[CrossRef](#)]
77. Wigneron, J.P.; Kerr, Y.; Waldteufel, P.; Saleh, K.; Escorihuela, M.J.; Richaume, P.; Ferrazzoli, P.; de Rosnay, P.; Gurney, R.; Calvet, J.C.; et al. L-Band Microwave Emission of the Biosphere (L-MEB) Model: Description and Calibration against Experimental Data Sets over Crop Fields. *Remote Sens. Environ.* **2007**, *107*, 639–655. [[CrossRef](#)]
78. Davidson, M.; Toan, T.L.; Mattia, F.; Satalino, G.; Manninen, T.; Borgeaud, M. On the Characterization of Agricultural Soil Roughness for Radar Remote Sensing Studies. *IEEE Trans. Geosci. Remote Sens.* **2000**, *38*, 630–640. [[CrossRef](#)]
79. Picard, G.; Le Toan, T.; Mattia, F. Understanding C-Band Radar Backscatter from Wheat Canopy Using a Multiple-Scattering Coherent Model. *IEEE Trans. Geosci. Remote Sens.* **2003**, *41*, 1583–1591. [[CrossRef](#)]
80. Dobson, M.C.; Ulaby, F.T.; Hallikainen, M.T.; El-rayes, M.A. Microwave Dielectric Behavior of Wet Soil-Part II: Dielectric Mixing Models. *IEEE Trans. Geosci. Remote Sens.* **1985**, *GE-23*, 35–46. [[CrossRef](#)]
81. Khabbazan, S.; Vermunt, P.; Steele-Dunne, S.; Ratering Arntz, L.; Marinetti, C.; van der Valk, D.; Iannini, L.; Molijn, R.; Westerdijk, K.; van der Sande, C. Crop Monitoring Using Sentinel-1 Data: A Case Study from The Netherlands. *Remote Sens.* **2019**, *11*, 1887. [[CrossRef](#)]
82. Allen, S.T.; Whitsell, M.L.; Keim, R.F. Leaf Area Allometrics and Morphometrics in Baldcypress. *Can. J. For. Res.* **2015**, *45*, 963–969. [[CrossRef](#)]
83. He, L.; Tong, L.; Li, Y.; Chen, Y.; Tan, L.; Guo, C. Polarimetric Analysis of Radar Backscatter from Ground-Based Scatterometers and Wheat Biomass Monitoring with Advanced Synthetic Aperture Radar Images. *J. Appl. Remote Sens.* **2016**, *10*, 026008. [[CrossRef](#)]
84. Meier, U.; Bleiholder, H.; Buhr, L.; Feller, C.; Hack, H.; Heß, M.; Lancashire, P.D.; Schnock, U.; Stauß, R.; van den Boom, T.; et al. The BBCH System to Coding the Phenological Growth Stages of Plants—History and Publications. *J. Für Kult.* **2009**, *61*, 41–52. [[CrossRef](#)]
85. Riedel, T.; Liebeskind, P.; Schullius, C. Seasonal and Diurnal Changes of Polarimetric Parameters from Crops Derived by the Cloude Decomposition Theorem at L-Band. In Proceedings of the IEEE International Geoscience and Remote Sensing Symposium, Toronto, ON, Canada, 24–28 June 2002; Volume 5, pp. 2714–2716. [[CrossRef](#)]
86. Riedel, T.; Pathe, C.; Thiel, C.; Herold, M.; Schullius, C. Systematic Investigation on the Effect of Dew and Interception on Multifrequency and Multipolarimetric Radar Backscatter Signals. *Sao/NASA Astrophys. Data Syst.* **2002**, *475*, 99–104.
87. Way, J.; Paris, J.; Dobson, M.; McDouals, K.; Ulaby, F.; Weber, J.; Ustin, L.; Vanderbilt, V.; Kasischke, E. Diurnal Change in Trees as Observed by Optical and Microwave Sensors: The EOS Synergism Study. *IEEE Trans. Geosci. Remote Sens.* **1991**, *29*, 807. [[CrossRef](#)]

88. Hornbuckle, B.K.; Rowlandson, T.L.; Russell, E.; Kaleita, A.; Logsdon, S.; Kruger, A.; Yueh, S.; De Roo, R.D. How does Dew Affect L-Band Backscatter? Analysis of Pals Data at the Iowa Validation Site and Implications for Smap. In Proceedings of the 2010 IEEE International Geoscience and Remote Sensing Symposium, Honolulu, HI, USA, 25–30 July 2010; pp. 4835–4838. [[CrossRef](#)]
89. Konings, A.G.; Piles, M.; Rötzer, K.; McColl, K.A.; Chan, S.K.; Entekhabi, D. Vegetation Optical Depth and Scattering Albedo Retrieval Using Time Series of Dual-Polarized L-Band Radiometer Observations. *Remote Sens. Environ.* **2016**, *172*, 178–189. [[CrossRef](#)]



© 2020 by the authors. Licensee MDPI, Basel, Switzerland. This article is an open access article distributed under the terms and conditions of the Creative Commons Attribution (CC BY) license (<http://creativecommons.org/licenses/by/4.0/>).

## 3.2 Transition to Publication II

Publication I demonstrated that the analyzed RT models are capable of simulating radar backscatter in winter wheat fields using soil moisture, the LAI as a vegetation descriptor, and a non-static empirical parameter. However, the use of a dense Sentinel-1 C-band time series, and consequently, images with different satellite acquisition geometries (varying azimuth and incidence angles), revealed a mismatch between observed and modeled backscatter for consecutive daily images.

While the models successfully capture the general temporal evolution, a trend mismatch in backscatter is consistently observed between consecutive images with different satellite acquisition geometries. Since the models only account for changes in incidence angles, the variation in azimuth angles might be responsible for this discrepancy. However, without a detailed analysis of the model's sensitivity to azimuth and incidence angles, no definitive conclusions can be drawn.

In response, Publication II further investigates a dense Sentinel-1 time series composed of images with varying incidence and azimuth angles. Subsets of this time series are analyzed to quantify the impact on model performance when images with different acquisition geometries are used. The results suggest that incidence angle is the primary driver of backscatter differences between consecutive acquisitions, even though it is accounted for in the models. In contrast, changes in azimuth angles were found to have a negligible effect. Additionally, a polarimetric analysis using eigen-decomposition of dual-polarimetric data (polarimetric entropy and scattering alpha angle) indicates that shifts in scattering mechanisms are predominantly driven by variations in the incidence angle.

### 3.3 Publication II: Sentinel-1 Backscatter Analysis and Radiative Transfer Modeling of Dense Winter Wheat Time Series

**Reference:** Weiß, T., Ramsauer, T., Jagdhuber, T., Löw, A., Marzahn, P., 2021. Sentinel-1 Backscatter Analysis and Radiative Transfer Modeling of Dense Winter Wheat Time Series. *Remote Sensing* 13, 2320. doi:10.3390/rs13122320.

**Status:** published

**Plain language summary:** The twin Sentinel-1 satellites, A and B, map the entire globe with a joint repeat cycle of 6 days. When considering images with varying satellite acquisition geometries, the Sentinel-1 satellites provide an even greater number of repeat cycles for certain regions, particularly in Europe. As a result, a dense time series with a mean temporal resolution of 1.5 days is available for the MNI test site in Germany for the year 2017. This time series consists of images captured under four different acquisition geometries: two with similar incidence angles but different azimuth angles, and two with similar azimuth angles but different incidence angles. The availability of such a dense time series allows for an in-depth analysis of the behavior of RT models when different images with varying acquisition geometries are utilized.

In this study, various subsets of the time series are analyzed, including all images, images with similar incidence angles, images with similar azimuth angles, images normalized by incidence angle, and images separated by both incidence and azimuth angles. The findings indicate that the incidence angle primarily accounts for the differences in Sentinel-1 VV-polarized radar backscatter values, while the effect of the azimuth angle is negligible. Furthermore, an analysis of the scattering mechanisms using dual polarimetric eigen-decomposition reveals that different incidence angles can lead to changes in the scattering mechanism, whereas variations in azimuth angles remain negligible. Although the incidence angle is incorporated into the model equations, the original RT models are unable to effectively handle Sentinel-1 time series comprising images with varying incidence angles. To address this limitation, an empirical calibration parameter (coef) that influences transmissivity is introduced.

**Author contributions:** Conceptualization, T.W. and P.M.; Methodology and data analyses, T.W., T.J., T.R., and P.M.; Software, T.W. and A.L.; Writing-original draft preparation, T.W.; Writing-review and editing, T.W., T.J., T.R., and P.M.; Resources, T.W., T.R., and P.M.; Visualization, T.W., T.J., T.R., and P.M.; Supervision, A.L and P.M.; Project administration, A.L. and P.M.; Funding acquisition, A.L.

**Journal:** Remote Sensing - MDPI

**Impact factor:** 5.349

**CiteScore:** 7.4



## Article

# Sentinel-1 Backscatter Analysis and Radiative Transfer Modeling of Dense Winter Wheat Time Series

Thomas Weiß <sup>1,\*</sup> , Thomas Ramsauer <sup>1</sup> , Thomas Jagdhuber <sup>2,3</sup> , Alexander Löw <sup>1</sup> and Philip Marzahn <sup>1</sup>

<sup>1</sup> Department of Geography, Ludwig-Maximilians-Universität München, Luisenstraße 37, 80333 Munich, Germany; t.ramsauer@iggf.geo.uni-muenchen.de (T.R.); alexander.loew@lmu.de (A.L.); p.marzahn@iggf.geo.uni-muenchen.de (P.M.)

<sup>2</sup> Microwaves and Radar Institute, German Aerospace Center, Münchener Straße 20, 92234 Wessling, Germany; Thomas.Jagdhuber@dlr.de

<sup>3</sup> Institute of Geography, University of Augsburg, Alter Postweg 118, 86159 Augsburg, Germany

\* Correspondence: weiss.thomas@lmu.de

**Abstract:** This study evaluates a temporally dense VV-polarized Sentinel-1 C-band backscatter time series (revisit time of 1.5 days) for wheat fields near Munich (Germany). A dense time series consisting of images from different orbits (varying acquisition) is analyzed, and Radiative Transfer (RT)-based model combinations are adapted and evaluated with the use of radar backscatter. The model shortcomings are related to scattering mechanism changes throughout the growth period with the use of polarimetric decomposition. Furthermore, changes in the RT modeled backscatter results with spatial aggregation from the pixel to field scales are quantified and related to the sensitivity of the RT models, and their soil moisture output are quantified and related to changes in backscatter. Therefore, various (sub)sets of the dense Sentinel-1 time series are analyzed to relate and quantify the impact of the abovementioned points on the modeling results. The results indicate that the incidence angle is the main driver for backscatter differences between consecutive acquisitions with various recording scenarios. The influence of changing azimuth angles was found to be negligible. Further analyses of polarimetric entropy and scattering alpha angle using a dual polarimetric eigen-based decomposition show that scattering mechanisms change over time. The patterns analyzed in the entropy-alpha space indicate that scattering mechanism changes are mainly driven by the incidence angle and not by the azimuth angle. Besides the analysis of differences within the Sentinel-1 data, we analyze the capability of RT model approaches to capture the observed Sentinel-1 backscatter changes due to various acquisition geometries. For this, the surface models “Oh92” or “IEM\_B” (Baghdadi’s version of the Integral Equation Method) are coupled with the canopy model “SSRT” (Single Scattering Radiative Transfer). To resolve the shortcomings of the RT model setup in handling varying incidence angles and therefore the backscatter changes observed between consecutive time steps of a dense winter wheat time series, an empirical calibration parameter (*coef*) influencing the transmissivity (*T*) is introduced. The results show that shortcomings of simplified RT model architectures caused by handling time series consisting of images with varied incidence angles can be at least partially compensated by including a calibration coefficient to parameterize the modeled transmissivity for the varying incidence angle scenarios individually.

**Keywords:** soil moisture; radiative transfer models; winter wheat; Sentinel-1; time series



**Citation:** Weiß, T.; Ramsauer, T.; Jagdhuber, T.; Löw, A.; Marzahn, P. Sentinel-1 Backscatter Analysis and Radiative Transfer Modeling of Dense Winter Wheat Time Series. *Remote Sens.* **2021**, *13*, 2320. <https://doi.org/10.3390/rs13122320>

Academic Editors: Prasad S. Thenkabail, Jochem Verrelst, Clement Atzberger and François Waldner

Received: 3 March 2021

Accepted: 10 June 2021

Published: 13 June 2021

**Publisher’s Note:** MDPI stays neutral with regard to jurisdictional claims in published maps and institutional affiliations.



**Copyright:** © 2021 by the authors. Licensee MDPI, Basel, Switzerland. This article is an open access article distributed under the terms and conditions of the Creative Commons Attribution (CC BY) license (<https://creativecommons.org/licenses/by/4.0/>).

## 1. Introduction

The Sentinel-1 mission was designed for systematically mapping land surfaces with enhanced revisit frequency, coverage, timeliness, and reliability for applications and operational services requiring a long time series [1]. Two of these applications, using freely available Sentinel-1 data, are agricultural monitoring and modeling on regional or global scales [2,3]. The mission currently comprises a constellation of twin satellites, each with a revisit time of 12 days [4,5]. Thus, observations with the same acquisition geometry (exact

same orbit) are provided every six days. If multiple orbits (ascending and descending) and, therefore, various satellite acquisition geometries are considered, a revisit time of less than two days can be accomplished for most parts of Europe [6]. Furthermore, with the provision of space-borne radar data at such an unprecedented spatial and temporal resolution, research on crucial societal and economic challenges such as climate change [7,8] or food security [9–11] can be assessed. For future food security, the monitoring of winter wheat, as one of the most important cereals in Europe [12] and the crop type with the second-largest coverage worldwide, is considered fundamental [13]. One important environmental parameter for winter wheat growth is soil moisture, which shows high spatiotemporal variability [14,15]. Monitoring of the diurnal cycles of soil moisture and other natural fast changing processes with a dense time series [16] reveals possibilities for real-time management, such as of droughts or precision agriculture [17,18].

Lately, more and more studies using microwave time series data to estimate the soil moisture of agricultural areas—especially for the crop type winter wheat—have been conducted [19–21]. Often, only a single satellite orbit constellation and, therefore, data from one satellite with the same acquisition geometry are used [19,22–24]. Occasionally, the time series used consists of data from the same satellite but related to different orbits and, thus, various azimuth or/and incidence angles [20,23,25–27]. Only a few of these studies also use data from different sensors to retrieve soil moisture values [23,27,28]. Summarizing the above studies, one established approach is to simulate radar backscatter or to estimate soil moisture of vegetated areas by using radar backscattering models based on the Radiative Transfer (RT) equation [29,30]. These model simulations of radar backscatter from agricultural fields are based on sensor and platform configurations (e.g., incidence angle, azimuth angle, frequency, and polarization), soil properties (e.g., soil moisture, texture, and surface roughness), and vegetation parameters (e.g., Leaf Area Index (LAI), Normalized Difference Vegetation Index (NDVI), Vegetation Water Content (VWC), and biomass) [19,29]. In recent decades, several complex models such as the Michigan Canopy Scattering Model (MIMICS) [31], the Tor Vergata model [32], a first-order radiative transfer model from Quast [33,34], and a Wheat Canopy Scattering Model (WCSM) [27] have been developed for modeling the electromagnetic scattering of different vegetation types by using the first or second order of the RT equation. For precisely modeling the backscatter characteristics that occur during different phenology stages of winter wheat, complex models with detailed information, such as their canopy element size and distribution (length; diameter; thickness; and water content fraction of the stem, leaf, and ears) are needed to account for a multi-layer volume canopy [27]. Thus, different electromagnetic scattering interactions, for example, direct canopy scattering and single or multiple interactions between canopy parts (the ear, leaf, and stem) and the surface, can be modeled. A problem with using these complex models is the provision of additional input data for characterization of the canopy. Therefore, canopy models with fewer input parameters such as the empirical WCM [35], in which only the direct volume backscatter part is considered; a modified version of WCM (MWCM) [36]; or a Single Scattering Radiative Transfer (SSRT) model described by Ulaby [30] or De Roo [37], in which various scattering mechanisms are modeled in a simpler way, are regularly used [26,30,37–40]. Additionally, information about the surface scattering contribution under winter wheat fields for the estimation of soil moisture is crucial. Commonly used surface backscattering models are the surface scattering part of the empirical Water Cloud Model (WCM) [35]; the semi-empirical models of Oh (Oh92, Oh04) [41,42] and Dubois [43]; and physical models, such as the Integral Equation Method (IEM) [44] in its original form or as adapted by Baghdadi (IEM\_B) [45].

In the scope of using dense microwave time series for monitoring winter wheat fields around the world, complex model approaches might not be applicable most of the time due to the lack of detailed in situ measurements on soil and winter wheat characteristics. Model approaches with a low number of required input parameters that can be provided by satellite remote sensing (e.g., LAI) are preferred when applied on the global scale. Therefore, in this study, we investigate how a simplified RT model for the canopy part

(SSRT) in combination with two surface backscattering models (Oh92 and IEM\_B) are able to simulate backscattering for a dense time series with various acquisition geometries and how far the RT model can be adapted by means of an empirical parameter to compensate for the lack of detailed in situ wheat canopy information. The simple RT models used in their original form are not completely optimized for wheat scattering, and a separation of contributions from vegetation growth and geometric configuration is a challenging task. Thus, the main focus is set on how changes in acquisition geometries (changes in azimuth and incidence angles) affect the simplified backscattering models throughout the entire wheat growing period and if an empirical parameter is able to compensate for these effects up to a certain extent. The contributions from vegetation growth and the geometric configuration difference in the multi-temporal signature are separated.

By investigating a dense Sentinel-1 time series of winter wheat fields in southern Germany, the following questions are answered within this paper:

- (A) Do backscatter variations between individual Sentinel-1 scenes with various acquisition geometries depend on changes in incidence and/or azimuth angle?
- (B) How do backscatter calculations of simple RT model approaches react to changes in terms of acquisition geometry, and what are the probable scattering mechanism variations for winter wheat fields?
- (C) What influence (in dB) do different spatial backscatter aggregation scenarios have on RT model results?
- (D) How do uncertainties in backscatter (variation by 0.2 dB, 0.5 dB, and 1.0 dB) influence soil moisture estimations in the RT models analyzed during the vegetation growing period of winter wheat?
- (E) How should one best assess scattering from wheat fields in terms of acquisition scenario, preprocessing, and soil moisture estimation using time series information?

## 2. Data Sets

### 2.1. Study Area

In situ measurements obtained from the Munich North Isar (MNI) test site in 2017 were used for this study. The study area (48°13'N–48°20'N, 11°39'E–11°45'E, Figure 1) is located to the north of Munich, Bavaria, southern Germany. The test site was established in 2014, and since then, almost every year during the vegetation period, in situ campaigns are carried out to survey the agriculturally relevant key variables [26,46–49]. The main crop types within the MNI test site were wheat, maize, and grassland. The meteorological measurements were provided by three meteorological stations: in Freising, in Eichenried, and at the Munich airport. All three stations are situated within a 10 km radius around the MNI test site. The permanently installed facilities in Freising (470 m a.s.l.) and Eichenried (475 m a.s.l.) are operated by the Bavarian State Research Center for Agriculture (LFL). The meteorological station at the Munich airport (446 m a.s.l.) is operated by the German Meteorological Service (DWD). The meteorological station records reported an annual mean temperature of 9 °C (Freising) to 9.3 °C (Eichenried) and an average annual precipitation of 753 mm (Munich-airport) to 853 mm (Eichenried) for the year 2017. The region around the test site exhibits only marginal changes in height (above sea level) and has no significant topographic variation.

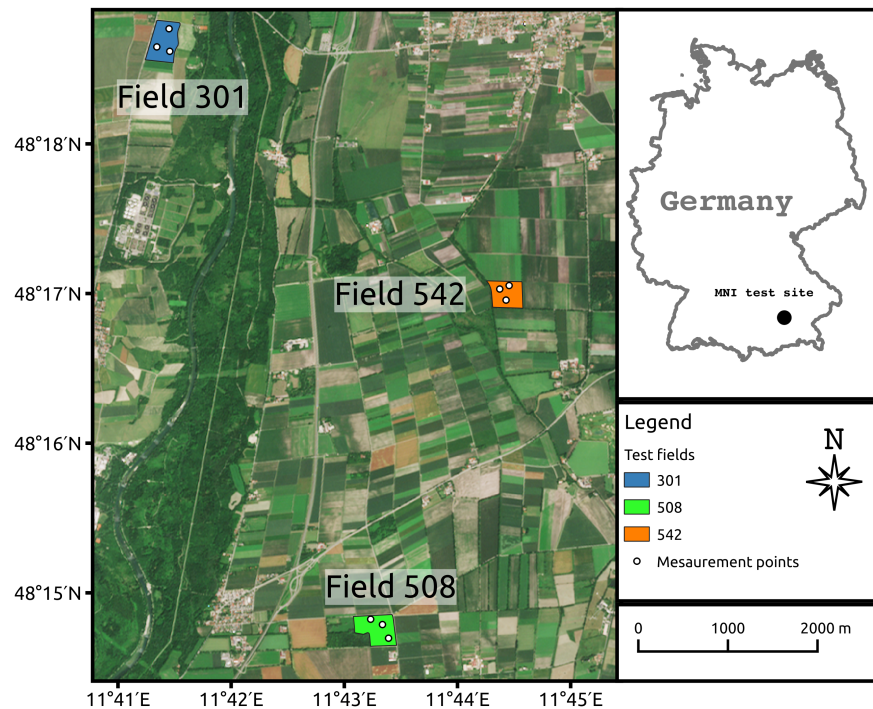


**Figure 1.** Overview of the study area Munich-North-Isar (MNI) with test fields 508 (green), 542 (orange), and 301 (blue), each with three sampling points.

## 2.2. Field Data

Between March and July 2017, in situ measurements of soil and vegetation parameters of wheat fields for the validation of retrieval schemes based on different satellite sensors, such as Sentinel-1, Sentinel-2, or Environmental Mapping and Analysis Program (EnMAP), were conducted (Table 1). For each field under investigation, three sample points were chosen (Figure 1). At each location, weekly vegetation height and LAI measurements as well as assessments of plant phenology (based on BBCH-scale) were taken. For total LAI measurements, the average of 14 samples from the same area measured with a LI-COR Biosciences LAI-2200C device (LI-COR Biosciences Inc., Lincoln, NE, USA) was used. The LAI measurements reach a calculated accuracy of  $0.45 \text{ m}^2/\text{m}^2$  to  $0.52 \text{ m}^2/\text{m}^2$  in terms of the mean standard deviation of repeated measurements within fields. Soil moisture was monitored using permanently installed Decagon TM5 sensors (Decagon Devices Inc., Pullman, WA, USA). The soil moisture devices were installed within the first five centimeters of the soil surface with a monitoring time interval of 10 min. Laboratory analysis of the soil texture of previous field campaigns reports no evidence of significant micro-localational soil variations within the test site [48]. The soil properties presented in Table 2 show values for soil bulk density,  $1.45 \pm 0.13 \text{ g}/\text{cm}^3$ ; for clay content,  $7.38 \pm 1.8\%$ ; for silt content,  $68.55 \pm 11.64\%$ ; and for sand content,  $24.08 \pm 10.46\%$ .

**Table 1.** Acquisition time, time interval, and range of dynamic in situ measurements.

Variable	Acquisition Time	Time Interval	Range
Canopy height [cm]	24 March–17 July 2017	weekly	7–105
LAI	24 March–17 July 2017	weekly	0.35–6.25
Soil moisture [ $\text{m}^3/\text{m}^3$ ]	24 March–17 July 2017	every 10 min	0.09–0.38

**Table 2.** Laboratory results for sand, clay, and bulk content of the soil surface samples.

Variable	Time Interval	Mean	Std
Soil sand content [%]	once (several locations)	24.08	10.46
Soil silt content [%]	once (several locations)	68.55	11.64
Soil clay content [%]	once (several locations)	7.38	1.80
Bulk density [g/cm <sup>3</sup> ]	once (several locations)	1.45	0.13

### 2.3. Satellite Data

A dense time series of Sentinel-1 A/B (C-band, Level-1 SLC) satellite data was used for this study. Preprocessing of the SAR data was accomplished by using ESA's SNAP Toolbox Version 7.0.3. SRTM data with 1 arc-second spatial resolution were used as a digital elevation model for geometric correction of the SAR data [50,51]. For radiometric correction, the method of Kelldorfer et al. [52] was applied. To reduce the impact of speckle by simultaneously maintaining the spatial resolution, a multi-temporal Lee-sigma filter was chosen. For each Sentinel-1 acquisition, information from six other acquisitions (three before and three after the target) was used for temporal filtering. A spatial window of  $5 \times 5$  pixels, sigma of 0.9, and a target window size of  $3 \times 3$  served as the Lee filter parameters. For the images used during temporal filtering, no separation with respect to different orbits was performed. A comparison of the temporal filtered data—using images from different orbits versus using images from the same orbit—shows almost no difference between the filtered output data. After all of the preprocessing steps, the data were resampled to a spatial resolution of  $10 \times 10$  m [26]. In 2017, the MNI test site area was covered by four different Sentinel-1 tracks with individual acquisition geometries regarding incidence angle, azimuth angle, and orbit direction. Considering all available Sentinel-1 images for 2017 at the MNI test site, a revisit time of 1.5 days was reached. A total of 78 Sentinel-1 scenes during the time of the field campaign are available. For our study, the focus was set to VV polarization, motivated by previous findings where, to retrieve soil moisture, the usage of VH polarization alone or in addition to VV polarization was not suitable for well-developed agricultural vegetation [23,53]. Table 3 summarizes the Sentinel-1 data set used and its respective image properties.

**Table 3.** Available Sentinel-1A/B satellite data for the MNI field campaign period in 2017 (23 March–17 July 2017).

Orbit Mode	Orbit		Mean Incidence Angle of Test Site Area [°]	Azimuth Angle Relative to North [°]	Acquisition Time	Amount	Revisit Time [Days]
	Rel. Nr.						
Asc	44		36	−15	4:58 p.m.	19	6
	117		45	−15	5:06 p.m.	19	6
Des	95		43	−165	5:17 a.m.	20	6
	168		35	−165	5:25 a.m.	20	6

### 3. Method

Our study focused on investigating a dense Sentinel-1 C-band backscatter time series under varying acquisition geometries and on RT-based backscatter modeling of the time series. Two different RT model combinations calculating VV-polarized backscatter were analyzed. The soil surface scattering models used were Oh92 [41] and Baghdadi's version of the IEM [45], hereafter referred to as IEM\_B. The surface models were coupled with the Single Scattering Radiative Transfer Model (SSRT) of [30,37]. The SSRT was chosen because it calculates the direct vegetation volume backscatter and backscatter contributions due to the surface–canopy interactions. The calibration approach of Weiß et al. [26] with a non-static empirical parameter (*coef*) influencing the one-way transmissivity of the canopy (*T*) was used. Therefore, only one empirical parameter was calibrated for the different model combinations. The approximations applied by Weiß et al. [26] for parameters with missing in situ data such as rms height (1.2 cm) or scattering albedo (0.03) were used. The other input parameters for the surface models were in situ data for soil properties such

as clay and sand content, bulk density, and soil moisture measurements. For the canopy model part, in situ data of canopy height and LAI were used as vegetation descriptors. The various scattering components (ground component  $\sigma_{g pq}^0$ , canopy component  $\sigma_{c pq}^0$ , total canopy ground contribution  $\sigma_{cgt pq}^0$ , and ground canopy ground contribution  $\sigma_{gcg pq}^0$ ) of the SSRT used by De Roo et al. [37] and Ulaby [30] are defined as

$$\sigma_{pq}^0 = \sigma_{g pq}^0 + \sigma_{c pq}^0 + \sigma_{cgt pq}^0 + \sigma_{gcg pq}^0 \quad (1)$$

with

$$\sigma_{g pq}^0 = T_p T_q \sigma_{s pq}^0 \quad (2)$$

$$\sigma_{c pq}^0 = \frac{\sigma_{V pq}^{back} \cos \theta}{k_e^p + k_e^q} (1 - T_p T_q), \quad (3)$$

$$\sigma_{cgt pq}^0 = \sigma_{V pq}^{bist} H [R_p + R_q] T_p T_q \quad \text{and} \quad (4)$$

$$\sigma_{gcg pq}^0 = \frac{\sigma_{V pq}^{back} \cos \theta}{k_e^p + k_e^q} (R_p R_q - T_p T_q). \quad (5)$$

where  $\sigma_{s pq}^0$  represents the surface scattering,  $T_p$  and  $T_q$  symbolize the transmissivity of the canopy,  $\sigma_{V pq}^{back}$  is the volume backscattering coefficient of the vegetation medium,  $\sigma_{V pq}^{bist}$  is the bi-static scattering cross section,  $\theta$  is the incidence angle,  $k_e$  is the extinction coefficient for the different polarizations,  $H$  is the canopy height, and  $R$  describes the Fresnel reflectivity by polarization  $pq$ .  $T$  is defined as

$$T_p = e^{-k_e^p H \sec \theta}. \quad (6)$$

To calibrate the transmissivity of the canopy ( $T$ ) for different time steps and various acquisition scenarios, the extinction coefficient  $k_e$  for polarization  $p$  and  $q$  is defined as

$$k_e^p = coef * \sqrt{LAI}, \quad (7)$$

with LAI as the vegetation descriptor and  $coef$  as the calibration coefficient. A more detailed overview of the different RT models is provided in Weiß et al. [26]. A summary of validity ranges, model types, and input parameters required for the applied models is listed in Table 4.

**Table 4.** Overview of the different surface models Oh92 and IEM\_B as well as the canopy model SSRT in terms of type, validity range, required input parameters, and polarization. Separation of the input parameter applied for the RT models in calibrated parameters and in parameters from field measurements or literature values.

	Type	Validity Range	Required Parameters		Polarization
			Calibrated	Field Measurements or Literature Values	
Oh92	semi-empi.	$10^\circ < \theta < 70^\circ$ $0.1 < ks < 6$ $9 < mv < 31$ Vol.%		$s, k, \theta, \epsilon$ (clay, sand, bulk, mv)	HH, VV VH
IEM_B	semi-empi.	$10^\circ < \theta < 70^\circ$ $ks \leq 3$		$s, k, l, \theta, \epsilon$ (clay, sand, bulk, mv)	HH, VV VH
SSRT	semi-empi.		$ke$ (coef)	$H, LAI, \theta, \omega$	HH, VV VH

### 3.1. Calibration and Analyzed Data Sets

Figure 2 schematically explains the calibration approach from Weiß et al. [26] that was applied. Depending on the analysis approach, the images of the dense Sentinel-1 time series were separated into different subsets (blue box in Figure 2). An overview of the

data subsets used is provided in Table 5. Additionally, variations due to diverse spatial aggregation scenarios of the Sentinel-1 backscatter were investigated. An overview of the analyzed aggregation scenarios is given in Table 6. For each (sub)set and each aggregation scenario, the empirical parameter *coef* is calibrated separately. Therefore, the sum of the squared difference between the modeled and measured VV-polarized backscatters were used as a minimization function to calibrate the parameter *coef* and thus the transmissivity *T* (see Equations (6) and (7)). In the end, a final time series for *coef* and thus a final RT modeled VV polarized radar backscatter time series was obtained.

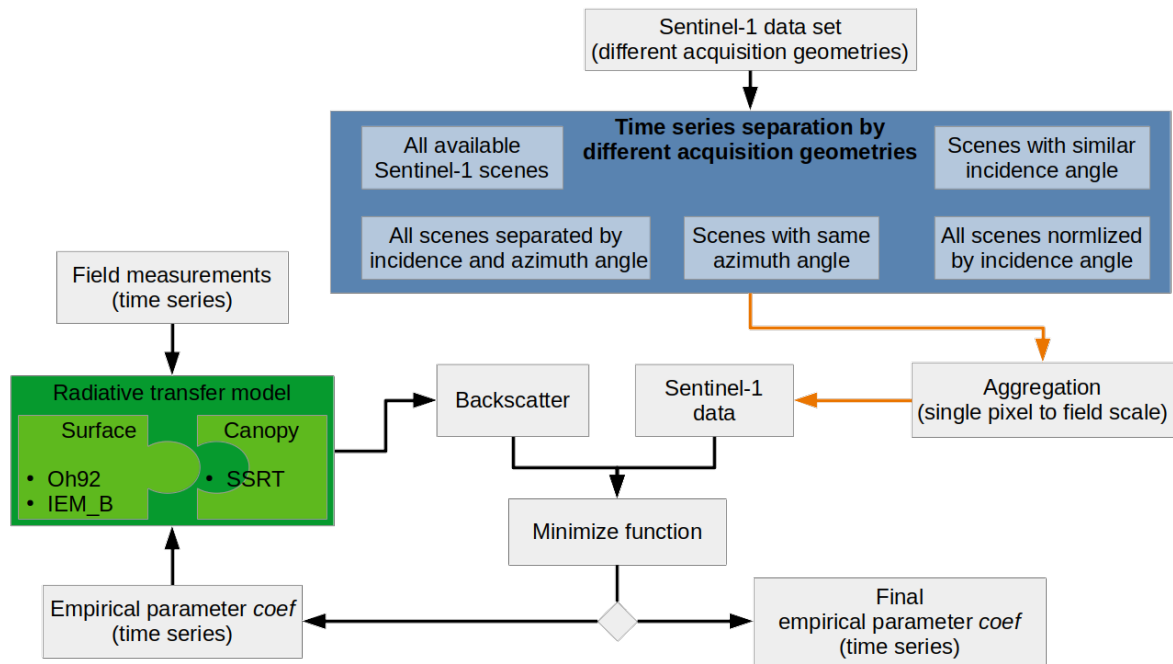


**Figure 2.** Schematic illustration of the calibration approach. Green box show used RT model combinations. The blue box illustrates the various (sub)sets analyzed for the dense time series. The orange arrows symbolize that several data (sub)sets and spatial aggregation scenarios were used.

**Table 5.** Investigated time series (sub)sets.

Abbreviation	Data Sets	Amount of Scenes	Rel. Orbit
All	All available Sentinel-1 scenes	78	44 + 95 + 117 + 168
Inci	Sentinel-1 scenes with similar incidence angle but different azimuth angle	2 sets of 39	44 + 168; 95 + 117
Azi	Sentinel-1 scenes with same orbit mode and azimuth angle	2 sets of 39	44 + 117; 95 + 168
Sep	Sentinel-1 scenes separated by incidence and azimuth angle	4 sets of 19–20	44; 95; 117; 168
Norm	All available Sentinel-1 scenes normalized to an incidence angle of 35°	78	44 + 95 + 117 + 168

**Table 6.** The backscatter aggregations investigated.

Abbreviation	Backscatter Aggregation	Area Size	Amount of Pixel
SP	Single pixel	10 × 10 m	1
30 m	15 m buffer	30 × 30 m	9
50 m	25 m buffer	50 × 50 m	25
100 m	50 m buffer	100 × 100 m	100
FS	Field scale		724–963

### 3.2. Leave-One-Out-Cross-Validation of Calibrated Model Combinations

A leave-one-out cross-validation approach was chosen to validate the calibrated model results of the different measurement points. Thus, the mean of eight out of nine measurement points of calibrated parameter *coef* was validated with the remaining one. Since the model input parameters used show multi-dimensional and unstructured inter- and intra-field correlations, independence between the different measurement points was assumed [26]. To evaluate the RT model fit of the time series sets analyzed (Table 5), the unbiased Root Mean Square Error (ubRMSE) [54] as a statistical metric was used. The ubRMSE is calculated as follows

$$\text{ubRMSE} = \sqrt{\frac{1}{N} \sum_{i=1}^N [(x_i - \bar{x}) - (y_i - \bar{y})]^2} \quad (8)$$

where  $x$  represents the backscatter modeled,  $\bar{x}$  represents the backscatter modeled and averaged,  $y$  represents the Sentinel-1 backscatter observation,  $\bar{y}$  represents the averaged Sentinel-1 backscatter observation,  $i$  represents a specific sample, and  $N$  represents the total number of samples.

### 3.3. Sensitivity Analysis of Soil Moisture and Polarimetric Eigen-Based Decomposition for the RT Model

A sensitivity analysis of the RT models was conducted for a comprehensive interpretation of improvements in terms of backscatter values by using different Sentinel-1 time series sets (Table 5) and/or various spatial aggregations (Table 6). To test the RT models' sensitivity to changes in soil moisture, artificial deviations in soil moisture were assumed, leading to changes in backscatter values of 0.2 db, 0.5 db, or 1.0 db. The artificial deviations in backscatter were calculated for each time step of the time series individually. In this way, the sensitivity of the backscatter to soil moisture during the phenological cycle and different meteorological conditions could be assessed.

In addition, a dual-polarized (VV and VH) eigen-based (entropy (H)-scattering alpha (alpha)) decomposition of the entire Sentinel-1 time series, having variations in the acquisition scenario, was performed to investigate and understand the occurring scattering mechanisms and changes in scattering mechanisms during the growing season. The H-alpha dual polarized decomposition [55] was performed by using an internal processing step of ESA's SNAP toolbox. Special focus was set on the comparison of images of consecutive time steps with various acquisition geometries. The dual-polarimetric eigen-based decomposition comes with a caveat, as the separation of different scattering mechanisms in the H-alpha plane is only possible with fully, quad-, or co- (VV and HH) polarized data [56]. Therefore, the exact identification and detailed distinction of the scattering mechanism that occurs for each time step is beyond the scope of information from the recorded data set. Nevertheless, the H-alpha results can be used as a first-order indicator of scattering mechanism change over time and, owing to acquisition scenario, even if the exact types of scattering mechanisms and their change cannot be identified directly. However, the scattering mechanism changes that were revealed might further improve our understanding of the deficits of simplified model approaches and how they might be compensated.

## 4. Results

### 4.1. All Sentinel-1 Tracks Analyzed as One Time Series

The calibration results analyzing the usage of different dense time series (sub)sets are presented for field point 508-1 as an example. The other fields analyzed and the respective intra-field points show similar patterns and are only included for validation of the backscattering model results (Section 4.3). Accordingly, a time series of VV-polarized backscatter of all available Sentinel-1 images for field point 508-1 (black line) is illustrated in Figure 3a. The model results (green and blue line) are based on a calibration of the empirical parameter *coef* (Equation (7)) as part of the transmissivity (Equation (6)) considering all available Sentinel-1 images as one data set (Tables 5 and 6, “All-50 m”). The background colors red, blue, green, and yellow symbolize the Sentinel-1 data, and the respective acquisition geometries represent four consecutive days of Sentinel-1 data acquisition. A closer look at the four consecutive time steps (yellow to green background colors), while disregarding backscatter changes due to soil moisture and vegetation dynamics, shows that, during early vegetation stages (tillering and stem elongation), higher Sentinel-1 backscatter values are observed for more steep incidence angles (around 35°) than for more shallow ones (around 44°). Starting from the beginning of June (phenology stage booting), the backscatter behavior pattern in terms of the incidence angle variation of the four consecutive time steps varied. Accordingly, higher backscatter values were observed for incidence angles of 44° than for 35°. A pattern regarding variations in azimuth angles was not observed here. Comparing the modeled results of IEM\_B with SSRT (green line) and of Oh92 with SSRT (blue line), higher sensitivities to incidence angle deviations are observed for the Oh92 model. Backscatter modeling for the phenology stages tillering and stem elongation of model Oh92 with SSRT reveals a high correlation with the Sentinel-1 backscatter observed in terms of absolute values and the changes in backscatter observed due to the various acquisition geometries. Starting from phenology stage booting to senescence, Sentinel-1 backscatter reveals a different behavior from the modeled results. For these phenology stages, the Sentinel-1 backscatter values of consecutive time steps with varying incidence angles (background colors yellow to red) increased whereas the RT model results exhibited a decrease in backscatter. For the other consecutive time steps with varying incidence angles (background colors blue to green), the Sentinel-1 backscatter values decreased whereas the RT model results showed an increase in backscatter. The different results of the Sentinel-1 and RT models are hereinafter referred to as a trend mismatch of consecutive time steps. Summarizing the findings, the simple RT model approaches experience difficulties in accurately modeling time series comprising observations from different orbits (different observation geometries) for a winter wheat field with a fully developed canopy. A trend mismatch is observed. In the end, the model combination of Oh92 with SSRT has a higher sensitivity to observation geometry changes than the model combination of IEM\_B with SSRT.

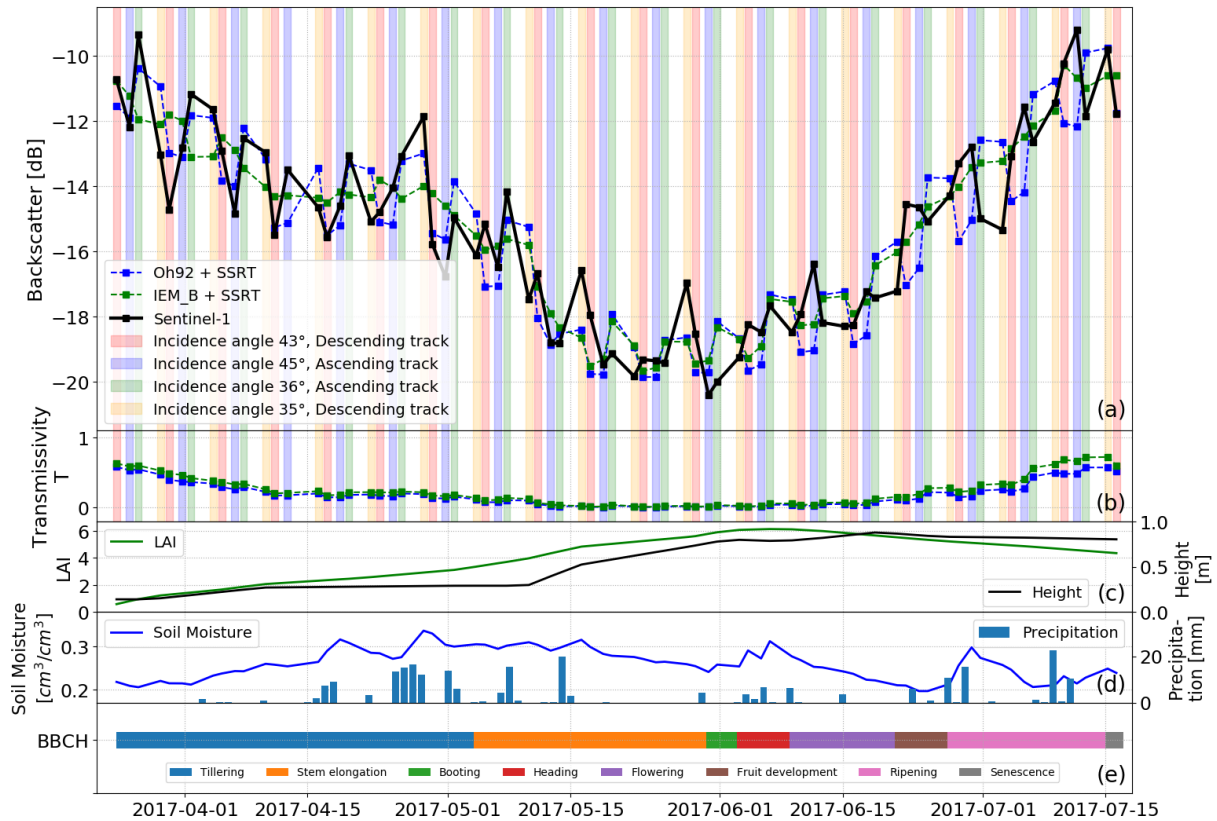


**Figure 3.** Sentinel-1 backscatter data for field point 508-1. Modeled backscatter results of IEM\_B and Oh92 with SSRT (a). Different background colors (red, blue, green, and yellow) represent Sentinel-1 images with various acquisition geometries (a,b). Calibrated transmissivity  $T$  for each time step (b). In situ data of vegetation height and LAI (c). Soil moisture and precipitation measurements (d). Observed vegetation phenology according to the BBCH scale [57] (e).

## 4.2. Subsets of Dense Sentinel-1 Time Series

### 4.2.1. Analyzing Incidence Angle Variety

The data set was separated into two subsets to analyze the effect of varying incidence angles within the dense Sentinel-1 time series on the RT model results. Therefore, one subset consists only of images acquired in the same orbit direction and with the same azimuth angle (“Azi-50 m”). The azimuth angle itself is not an input parameter within the RT models, and therefore, deviations in backscatter caused by the various azimuth angles were not considered in our simple model approach. The variation in incidence angle on the other hand should cause variations in the backscatter modeled as the incidence angle is implemented as an input parameter within the RT models. The empirical model parameter *coef* as part of the transmissivity  $T$  was calibrated for each time step using the Sentinel-1 data of each subset separately. Figure 4 illustrates the results for an azimuth angle of  $-15^\circ$  (relative to north), and Figure 5 illustrates the results for an azimuth angle of  $-165^\circ$  (relative to north). Sentinel-1 backscatter (black line), total backscatter, and the two main contributors to the total backscatter (surface and canopy part) of the models analyzed (blue and green lines) are shown in Figures 4a and 5a. For both subsets, deviations in Sentinel-1 backscatter in the range from 2 db to 3 db between two consecutive time steps with varied incidence angles (background colors blue to green or yellow to red) are still apparent. Similar to the results shown in Figure 3, the Sentinel-1 backscatter differences of consecutive time steps observed were modeled well until the end of May. However, starting with the phenology stage of booting at the beginning of June, a trend mismatch

is observed between two consecutive time steps of Sentinel-1 and modeled data, similar to the one in Figure 3. The differences within the time series of  $T$  of Figures 4b and 5b between two consecutive time steps are similar to the modeled transmissivity illustrated in Figure 3. Since the simple RT models' sensitivity towards accurately calculating backscatter with varying incidence angles seems to be imperfect, an incidence angle normalization approach might be able to resolve or at least mitigate this issue. One of the challenges of applying incidence angle normalization approaches to the entire time series is experienced when using the analyzed Sentinel-1 data itself. The Sentinel-1 backscatter (black line within Figures 4 and 5) of consecutive time steps with different incidence angles shows higher backscatter values for steep incidence angles until the end of May and lower backscatter values for shallow incidence angles from the beginning of June. Due to this behavior, an incidence angle normalization results in either lower backscatter differences due to varying incidence angles during early phenology stages (tillering and stem elongation) and higher differences for later phenology stages (booting to senescence), or vice versa. The desired effect of the normalization in providing a smooth time series of backscatter data from wheat fields cannot be accomplished by applying one normalization approach to the entire data set. The findings indicate that a simple model approach has some deficits in simulating backscatter under various incidence angles within one time series, although the incidence angle is used as an input parameter to the models.

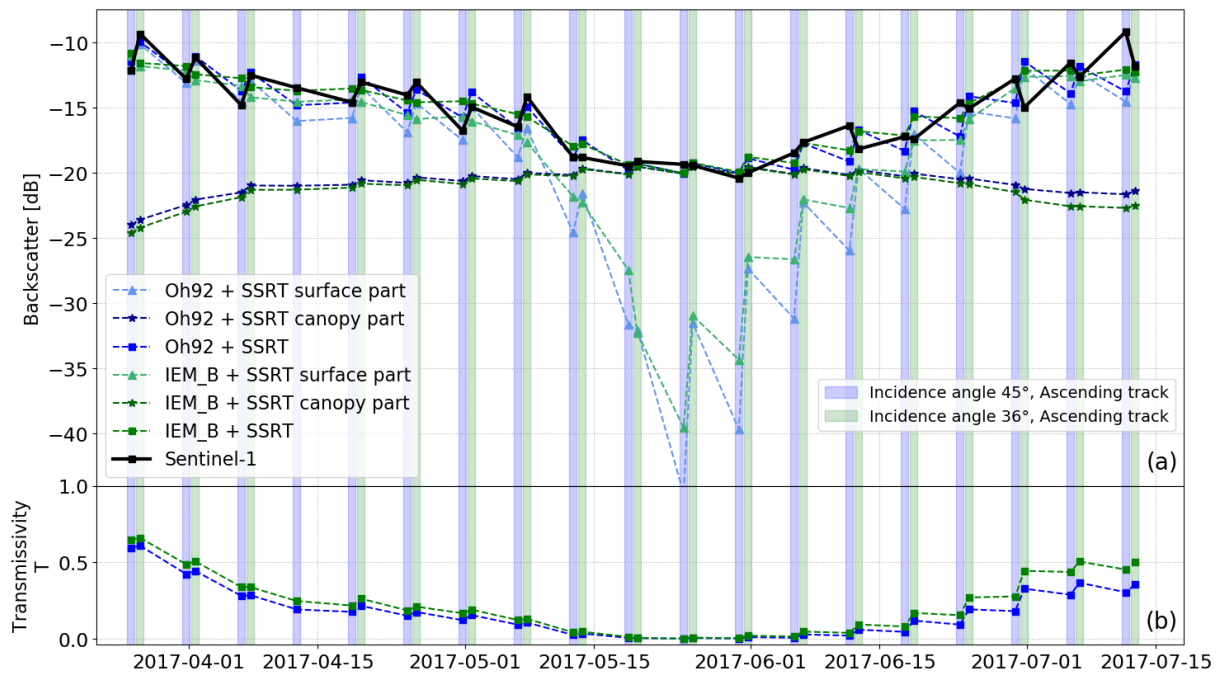


**Figure 4.** Sentinel-1 time series and RT model results considering images with an ascending orbit direction and an azimuth angle of  $-15^\circ$  (relative to north) (a). Different background colors (red, blue, green, and yellow) represent Sentinel-1 images with various acquisition geometries (a,b). Calibrated transmissivity  $T$  (b).

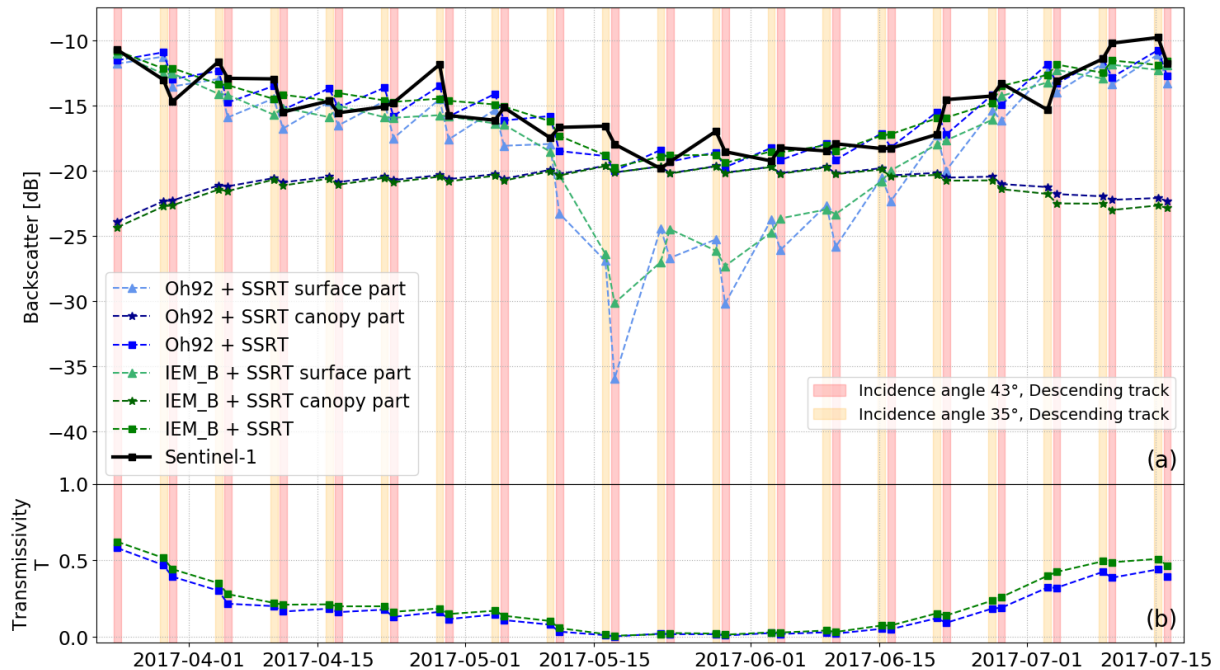


**Figure 5.** Sentinel-1 time series and RT model results considering images with a descending orbit direction and an azimuth angle of  $-165^\circ$  (relative to north) (a). Different background colors (red, blue, green, and yellow) represent Sentinel-1 images with various acquisition geometries (a,b). Calibrated transmissivity  $T$  (b).

#### 4.2.2. Analyzing Azimuth Angle Variety

The data set was split into two subsets to analyze the effect of varying azimuth angles within the dense Sentinel-1 time series and on the RT model results. Therefore, each new subset consists of acquisitions with similar incidence angles (“Inci-50 m”). Equivalent to the approach of Section 4.2.1, parameter *coef* of the RT model combinations was calibrated using the Sentinel-1 data of each subset separately. Figure 6 shows the results for incidence angles of  $35^\circ$  to  $36^\circ$ , while Figure 7 illustrates the results for  $43^\circ$  to  $45^\circ$ . For incidence angles of  $35^\circ$  and  $36^\circ$ , higher deviations in terms of Sentinel-1 backscatter values between consecutive time steps are only visible with a significant change in soil moisture content (Figure 6c). Otherwise, distinct backscatter differences between consecutive time steps for the Sentinel-1 and RT model results are not identifiable. Additionally, the trend mismatch between the Sentinel-1 and RT model results for the phenology stages booting to senescence is not present for incidence angles  $35^\circ$  to  $36^\circ$ . The backscatter variation with incidence angles of  $43^\circ$  and  $45^\circ$  present a slightly different picture. Small discrepancies between consecutive time steps of the Sentinel-1 data are visible. However, no real trend mismatches between the backscatter values of the Sentinel-1 and RT model results are evident. For both subsets, it can be stated that, overall, the RT model predictions are in sufficient agreement with the Sentinel-1 data. Summarizing the findings, it can be stated that, although the azimuth angle is not considered as a parameter within the models, no obvious deviations between the backscatter modeled and the Sentinel-1 backscatter is observed and, thus, deviations in azimuth angles within a dense time series seems to be negligible for the model approach presented.

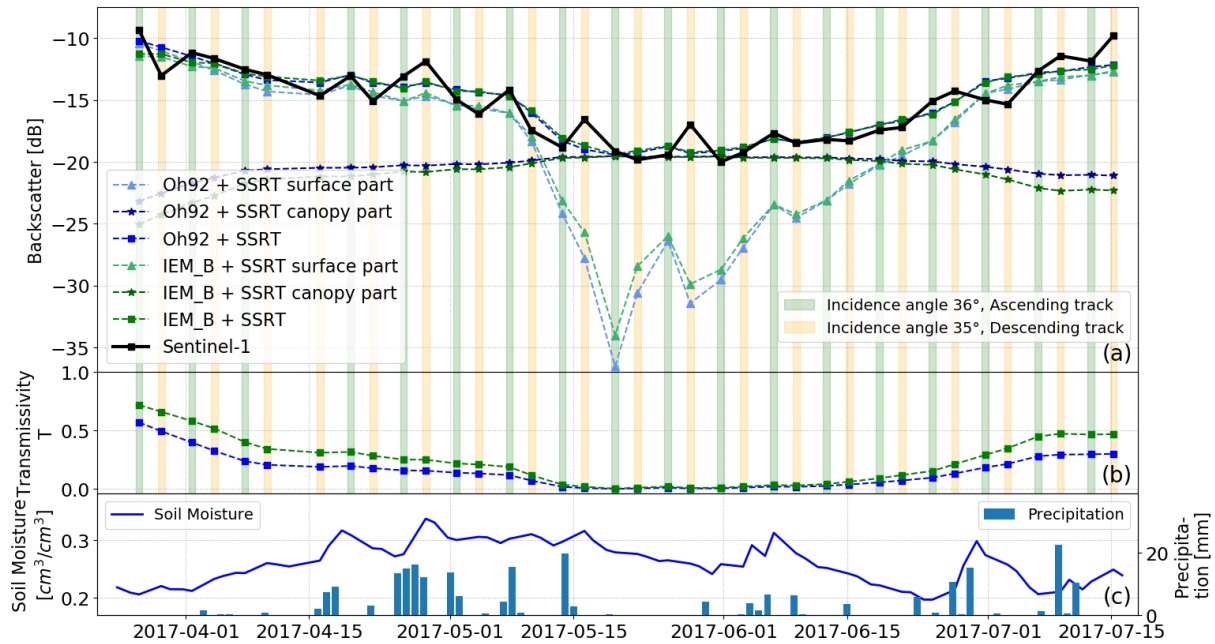


**Figure 6.** Sentinel-1 VV backscatter time series and RT model results for canopy and surface scattering considering images with similar incidence angles (35°, 36°) (a). Different background colors (red, blue, green, and yellow) represent Sentinel-1 images with various acquisition geometries (a,b). Calibrated transmissivity  $T$  (b). Soil moisture and precipitation measurements (c).

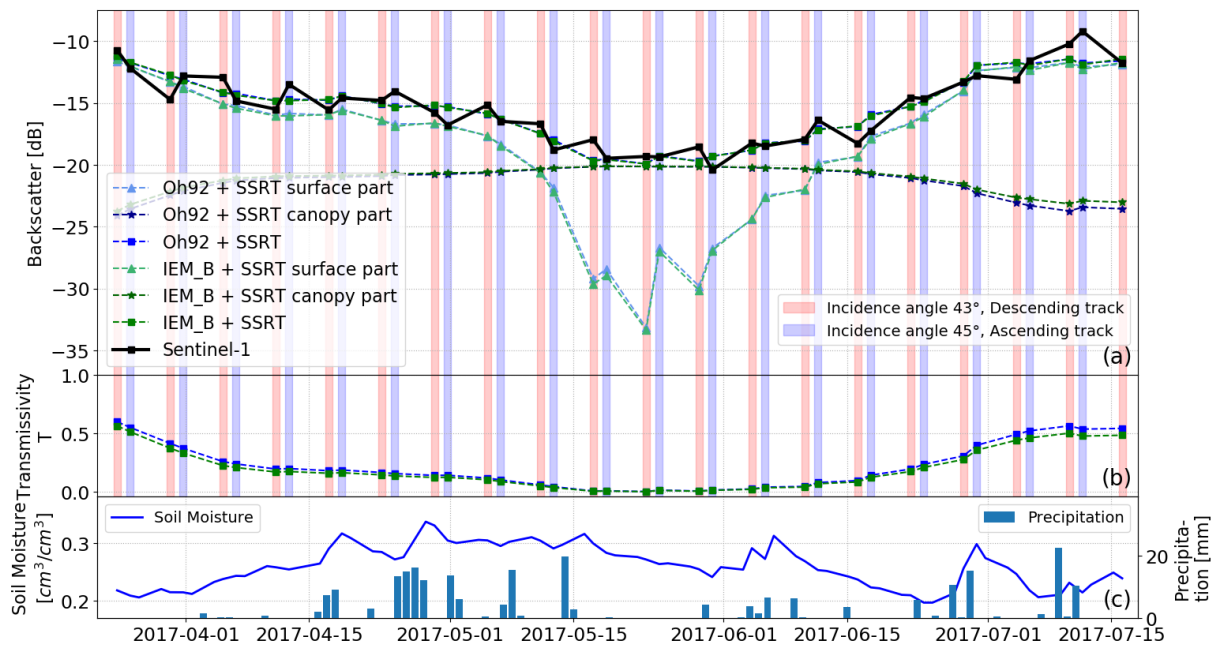


**Figure 7.** Sentinel-1 VV backscatter time series and RT model results for canopy and surface scattering considering images with similar incidence angles (43°, 45°) (a). Different background colors (red, blue, green, and yellow) represent Sentinel-1 images with various acquisition geometries (a,b). Calibrated transmissivity  $T$  (b). Soil moisture and precipitation measurements (c).

#### 4.2.3. Separation of Dense Sentinel-1 Time Series into Mono-Incidence Data Sets

After analyzing the effects of different azimuth and incidence angles on the backscatter, the dense time series was separated into four subsets with the same orbit and, thus, the same acquisition geometry (“Sep-50 m”). The transmissivity  $T$  was calibrated by the empirical parameter  $coef$  for each subset individually, and the results were reassembled into one time series afterwards. The trend mismatch between the data modeled and the Sentinel-1 data of consecutive time steps with various acquisition geometries after the beginning of June, which was detected in Figure 3, was resolved. Figure 8 shows these calibrated model results of a reassembled dense time series. Furthermore, compared to Figure 3, a sensitivity increase in the IEM\_B model results in backscatter changes due to varied incidence angles being observed. The resolved trend issue and the higher incidence angle sensitivity effect result in dynamic transmissivity values by separately calibrating the empirical parameter  $coef$  for varying time series subsets. Contrarily, in Figure 3, no differences of  $T$  between consecutive time steps are visible, but various values for  $T$  can be observed in Figure 8. The model combination Oh92 with SSRT shows variations in  $T$  (between Figures 3b and 8b) only after mid-July (flowering to senescence), whereas IEM\_B exhibits variations during the early (tillering) and late (flowering to senescence) phenology stages. The calibrated parameter  $coef$  seems to compensate for the lack of RT models in handling various acquisition scenarios in our model setup. This compensation might be forced by the model architecture and/or calibration and needs further investigation. During the phenology stages flowering to senescence, higher  $T$  values (Figure 8b) as well as higher surface model contributions (Figure 8a, triangle symbol) are observed for IEM\_B and Oh92 for shallow than for steep incidence angles. Theoretically, by considering a canopy layer of 90–100 cm, the electromagnetic wave travels a farther distance through the canopy for shallow incidence angles than for steep incidence angles. Under the assumption that farther distances (shallow incidence angle) through the canopy leads to lower canopy transmissivity of the electromagnetic wave, the modeled  $T$  and the model surface component of Oh92 and IEM\_B should be lower for shallow incidence angles and not the other way around. Although the model theory described cannot be seen in Figure 8, Figure 4 shows this theoretical behavior of the surface model component (Figure 4a, triangle symbol) and transmissivity (Figure 4b). However, comparing Sentinel-1 and the total modeled backscatter within Figure 4, a trend mismatch between consecutive time steps for phenology stages flowering to senescence and, therefore, differences between the Sentinel-1 and RT model total backscatter are observed.

For the results illustrated in Figure 8, no trend mismatch and thus a better fit of the data modeled and the Sentinel-1 data are observed. The reason for the discrepancy between the model theory assumed and the behavior observed might be caused by insufficient—or missing—consideration of the scattering mechanisms in the applied simplified model architecture. For a change detection analysis on scattering mechanisms and/or backscatter effects, a VV–VH dual polarimetric eigen-based (entropy (H)-scattering angle (alpha)) decomposition is performed [56]. The H-alpha results of the eigen-based decomposition are reported in Figure 9. The rows illustrate the results of consecutive time steps with various acquisition geometries ( $x$ -axis) for different vegetation stages of tillering, stem elongation, heading, and ripening ( $y$ -axis). The columns indicate the results for different incidence angles and orbit directions. During the wheat crop’s tillering stage, no obvious deviations between the H-alpha results of the different acquisition geometries are recognizable. Changes in scattering effects moving from the tillering to stem elongation stages are indicated by a shift to higher H- and alpha-values. Stronger variations in the H- and alpha-values are observed for incidence angles around  $35^\circ$  than for  $44^\circ$ . The H-alpha values of the wheat fields of consecutive time steps confirm insensitivity to variations in azimuth angles of individual scenes, similar to that for backscatter. However, differences in the H- and alpha-values are observed between acquisitions with various incidence angles. Lower incidence angles of  $35^\circ$  reveal higher shifts in the H- and alpha-values between the tillering and stem elongation phases as well as higher H- and alpha-values

compared to incidence angles around  $44^\circ$ . When comparing the phenology stages stem elongation and heading, a slight decrease in H- and alpha-values is apparent. Therefore, a clear separation by incidence angle due to deviations in H- and alpha-values is possible, whereas a separation due to azimuth angles is difficult. During the ripening stage, a further decrease in H- and alpha-values is observed. Separation due to various incidence angles is possible, although not as clear as during the stem elongation or heading stages. The H- and alpha-values are similar to the values during the early vegetation stages, such as tillering. Further analysis of the different scattering mechanisms is difficult as Ji and Wu [56] found that, for VV-VH dual polarimetric eigen-based decomposition, the classification of scattering mechanisms is not as precise as for fully polarimetric ones. The various scattering mechanism classes in the H-alpha plane can have high overlap for the VV-VH dual decomposition results. Nevertheless, the change detection results show that variations in the scattering mechanism of consecutive time steps are mainly driven by the incidence angle during acquisition and not by the azimuth angle. Furthermore, similar scattering mechanisms are observed for the early (tillering) and late (ripening) vegetation stages. During the vegetation period from stem elongation to flowering stage, higher changes in scattering effects (dynamics in H- and alpha-values) are observed for steep incidence angles ( $35^\circ$ ) than for shallow incidence angles ( $44^\circ$ ). Summarizing the findings, it can be stated that, although the simplified RT models have some deficits when handling different incidence angles within one dense time series, the empirical parameter *coef* can partly compensate for model deficiencies if each orbit is modeled separately. H-alpha decomposition is an analysis tool to explore variations in scattering mechanisms. These variations might be a possible reason for the simple model approaches having deficits in accurate backscatter modeling. H-alpha analysis indicates that, indeed, different scattering mechanism changes occur over time for different incidence angles. Moreover, variations in azimuth angles are not responsible for changes in backscatter or scattering mechanisms.

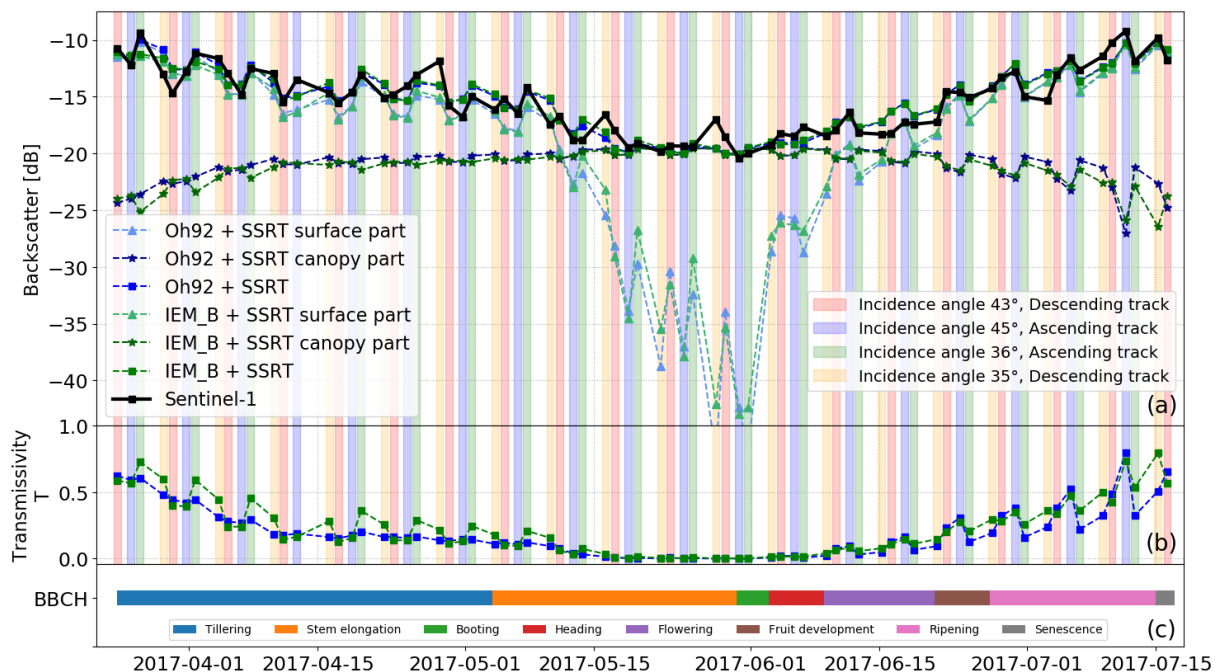


**Figure 8.** Joint Sentinel-1 VV backscatter time series and RT model results for canopy and surface scattering considering four mono-incidence angle data sets (a). Different background colors (red, blue, green, and yellow) represent Sentinel-1 images with various acquisition geometries (a,b). Calibrated transmissivity  $T$  (b). Observed vegetation phenology according to BBCH scale [57] (c).

#### 4.3. Validation and Quantification of RT Model Results

Validation of the RT model calibration approach for the various dense time series (sub)sets was performed by a leave-one-out-cross-validation method. The mean ubRMSE of the Sentinel-1 and modeled data for all measurement field points is illustrated in Figure 10. The results are categorized by different spatial backscatter aggregations ( $x$ -axis), RT model combinations ( $x$ -axis), and (sub)sets of the dense Sentinel-1 time series used (color separation). It is expected that intra-field variances are reduced by averaging, and in this way, agreements between the model and observations might be facilitated. However, this analysis wants to quantify the model performance of the different aggregation scenarios in dB to understand the loss of precision where intra-field variance is vital. Comparing the results of Oh92 with SSRT and of IEM\_B with SSRT for various Sentinel-1 data (sub)sets, greater variability in ubRMSE is shown for the Oh92 model combination. For both models as well as for the various data (sub)sets, spatial aggregations lead to improved ubRMSE values. The IEM\_B and Oh92 results reveal improvements on the pixel to field scales by up to 0.5 dB. The best model fit in terms of ubRMSE is provided when using a time series that only considers Sentinel-1 images with incidence angles of around  $35^\circ$  (light green). Moreover, the ubRMSE results in a similar range to that of the best model fit are shown by using a data set with incidence angles of  $43^\circ$  to  $45^\circ$  (dark green) or if all acquisition geometry scenarios are analyzed separately (black). Overall, the IEM\_B model combination reveals slightly better results than the Oh92 model combination for the different categorizations. Both model combinations analyzed by using only images with incidence angles of  $35\text{--}36^\circ$  (light green) compared to the entire Sentinel-1 data set (gray) improved by up to 0.3 dB. The ubRMSE of the best model fit (light green) is 1.43 dB for IEM\_B and 1.64 dB for Oh92. Summarizing the results, it can be stated that the best model agreement is obtained by aggregation to the field level and by using steep incidence angles. The differences between single pixel and  $30 \times 30$  m resolution are up to 0.2 dB, and the differences between single pixel and field scale aggregations are up to 0.5 dB.

#### 4.4. Sensitivity to Soil Moisture Estimations over Time for the RT Model

For a comprehensive interpretation of the quantitative results illustrated in Figure 10, sensitivity analyses of the model combinations IEM\_B and Oh92 with SSRT are provided in Figures 11 and 12, respectively. The figures show the deviation in estimated soil moisture with artificial variations of backscatter of 0.2 dB, 0.5 dB, and 1.0 dB. This helps in understanding how the backscatter differences modeled for different aggregation scenarios (Figure 10) result in uncertainty regarding soil moisture. It is interesting to understand that the uncertainty in soil moisture estimation differs for different phenology stages during the vegetation growing period. Uncertainty starts to increase during the stem elongation stage. This is in seen alongside an increase in vegetation height from 20 cm to 90 cm as well as an increase in LAI from 3 to 6. Due to a larger canopy layer, the transmissivity decreases, and therefore, less information about the soil and its moisture content is present within the SAR signal. During the heading stage of plants, the uncertainty begins to decrease again and it reaches its minimum during the ripening stage. Although the maximum height of the canopy is reached, the transmissivity increases and, therefore, the uncertainty of soil moisture estimations decreases. The higher transmissivity might be explained by the loss of water within the vegetation, whereby the SAR signal is less attenuated by the canopy, and therefore, the SAR signal provides more information about the soil [58–60]. Changes in incidence angles do not result in varying soil moisture uncertainties for the IEM\_B model combination, whereas within the phenology stages stem elongation to fruit development, the Oh92 model combination exhibits differences in soil moisture uncertainties for varying incidence angles. For Oh92 with SSRT, a deviation in backscatter of 0.2 dB for an incidence angle change from  $35^\circ$  to  $44^\circ$  does result in an uncertainty disparity of up to  $0.08 \text{ cm}^3/\text{cm}^3$ . The results show that the uncertainties in soil moisture estimation of IEM\_B and Oh92 have similar values; are highly correlated to different vegetation stages; and in the case of Oh92, are also dependent on the incidence angle.

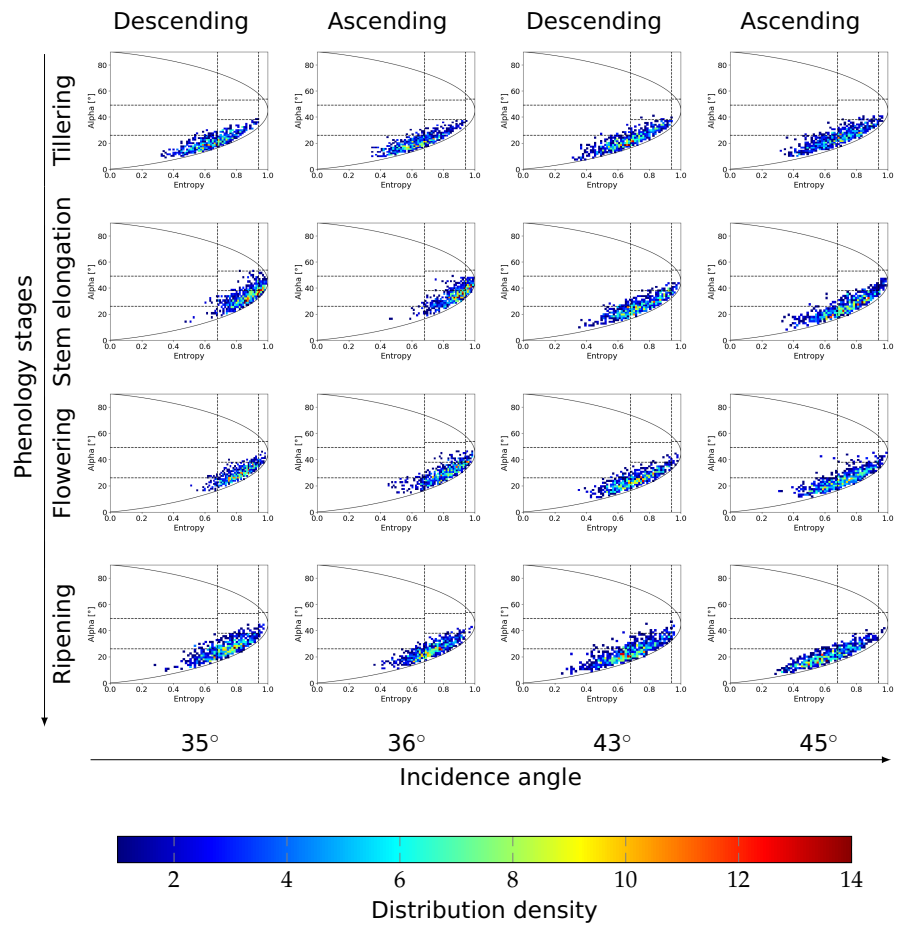


**Figure 9.** Polarimetric entropy to scattering alpha angle plane of dual (VV/VH) polarimetric eigen-decomposition for different incidence angles ( $x$ -axis) and various phenology stages ( $y$ -axis) of wheat field 508. Colors from blue to red symbolize the distribution density. The H-alpha plane segmentation for dual (VV/VH) polarimetric eigen-decomposition is from Ji and Wu [56].

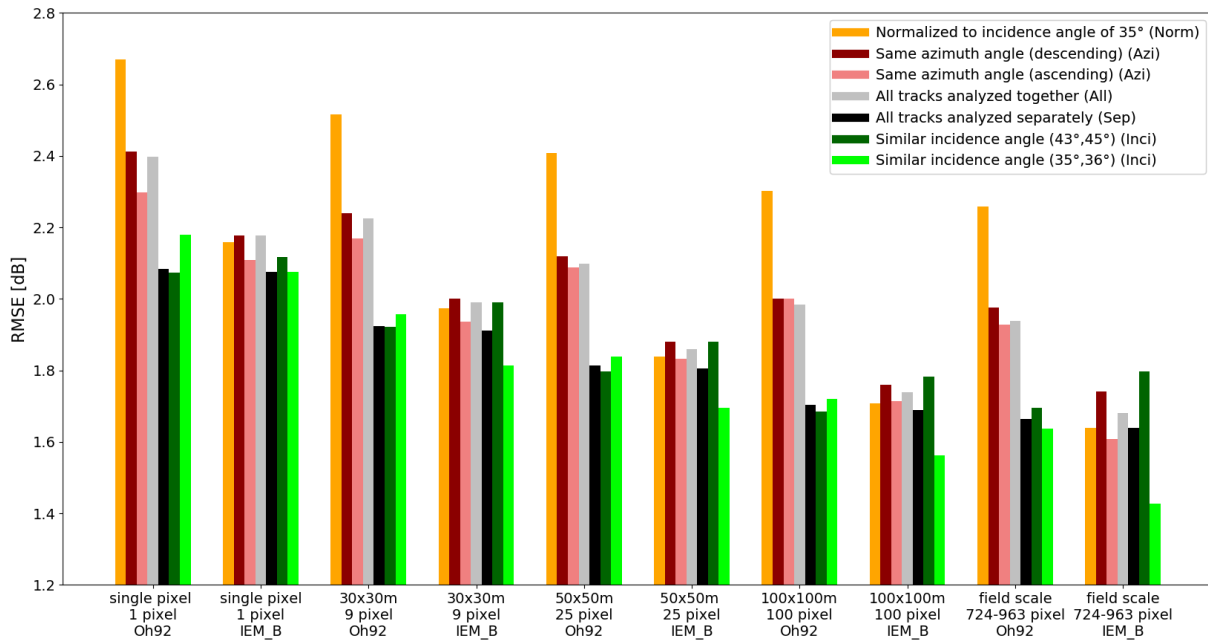


**Figure 10.** Validation results in terms of ubRMSE for RT models Oh92 and IEM\_B with SSRT. The results are segmented in the x axis by different spatial aggregations (single pixel to field scale). Different colors symbolize the data (sub)sets used due to separation of incidence and azimuth angles.

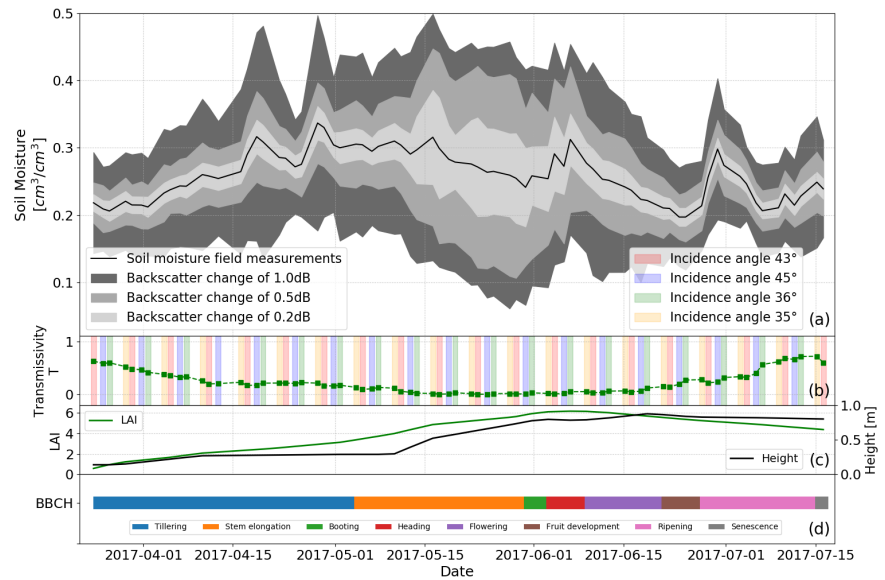


**Figure 11.** Sensitivity analysis of the RT model IEM\_B with SSRT. Deviations in the backscatter of 0.2 dB, 0.5 dB, and 1.0 dB are correlated with soil moisture uncertainty (a). Different acquisition geometries (indicated by the colors red, blue, green, and yellow) of the data set used and the calibrated transmissivity for each time step (b). In situ data of vegetation descriptors height and LAI (c). Vegetation phenology observed according to the BBCH scale [57] (d).

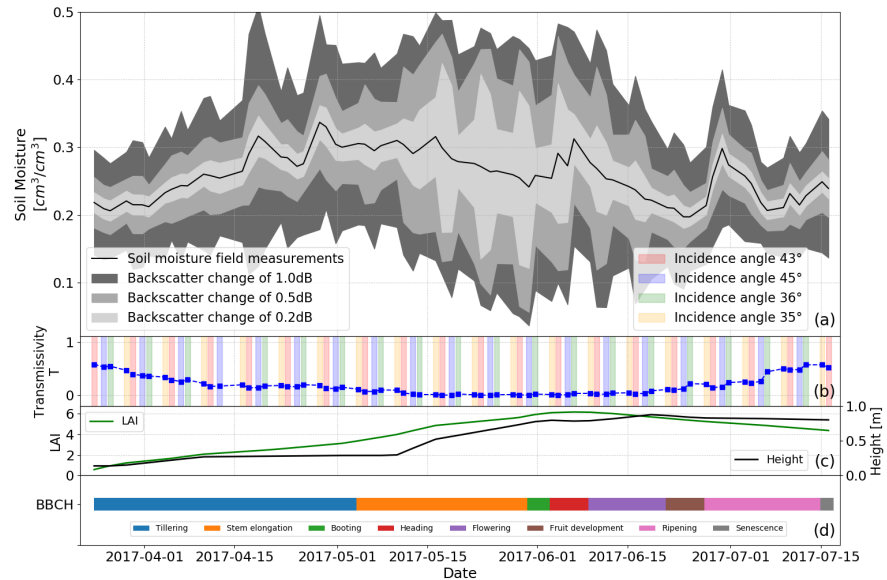


**Figure 12.** Sensitivity analysis of RT model Oh92 with SSRT. Deviations in the backscatter of 0.2 dB, 0.5 dB, and 1.0 dB are correlated with soil moisture uncertainty (a). Different acquisition geometries (indicated by the colors red, blue, green, and yellow) of the data set used and the calibrated transmissivity for each time step (b). In situ data of vegetations descriptors height and LAI (c). Vegetation phenology observed according to the BBCH scale [57] (d).

## 5. Discussion

To monitor high temporal dynamics of soil moisture, a time series with up to daily acquisitions is very useful. Currently, the Sentinel-1 satellites can provide time series with almost daily (1.5 days) acquisitions at mid-latitudes. However, due to different acquisition orbits, the images can vary in acquisition geometry and timing, which has an effect on the SAR signal. Our results show that various azimuth angles for daily consecutive acquisitions of wheat fields have only a minor impact on observed Sentinel-1 backscatter differences. However, a comparison of images with various incidence angles reveals backscatter variations in the range of up to 3 dB. Using images with similar incidence and diverse azimuth angles, backscatter variations between images of consecutive acquisition days are minimal to negligible. Lower differences in backscatter are observed for incidence angles around  $35^\circ$  than for  $44^\circ$ . A different spread of incidence angle variation in the observations ( $35\text{--}36^\circ$  vs.  $43\text{--}46^\circ$ ) might cause these differences in the backscatter. The lower backscatter differences between incidence angles  $35\text{--}36^\circ$  compared to  $43\text{--}46^\circ$  might be caused by the slightly higher incidence angle variation between the observations used for the different orbits. A comparison of the RT model results and Sentinel-1 backscatter observations for “All-50 m” (Figure 3) and “Azi-50 m” (Figures 4 and 5) reveal trend mismatches between the RT modeled and observed Sentinel-1 backscatter for consecutive time steps with incidence angle variations from the beginning of June until harvesting (corresponds to phenology stages from booting to senescence). When using (sub)sets with similar incidence angle and varying azimuth angles (“Inci-50 m” Figures 6 and 7), a trend mismatch between the RT model and Sentinel-1 backscatter is not found. Since the incidence angle is implemented as an input variable within the RT models applied [23,30,37,41], we expect that the RT models should be able to sufficiently consider Sentinel-1 backscatter differences due to incidence angle variations for the entire growing season. However, the trend mismatch observed in later phenological stages (booting to senescence) of the wheat fields implies that the simple model approach falls short in handling variations within a dense time series if the

canopy layer is fully developed. By calibrating the empirical parameter *coef* for each orbit constellation separately (Figure 8), the drawbacks in precise modeling of all scattering mechanisms by simplified models (vegetation and soil) can be compensated. While more complex models might account for incidence angle variations in a more accurate way, they may be more inappropriately applied due to missing but necessary a priori/input measurements. As several studies have already found that backscatter characteristics change during or after the phenology stage of heading [60–62], we explored simple RT models by handling variations in incidence angles by performing a dual polarimetric (VV and VH) eigen-based decomposition (Figure 9). These results indicate that a change in the scattering mechanisms starts at the end of the phenology stage of stem elongation. Furthermore, they convey that varied backscatter characteristics for wheat fields might significantly depend on the incidence angle, whereas the azimuth angle seems to play a minor role. The shortcoming of simplified RT model approaches when handling various incidence angle scenarios is most likely related to inaccurate modeling of the different scattering mechanisms. As simplified models are often preferred over complex scattering models, further investigations with a larger sample of wheat fields and preferably with fully polarimetric SAR data should be carried out to verify the obtained results and to find a simple empirical or physical model solution that might be able to enhance the models by keeping their simplicity. In this context, an often-used strategy of incidence angle variations by normalizing the incidence angle [40,63–65] was ruled out. An examination of the Sentinel-1 time series of winter wheat fields observed revealed that incidence angle normalization of the entire time series are not useful due to contradicting trends between consecutive Sentinel-1 observations, variations in acquisition scenarios, and different phenology stages in the wheat growing season.

In light of exploring the possible use of Sentinel-1 data and simplified backscattering models for precision farming purposes, where sub-field variability needs to be preserved, a quantification of model-to-observation mismatch was carried out in absolute numbers (dB) for different aggregation scenarios (Figure 10). With a larger spatial aggregation, an accuracy increase in backscatter estimation (in comparison to the Sentinel-1 observations) was found that is similar to that in Pierdicca et al. [66] or Carranza et al. [64]. This was expected. However, the quantification in dB shows differences between single-pixel (SP) and  $30 \times 30$  m (30 m) resolutions as well as single-pixel and field-scale (FS) aggregations of up to 0.2 dB and 0.5 dB, respectively. The backscatter differences found are related to small deviations in the soil moisture estimation by  $0.01 \text{ cm}^3/\text{cm}^3$  (SP to 30 m) and  $0.02 \text{ cm}^3/\text{cm}^3$  (SP to FS) for the early and late vegetation stages and up to large variations of  $0.13 \text{ cm}^3/\text{cm}^3$  (SP to 30 m) and  $0.19 \text{ cm}^3/\text{cm}^3$  (SP to FS) for the phenology stages stem elongation to fruit development. The variations in soil moisture during the early and late vegetation stages indicate some opportunities for providing information for precision farming. However, during the phenology stages of significant vegetation growth (late stage of stem elongation to heading) the deviations in possible soil moisture estimation increase, greatly hampering precision farming applications. Since accurate soil moisture estimation highly depends on reliable information about the canopy, the fusion of optical (Sentinel-2) and microwave (Sentinel-1) time series [67–69] might provide useful phenology stage-based information in terms of LAI, NDVI, VWC, or biomass. The increase in soil moisture sensitivity of the radar signal for later vegetation stages is further related to the loss of plant water after the heading stage, which leads to a more transparent canopy layer and higher sensitivity of the radar waves to the soil surfaces [26,58,60,70]. These findings of high surface scattering during the end of the vegetation period are also supported by similar polarimetric entropy and scattering alpha values for the tillering and ripening stages (Figure 9).

## 6. Conclusions

Simulations of the RT model combinations (IEM\_B with SSRT and Oh92 with SSRT) were compared to a dense Sentinel-1 VV backscatter time series. By considering Sentinel-1 images recorded with the available acquisition geometry, a dense time series with a mean

revisit time of 1.5 days was achieved for the winter wheat test site near Munich, Germany. Thus, different (sub)sets (separation by acquisition geometry) of the dense time series were evaluated in time and space.

Backscatter variations between individual Sentinel-1 scenes with various acquisition geometries (different orbits) were found to be mainly driven by changes in incidence angles, whereas the azimuth angle was found to be negligible. The RT models used appear incomplete regarding accurately modeling backscatter variations due to incidence angle changes for a fully developed winter wheat canopy. It was demonstrated that, when using Sentinel-1 images with the same incidence angle (mono-incidence case), the ubRMSE between the backscatter modeled and the Sentinel-1 backscatter decreases by up to 0.3 dB compared to the multi-incidence case with ubRMSEs of 1.93 dB (Oh92 with SSRT, "Sep-FS") and 1.68 dB (IEM\_B with SSRT, "Sep-FS"). The best fit results between the backscatter modeled and the Sentinel-1 backscatter were achieved by selecting scenes with incidence angles around 35°. Further investigations of the scattering mechanism changes by a dual polarimetric eigen-based decomposition of the VV and VH Sentinel-1 backscatter data for wheat fields showed more significant divergence during the vegetation period for steep incidence angles of 35°. During phenological stages from stem elongation to fruit development, a clear separation in terms of polarimetric entropy and scattering alpha angle values could be made between steep (35–36°) and shallow (43–45°) incidence angles. Differences between the early vegetation stages (tillering) and late vegetation stages (ripening) were marginal. It was found that the types of scattering mechanisms that appeared during the vegetation period are also dependent on the incidence angle used during acquisition. Hence, observing with a dense time series of Sentinel-1 and therefore diversity in incidence angle could mean mixing various scattering mechanisms, as observed in our study. Therefore, when modeling a dense Sentinel-1 time series using RT models, the models applied might need a certain flexibility in terms of model design to take into account potentially occurring scattering mechanisms and their weighting depending on acquisition scenarios and phenology stages.

An analysis of different spatial backscatter aggregation scenarios (single pixel to field scale) revealed improvements in the ubRMSE by up to 0.5 dB. Changes in backscatter between single-pixel and 30 × 30 m aggregation as well as single-pixel and field-scale aggregation were related to possible soil moisture uncertainties. Only small soil moisture uncertainty differences between different aggregation scenarios were shown for the early vegetation stages with a small canopy layer (tillering) and the late vegetation stages (ripening and senescence), where the winter wheat canopy should be almost transparent for C-band microwaves. Higher soil moisture uncertainties occurred for the vegetation stages stem elongation to heading. The sensitivity change is related to a canopy layer with 95 cm height by using C-band (5 cm wavelength) data. Hence, to estimate soil moisture under a changing vegetation cover (growing season of wheat), a variety of biomass, structure, and vegetation water scenarios have to be accounted for. Unfortunately, these changes in conditions are not easy to simulate electromagnetically with one scattering model or one model-combination. Hence, further research on approaches using shorter time series or RT models with limited variable parameters for calibration of the model might be promising prospects.

Simplified RT model approaches, such as that applied in this study, are well established for soil moisture estimation from active microwave (SAR) data. However, little attention is paid to differences caused by incidence angle variations between consecutive images. The implementation of the incidence angle within the RT models used can mislead one to assume that backscatter diversity due to variation in incidence angles is sufficiently accounted for. These differences lead to imprecise soil moisture estimations. Our study on the winter wheat fields of one growing season shows that the shortcomings of simplified RT model architectures used to handle time series consisting of images with varied incidence angles can be at least partly compensated for by including a calibration coefficient to individually parameterize the modeled transmissivity for the varying incidence angle

scenarios. Our simple approach of just calibrating one empirical parameter sheds light on the possibilities for adjusting model simulations for a dense time series of Sentinel-1 observations on winter wheat. Nevertheless, further investigations have to be carried out on the simple adaption of the RT models developed in terms of the applied calibration parameter. The usefulness of integrating possible the scattering mechanism changes between different phenology stages or the adaption of the approach presented to other crop types might be an interesting follow-up research topic.

**Author Contributions:** Conceptualization, T.W. and P.M.; methodology and data analyses, T.W., T.J., T.R., and P.M.; software, T.W. and A.L.; writing—original draft preparation, T.W.; writing—review and editing, T.W., T.J., T.R., and P.M.; resources, T.W., T.R., and P.M.; visualization, T.W., T.J., T.R., and P.M.; supervision, A.L. and P.M.; project administration, A.L. and P.M.; funding acquisition, A.L. All authors have read and agreed to the published version of the manuscript.

**Funding:** The project leading to this application received funding from the European Union’s Horizon 2020 research and innovation program under grant agreement No. 687320.

**Acknowledgments:** Thomas Weiß is truly thankful for the inspiration, ideas, and support that Alexander Löw (2 July 2017) provided.

**Conflicts of Interest:** The authors declare no conflicts of interest.

## References

- Erick, K. *Review of the Available Remote Sensing Tools, Products, Methodologies and Data to Improve Crop Production Forecasts*; FAO: Rome, Italy, 2017.
- Torres, R.; Snoeij, P.; Davidson, M.; Bibby, D.; Lokas, S. The Sentinel-1 mission and its application capabilities. In Proceedings of the IEEE International Geoscience and Remote Sensing Symposium (IGARSS), Munich, Germany, 22–27 July 2012; pp. 1703–1706. [\[CrossRef\]](#)
- Attema, E.; Snoeij, P.; Davidson, M.; Floury, N.; Levrini, G.; Rommen, B.; Rosich, B. The European GMES Sentinel-1 Radar Mission. In Proceedings of the IEEE International Geoscience and Remote Sensing Symposium (IGARSS), Boston, MA, USA, 7–11 July 2008; Volume 1, pp. I-94–I-97. [\[CrossRef\]](#)
- Miranda, N.; Meadows, P.; Piantanida, R.; Recchia, A.; Small, D.; Schubert, A.; Vincent, P.; Geudtner, D.; Navas-Traver, I.; Vega, F.C. The Sentinel-1 constellation mission performance. In Proceedings of the IEEE International Geoscience and Remote Sensing Symposium (IGARSS), Fort Worth, TX, USA, 23–28 July 2017; pp. 5541–5544. [\[CrossRef\]](#)
- Torres, R.; Geudtner, D.; Lokas, S.; Bibby, D.; Snoeij, P.; Traver, I.N.; Vega, F.C.; Poupaert, J.; Osborne, S. Sentinel-1 Satellite Evolution. In Proceedings of the IEEE International Geoscience and Remote Sensing Symposium (IGARSS), Valencia, Spain, 22–27 July 2018; pp. 1555–1558. [\[CrossRef\]](#)
- Geudtner, D.; Torres, R.; Snoeij, P.; Davidson, M.; Rommen, B. Sentinel-1 System capabilities and applications. In Proceedings of IEEE Geoscience and Remote Sensing Symposium, Québec City, QC, Canada, 13–18 July 2014; pp. 1457–1460. [\[CrossRef\]](#)
- Forgotson, C.; O’Neill, P.E.; Carrera, M.L.; Bélair, S.; Das, N.N.; Mladenova, I.E.; Bolten, J.D.; Jacobs, J.M.; Cho, E.; Escobar, V.M. How Satellite Soil Moisture Data Can Help to Monitor the Impacts of Climate Change: SMAP Case Studies. *IEEE J. Sel. Top. Appl. Earth Obs. Remote Sens.* **2020**, *13*, 1590–1596. [\[CrossRef\]](#)
- Malenovský, Z.; Rott, H.; Cihlar, J.; Schaepman, M.E.; García-Santos, G.; Fernandes, R.; Berger, M. Sentinels for science: Potential of Sentinel-1, -2, and -3 missions for scientific observations of ocean, cryosphere, and land. *Remote Sens. Environ.* **2012**, *120*, 91–101. [\[CrossRef\]](#)
- Veloso, A.; Mermoz, S.; Bouvet, A.; Le Toan, T.; Planells, M.; Dejoux, J.F.; Ceschia, E. Understanding the temporal behavior of crops using Sentinel-1 and Sentinel-2-like data for agricultural applications. *Remote Sens. Environ.* **2017**, *199*, 415–426. [\[CrossRef\]](#)
- Van Tricht, K.; Gobin, A.; Gilliams, S.; Piccard, I. Synergistic Use of Radar Sentinel-1 and Optical Sentinel-2 Imagery for Crop Mapping: A Case Study for Belgium. *Remote Sens.* **2018**, *10*, 1642. [\[CrossRef\]](#)
- Sadri, S.; Pan, M.; Wada, Y.; Vergopolan, N.; Sheffield, J.; Famiglietti, J.S.; Kerr, Y.; Wood, E. A global near-real-time soil moisture index monitor for food security using integrated SMOS and SMAP. *Remote Sens. Environ.* **2020**, *246*, 111864. [\[CrossRef\]](#)
- Schlund, M.; Erasmi, S. Sentinel-1 time series data for monitoring the phenology of winter wheat. *Remote Sens. Environ.* **2020**, *246*, 111814. [\[CrossRef\]](#)
- Trnka, M.; Rötter, R.P.; Ruiz-Ramos, M.; Kersebaum, K.C.; Olesen, J.E.; Žalud, Z.; Semenov, M.A. Adverse weather conditions for European wheat production will become more frequent with climate change. *Nat. Clim. Chang.* **2014**, *4*, 637–643. [\[CrossRef\]](#)
- Dari, J.; Morbidelli, R.; Saltalippi, C.; Massari, C.; Brocca, L. Spatial-temporal variability of soil moisture: Addressing the monitoring at the catchment scale. *J. Hydrol.* **2019**, *570*, 436–444. [\[CrossRef\]](#)
- Brocca, L.; Melone, F.; Moramarco, T.; Morbidelli, R. Spatial-temporal variability of soil moisture and its estimation across scales. *Water Resour. Res.* **2010**, *46*. [\[CrossRef\]](#)

16. Balenzano, A.; Mattia, F.; Satalino, G.; Davidson, M.W.J. Dense Temporal Series of C- and L-band SAR Data for Soil Moisture Retrieval Over Agricultural Crops. *IEEE J. Sel. Top. Appl. Earth Obs. Remote Sens.* **2011**, *4*, 439–450. [[CrossRef](#)]
17. Sishodia, R.P.; Ray, R.L.; Singh, S.K. Applications of Remote Sensing in Precision Agriculture: A Review. *Remote Sens.* **2020**, *12*, 3136. [[CrossRef](#)]
18. Zeri, M.; Alvalá, R.C.S.; Carneiro, R.; Cunha-Zeri, G.; Costa, J.M.; Rossato Spatafora, L.; Urbano, D.; Vall-Llossera, M.; Marengo, J. Tools for Communicating Agricultural Drought over the Brazilian Semiarid Using the Soil Moisture Index. *Water* **2018**, *10*, 1421. [[CrossRef](#)]
19. Tao, L.; Wang, G.; Chen, X.; Li, J.; Cai, Q. Estimation of soil moisture using a vegetation scattering model in wheat fields. *J. Appl. Remote Sens.* **2019**, *13*, 044503. [[CrossRef](#)]
20. Ouadi, N.; Jarlan, L.; Ezzahar, J.; Zribi, M.; Khabba, S.; Bouras, E.; Bousbih, S.; Frison, P.L. Monitoring of wheat crops using the backscattering coefficient and the interferometric coherence derived from Sentinel-1 in semi-arid areas. *Remote Sens. Environ.* **2020**, *251*, 112050. [[CrossRef](#)]
21. Wu, S.; Ren, J.; Chen, Z.; Yang, P.; Li, H. Soil moisture estimation based on the microwave scattering mechanism during different crop phenological periods in a winter wheat-producing region. *J. Hydrol.* **2020**, *590*, 125521. [[CrossRef](#)]
22. El Hajj, M.; Baghdadi, N.; Zribi, M.; Bazzi, H. Synergic Use of Sentinel-1 and Sentinel-2 Images for Operational Soil Moisture Mapping at High Spatial Resolution over Agricultural Areas. *Remote Sens.* **2017**, *9*, 1292. [[CrossRef](#)]
23. Baghdadi, N.; El Hajj, M.; Zribi, M.; Bousbih, S. Calibration of the Water Cloud Model at C-Band for Winter Crop Fields and Grasslands. *Remote Sens.* **2017**, *9*, 969. [[CrossRef](#)]
24. Liu, Z.; Li, P.; Yang, J. Soil Moisture Retrieval and Spatiotemporal Pattern Analysis Using Sentinel-1 Data of Dahra, Senegal. *Remote Sens.* **2017**, *9*, 1197. [[CrossRef](#)]
25. Ma, C.; Li, X.; McCabe, M.F. Retrieval of High-Resolution Soil Moisture through Combination of Sentinel-1 and Sentinel-2 Data. *Remote Sens.* **2020**, *12*, 2303. [[CrossRef](#)]
26. Weiß, T.; Ramsauer, T.; Löw, A.; Marzahn, P. Evaluation of Different Radiative Transfer Models for Microwave Backscatter Estimation of Wheat Fields. *Remote Sens.* **2020**, *12*, 3037. [[CrossRef](#)]
27. Yan, W.; Yang, B.; Zhang, Y. Characterizing the C-Band Backscattering of Winter-Wheat Canopy with a Microwave Radiative Transfer Model. In Proceedings of the 7th International Conference on Agro-Geoinformatics (Agro-Geoinformatics), Hangzhou, China, 6–9 August 2018; pp. 1–6. [[CrossRef](#)]
28. Yan, W.; Zhang, Y.; Yang, T.; Liu, X. A Microwave Scattering Model for Simulating the C-Band SAR Backscatter of Wheat Canopy. *Am. J. Remote Sens.* **2019**, *7*, 13. [[CrossRef](#)]
29. Steele-Dunne, S.C.; McNairn, H.; Monsivais-Huertero, A.; Judge, J.; Liu, P.W.; Papathanassiou, K. Radar Remote Sensing of Agricultural Canopies: A Review. *IEEE J. Sel. Top. Appl. Earth Obs. Remote Sens.* **2017**, *10*, 2249–2273. [[CrossRef](#)]
30. Ulaby, F.; Long, D.; Blackwell, W.; Elachi, C.; Fung, A.; Ruf, C.; Sarabandi, K.; Zyl, J.; Zebker, H. *Microwave Radar and Radiometric Remote Sensing*; University of Michigan Press: Ann Arbor, MI, USA, 2014.
31. Ulaby, F.T.; Sarabandi, K.; McDonald, K.; Whitt, M.; Dobson, M.C. Michigan microwave canopy scattering model. *Int. J. Remote Sens.* **1990**, *11*, 1223–1253. [[CrossRef](#)]
32. Ferrazzoli, P.; Guerriero, L. Radar sensitivity to tree geometry and woody volume: A model analysis. *IEEE Trans. Geosci. Remote Sens.* **1995**, *33*, 360–371. [[CrossRef](#)]
33. Quast, R.; Wagner, W. Analytical solution for first-order scattering in bistatic radiative transfer interaction problems of layered media. *Appl. Opt.* **2016**, *55*, 5379–5386. [[CrossRef](#)]
34. Quast, R.; Albergel, C.; Calvet, J.C.; Wagner, W. A Generic First-Order Radiative Transfer Modelling Approach for the Inversion of Soil and Vegetation Parameters from Scatterometer Observations. *Remote Sens.* **2019**, *11*, 285. [[CrossRef](#)]
35. Attema, E.P.W.; Ulaby, F.T. Vegetation modeled as a water cloud. *Radio Sci.* **1978**, *13*, 357–364. [[CrossRef](#)]
36. Kweon, S.K.; Oh, Y. A Modified Water-Cloud Model With Leaf Angle Parameters for Microwave Backscattering From Agricultural Fields. *IEEE Trans. Geosci. Remote Sens.* **2015**, *53*, 2802–2809. [[CrossRef](#)]
37. de Roo, R.; Du, Y.; Ulaby, F.; Dobson, M. A semi-empirical backscattering model at L-band and C-band for a soybean canopy with soil moisture inversion. *IEEE Trans. Geosci. Remote Sens.* **2001**, *39*, 864–872. [[CrossRef](#)]
38. Prévot, L.; Champion, I.; Guyot, G. Estimating surface soil moisture and leaf area index of a wheat canopy using a dual-frequency (C and X bands) scatterometer. *Remote Sens. Environ.* **1993**, *46*, 331–339. [[CrossRef](#)]
39. Kumar, K.; Rao, H.P.S.; Arora, M.K. Study of water cloud model vegetation descriptors in estimating soil moisture in Solani catchment. *Hydrol. Process.* **2015**, *29*, 2137–2148. [[CrossRef](#)]
40. Li, J.; Wang, S. Using SAR-Derived Vegetation Descriptors in a Water Cloud Model to Improve Soil Moisture Retrieval. *Remote Sens.* **2018**, *10*, 1370. [[CrossRef](#)]
41. Oh, Y.; Sarabandi, K.; Ulaby, F. An empirical model and an inversion technique for radar scattering from bare soil surfaces. *IEEE Trans. Geosci. Remote Sens.* **1992**, *30*, 370–381. [[CrossRef](#)]
42. Oh, Y. Quantitative retrieval of soil moisture content and surface roughness from multipolarized radar observations of bare soil surfaces. *IEEE Trans. Geosci. Remote Sens.* **2004**, *42*, 596–601. [[CrossRef](#)]
43. Dubois, P.; van Zyl, J.; Engman, T. Measuring soil moisture with imaging radars. *IEEE Trans. Geosci. Remote Sens.* **1995**, *33*, 915–926. [[CrossRef](#)]

44. Fung, A.; Liu, W.; Chen, K.; Tsay, M. An Improved Iem Model for Bistatic Scattering From Rough Surfaces. *J. Electromagn. Waves Appl.* **2002**, *16*, 689–702. [[CrossRef](#)]
45. Baghdadi, N.; Abou Chaaya, J.; Zribi, M. Semiempirical Calibration of the Integral Equation Model for SAR Data in C-Band and Cross Polarization Using Radar Images and Field Measurements. *IEEE Geosci. Remote Sens. Lett.* **2011**, *8*, 14–18. [[CrossRef](#)]
46. Berger, K.; Atzberger, C.; Danner, M.; Woche, M.; Mauser, W.; Hank, T. Modellbasierte Selektion hyperspektraler EnMAP Kanäle zur optimalen Invertierung von Strahlungstransfermodellen für landwirtschaftliche Kulturen. *PFG—J. Photogramm. Remote Sens. Geoinf. Sci.* **2018**, *86*, 263–272. [[CrossRef](#)]
47. Danner, M.; Berger, K.; Woche, M.; Mauser, W.; Hank, T. Retrieval of biophysical crop variables from multi-angular canopy spectroscopy. *Remote Sens.* **2017**, *9*, 726. [[CrossRef](#)]
48. Danner, M.; Berger, K.; Woche, M.; Mauser, W.; Hank, T. Fitted PROSAIL Parameterization of Leaf Inclinations, Water Content and Brown Pigment Content for Winter Wheat and Maize Canopies. *Remote Sens.* **2019**, *11*, 1150. [[CrossRef](#)]
49. Woche, M.; Berger, K.; Danner, M.; Mauser, W.; Hank, T. Physically-based retrieval of canopy equivalent water thickness using hyperspectral data. *Remote Sens.* **2018**, *10*, 1924. [[CrossRef](#)]
50. Jiang, W.; Yu, A.; Dong, Z.; Wang, Q. Comparison and Analysis of Geometric Correction Models of Spaceborne SAR. *Sensors* **2016**, *16*, 973. [[CrossRef](#)]
51. Truckenbrodt, J.; Freemantle, T.; Williams, C.; Jones, T.; Small, D.; Dubois, C.; Thiel, C.; Rossi, C.; Syriou, A.; Giuliani, G. Towards Sentinel-1 SAR Analysis-Ready Data: A Best Practices Assessment on Preparing Backscatter Data for the Cube. *Data* **2019**, *4*, 93. [[CrossRef](#)]
52. Kellndorfer, J.; Pierce, L.; Dobson, M.; Ulaby, F. Toward consistent regional-to-global-scale vegetation characterization using orbital SAR systems. *IEEE Trans. Geosci. Remote Sens.* **1998**, *36*, 1396–1411. [[CrossRef](#)]
53. El Hajj, M.; Baghdadi, N.; Zribi, M.; Belaud, G.; Cheviron, B.; Courault, D.; Charron, F. Soil moisture retrieval over irrigated grassland using X-band SAR data. *Remote Sens. Environ.* **2016**, *176*, 202–218. [[CrossRef](#)]
54. Liu, Y.; Yang, Y.; Yue, X. Evaluation of Satellite-Based Soil Moisture Products over Four Different Continental In-Situ Measurements. *Remote Sens.* **2018**, *10*, 1161. [[CrossRef](#)]
55. Cloude, S. The dual polarisation entropy/alpha decomposition: A palar case study. In Proceedings of the 3th International Workshop on Science and Applications of SAR Polarimetry and Polarimetric Interferometry (PolInSAR), Frascati, Italy, 22–26 January 2007.
56. Ji, K.; Wu, Y. Scattering Mechanism Extraction by a Modified Cloude-Pottier Decomposition for Dual Polarization SAR. *Remote Sens.* **2015**, *7*, 7447–7470. [[CrossRef](#)]
57. Meier, U.; Bleiholder, H.; Buhr, L.; Feller, C.; Hack, H.; Heß, M.; Lancashire, P.D.; Schnock, U.; Stauß, R.; Boom, T.v.d.; et al. The BBCH system to coding the phenological growth stages of plants—history and publications. *J. Für Kult.* **2009**, *61*, 41–52. [[CrossRef](#)]
58. He, L.; Tong, L.; Li, Y.; Chen, Y.; Tan, L.; Guo, C. Polarimetric analysis of radar backscatter from ground-based scatterometers and wheat biomass monitoring with advanced synthetic aperture radar images. *J. Appl. Remote Sens.* **2016**, *10*, 026008. [[CrossRef](#)]
59. Khabbazan, S.; Vermunt, P.; Steele-Dunne, S.; Ratering Arntz, L.; Marinetti, C.; van der Valk, D.; Iannini, L.; Molijn, R.; Westerdijk, K.; van der Sande, C. Crop Monitoring Using Sentinel-1 Data: A Case Study from The Netherlands. *Remote Sens.* **2019**, *11*, 1887. [[CrossRef](#)]
60. Mattia, F.; Le Toan, T.; Picard, G.; Posa, F.; D’Alessio, A.; Notarnicola, C.; Gatti, A.; Rinaldi, M.; Satalino, G.; Pasquariello, G. Multitemporal C-band radar measurements on wheat fields. *IEEE Trans. Geosci. Remote Sens.* **2003**, *41*, 1551–1560. [[CrossRef](#)]
61. Brown, S.C.M.; Quegan, S.; Morrison, K.; Bennett, J.C.; Cookmartin, G. High-resolution measurements of scattering in wheat canopies-implications for crop parameter retrieval. *IEEE Trans. Geosci. Remote Sens.* **2003**, *41*, 1602–1610. [[CrossRef](#)]
62. Harfenmeister, K.; Spengler, D.; Weltzien, C. Analyzing Temporal and Spatial Characteristics of Crop Parameters Using Sentinel-1 Backscatter Data. *Remote Sens.* **2019**, *11*, 1569. [[CrossRef](#)]
63. Mladenova, I.E.; Jackson, T.J.; Bindlish, R.; Hensley, S. Incidence Angle Normalization of Radar Backscatter Data. *IEEE Trans. Geosci. Remote Sens.* **2013**, *51*, 1791–1804. [[CrossRef](#)]
64. Carranza, C.; Benninga, H.j.; van der Velde, R.; van der Ploeg, M. Monitoring agricultural field trafficability using Sentinel-1. *Agric. Water Manag.* **2019**, *224*, 105698. [[CrossRef](#)]
65. Topouzelis, K.; Singha, S.; Kitsiou, D. Incidence angle normalization of Wide Swath SAR data for oceanographic applications. *Open Geosci.* **2016**, *8*. [[CrossRef](#)]
66. Pierdicca, N.; Pulvirenti, L.; Pace, G. A Prototype Software Package to Retrieve Soil Moisture From Sentinel-1 Data by Using a Bayesian Multitemporal Algorithm. *IEEE J. Sel. Top. Appl. Earth Obs. Remote Sens.* **2014**, *7*, 153–166. [[CrossRef](#)]
67. Pipia, L.; Muñoz-Marí, J.; Amin, E.; Belda, S.; Camps-Valls, G.; Verrelst, J. Fusing optical and SAR time series for LAI gap filling with multioutput Gaussian processes. *Remote Sens. Environ.* **2019**, *235*, 111452. [[CrossRef](#)]
68. Orynbaikyzy, A.; Gessner, U.; Mack, B.; Conrad, C. Crop Type Classification Using Fusion of Sentinel-1 and Sentinel-2 Data: Assessing the Impact of Feature Selection, Optical Data Availability, and Parcel Sizes on the Accuracies. *Remote Sens.* **2020**, *12*, 2779. [[CrossRef](#)]

- 
69. Han, D.; Liu, S.; Du, Y.; Xie, X.; Fan, L.; Lei, L.; Li, Z.; Yang, H.; Yang, G. Crop Water Content of Winter Wheat Revealed with Sentinel-1 and Sentinel-2 Imagery. *Sensors* **2019**, *19*, 4013. [[CrossRef](#)] [[PubMed](#)]
  70. Hajnsek, I.; Jagdhuber, T.; Schon, H.; Papathanassiou, K.P. Potential of Estimating Soil Moisture Under Vegetation Cover by Means of PolSAR. *IEEE Trans. Geosci. Remote Sens.* **2009**, *47*, 442–454. [[CrossRef](#)]

## 3.4 Transition to Publication III

Publication I evaluates the advantages and disadvantages of various RT models for simulating microwave radar backscatter at the field scale, utilizing in-situ soil moisture data. A further analysis of a dense Sentinel-1 time series, consisting of images captured at different incidence and azimuth angles, and its implications within the RT models, is presented in Publication II.

Building on the insights gained from the preliminary work in Publications I and II, Publication III introduces an approach for deriving high spatial (100 m) and temporal (1.5 days) soil moisture estimates for agricultural fields at the MNI test site. This approach emphasizes the easy transferability of the method to other regions, ensuring that all necessary auxiliary information can be derived from data provided by freely available, operational remote sensing sensors. A medium-resolution (1 km  $\times$  1 km) RADOLAN soil moisture product (Ramsauer et al., 2021) is downscaled using a combination of the Oh04 (Oh, 2004) and SSRT (Ulaby and Long, 2014) models, driven by Sentinel-1 VV-polarized backscatter and VWC information derived from Sentinel-2. High spatio-temporal maps illustrating soil moisture changes due to precipitation events and soil drying behavior are generated. Thus, Publication III demonstrates that a high spatio-temporal soil moisture time series can be established for the test area using solely remotely sensed input data.

With the provision of near-daily soil moisture estimates at the field scale, Publications I, II, and III represent significant advancements in improving the accuracy of soil moisture information for precision farming applications.

## 3.5 Publication III: RTM-based Downscaling of Medium Resolution Soil Moisture using Sentinel-1 Data over Agricultural Fields

**Reference:** Weiß, T., Jagdhuber, T., Ramsauer, T., Löw, A., Marzahn, P., 2024. RTM-Based Downscaling of Medium Resolution Soil Moisture Using Sentinel-1 Data Over Agricultural Fields. *IEEE Journal of Selected Topics in Applied Earth Observations and Remote Sensing* 17, 15463–15479. doi:10.1109/JSTARS.2024.3448625

**Status:** published

**Plain language summary:** Soil moisture is a key parameter that describes processes in climate, hydrological, and agricultural systems. Therefore, continuous monitoring is essential but challenging due to the high spatio-temporal variability of soil moisture. Coarse- and medium-resolution soil moisture data are already operationally provided by various remote sensing sensors. However, global operational derivation at high resolution is even more difficult because of the usual need for auxiliary information at the field scale, which is often unavailable. Nevertheless, soil moisture at the field scale is necessary; when available, it can be used for smart farming decisions, field irrigation management, or soil erosion modeling.

Thus, this study analyzes the feasibility of downscaling medium-resolution (1 km x 1 km) soil moisture using RT models driven solely by information derived from globally operational remote sensing sensors. With the aid of a RT model combination of Oh04 and SSRT, along with Sentinel-1 VV-polarized radar backscatter and VWC information derived from Sentinel-2, a soil moisture time series with spatial and temporal resolutions of 10 m and 1.5 days, respectively, is produced. With mean ubRMSEs of  $0.045 \text{ m}^3/\text{m}^3$  and  $0.037 \text{ m}^3/\text{m}^3$  for the years 2017 and 2018, the soil moisture results fall within the accuracy range targeted by existing operationally available coarse- and medium-resolution products. Furthermore, with soil moisture values ranging from  $0.05 \text{ m}^3/\text{m}^3$  to  $0.4 \text{ m}^3/\text{m}^3$ , the entire possible range of soil moisture values within agriculturally used fields is covered.

**Author contributions:** Conceptualization, T.W., T.J., and P.M.; Methodology and data analyses, T.W., T.J., and P.M.; Software, T.W. and A.L.; Writing-original draft preparation, T.W.; Writing-review and editing, T.W., T.J., T.R., and P.M.; Resources, T.W. and T.R.; Visualization, T.W.; Supervision, T.J. and P.M.; Project administration, A.L. and P.M.; Funding acquisition, A.L.

**Journal:** *IEEE Journal of Selected Topics in Applied Earth Observations and Remote Sensing*

**Impact factor:** 4.7

**CiteScore:** 9.3

# RTM-Based Downscaling of Medium Resolution Soil Moisture Using Sentinel-1 Data Over Agricultural Fields

Thomas Weiß<sup>1</sup>, Thomas Jagdhuber<sup>2</sup>, *Senior Member, IEEE*, Thomas Ramsauer<sup>3</sup>,  
Alexander Löw<sup>4</sup>, and Philip Marzahn<sup>5</sup>

**Abstract**—High temporal soil moisture at field scale resolution (10 m–100 m) is important for smart farming decisions. Although, medium and coarse resolution (1 km–50 km) soil moisture information is operationally available on a large scale, high resolution (field scale) datasets are not. This study propose a data assimilation approach to downscale medium resolution (1 km × 1 km) soil moisture information—of intense agriculturally cultivated areas—to field scale. For achieving high transferability of the proposed method, the used input data (Sentinel-1 VV backscatter, Sentinel-2 derived vegetation water content, literature values) can be provided systematically from global operational satellites. Microwave and optical data are used together as input data of a radiative transfer model to derive soil moisture information with high temporal and spatial resolution. The retrieval approach shows a mean uBRMSE for soil moisture estimates of all test fields (Munich-North-Isar test site, Bavaria, Germany) with 0.045 m<sup>3</sup>/m<sup>3</sup> and 0.037 m<sup>3</sup>/m<sup>3</sup> for 2017 and 2018. Furthermore, the retrieved soil moisture estimates cover a broad range of values from 0.05 m<sup>3</sup>/m<sup>3</sup> to 0.4 m<sup>3</sup>/m<sup>3</sup>. In addition, the temporal evolution of the soil moisture patterns are in line with precipitation events. Moreover, the drying behavior is matched as well. The proposed method showed that for the test area, high resolution soil moisture time series can be provided by only using remote sensing derived input data. In this way, this study is another step towards providing high spatio-temporal soil moisture information for precision farming purposes.

**Index Terms**—Radiative transfer, Sentinel-1, Sentinel-2, soil moisture, time series, vegetation water content (VWC).

## I. INTRODUCTION

SOIL moisture has an indisputable impact on climate, hydrological, and agricultural systems [1], [2], [3]. As soil

moisture has a high variability in time and space, continuous monitoring is essential [4], [5]. Moreover, different model applications, flood forecasting, or precision farming rely heavily on spatio-temporal distributed soil moisture information. Compared to remote sensing derived soil moisture products, traditional in-situ measurements at the point scale are expensive and fall short of providing spatio-temporal patterns on a larger (e.g., subcatchment) scale [6]. Today, several operational NASA and ESA missions (Soil Moisture Active Passive (SMAP), Soil Moisture and Ocean Salinity (SMOS), or Advanced Scatterometer (ASCAT)) produce global soil moisture maps at a coarse spatial resolution of 25 km to 50 km [7]. Further products of medium spatial resolution (1 km to 10 km) are mostly achieved by downscaling coarse resolution products [8], [9] or combining information from coarse and medium/high resolution sensors [10], [11]. Thus, medium resolution soil moisture products are available at a regional scale, e.g., a RADOLAN (radar online calibration)-based soil moisture product for Germany (RADOLAN Antecedent Precipitation Index—A Soil Moisture Dataset derived from Weather Radar Data; Ramsauer et al. [12]) or a SMAP-based product for China [13]. Other soil moisture products provided by the Copernicus Global Land Service [10] or NASA [11] reach even global coverage. However, global and regional products differ in their retrieval approach as well as in temporal (hourly to several days) and spatial resolutions. Compared to the the 1 km RADOLAN product which offers absolute soil moisture values in vol.%, the 1 km Copernicus soil moisture product is a change detection approach which leads to relative soil moisture values in % from 0 to 100. However, compared to medium resolution soil moisture products, operationally produced high resolution (field scale, meaning below 1 km) datasets on a global scale are not yet available [7]. But regional studies using polarimetric decomposition [14], [15], machine learning approaches [16], data fusion [17], statistical modeling [18], or radiative transfer models (RTMs) [19] show promising results in estimating soil moisture from synthetic aperture radar (SAR) data at the field scale. The use of RTMs and radar observations has been proven to be a suitable approach [20], [21]. With RTM a logical linkage between observations and physical processes can be established [22]. Thus, a better physical understanding as well as simulations of interactions between electromagnetic waves and the land surface is possible. Furthermore, RTMs are not only able to interpret satellite measurements, but also capable

Received 29 April 2024; revised 25 June 2024 and 8 August 2024; accepted 15 August 2024. Date of publication 23 August 2024; date of current version 9 September 2024. (Corresponding author: Thomas Weiß.)

Thomas Weiß is with the Department of Geography, Ludwig-Maximilians-Universität of Munich, 80333 Munich, Germany, also with the Faculty of Agricultural and Environmental Sciences, University of Rostock, 18059 Rostock, Germany, and also with the Fraunhofer Insitut for Computer Graphics Research (IGD), University of Rostock, 18059 Rostock, Germany (e-mail: weiss.thomas@lmu.de).

Thomas Jagdhuber is with the German Aerospace Center, Microwaves and Radar Institute, 82234 Weßling, Germany, and also with the Faculty of Applied Computer Science, Institute of Geography, University of Augsburg, 86159 Augsburg, Germany.

Thomas Ramsauer and Alexander Löw are with the Department of Geography, Ludwig-Maximilians-Universität of Munich, 80333 Munich, Germany.

Philip Marzahn is with the Faculty of Agricultural and Environmental Sciences, University of Rostock, 18059 Rostock, Germany.

Digital Object Identifier 10.1109/JSTARS.2024.3448625

of providing predictions under different conditions [23]. For bare soil applications, forward models of Oh [24], [25], Dubois [26], or the Integral Equation Model developed by Fung et al. [27] are often applied, among others. A study by Baghdadi et al. [28] showed that the accuracy on plot scale of bare soil moisture estimates is highly dependent on the surface roughness state. By using Sentinel-1 images an overestimation of soil moisture by high soil roughness and an underestimation of soil moisture by low surface roughness is observed [28]. For vegetated areas, the bare soil models need to be combined with vegetation scattering models. Here, the Water Cloud Model (WCM) approach by Attema and Ulaby [29] or a Single Scattering Radiative Transfer (SSRT) [30], [31] model is used for inverting radar backscatter to retrieve soil moisture information. The main uncertainty of radar based soil moisture retrievals in vegetated areas is the influence of the canopy layer on the backscatter signal [32], [33], [34]. The WCM considers the canopy layer as a collection of identical spherical particles, that are uniformly distributed [29]. Thus, the vegetation contribution within WCM (only considering direct scattering contributions from plants) is simplified by not differentiating between additional occurring scattering mechanisms (plant–ground, ground–plant, or ground–plant–ground scattering contributions). In contrast, the SSRT distinguishes the canopy layer by scattering mechanisms, so direct vegetation contribution as well as canopy–soil and soil–canopy–soil interactions are considered [31]. For accurate soil moisture retrievals, information about vegetation in terms of crop type, structure, phenology, and water content is necessary. Therefore, Vegetation Optical Depths (VOD), Normalized Difference Vegetation Index (NDVI), Normalized Difference Water Index (NDWI), or Vegetation Water Content (VWC) are used as remote sensing-based indicators from optical and radar observations. [35], [36], [37]. Over large areas, optical remote sensing data has proven useful in obtaining information on vegetation at field resolution. [38], [39], [40]. Thus, a combination of SAR (Sentinel-1) and optical data (Sentinel-2) provides unique possibilities for improving soil moisture estimates by using microwave RTMs with additional information provided by optical sensors [41], [42].

This article aims to investigate the potential of accurate down-scaling of a soil moisture product at medium resolution (1 km) to field scale by combining high-resolution SAR and optical remote sensing data based on RTM. The approach is deliberately based on a few input parameters, which can already be derived from remote sensing sensors, to ensure easy transferability of the approach to other areas worldwide. The used remote sensing information are a RADOLAN-based soil moisture product at 1-km resolution, VV-polarized backscatter (Sentinel-1), and as a vegetation descriptor, the VWC (calculated from NDWI information obtained from Sentinel-2). The spatio-temporal distributed data is used to drive an inversion process for models Oh04 and SSRT. Thus, a time series of almost daily spatially distributed absolute soil moisture estimates (Vol.%) is achieved.

## II. DATASETS

### A. Test Site

For our study, the Munich-North-Isar (MNI) test site [43], [44] with in-situ measurements of winter wheat and maize fields for

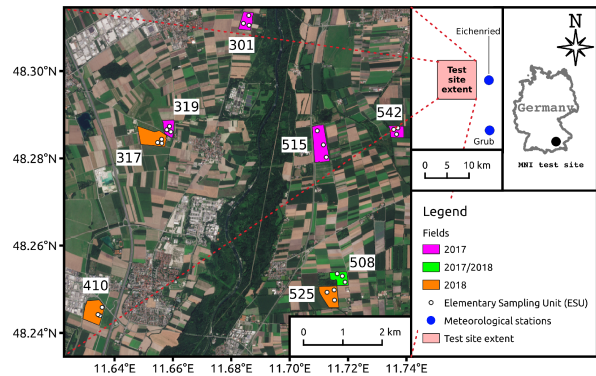


Fig. 1. Munich-North-Isar (MNI) test site with sampled wheat and maize fields of 2017 and 2018. The inset map shows the spatial relationship between meteorological stations and the test site.

the years 2017 and 2018 was chosen. The winter wheat fields were sowed beginning of October and harvested mid/end of July in both years. The maize fields were sowed end of May in 2017 and beginning of May in 2018. The harvest of the maize took place end of September in 2017 and beginning of September in 2018. Besides the two main crop types (wheat and maize), grassland is the third major type of agricultural cultivation. The test site (48° 13'N–48° 20'N, 11° 39'E–11° 45'E, Fig. 1) is located near Munich, southern Germany. Two meteorological stations (Eichenried and Grub) provide measurements within a 15-km radius around the study area. For the year 2017, the measurements show an annual mean temperature of 9.3 °C (Eichenried) and 9.5 °C (Grub). Furthermore, an average annual precipitation of 853 mm (Eichenried) and 863 mm (Grub) was observed in 2017. For the year 2018, the measurements show a higher annual mean temperature of 10.3 °C (Eichenried and Grub) and a more diverse average annual precipitation of 663 mm (Eichenried) and 926 mm (Grub). The river Isar within the test site is embanked and has no significant influence on the water availability of the agricultural areas in the vicinity. Furthermore, no irrigation practices were observed during the years 2017 and 2018 within the MNI test site.

### B. In-Situ Data

For 2017, in-situ data comprising five different fields (three wheat and two maize fields) and for 2018, measurements of four different fields (two wheat and two maize fields) are available for detailed and local analyses. Field measurements were taken at three different locations (Elementary Sampling Points ESU) on every test field. At each location, the plants of half a square meter were taken, the wet and dry (drying temperature 102°C) weights of the plants were measured, and the VWC was calculated. Soil moisture time series were provided by permanently installed sensors (Decagon TM5 sensors, Decagon Devices Inc., Pullman, WA, USA) within the upper soil layer (first five centimeters). The monitoring interval was ten minutes. Further information about the in-situ measurements are summarized in Table I.

TABLE I  
ACQUISITION TIME, TIME INTERVAL, AND RANGE OF IN-SITU MEASUREMENTS  
(VEGETATION WATER CONTENT AND SOIL MOISTURE)

Variable	Type	Acquisition time		Range	Time interval
		2017	2018		
VWC [kg/m <sup>2</sup> ]	Wheat	03/24	04/04	0.04	weekly
		—	—	—	
	07/17	07/13	6.3		
	06/08	05/25	0.02		
Maize	—	—	—	—	
	09/22	08/29	10.2		
	03/24	04/20	0.02		
Soil Moisture [m <sup>3</sup> /m <sup>3</sup> ]	Wheat	—	—	—	ten minutes
		07/17	07/13	0.38	
	07/06	05/16	0.03		
	Maize	—	—	—	
		09/22	08/29	0.39	

TABLE II  
USED REMOTE SENSING DATA FOR MNI TEST SITE OF 2017  
(03/24/2017-09/22/2017) AND 2018 (04/04/2018-08/29/2018)

Data set	Amount		Bands	Resolution [m]
	2017	2018		
Sentinel-1	121	86	VV	10 × 10
Sentinel-2	16	17	8a, 11	20 × 20
RADOLAN API	—	—	—	1000 × 1000

### C. Remote Sensing Data

1) *Sentinel-1*: The Sentinel-1 satellites (C-band) provide continuous images for the MNI test site. In 2017 and 2018, Sentinel-1A and Sentinel-1B provide four different overpasses (relative orbit number 44,95,117,168). The MNI test site is observed with two incidence angle sets of 35°–36° and 43°–45°. The usage of all available scenes led to an average temporal revisit time of 1.5 days. The Level-1 Single Look Complex (SLC) data product was preprocessed by using the default configuration for time series processing of the python package SenSARP [45]. SenSARP utilizes ESA’s SNAP Toolbox to apply thermal noise removal, radiometric calibration, geometric correction, radiometric correction, co-registering, and multitemporal speckle filtering. Thus, a radiometric and geometric corrected as well as temporal speckle filtered time series of Sentinel-1 images is provided. El Hajj et al. [46] and Baghdadi et al. [47] suggested that VV polarization is more suitable to monitor soil moisture under well-developed agricultural vegetation than VH. Therefore, VV polarized backscatter is the main focus of the study. Table II summarizes the information from the used Sentinel-1 images.

2) *Sentinel-2*: Sentinel-2 satellites provide free multispectral data with systematic global coverage. The Multispectral Imager sensor on Sentinel-2 has 13 spectral bands covering wavelength from 443 nm (Ultra Blue) to 2190 nm (Short Wave Infrared (SWIR)). The spatial resolution of different bands ranges from 10 to 60 m. Within our study a combination of Bands B8a (10 m, 842 nm—Visible and Near Infrared) and B11 (20 m, 1610 nm—SWIR) is used. Observations from Sentinel-2 of the MNI test site are available every 2–3 days. However, only 32 images for the time period under investigation (2017 + 2018) have a cloud coverage below 10% and were therefore used in this study. The Sentinel-2 images are preprocessed and retrieved

using the Google Earth Engine. In order to transform the top-of-atmosphere to surface reflectance values and hence account for atmospheric artifacts in the imagery, the 6S radiative transfer code is used [48], [49]. Table II summarizes the information from the Sentinel-2 data.

3) *RADOLAN API*: The utilized RADOLAN API dataset [50] is an empirically retrieved soil moisture dataset based on the German weather radar product RADOLAN RW [51], [52]. It extends the idea of the Antecedent Precipitation Index (API) [53], integrating information on local soil characteristics (SoilGrids; Hengl et al. [54]) and spatially distributed temperature data. The algorithm accounts for general physical boundaries in soil hydrology (e.g., moisture content limits) when empirically modeling saturation state dependent soil moisture gains and losses. The hourly RADOLAN API dataset with a spatial resolution of 1 km × 1 km is openly available for the spatial domain of Germany (utilized version 1.0.0 (2015–2019)) [12].

### D. CORINE Land Cover

The CORINE land cover class 2 from 2018 [55], in particular 211 (“nonirrigated arable land”) and 231 (“pasture, meadows, and other permanent grasslands under agricultural use”) are used as a mask. Thus the algorithm is only applied on agricultural areas excluding vineyards and forest areas. It has to be mentioned that although forestry areas are excluded some scrub vegetation/forestry areas are wrongly found within the 211 and 231 CORINE land cover classes.

## III. METHODOLOGY

The main objective is the development of an approach to downscale a medium resolution soil moisture product to field scale by using RTMs. The proposed method was developed and tested at a test site in southern Germany, Bavaria. Enabling transferability to other regions, the focus during method development was set on a minimal set of input parameters for the RTMs, which can already be operationally derived by remote sensing products.

### A. Radiative Transfer Model

This section introduces a first order radiative transfer model (SSRT), which is used in an inversion process for the retrieval of soil moisture information in agricultural areas with vegetation cover. The original SSRT [30], [31] can be described as

$$\sigma_{pq}^0 = \sigma_{g_{pq}}^0 + \sigma_{c_{pq}}^0 + \sigma_{cgt_{pq}}^0 + \sigma_{gc_{g_{pq}}}^0. \quad (1)$$

An overview of the different scattering contributions simulated by SSRT is given in Fig. 2. The ground contribution  $\sigma_{g_{pq}}^0$  (p and q stand for the polarization) can be further described by

$$\sigma_{g_{pq}}^0 = T_p T_q \sigma_{s_{pq}}^0 \quad (2)$$

where  $\sigma_{s_{pq}}^0$  represents the surface scattering and  $T_p$  and  $T_q$  are the transmissivity of the canopy for the respective polarization. The transmissivity (11) accounts for the signal loss of the surface scattering when passing through the canopy covers. For the surface scattering, the model of Oh [25] (Oh04) is used. Oh04

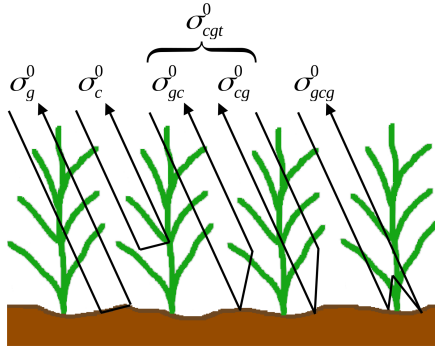


Fig. 2. SSRT modeled scattering contributions in a vegetation canopy. Direct backscatter from soil ( $\sigma_g^0$ ), direct backscatter from plants ( $\sigma_c^0$ ), ground-plant ( $\sigma_{gc}^0$ ), plant-ground ( $\sigma_{cg}^0$ ) scattering, and ground-plant-ground scattering ( $\sigma_{gcg}^0$ ). Figure adapted from Ulaby and Long [31].

is a semiempirical model that was developed by using in-situ measurements of a variety of soil types, primarily silt loam, loam, and sandy loam [56]. One advantage of Oh04 is that no additional information about the soil type is necessary. The authors claim that the backscatter has only a weak dependency on soil type but is, in comparison, highly influenced by soil moisture (sm) and surface roughness [56]. The backscatter  $\sigma_{svv}^0$  of Oh04 is defined as

$$\sigma_{svv}^0 = \frac{0.11 \text{ sm}^{0.7} (\cos\theta)^{2.2} [1 - e^{-0.32 (ks)^{1.8}}]}{0.095 (0.13 + \sin^{1.5}\theta)^{1.4} [1 - e^{-1.3 (ks)^{0.9}}]} \quad (3)$$

Therefore, the soil moisture by Oh04 can be calculated with information about the backscatter  $\sigma_{svv}^0$ , the local incidence angle  $\theta$ , and the soil roughness  $ks$ . The soil roughness can be further specified by  $k$  as the radar wave number ( $k = 2\pi/\lambda$ ) and  $s$  as the rms height of the soil surface. The rms height ( $s$ ) characterizes the surface height variation and as such describes the scattering effects of natural surfaces in the vertical domain (profile). Furthermore, the soil roughness is dependent on the sensor wavelength ( $\lambda$ ). The canopy scattering components of the SSRT [30], [31] are defined as

$$\sigma_{c_{pq}}^0 = \frac{\sigma_{V_{pq}}^{\text{back}} \cos\theta}{k_e^p + k_e^q} (1 - T_p T_q), \quad (4)$$

$$\sigma_{c_{gt_{pq}}}^0 = \sigma_{V_{pq}}^{\text{bist}} H [R_p + R_q] T_p T_q \quad \text{and} \quad (5)$$

$$\sigma_{g_{c_{pq}}}^0 = \frac{\sigma_{V_{pq}}^{\text{back}} \cos\theta}{k_e^p + k_e^q} (R_p R_q - T_p T_q) \quad (6)$$

with  $\theta$  as incidence angle,  $H$  as canopy height, and  $R$  represents the Fresnel coefficients of the respective polarization. The Fresnel coefficients for horizontal  $R_H$  and vertical  $R_V$  polarization are defined [31] as

$$R_H = \frac{\mu_r \cos\theta - \sqrt{\mu_r \epsilon_r - \sin^2\theta}}{\mu_r \cos\theta + \sqrt{\mu_r \epsilon_r - \sin^2\theta}}, \quad (7)$$

$$R_V = \frac{\epsilon_r \cos\theta - \sqrt{\mu_r \epsilon_r - \sin^2\theta}}{\epsilon_r \cos\theta + \sqrt{\mu_r \epsilon_r - \sin^2\theta}} \quad (8)$$

where  $\mu_r$  is the relative permittivity. Under the assumption of isotropic canopy scatterers [31] following relationship is assumed for the volume backscattering coefficient  $\sigma_{V_{pq}}^{\text{back}}$  and the volume bistatic scattering coefficient  $\sigma_{V_{pq}}^{\text{bist}}$ :

$$\sigma_V^{\text{bist}} = \sigma_V^{\text{back}} = k_s. \quad (9)$$

The scattering component  $k_s$  is defined by the single scattering albedo  $\omega$  and the extinction coefficient  $k_e$  as

$$k_s = \omega k_e. \quad (10)$$

The transmissivity  $T$  for the polarization  $p$  can be written as

$$T_p = e^{-k_e^p H \sec\theta} \quad (11)$$

whereas  $k_e^p H$  is often referred to as VOD. VOD can be retrieved from passive and active microwave systems. In the passive domain empirical studies showed a good correlation between VOD and the Vegetation Water Content (VWC). Thus, VOD can be expressed by  $k_e^p H$  (active microwave domain) and  $b$  VWC (passive microwave domain) as

$$\text{VOD} = k_e^p H = b \text{ VWC} \quad (12)$$

where the  $b$  parameter from the passive domain is empirical derived and depends on vegetation type, structure, growth stage, and water status [57], [58]. The Soil Moisture Active Passive (SMAP) mission uses a static  $b$  parameter differentiated by land cover type. However, recent studies found that  $b$  does vary throughout the vegetation season due to significant change of crop water [58], [59]. Thus, in order to archive a temporal dynamic for  $b$  along the growing period, we found that linking  $b$  to a normalized VWC parameter (range 0 to 1) works quite well for the active microwave domain. Therefore, the utilized  $b$  in our case can be written as

$$b = b' \text{ VWC}^{\text{norm}} \quad (13)$$

with  $\text{VWC}^{\text{norm}}$  for a specific timestep  $i$  as

$$\text{VWC}_i^{\text{norm}} = 1 - \frac{\text{VWC}_i - \min(\text{VWC})}{\max(\text{VWC}) - \min(\text{VWC})}. \quad (14)$$

The min and max values of the VWC are calculated on pixel basis and for each growing period separately. Due to the inversion within (14),  $\text{VWC}^{\text{norm}}$  decreases while the original VWC increases. Based on the VWC normalization in (14) the dependency of  $b$  and also of VOD changes to a more parabolic form which helps the algorithm fitting process. In order to better distinguish between the original transmissivity of the SSRT model ( $T$ ) and the introduced changes, we refer the used transmissivity as  $T'$ . Combining (11), (12), and (13), the used transmissivity of the canopy  $T'$  can be written as

$$T'_p = e^{-b \text{ VWC} \sec\theta} \quad (15)$$

$$T'_p = e^{-b' \text{ VWC}^{\text{norm}} \text{ VWC} \sec\theta}. \quad (16)$$

To minimize the required input parameters, a literature value for the single scattering albedo ( $\omega = 0.03$ ) [20], [60] was used.

Furthermore, during the analysis published in Weiß et al. [20] and Weiß et al. [60] the vegetation height  $H$  was found to be a nonsensitive parameter within (5) and thus in absence of height information,  $H=1$  m is assumed. Thus, considering only polarization VV the final equations for the canopy scattering component can be written as

$$\sigma_{cvv}^0 = \frac{1}{2} \omega \cos\theta (1 - T_V' T_V'), \quad (17)$$

$$\sigma_{cgtvv}^0 = \omega b' \text{VWC}^{\text{norm}} \text{VWC} [R_V + R_V'] T_V' T_V', \quad (18)$$

$$\sigma_{gcgpa}^0 = \frac{1}{2} \omega \cos\theta (R_V R_V - T_V' T_V') \quad (19)$$

by considering  $R_V$  (8) and  $T_V'$  (16).

### B. Vegetation Water Content (VWC)

VWC is often used as a parameter to characterize the vegetation above the ground. But unlike, e.g., NDWI, VWC cannot be easily measured by optical satellites such as Sentinel-2. Nevertheless, a high correlation between VWC and NDWI was found in numerous studies ( $R^2$ : 0.57–0.89) [39], [61], [62], [63]. The  $\text{NDWI}_{1640}$  is described as

$$\text{NDWI}_{1640} = \frac{\text{NIR}_{860} - \text{SWIR}_{1640}}{\text{NIR}_{860} + \text{SWIR}_{1640}} \quad (20)$$

where the near infrared channel at  $\lambda=860$  nm ( $\text{NIR}_{860}$ ) and short wave infrared channel at  $\lambda=1640$  nm ( $\text{SWIR}_{1640}$ ) corresponded to Band 8a and Band 11 of the Sentinel-2 satellites. For a NDWI-based VWC calculation, several crop type specific empirical equations exist in the literature [39]. For simplicity of the approach, we used the wheat specific equation in Maggioni et al. [62] to calculate the VWC for the entire test site. The equation for VWC over wheat fields from Maggioni et al. [62] is

$$\text{VWC} = 13.2 \text{NDWI}_{1640}^2 + 1.62 \text{NDWI}_{1640}. \quad (21)$$

### C. Soil Moisture Downscaling Approach

The RTM combination Oh04 and SSRT (Section III-A) is used in an inversion process to downscale a medium resolution soil moisture dataset (RADOLAN API [50]) by using a cost function  $J$ , defined as

$$J = J_{\text{obs}} + J_{\text{prior}} \quad (22)$$

and minimized by Limited-memory Broyden-Fletcher-Goldfarb-Shanno with Box constraint (L-BFGS-B) [64] which is a gradient descent approach. The cost function is described by the model fit to the observations  $J_{\text{obs}}$  and deviations from a priori information  $J_{\text{prior}}$  of the observation variables.  $J_{\text{obs}}$  as the mismatch between Sentinel-1 backscatter and modeled RTM backscatter is described by

$$J_{\text{obs}} = \frac{1}{2} (y - H(x))^T C_0^{-1} (y - H(x)) \quad (23)$$

where  $y$  is the time series of Sentinel-1 VV polarized radar backscatter ( $\sigma_{VV}^0$ ).  $H(x)$  is the RTM backscatter with  $x$  describing the state variables  $sm$  (3), VWC (21),  $b$  (13), and rms height  $s$  (3). The observation uncertainty is represented by the covariance

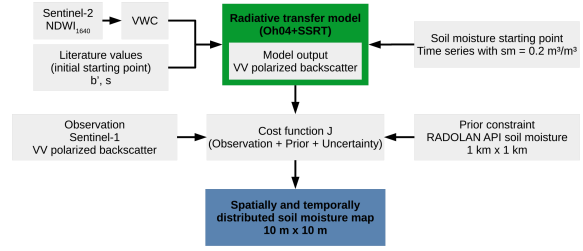


Fig. 3. Schematic illustration of methodology.

matrix  $C_0$ . Another important part of the optimization process is the prior information. Thus,  $J_{\text{prior}}$  is defined as

$$J_{\text{prior}} = \frac{1}{2} (x - x_p)^T C_P^{-1} (x - x_p) \quad (24)$$

with a vector  $x$  again describing the state variables,  $x_p$  referring to the prior estimates, and the covariance matrix  $C_P$  as the uncertainty of the prior. Before the start of the parameter estimation process, realistic boundaries based on the model physics as well as a starting value were set for the applied optimization algorithm L-BFGS-B. The possible equifinality problem in an underdetermined system is addressed by the usage of a guided optimization (weak constraint) approach. The derived parameters ( $sm$ , VWC,  $b'$ , and  $s$ ) are not completely unknown parameters. Due to the absence of tillage practices rms height  $s$  is assumed to be static throughout the vegetation growing period, thus only one value for  $s$  for each pixel needs to be optimized. Prior information for  $sm$  (RADOLAN API) and VWC (derived from Sentinel-2 observations) as well as literature values for the initial starting points of  $b'$  and  $s$  form in conjunction with provided uncertainty information a weak constraint data assimilation system [65], [66]. An overview of the boundaries, priors, starting values, and uncertainty ranges is given in Table III. During the inversion process, the entire state vector ( $sm$ , VWC,  $b'$ , and  $s$ ) is optimized for each satellite pixel by comparing the entire time series of Sentinel-1 VV polarized backscatter with a time series of RTM derived backscatter values that depend on the respective state vector values, priors ( $sm$ , VWC), boundaries ( $sm$ , VWC,  $b'$ ,  $s$ ) and uncertainty (VV backscatter,  $sm$ , VWC,  $b'$ ,  $s$ ). The optimized state vector values for  $sm$ , VWC, and  $b'$  are allowed to differ between each time step, whereas for rms height  $s$  only one value for the entire time series is optimized. The entire methodology is schematically illustrated in Fig. 3.

### D. Applied Statistical Metrics

For the evaluation of the RTM based soil moisture downscaling approach, statistical metrics were used. The Root Mean Square Error (RMSE), the bias, the unbiased Root Mean Square Error (ubRMSE), the correlation coefficient  $R$  and the coefficient of variation (CV) are defined as

$$\text{RMSE} = \sqrt{\frac{1}{N} \sum_{i=1}^N (P_i - O_i)^2} \quad (25)$$

TABLE III  
APPLIED PARAMETER BOUNDARIES, PRIORS, STARTING VALUES, AND UNCERTAINTY RANGES

Parameter	Boundaries	Prior	Starting point	Uncertainty
$sm$ [ $m^3/m^3$ ]	0.01 – 0.7	API	0.2	0.13
VWC [ $kg/m^2$ ]	0 – 7.5	Sentinel-2	Sentinel-2	0.1
$s$ [m]	0.005 – 0.03	–	0.025	0.1
$b$ [ $Npm^2/kg$ ]	0 – 1	13	0.4/0.6	0.5
VV backscatter [dB]	–	–	–	1

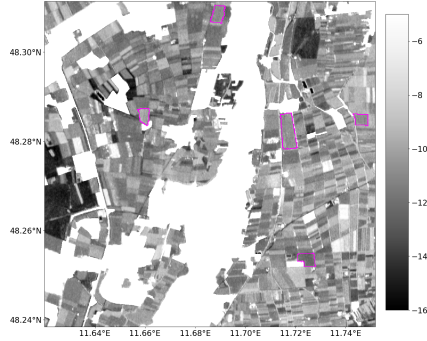


Fig. 4. Mean Sentinel-1 VV backscatter ( $10\text{ m} \times 10\text{ m}$ ) of investigation time period March to September 2017.



Fig. 5. Sentinel-2 derived mean VWC ( $20\text{ m} \times 20\text{ m}$ ) of investigation time period March to September 2017.

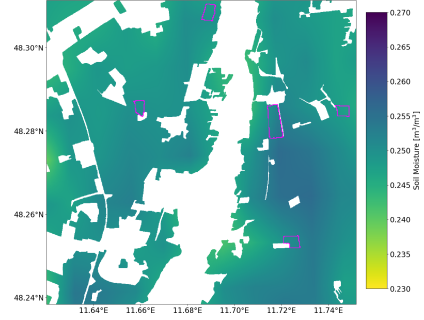


Fig. 6. Mean value of RADOLAN API soil moisture ( $1\text{ km} \times 1\text{ km}$ ) of investigation time period March to September 2017.

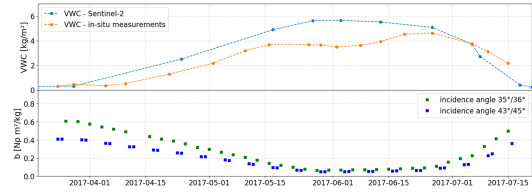


Fig. 7. VWC and evolution of  $b$  for winter wheat field 508.

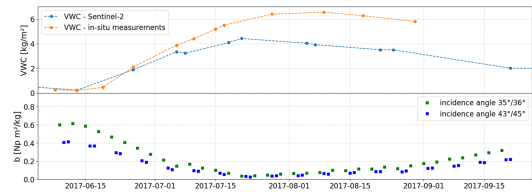


Fig. 8. VWC and evolution of  $b$  for maize field 515.

$$\text{bias} = \frac{1}{N} \sum_{i=1}^N (P_i - O_i) \quad (26)$$

$$\text{ubRMSE} = \sqrt{\frac{1}{N} \sum_{i=1}^N [(P_i - \text{bias}) - O_i]^2} \quad (27)$$

$$R = \frac{\sum_{i=1}^N [(P_i - \bar{P})(O_i - \bar{O})]}{\sqrt{\sum_{i=1}^N (P_i - \bar{P})^2 \sum_{i=1}^N (O_i - \bar{O})^2}} \quad (28)$$

$$\text{CV} = \frac{\sigma}{\mu} \quad (29)$$

with  $N$  as total number of observation,  $O_i$  as  $i$ th observation,  $P_i$  as  $i$ th prediction,  $\bar{O}$  and  $\bar{P}$  as average of observation and predictions,  $\sigma$  as standard deviation, and  $\mu$  as mean.

## IV. RESULTS

### A. Spatial Distributed Model Input

Spatially distributed model input data are the VV-polarized Sentinel-1 backscatter (Fig. 4), Sentinel-2 derived VWC (Fig. 5), and a coarse resolution soil moisture product based on RADOLAN data (Fig. 6). Looking at the high resolution ( $10\text{ m} \times 10\text{ m}$ ) mean VV backscatter (Fig. 4) for the investigation time period of March to September 2017, field boundaries are clearly visible, whereas intra-field differences are low. The mean backscatter of the entire scene is 10.5 dB for 2017 and 10.7 dB for 2018. Certain areas with low backscatter values (black/dark color) correspond to forestry or other nonagricultural areas, which will not be considered in the quality assessment of the

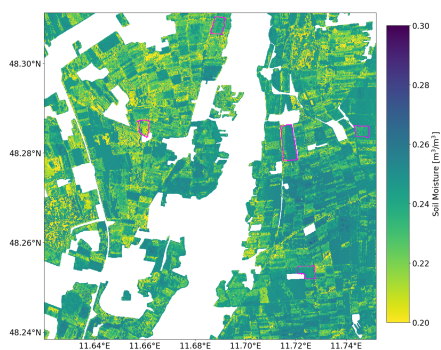


Fig. 9. Mean downscaled high resolution soil moisture (10 m × 10 m) of investigation time period March to September 2017.

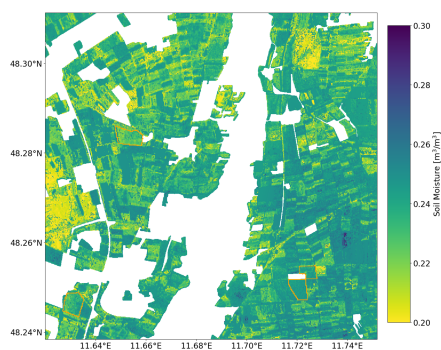


Fig. 12. Mean downscaled high resolution soil moisture (10 m × 10 m) of investigation time period April to September 2018.



Fig. 10. Coefficient of variation of downscaled high resolution soil moisture of investigation time period March to September 2017.



Fig. 13. Coefficient of variation of downscaled high resolution soil moisture of investigation time period April to September 2018.

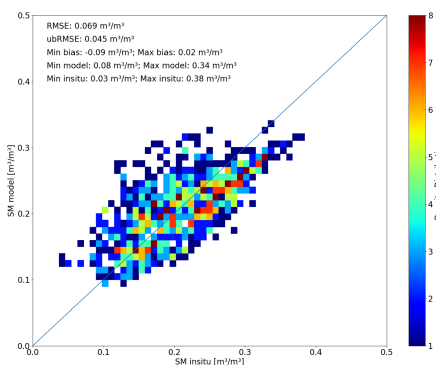


Fig. 11. Unbiased in-situ soil moisture (five fields with three ESUs) compared with downscaled soil moisture of year 2017.

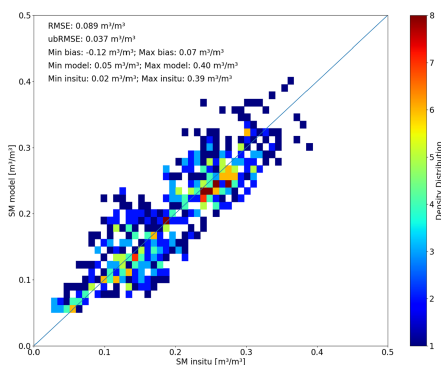


Fig. 14. Unbiased in-situ soil moisture (four fields with three ESUs) compared with downscaled soil moisture of year 2018.

approach later on. Field boundaries can be distinguished within the high resolution (20 m × 20 m) mean VWC image (Fig. 4) for the investigation time period of 2017 too. The mean VWC of the entire scene is 1.37 kg/m<sup>2</sup> for 2017 and 1.25 kg/m<sup>2</sup> for 2018. Contrary to the backscatter information, intrafield differences for certain fields (515 or 301) are visible. The coarse resolution (1 km × 1 km) mean RADOLAN API soil moisture

product (Fig. 6) for the investigation time period of 2017 shows, compared to the backscatter and VWC, no field boundaries and low overall differences (the legend of soil moisture range is within 0.05 m<sup>3</sup>/m<sup>3</sup>). The mean soil moisture of the entire scene is 0.25 m<sup>3</sup>/m<sup>3</sup> for both years. Input data for the year 2018 is not shown due to similar patterns with small differences in backscatter and VWC content based on field crop rotation.

TABLE IV  
PERFORMANCE METRICS (RMSE, BIAS, ubRMSE) FOR DIFFERENT GROWING PERIODS (TS=ENTIRE TIME SERIES; BBCH<40=TILLERING AND STEM ELONGATION; BBCH>39=HEADING, FLOWERING, FRUIT DEVELOPMENT AND RIPENING) AS WELL AS FOR INDIVIDUAL FIELDS SEPARATED BY YEAR AND CROP TYPE

Year	Field	Crop Type	RMSE [m <sup>3</sup> /m <sup>3</sup> ]			Bias [m <sup>3</sup> /m <sup>3</sup> ]			ubRMSE [m <sup>3</sup> /m <sup>3</sup> ]		
			TS	BBCH<40	BBCH>39	TS	BBCH<40	BBCH>39	TS	BBCH<40	BBCH>39
2017	301	Wheat	0.093	0.079	0.100	-0.09	-0.07	-0.08	0.049	0.038	0.048
2017	319	Maize	0.073	0.089	0.043	-0.08	-0.08	-0.03	0.038	0.022	0.025
2017	508	Wheat	0.059	0.018	0.040	-0.01	-0.01	-0.02	0.033	0.018	0.032
2017	515	Maize	0.055	0.058	0.033	-0.03	-0.05	0.01	0.046	0.028	0.032
2017	542	Wheat	0.056	0.039	0.063	0.02	0.03	-0.04	0.053	0.014	0.045
2018	317	Wheat	0.126	0.133	0.117	-0.12	-0.13	-0.11	0.046	0.004	0.043
2018	410	Maize	0.113	0.109	0.105	-0.11	-0.10	-0.10	0.033	0.030	0.028
2018	508	Maize	0.035	0.042	0.027	0.01	0.01	0.02	0.034	0.039	0.015
2018	525	Wheat	0.056	0.021	0.033	0.07	0.02	0.01	0.032	0.008	0.032

### B. Parameter $b$

Figs. 7 and 8 show the change of parameter  $b$  based on the temporal evolution of VWC. As the VWC is normalized and multiplied with  $b$  (13), higher VWC values result in lower  $b$  values and vice versa. Figs. 7 and 8 show the Sentinel-2 derived VWC content for wheat field 508 and maize field 515. The derived VWC content matches the temporal evolution of the in-situ measurements quite well ( $R > 0.9$ ). But a slight intensity mismatch between the observed and calculated VWC can be observed for wheat as well as for maize fields. The starting point of  $b$  depends on the incidence angle of the respective VV backscatter observations [60].

### C. Downscaled Soil Moisture Results

Figs. 9 and 12 illustrate the mean downscaled soil moisture of the investigation time period for 2017 and 2018, respectively. Test fields with in-situ measurements show similar mean soil moisture values despite crop rotation practices between the years. The average soil moisture of the test area for 2017 and 2018 was 0.236 m<sup>3</sup>/m<sup>3</sup> and 0.235 m<sup>3</sup>/m<sup>3</sup>, respectively. Within the test area, different fields show partly differing soil moisture values. Thus, field boundaries are detectable, although not as visible as the boundaries in the input variables of VV backscatter and VWC. In order to analyze the temporal dynamics of soil moisture, Figs. 10 and 13 illustrate the CV of the downscaled soil moisture within the investigation time period for 2017 and 2018. Overall, slightly higher CV values were retrieved for 2018 (mean CV = 0.138) than for 2017 (mean CV = 0.109). This is in line with in-situ observations, which indicate a drier summer and wetter spring for 2018 than for 2017. Isolated pixels within some crop fields show high CV values of  $> 0.4$ . These high CV values might be the result of remaining speckle disturbances within the backscatter data. Furthermore, areas with high CV values ( $> 0.4$ ) show very low mean backscatter values of  $< -15$  dB. A comparison of in-situ and bias corrected downscaled soil moisture for wheat and maize fields are illustrated in Figs. 11 and 14. The mean RMSE for all ESUs is 0.069 m<sup>3</sup>/m<sup>3</sup> and 0.089 m<sup>3</sup>/m<sup>3</sup> for 2017 and 2018, respectively. Considering the ubRMSE, values of 0.045 m<sup>3</sup>/m<sup>3</sup> and 0.037 m<sup>3</sup>/m<sup>3</sup> are shown. A higher improvement of RMSE and ubRMSE is seen for 2018, though a higher bias range is calculated for 2018 (Fig. 14) than for 2017 (Fig. 11). Furthermore, both years show a similar range of in-situ soil moisture measurements (2017: 0.03–0.38 m<sup>3</sup>/m<sup>3</sup>; 2018:

0.02–0.39 m<sup>3</sup>/m<sup>3</sup>). In addition, a higher soil moisture range is seen within the downscaled values for 2018 (0.05 - 0.40 m<sup>3</sup>/m<sup>3</sup>) than 2017 (0.08 - 0.34 m<sup>3</sup>/m<sup>3</sup>). In general, the soil moisture results are well located around the 1:1 line. The performance metrics for the individual fields, separated by year and crop type, are illustrated in Table IV. To differentiate between phenological stages, the Biologische Bundesanstalt, Bundessortenamt and Chemical (BBCH) [67] developed a system for uniform coding of growth stages for all mono- and dicotyledonous plant types. Performance metrics for different vegetation growing period can be also found in Table IV as well. Considering the results for the entire time series of the individual fields, no obvious pattern which would suggest that the method works better for wheat or maize fields can be detected. But a high RMSE goes along with a high bias. The ubRMSE for the entire time series shows for all test fields a similar performance of 0.032 to 0.053 m<sup>3</sup>/m<sup>3</sup>. This indicates that the temporal evolution is well met even for fields with high RMSE values. Comparing the RMSE and ubRMSE of wheat fields, a better RMSE and ubRMSE are observed for BBCH<40 than BBCH>39. This suggests that the retrieval works better for lower vegetation stages. The same behavior can be observed for maize fields in 2017 whereas the results from 2018 are contradicting.

The correlation coefficient and standard deviation of downscaled and in-situ soil moisture values as well as RADOLAN API and in-situ values are illustrated on a field basis in Figs. 15–17. For the results in Fig. 15, the entire investigation period is considered, whereas in Figs. 16 and 17, the time series is separated according to different phenological phases. Fig. 16 shows the soil moisture results for the time period with BBCH values lower than 40 (tillering and stem elongation), and Fig. 17 shows the results with BBCH values higher than 39 (heading, flowering, fruit development, and ripening). Overall, the time series and subsets show a low standard deviation of  $< 0.04$  m<sup>3</sup>/m<sup>3</sup>. The correlation coefficient for the entire time series has a broad range from 0.06 to 0.78 for the RT retrieved soil moisture. High and low correlation coefficients are observed for maize as well as wheat fields. Thus, no real crop-specific pattern between maize and wheat fields is detectable. Considering only time steps with BBCH values below 40 (sparse to medium vegetation cover), the correlation coefficient of the wheat fields increases significantly due to lower vegetation cover. Only one wheat field remains with a correlation coefficient of 0.22, whereas the other test

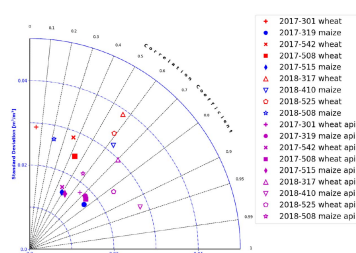


Fig. 15. Standard deviation and correlation coefficient of downscaled and in-situ soil moisture values (red/blue represents wheat/maize; filled/nonfilled represents 2017/2018) as well as RADOLAN API and in-situ values (magenta), for the entire investigation period of 2017 and 2018.

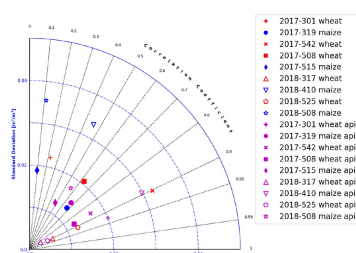


Fig. 16. Standard deviation and correlation coefficient of downscaled and in-situ soil moisture values (red/blue represents wheat/maize; filled/nonfilled represents 2017/2018) as well as RADOLAN API and in-situ value (magenta), for the time period with BBCH values lower than 40 (tillering and stem elongation).

fields, with crop type wheat, show values of up to 0.91. For all maize fields, the correlation coefficient of the RT retrieved soil moisture is dropping compared to the entire time series. Maize fields of 2017 (blue filled icon) show a significantly lower standard deviation for the entire time series as well as for the time series with BBCH values lower than 40 (Figs. 15 and 16) compared to maize fields of 2018 (blue nonfilled icon). However, for the time series with BBCH values higher than 39 (Fig. 17), the standard deviation of all maize fields (blue icons) is similar. Comparing the RADOLAN API and RT retrieved soil moisture results predominantly a lower standard deviation is observed for the RADOLAN API. This is expected as the RADOLAN API has a lower resolution. Furthermore, the RADOLAN API generally shows better correlation with the in-situ data. It is suspected that this is due to the lower resolution. Through spatial aggregation, it is often observed that soil moisture estimates tend to have a better correlation with in-situ data since local variation and measurement noise are smoothed out.

Fig. 18 shows the downscaled soil moisture pattern of the test site from the end of May to the beginning of June 2017. Fig. 18(f) presents the soil moisture distribution and the precipitation measurements of two meteorological stations (for location relative to the test site, see Fig. 1) for the 29th of May until the 6th of June. A precipitation event occurred on May 30th after the Sentinel-1 overflight. Hence, the precipitation event is not visible in the downscaled soil moisture image [Fig. 18(a)]. Moisture patterns of May 31st indicate higher values for the northern part and almost no soil moisture change in the southern part of the test

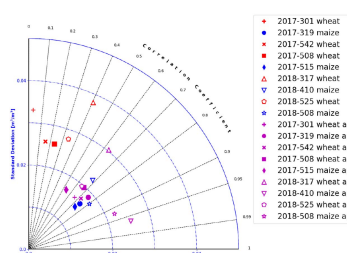


Fig. 17. Standard deviation and correlation coefficient of downscaled and in-situ soil moisture values (red/blue represents wheat/maize; filled/nonfilled represents 2017/2018) as well as RADOLAN API and in-situ value (magenta), for the time period with BBCH values higher than 39 (heading, flowering, fruit development and ripening).

site. This behavior can be explained by the observations at the meteorological stations, where high precipitation was measured at Eichenried (latitude 48.27°) and low to no precipitation was measured southward at Grub (latitude 48.17°). With almost no precipitation between June 1st and 3rd, a conversion of the northern and southern soil moisture values is visible in Fig. 18(c). Another spatially distributed precipitation event occurred on June 4th, with marginal soil moisture changes in the southeast and high changes for the rest of the test area [Fig. 18(d)]. Similar to the situation on June 30th, 2017, the meteorological stations show the same behavior. After two days of precipitation (June 5th and 6th) within the entire test site area, a homogeneous soil moisture pattern with high moisture values is illustrated in Fig. 18(e). The downscaled soil moisture distribution of the test site and the measured precipitation at stations Eichenried and Grub are shown for April to July 2017 in Fig. 19. A comparison of soil moisture changes of the downscaled soil moisture product and the measured precipitation measurements reveal a high alignment of dry-down phases and precipitation events within the data.

Exemplary for the time period of July 19th to 24th of 2018, Fig. 20 illustrates the drying process on the field scale of the MNI test site. Low to no precipitation was measured between July 18 and 20 [Fig. 20(e)]. The precipitation events on July 21st and 22nd are clearly visible by comparing the downscaled soil moisture patterns of July 19th [Fig. 20(a)] and 22nd [Fig. 20(b)]. With almost no precipitation from July 23rd to 26th, the downscaled drying process within the test area can be seen by comparing Fig. 20(b)–(d) and by looking at the soil moisture distribution of July 22nd to 24th in Fig. 20(e). Furthermore, comparing Fig. 20(e) top (downscaled soil moisture distribution) and bottom (precipitation at stations Eichenried and Grub) dry-down phases and precipitation events are mapped very well in the downscaled soil moisture distribution of the test site.

## V. DISCUSSION

Continuous, high-resolution, large scale monitoring of a variable like soil moisture with its high spatial and temporal variability is challenging. Current operationally retrieved soil moisture products do not fulfill the demand for temporal and spatial

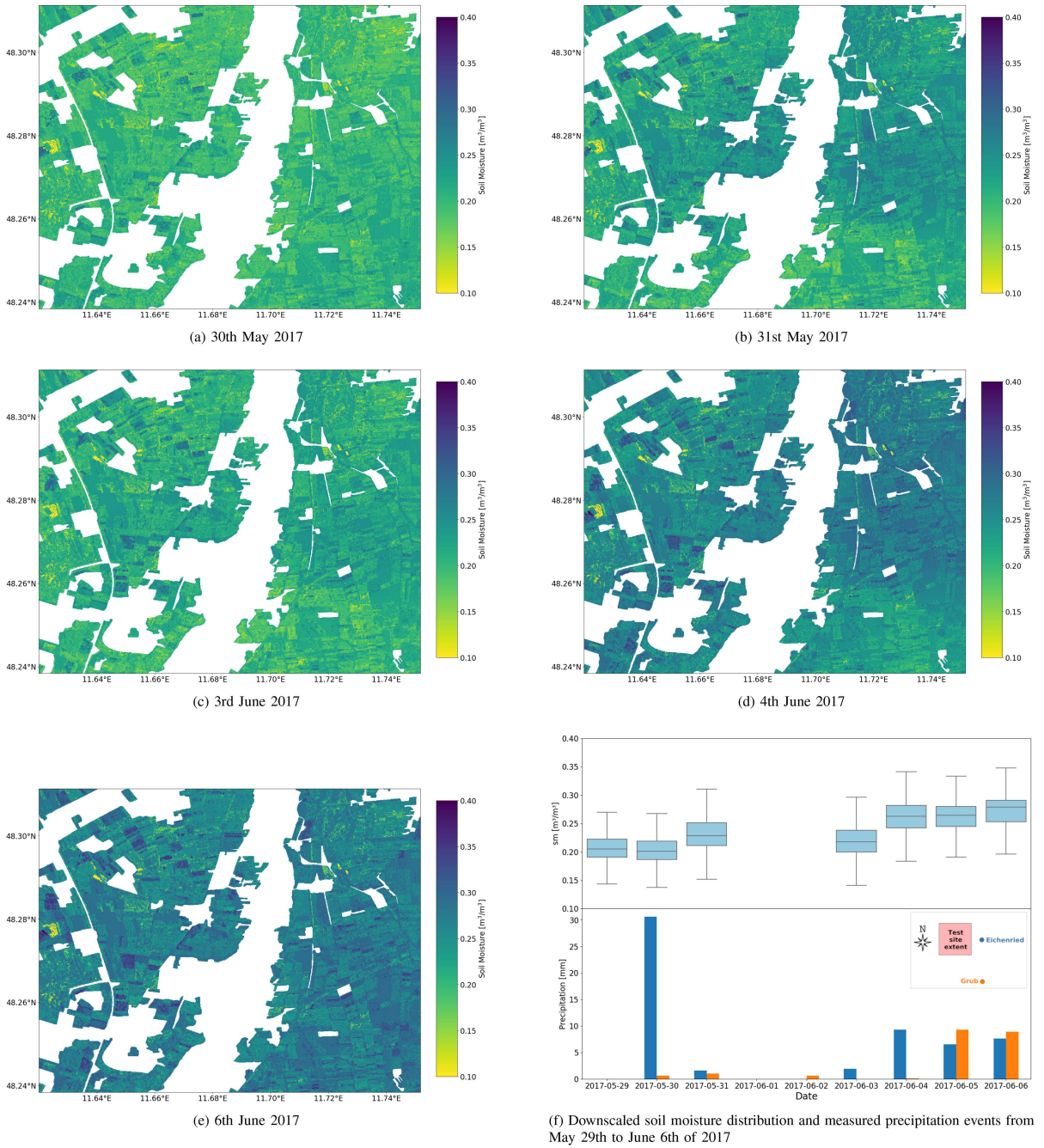


Fig. 18. Downscaled soil moisture pattern of the test site for (a) May 30th, (b) May 31st, and (c) June 3rd, (d) June 4th, and (e) June 6th of 2017. Downscaled soil moisture distribution and measured precipitation events of meteorological stations Eichenried and Grub (f).

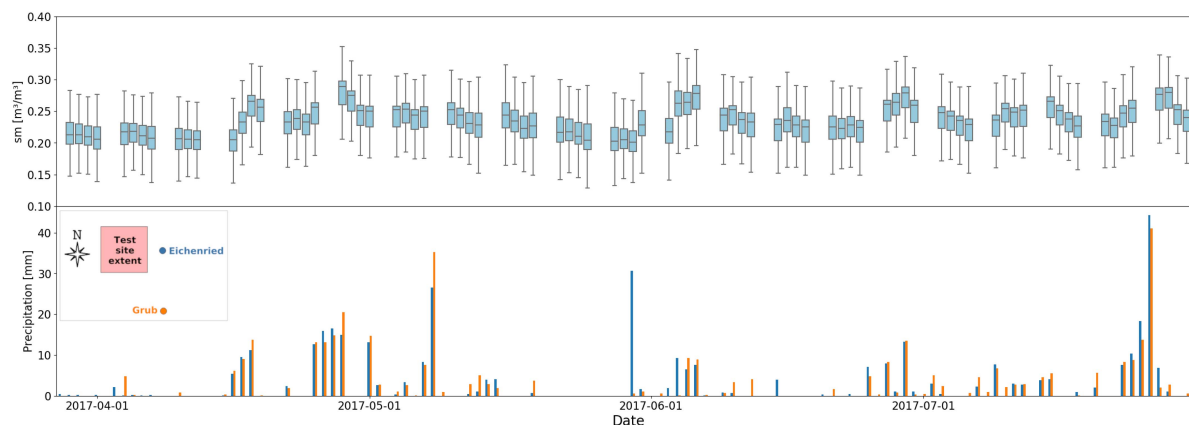


Fig. 19. Downscaled soil moisture distribution (top) and measured precipitation events of meteorological stations Eichenried and Grub (bottom) from April to July 2017.

resolution for smart farming operations [68]. With the Sentinel satellites in orbit, remote sensing data with suitable high spatio-temporal resolution is available for further investigations of soil moisture retrieval approaches. Sentinel-1 (SAR) and Sentinel-2 (optical spectrometer) provide information with a spatial resolution of 10 m (Sentinel-1) and 10–6 m (Sentinel-2), respectively. Sentinel-1 and Sentinel-2 provide images over the same area with the same viewing angle every 6 or 5 days, respectively. The number of usable images from Sentinel-2 decreases when considering cloud cover. For the MNI test site, Sentinel-2 provides a usable image approximately every 10 days. A special challenge however results from a change in the Sentinel-1 observation geometry, namely, modeling the radar backscatter response in conjunction with the associated soil moisture value. Other high resolution soil moisture approaches of Baghdadi et al. [47], El Hajj et al. [19], or Nativel et al. [69] solely use Sentinel-1 images with similar incidence angle. Although, in theory they might be applicable to handle incidence angle changes, [60] has shown that the incidence angle implementation within common RT models (WCM, SSRT) are not sophisticated enough to handle incidence angle changes within one time series. Thus, either each incidence angle needs to be calculated as a separate time series or as we proposed some changes need to be applied. Although more observations (different observation geometries) might be available (depending on the location of the test area) most studies show only a time series based on the Sentinel-1A and Sentinel-1B 6-day repeat cycle. In respect to Sentinel-1A and Sentinel-1B it has to be mentioned that, Sentinel-1B was retired in December 2021 and does not provide images anymore. Nevertheless, the two satellite system should be restored with the planned launch of Sentinel-1C end of 2024. This study proposes a RTM based soil moisture downscaling method that allows for all available Sentinel-1 images (varying viewing angles) to be used, and thus a temporal resolution for the MNI test site of 1.5 days can be archived. However, it has to be mentioned that the soil moisture retrieval quality is also effected by the incidence angle. A study of Bazzi et al. [70] investigated the effect of the incidence angle on soil moisture retrievals from Sentinel-1 and

found that lower incidence angle were more suitable than higher ones. With such high spatio-temporal resolution, the results provide an almost daily overview of soil wetting and drying. Furthermore, a differentiation on the field scale is possible in contrast to the medium resolution soil moisture input data. But besides different field scale soil moisture levels, unique differentiated soil moisture patterns due to spatially scattered rain events are also captured (Fig. 20). Nevertheless, as Sentinel-1 images are snapshots of a specific acquisition time, a discrete and noncontinuous time series is produced. A rain event which might occur slightly after the Sentinel-1 overpass is only captured by the follow-on overpass.

The literature shows, that a relationship between the  $b$ -parameter and VWC is often used to parameterize vegetation attenuation (VOD) [57], [71], [72]. Furthermore, research of Togliatti et al. [58] indicated that the  $b$ -parameter is changing during the growing season. To account for changes in the growing season, the  $b$ -parameter was adapted by using normalized VWC information (13) and (16). In previous studies [20], [60], LAI, in combination with an empirical parameter similar to  $b$  were used to describe the vegetation status. It was found that the retrieval algorithm had problems deriving good soil moisture estimates for later vegetation stages. Since the used RT-models were not able to reproduce the backscatter increase during later vegetation stages seen in the Sentinel-1 data, LAI with its saturation in later vegetation stages was suspected to be part of the problem. By changing the vegetation descriptor from LAI to VWC, the retrieval algorithm produced better soil moisture results, but did not resolve the backscatter mismatch between the RT-model and the observed Sentinel-1. However, by implementing the proposed VWC normalization and thus changing the dependency of  $b$  to a more parabolic form, the retrieval results and the mismatch between the RT-model and Sentinel-1 backscatter could be further improved. Furthermore, previous research by Weiß et al. [60] has shown that a joint dense Sentinel-1 time series (all available images disregarding incidence angle changes) is usable within RTMs if considering a correction of the transmissivity term  $T$  based on the incidence

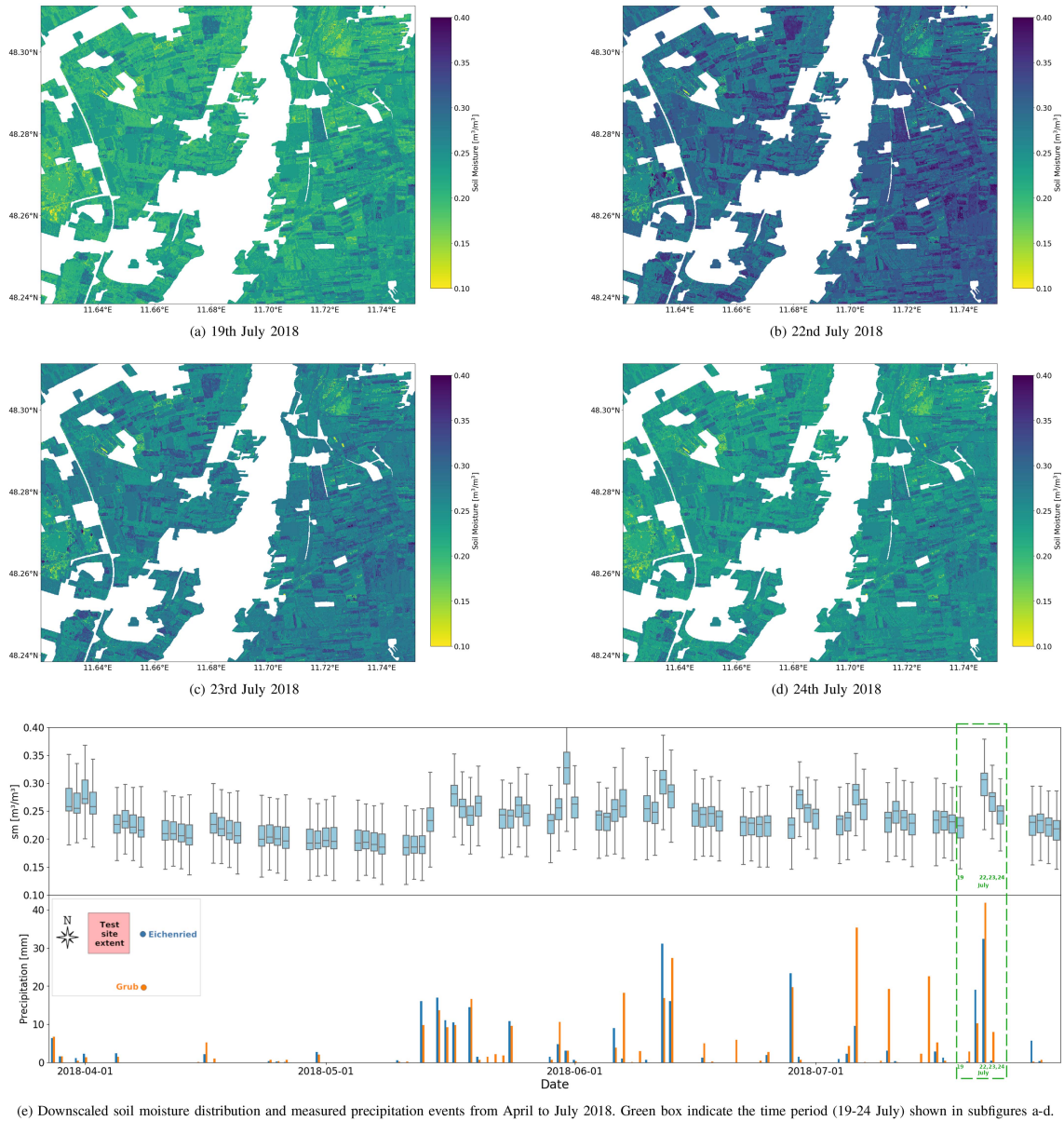


Fig. 20. Downscaled soil moisture pattern of the test site for (a) July 19th, (b) 22nd, (c) 23rd, and (d) 24th of 2018. Downscaled soil moisture distribution and measured precipitation events of meteorological stations Eichenried and Grub (e).

angle of Sentinel-1. Therefore, different starting points for parameter  $b$  based on the incidence angle were used. The VWC, representing the other important input parameter describing the vegetation state, can be derived by crop type specific empirical functions from optical sensors (Sentinel-2), as shown by Maggioni et al. [62], Cosh et al. [73], or Gao et al. [39]. But, as field scale crop type information is often not available on large scales, an empirical function for wheat, the worldwide most widely cultivated crop [74], was used for the entire test site. Although the applied wheat equation may not seem suitable

to derive VWC for multiple crop types, the calculation of an appropriate temporal VWC evolution during the growing season was possible and tested during algorithm development. The ubRMSE values on field scale for different wheat and maize fields range between  $0.032 \text{ m}^3/\text{m}^3$  and  $0.053 \text{ m}^3/\text{m}^3$  with a mean ubRMSE for the entire test site of  $0.045 \text{ m}^3/\text{m}^3$  (2017) and  $0.037 \text{ m}^3/\text{m}^3$  (2018). It is very probable that the methodology design and thus the modification of the  $b$  parameter and its temporal guidance through  $\text{VWC}^{\text{norm}}$  is what produced these good results for the maize fields.

Our results show a similar accuracy in terms of ubRMSE as other high resolution approaches from Tao et al. [75] (0.060 to 0.039  $\text{m}^3/\text{m}^3$ ), El Hajj et al. [19] (0.097 to 0.040  $\text{m}^3/\text{m}^3$ ), Ma et al. [32] (0.078 to 0.039  $\text{m}^3/\text{m}^3$ ) or Mengen et al. [76] (0.063  $\text{m}^3/\text{m}^3$ ). Furthermore, compared with the abovementioned studies, our method provides the highest temporal resolution with almost daily updates for soil moisture values.

#### A. Transferability

The proposed method is purely based on publicly available information, which can operationally be derived from remote sensing sensors like Sentinel-1, Sentinel-2, or the weather radar network RADOLAN. The applied RTM (Oh04 and SSRT) needs radar backscatter, VWC, and the starting value of the parameter  $b'$  (temporal evolution is coupled to VWC) as input data. Specific information about soil composition is not necessary. For VWC calculation, the literature offers different approaches, which are mostly based on spectral information provided by optical sensors like Sentinel-2 or MODIS [62], [73]. Unfortunately, different equations for different crop types are needed to accurately retrieve VWC in absolute terms [39]. Therefore also current crop type information is required. But with the proposed approach (relationship between  $\text{VWC}^{\text{norm}}$  and  $b$ ), the absolute value of VWC is not as important as the temporal dynamics of VWC during the vegetation growing period. Thus, for simplicity reasons, VWC is calculated using an empirical function suitable for wheat regardless of the crop type. Our study shows, that, although VWC calculation for maize fields is based on the wheat equation, reasonable soil moisture time series patterns (ubRMSE range between 0.032 and 0.053  $\text{m}^3/\text{m}^3$ ) for wheat and maize fields are retrieved. Due to the normalization of VWC, the actual temporal dynamic seems to be more important than the absolute value. This allows the approach to be applied on maize and wheat fields without specific crop type information if the temporal dynamic of VWC is matched. The transferability of the proposed method compared to other approaches from Kim and Liao [77] or Huang et al. [16] thereby is greatly enhanced, due to a lack of specific crop information on field basis for most parts of the world.

Another important input parameter of our study is a soil moisture proxy with medium resolution (1 km  $\times$  1 km), which represents the basis for the downscaling efforts. The utilized RADOLAN API product's hourly resolution makes it an excellent prior dataset, however it only covers the spatial domain of Germany. Nevertheless, Ramsauer and Marzahn [78] recently published the global soil moisture product equivalent based on GPM precipitation data (GPM\_API). Furthermore, for global use, soil moisture products with resolution from 25 km down to 1 km [11], [79] exist and can be used as soil moisture proxy instead of the RADOLAN based data. In addition, other countries like Poland with POLRAD [80], Switzerland with CombiPrecip [81], or the USA with NEXRAD [82] provide similar information, like the German RADOLAN network. In summary, the proposed approach qualifies for high transferability to be applied to other regions due to its limited set of input variables (VV-polarized backscatter, VWC, and medium resolution soil moisture proxy), which all are provided or can be derived from operational remote sensing sensors.

#### B. Limitations, Improvements, and Usage

The possible transferability of the approach was theoretically stated in Section V-A, but has to be proven by applying the method to other regions. Furthermore, because of the lack of in-situ measurements for other crop types, only the accuracy of the soil moisture results for wheat and maize fields could be validated in this study. Nevertheless, maize and wheat already account for 65% of the world's cereal production [83]. However, due to our approach (use of time variant  $b$  parameter which is normalized by VWC), we found that the evolution of VWC is more important than the absolute values for VWC. We do not expect, that the absolute VWC values of empirical equation defined for wheat will fit other crops like rapeseed or soybean, but as the VWC is based on the optical NDWI index an increase of VWC during the early growing season and an decrease during the drying phase should be matched for all summer cultivated plants. However, this has to be proven with in-situ data. Thus, summarizing the next research focus will be the usage of the method in other regions as well as testing different medium resolution soil moisture products.

One advantage of using microwave data is its penetration capabilities through vegetation cover, and thus the possible retrieval of information about soil moisture conditions under vegetation [84]. The penetration depth of electromagnetic waves into the canopy depends on frequency, polarization, and incidence angle [85]. C-band data is able to penetrate vegetation cover, but with a combination of shallow incidence angles and high vegetation cover (e.g., fully developed maize plants), the backscattering signal of the soil might be very low [85], [86]. For high incidence angles, Joseph et al. [87] and El Hajj et al. [33] showed that even at the biomass peak of maize fields, C-band microwaves were sensitive to soil moisture. They conclude that soil moisture sensitivity is given due to significant soil-vegetation scattering contributions. On the other hand, in case of a full developed wheat field, the penetration of C-band into the canopy was found limited [33]. During certain growing stages (booting, heading, flowering, fruit development) where wheat plants contain a lot of canopy water, the penetration of C-band is highly dampened [60]. However, for later wheat growing stages (ripening) the sensitivity of C-band to the soil and soil moisture does increase [88], [89]. The sensitivity increase can be attributed to the loss of canopy water which makes the vegetation layer more transparent for microwaves. We see the effect of changing C-band sensitivity during the growing season of wheat by comparing Figs. 16 and 17. The correlation coefficient drops significantly between the first and the second half of the growing season. In addition, the ubRMSE in Table IV for wheat fields shows better results for BBCH<40 than BBCH>39. But, the ubRMSE values for BBCH>39 are still in an acceptable range of 0.032 to 0.048  $\text{m}^3/\text{m}^3$ . Thus, we suspect that during growing stages like heading and flowering the proposed approach relies more on the soil moisture prior information. Therefore, in case of high vegetation cover, the application of radar sensors with lower frequencies, e.g., L-band might increase the accuracy of the retrieval results due to its higher vegetation penetration [90], especially at low incidence angles. Unfortunately, no operational L-band dataset with high

temporal and spatial resolution is currently available, but the NISAR mission of NASA is upcoming [91].

Promising results for large scale provision of crop type information are shown with optical data by Inglada et al. [92] and with combined optical and microwave data by Orynbaikyzy et al. [93], Ofori-Ampofo et al. [94], and Blickensdörfer et al. [95]. But as crop types might differ every year, and distinction levels might not exceed a differentiation of summer and winter crops [92], operational application might be difficult on global scales.

Another limitation of the proposed methodology in its current status is that the normalization of VWC is based on maximum and minimum values. This means that in its current status the method can only be applied after the growing period. However, additional crop specific a priori data from previous years might be usable to apply the methodology already during the growing period. Nevertheless, this needs more investigation. If the abovementioned limitation can be overcome, then we will be another step further towards providing high temporal and spatial soil moisture information for applications in terms of smart farming decisions [8] and improved crop yield estimations [96]. In areas with irrigation, high spatio-temporal information about soil moisture has the potential to improve water usage on a local to regional scale [97]. Furthermore, spatially distributed soil moisture information helps by minimizing fertilizer usage [7], and thus reducing pollution of surface and groundwater resources [98]. In addition, soil erosion often depends on local conditions, which means that for soil erosion modeling and agricultural adaptation strategies, high spatio-temporal soil moisture information is vital [68].

## VI. CONCLUSION

A soil moisture time series product with medium spatial resolution (RADOLAN API  $1 \text{ km} \times 1 \text{ km}$ ) was downscaled to field scale by applying an adapted microwave RTM. For model input, high spatio-temporal VV-polarized backscatter (Sentinel-1;  $10 \text{ m} \times 10 \text{ m}$ ) and VWC information derived from optical sensors (Sentinel-2;  $20 \text{ m} \times 20 \text{ m}$ ) were used. For parameters like soil roughness, which were considered static over the growing season, suitable literature values were chosen [60]. The retrieved high spatio-temporal distributed soil moisture information was further validated with in-situ measurements (MNI test site in Bavaria, Germany) of wheat and maize fields during the vegetation growing periods of 2017 and 2018.

A validation of soil moisture with in-situ measurements of several fields reveals good agreement with a mean ubRMSE of  $0.045 \text{ m}^3/\text{m}^3$  and  $0.037 \text{ m}^3/\text{m}^3$  for the years 2017 and 2018, respectively. Furthermore, the downscaled soil moisture covers a broad range of values from  $0.05 \text{ m}^3/\text{m}^3$  to  $0.4 \text{ m}^3/\text{m}^3$ . In addition, spatial patterns from precipitation events and drying behavior within the test site are clearly visible within the downscaled soil moisture images. Overall, it is demonstrated that with a small and well selected set of input parameters which are publicly provided by different optical and microwave remote sensing sensors, the generation of high spatio-temporal distributed soil moisture patterns is feasible by using RTM-based downscaling over the investigated agricultural fields.

One advantage of the proposed methodology is the usage of all available Sentinel-1 images regardless of the observation geometry which lead to changes of the radar backscatter response. Thus, the temporal resolution constraint due to the Sentinel-1A and Sentinel-1B 6-day repeat cycle (same observation geometry, same orbit, same incidence angle, same observation time) is overcome and in case of the MNI test site a 1.5 d temporal resolution is archived. Unfortunately, right now only Sentinel-1A provides images as Sentinel-1B had a power supply issue and was retired in December 2021. Nevertheless, the upcoming Sentinel-1C will hopefully restore the two satellite system before the end of 2024.

Another advantage of the proposed methodology is its high transferability to other regions, as the used retrieval algorithm relies only on information that can be systematically retrieved with existing global operational satellites (Sentinel-1 and Sentinel-2) and a coarse to medium resolution soil moisture prior. A comparison of different medium and low resolution soil moisture proxy as prior and the application of the methods on other test sites is needed to further explore and optimize the quality of the spatio-temporal soil moisture estimates at decameter resolution. Possible pitfalls of the transferability of this and other high resolution soil moisture retrieval approaches might be uncertainties due to landscape heterogeneity (soil properties, crop types, vegetation stages). Thus, in order to further reduce uncertainties, opportunities may arise by including site specific auxiliary information (soil texture or crop type) within the proposed downscaling scheme. Hence, the approach offers multiple opportunities for enhancement by including additional information which are or will be provided in the future by remote sensing sensors and techniques.

## ACKNOWLEDGMENT

The author Thomas Weißis would like to thank Alexander Läu ( $\dagger$  2. July 2017) for the inspiration, ideas, and support that he has given.

## REFERENCES

- [1] H. McNairn, A. Merzouki, A. Pacheco, and J. Fitzmaurice, "Monitoring soil moisture to support risk reduction for the agriculture sector using RADARSAT-2," *IEEE J. Sel. Topics Appl. Earth Observ. Remote Sens.*, vol. 5, no. 3, pp. 824–834, Jun. 2012.
- [2] R. Hollmann et al., "The ESA climate change initiative: Satellite data records for essential climate variables," *Bull. Amer. Meteorological Soc.*, vol. 94, no. 10, pp. 1541–1552, Mar. 2013, doi: [10.1175/BAMS-D-11-00254.1](https://doi.org/10.1175/BAMS-D-11-00254.1).
- [3] L. Brocca, L. Ciabatta, C. Massari, S. Camici, and A. Tarpanelli, "Soil moisture for hydrological applications: Open questions and new opportunities," *Water*, vol. 9, no. 2, Feb. 2017, Art. no. 140. [Online]. Available: <https://www.mdpi.com/2073-4441/9/2/140>
- [4] L. Brocca, F. Melone, T. Moramarco, and R. Morbidelli, "Spatial-temporal variability of soil moisture and its estimation across scales," *Water Resour. Res.*, vol. 46, no. 2, 2010, Art. no. W02516. [Online]. Available: <https://agupubs.onlinelibrary.wiley.com/doi/abs/10.1029/2009WR008016>
- [5] J. Dari, R. Morbidelli, C. Saltalippi, C. Massari, and L. Brocca, "Spatial-temporal variability of soil moisture: Addressing the monitoring at the catchment scale," *J. Hydrol.*, vol. 570, pp. 436–444, Mar. 2019. [Online]. Available: <http://www.sciencedirect.com/science/article/pii/S0022169419300575>
- [6] N. Sanchez, L. Almendra, J. Plaza, A. González-Zamora, and J. Martínez-Fernández, "Spatial averages of in situ measurements versus remote sensing observations: A soil moisture analysis," *J. Spatial Sci.*, vol. 67, no. 3, pp. 439–454, 2022, doi: [10.1080/14498596.2020.1833769](https://doi.org/10.1080/14498596.2020.1833769).

- [7] J. Peng et al., "Estimation and evaluation of high-resolution soil moisture from merged model and earth observation data in the Great Britain," *Remote Sens. Environ.*, vol. 264, Oct. 2021, Art. no. 112610. [Online]. Available: <https://www.sciencedirect.com/science/article/pii/S0034425721003308>
- [8] J. Peng, A. Loew, O. Merlin, and N. E. C. Verhoest, "A review of spatial downscaling of satellite remotely sensed soil moisture," *Rev. Geophys.*, vol. 55, no. 2, pp. 341–366, 2017. [Online]. Available: <https://onlinelibrary.wiley.com/doi/abs/10.1002/2016RG000543>
- [9] J. Peng, A. Loew, S. Zhang, J. Wang, and J. Niesel, "Spatial downscaling of satellite soil moisture data using a vegetation temperature condition index," *IEEE Trans. Geosci. Remote Sens.*, vol. 54, no. 1, pp. 558–566, Jan. 2016.
- [10] B. Bauer-Marschallinger et al., "Toward global soil moisture monitoring with Sentinel-1: Harnessing assets and overcoming obstacles," *IEEE Trans. Geosci. Remote Sens.*, vol. 57, no. 1, pp. 520–539, Jan. 2019.
- [11] N. N. Das et al., "The SMAP and copernicus sentinel 1 A/B microwave active-passive high resolution surface soil moisture product," *Remote Sens. Environ.*, vol. 233, Nov. 2019, Art. no. 111380. [Online]. Available: <https://www.sciencedirect.com/science/article/pii/S0034425719303992>
- [12] T. Ramsauer, T. Weiß, and P. Marzahn, "RADOLAN\_API - A soil moisture data set derived from weather radar data," Apr. 2021. [Online]. Available: <https://zenodo.org/record/4588904>
- [13] P. Rao, Y. Wang, F. Wang, Y. Liu, X. Wang, and Z. Wang, "Daily soil moisture mapping at 1 km resolution based on SMAP data for desertification areas in northern China," *Earth Syst. Sci. Data*, vol. 14, no. 7, pp. 3053–3073, Jul. 2022. [Online]. Available: <https://essd.copernicus.org/articles/14/3053/2022/>
- [14] T. Jagdhuber, I. Hajnsek, and K. P. Papathanassiou, "Refined soil moisture estimation by means of L-band polarimetry," in *2013 IEEE Int. Geosci. Remote Sens. Symp. - IGARSS*, Jul. 2013, pp. 2325–2328.
- [15] S. H. Alemohammad, T. Jagdhuber, M. Moghaddam, and D. Entekhabi, "Soil and vegetation scattering contributions in L-band and P-band polarimetric SAR observations," *IEEE Trans. Geosci. Remote Sens.*, vol. 57, no. 11, pp. 8417–8429, Nov. 2019.
- [16] X. Huang, B. Ziniti, M. H. Cosh, M. Reba, J. Wang, and N. Torbick, "Field-scale soil moisture retrieval using PALSAR-2 polarimetric decomposition and machine learning," *Agronomy*, vol. 11, no. 1, Jan. 2021, Art. no. 35. [Online]. Available: <https://www.mdpi.com/2073-4395/11/1/35>
- [17] N. S. Chauhan, S. Miller, and P. Ardanuy, "Spaceborne soil moisture estimation at high resolution: A microwave-optical/IR synergistic approach," *Int. J. Remote Sens.*, vol. 24, no. 22, pp. 4599–4622, Jan. 2003, doi: 10.1080/0143116031000156837.
- [18] A. Loew and W. Mauser, "On the disaggregation of passive microwave soil moisture data using a priori knowledge of temporally persistent soil moisture fields," *IEEE Trans. Geosci. Remote Sens.*, vol. 46, no. 3, pp. 819–834, Mar. 2008.
- [19] M. El Hajj, N. Baghdadi, M. Zribi, and H. Bazzi, "Synergic use of Sentinel-1 and Sentinel-2 images for operational soil moisture mapping at high spatial resolution over agricultural areas," *Remote Sens.*, vol. 9, no. 12, Dec. 2017, Art. no. 1292. [Online]. Available: <https://www.mdpi.com/2072-4292/9/12/1292>
- [20] T. Weiß, T. Ramsauer, A. Löw, and P. Marzahn, "Evaluation of different radiative transfer models for microwave backscatter estimation of wheat fields," *Remote Sens.*, vol. 12, no. 18, Jan. 2020, Art. no. 3037. [Online]. Available: <https://www.mdpi.com/2072-4292/12/18/3037>
- [21] M. Neelam and B. P. Mohanty, "On the radiative transfer model for soil moisture across space, time and hydro-climates," *Remote Sens.*, vol. 12, no. 16, Jan. 2020, Art. no. 2645. [Online]. Available: <https://www.mdpi.com/2072-4292/12/16/2645>
- [22] M. Owe, R. de Jeu, and J. Walker, "A methodology for surface soil moisture and vegetation optical depth retrieval using the microwave polarization difference index," *IEEE Trans. Geosci. Remote Sens.*, vol. 39, no. 8, pp. 1643–1654, Aug. 2001.
- [23] G. J. M. D. Lamoy, R. H. Reichle, and V. R. N. Pauwels, "Global calibration of the GEOS-5 L-band microwave radiative transfer model over nonfrozen land using SMOS observations," *J. Hydrometeorol.*, vol. 14, no. 3, pp. 765–785, Jun. 2013.
- [24] Y. Oh, K. Sarabandi, and F. Ulaby, "An empirical model and an inversion technique for radar scattering from bare soil surfaces," *IEEE Trans. Geosci. Remote Sens.*, vol. 30, no. 2, pp. 370–381, Mar. 1992.
- [25] Y. Oh, "Quantitative retrieval of soil moisture content and surface roughness from multipolarized radar observations of bare soil surfaces," *IEEE Trans. Geosci. Remote Sens.*, vol. 42, no. 3, pp. 596–601, Mar. 2004.
- [26] P. Dubois, J. van Zyl, and T. Engman, "Measuring soil moisture with imaging radars," *IEEE Trans. Geosci. Remote Sens.*, vol. 33, no. 4, pp. 915–926, Jul. 1995.
- [27] A. Fung, W. Liu, K. Chen, and M. Tsay, "An improved iem model for bistatic scattering from rough surfaces," *J. Electromagn. Waves Appl.*, vol. 16, no. 5, pp. 689–702, Jan. 2002. [Online]. Available: <https://www.tandfonline.com/doi/full/10.1163/156939302X01119>
- [28] N. Baghdadi et al., "Potential of Sentinel-1 images for estimating the soil roughness over bare agricultural soils," *Water*, vol. 10, no. 2, Feb. 2018, Art. no. 131. [Online]. Available: <https://www.mdpi.com/2073-4441/10/2/131>
- [29] E. P. W. Attema and F. T. Ulaby, "Vegetation modeled as a water cloud," *Radio Sci.*, vol. 13, no. 2, pp. 357–364, Mar. 1978.
- [30] R. de Roo, Y. Du, F. Ulaby, and M. Dobson, "A semi-empirical backscattering model at L-band and C-band for a soybean canopy with soil moisture inversion," *IEEE Trans. Geosci. Remote Sens.*, vol. 39, no. 4, pp. 864–872, Apr. 2001.
- [31] F. T. Ulaby and D. G. Long, *Microwave Radar and Radiometric Remote Sensing*. Ann Arbor, MI, USA: Univ. Michigan Press, 2014.
- [32] C. Ma, X. Li, and M. F. McCabe, "Retrieval of high-resolution soil moisture through combination of Sentinel-1 and Sentinel-2 data," *Remote Sens.*, vol. 12, no. 14, Jan. 2020, Art. no. 2303. [Online]. Available: <https://www.mdpi.com/2072-4292/12/14/2303>
- [33] M. El Hajj, N. Baghdadi, H. Bazzi, and M. Zribi, "Penetration analysis of SAR signals in the C and L bands for wheat, maize, and grasslands," *Remote Sens.*, vol. 11, no. 1, Jan. 2019, Art. no. 31. [Online]. Available: <https://www.mdpi.com/2072-4292/11/1/31>
- [34] H. Bazzi et al., "Detecting irrigation events over semi-arid and temperate climatic areas using Sentinel-1 data: Case of several summer crops," *Agronomy*, vol. 12, no. 11, Nov. 2022, Art. no. 2725. [Online]. Available: <https://www.mdpi.com/2073-4395/12/11/2725>
- [35] T. Meyer et al., "Estimating gravimetric water content of a winter wheat field from L-band vegetation optical depth," *Remote Sens.*, vol. 11, no. 20, Jan. 2019, Art. no. 2353. [Online]. Available: <https://www.mdpi.com/2072-4292/11/20/2353>
- [36] M. H. Cosh et al., "Estimating vegetation water content during the Soil Moisture Active Passive Validation Experiment 2016," *J. Appl. Remote Sens.*, vol. 13, no. 1, Feb. 2019, Art. no. 014516.
- [37] F. Frappart et al., "Global monitoring of the vegetation dynamics from the vegetation optical depth (VOD): A review," *Remote Sens.*, vol. 12, no. 18, Jan. 2020, Art. no. 2915. [Online]. Available: <https://www.mdpi.com/2072-4292/12/18/2915>
- [38] E. M. Perry, E. M. Morse-McNabb, J. G. Nuttall, G. J. O'Leary, and R. Clark, "Managing wheat from space: Linking MODIS NDVI and crop models for predicting Australian dryland wheat biomass," *IEEE J. Sel. Topics Appl. Earth Observ. Remote Sens.*, vol. 7, no. 9, pp. 3724–3731, Sep. 2014.
- [39] Y. Gao, J. P. Walker, M. Allahmoradi, A. Moneris, D. Ryu, and T. J. Jackson, "Optical sensing of vegetation water content: A synthesis study," *IEEE J. Sel. Topics Appl. Earth Observ. Remote Sens.*, vol. 8, no. 4, pp. 1456–1464, Apr. 2015.
- [40] X.-P. Song, W. Huang, M. C. Hansen, and P. Potapov, "An evaluation of landsat, Sentinel-2, Sentinel-1 and MODIS data for crop type mapping," *Sci. Remote Sens.*, vol. 3, Jun. 2021, Art. no. 100018. [Online]. Available: <https://www.sciencedirect.com/science/article/pii/S2666017221000055>
- [41] Q. Gao, M. Zribi, M. J. Escorihuela, and N. Baghdadi, "Synergic use of Sentinel-1 and Sentinel-2 data for soil moisture mapping at 100 m resolution," *Sensors*, vol. 17, no. 9, Sep. 2017, Art. no. 1966. [Online]. Available: <https://www.mdpi.com/1424-8220/17/9/1966>
- [42] F. Mattia et al., "Sentinel-1 & Sentinel-2 for SOIL moisture retrieval at field scale," in *2018 IEEE Int. Geosci. Remote Sens. Symp.*, Jul. 2018, pp. 6143–6146.
- [43] M. Woche, K. Berger, M. Danner, W. Mauser, and T. Hank, "Physically-based retrieval of canopy equivalent water thickness using hyperspectral data," *Remote Sens.*, vol. 10, no. 12, 2018, Art. no. 1924.
- [44] M. Danner, K. Berger, M. Woche, W. Mauser, and T. Hank, "Fitted PROSAIL parameterization of leaf inclinations, water content and brown pigment content for winter wheat and maize canopies," *Remote Sens.*, vol. 11, no. 10, 2019, Art. no. 1150.
- [45] T. Weiß and T. Fincke, "SenSARP: A pipeline to pre-process Sentinel-1 SLC data by using ESA SNAP Sentinel-1 toolbox," *J. Open Source Softw.*, vol. 7, no. 69, Jan. 2022, Art. no. 3337. [Online]. Available: <https://joss.theofig.org/papers/10.21105/joss.03337>
- [46] M. El Hajj et al., "Soil moisture retrieval over irrigated grassland using X-band SAR data," *Remote Sens. Environ.*, vol. 176, pp. 202–218, Apr. 2016. [Online]. Available: <http://www.sciencedirect.com/science/article/pii/S0034425716300281>

- [47] N. Baghdadi, M. El Hajj, M. Zribi, and S. Bousbih, "Calibration of the water cloud model at C-band for winter crop fields and grasslands," *Remote Sens.*, vol. 9, no. 9, Sep. 2017, Art. no. 969. [Online]. Available: <https://www.mdpi.com/2072-4292/9/9/969>
- [48] E. Vermote, D. Tanre, J. Deuze, M. Herman, and J.-J. Morcrette, "Second simulation of the satellite signal in the solar spectrum, 6S: An overview," *IEEE Trans. Geosci. Remote Sens.*, vol. 35, no. 3, pp. 675–686, May 1997.
- [49] R. T. Wilson, "Py6S: A python interface to the 6S radiative transfer model," *Comput. Geosci.*, vol. 51, pp. 166–171, Feb. 2013. [Online]. Available: <https://www.sciencedirect.com/science/article/pii/S0098300412002798>
- [50] T. Ramsauer, T. Weiß, A. Löw, and P. Marzahn, "RADOLAN\_API: An hourly soil moisture data set based on weather radar, soil properties and reanalysis temperature data," *Remote Sens.*, vol. 13, no. 9, Jan. 2021, Art. no. 1712. [Online]. Available: <https://www.mdpi.com/2072-4292/13/9/1712>
- [51] H. Bartels, "Projekt RADOLAN. Routineverfahren zur Online-A neichung der Radarniederschlagsdaten mit Hilfe von Automatischen Boden-niederschlagsstationen (Ombrometer)," Deutscher Wetterdienst, Offenbach, Germany, Tech. Rep., 2004.
- [52] T. Winterrath et al., "An overview of the new radar-based precipitation climatology of the Deutscher Wetterdienst—data, methods, products," in *Proc. 11th Int. Workshop Precipitation Urban Areas Rainfall Monit. Modelling Forecasting Urban Environ.*, ETH Zurich, Institute of Environmental Engineering, 2019, pp. 132–137. [Online]. Available: <https://www.research-collection.ethz.ch/handle/20.500.11850/347607>
- [53] M. A. Kohler and R. K. Linsley, *Predicting the Runoff from Storm Rainfall* vol. 30, US Department of Commerce, Weather Bureau, 1951.
- [54] T. Hengl et al., "SoilGrids250 m: Global gridded soil information based on machine learning," *PLoS One*, vol. 12, no. 2, Feb. 2017, Art. no. e0169748, doi: [10.1371/journal.pone.0169748](https://doi.org/10.1371/journal.pone.0169748).
- [55] European Environment Agency, "CORINE land cover 2018," 2018. [Online]. Available: <https://land.copernicus.eu/pan-european/corine-land-cover/clc2018>
- [56] Y. Oh, K. Sarabandi, and F. Ulaby, "Semi-empirical model of the ensemble-averaged differential mueller matrix for microwave backscattering from bare soil surfaces," *IEEE Trans. Geosci. Remote Sens.*, vol. 40, no. 6, pp. 1348–1355, Jun. 2002.
- [57] T. J. Jackson and T. J. Schmugge, "Vegetation effects on the microwave emission of soils," *Remote Sens. Environ.*, vol. 36, no. 3, pp. 203–212, Jun. 1991. [Online]. Available: <https://www.sciencedirect.com/science/article/pii/003442579190057D>
- [58] K. Togliatti, C. Lewis-Beck, V. A. Walker, T. Hartman, A. VanLoocke, and B. K. Hornbuckle, "The B-parameter relating L-VOD to satellite-scale crop plant water may not be constant over a growing season," in *2021 IEEE Int. Geosci. Remote Sens. Symp. IGARSS*, Jul. 2021, pp. 6857–6860.
- [59] T. Hartman, R. Cirone, K. Togliatti, B. K. Hornbuckle, and A. VanLoocke, "A spatial and temporal evaluation of the SMAP cropland b-parameter across the U.S. Corn Belt," *Remote Sens. Environ.*, vol. 297, Nov. 2023, Art. no. 113752. [Online]. Available: <https://www.sciencedirect.com/science/article/pii/S0034425723003036>
- [60] T. Weiß, T. Ramsauer, T. Jagdhuber, A. Löw, and P. Marzahn, "Sentinel-1 backscatter analysis and radiative transfer modeling of dense winter wheat time series," *Remote Sens.*, vol. 13, no. 12, Jan. 2021, Art. no. 2320. [Online]. Available: <https://www.mdpi.com/2072-4292/13/12/2320>
- [61] T. J. Jackson et al., "Vegetation water content mapping using landsat data derived normalized difference water index for corn and soybeans," *Remote Sens. Environ.*, vol. 92, no. 4, pp. 475–482, Sep. 2004. [Online]. Available: <https://www.sciencedirect.com/science/article/pii/S0034425703003353>
- [62] V. Maggioni et al., "A multi-sensor approach for high resolution airborne soil moisture mapping," in *Proc. 30th Hydrol. Water Resour. Symp.*, 2006, pp. 297–302.
- [63] H. Lu, T. Koike, H. Tsutsui, and H. Fujii, "Monitoring vegetation water content by using optical vegetation index and microwave vegetation index: Field experiments and applications," in *2011 IEEE Int. Geosci. Remote Sens. Symp.*, Jul. 2011, pp. 2468–2471.
- [64] SciPy Community, "SciPy: Open source scientific tools for Python," manual, 2024. [Online]. Available: <https://docs.scipy.org/doc/scipy/reference/optimize.minimize-lbfgsb.html#optimize-minimize-lbfgsb>
- [65] P. Lewis et al., "An earth observation land data assimilation system (EO-LDAS)," *Remote Sens. Environ.*, vol. 120, pp. 219–235, May 2012. [Online]. Available: <https://www.sciencedirect.com/science/article/pii/S0034425712000788>
- [66] T. Quaife et al., "Synergistic retrievals of leaf area index and soil moisture from Sentinel-1 and Sentinel-2," *Int. J. Image Data Fusion*, vol. 14, no. 3, pp. 225–242, Dec. 2022, doi: [10.1080/19479832.2022.2149629](https://doi.org/10.1080/19479832.2022.2149629).
- [67] U. Meier et al., "The BBCH system to coding the phenological growth stages of plants—history and publications," *J. für Kulturpflanzen*, vol. 61, no. 2, pp. 41–52, Feb. 2009. [Online]. Available: <https://ojs.openagrar.de/index.php/Kulturpflanzenjournal/article/view/12142>
- [68] J. Peng et al., "A roadmap for high-resolution satellite soil moisture applications—confronting product characteristics with user requirements," *Remote Sens. Environ.*, vol. 252, Jan. 2021, Art. no. 112162. [Online]. Available: <https://www.sciencedirect.com/science/article/pii/S0034425720305356>
- [69] S. Nativel et al., "Hybrid methodology using Sentinel-1/Sentinel-2 for soil moisture estimation," *Remote Sens.*, vol. 14, no. 10, Jan. 2022, Art. no. 2434. [Online]. Available: <https://www.mdpi.com/2072-4292/14/10/2434>
- [70] H. Bazzi et al., "Retrieving soil moisture from Sentinel-1: Limitations over certain crops and sensitivity to the first soil thin layer," *Water*, vol. 16, no. 1, Jan. 2024, Art. no. 40. [Online]. Available: <https://www.mdpi.com/2073-4441/16/1/40>
- [71] A. G. Konings, M. Piles, K. Rötzer, K. A. McColl, S. K. Chan, and D. Entekhabi, "Vegetation optical depth and scattering albedo retrieval using time series of dual-polarized L-band radiometer observations," *Remote Sens. Environ.*, vol. 172, pp. 178–189, Jan. 2016. [Online]. Available: <https://www.sciencedirect.com/science/article/pii/S003442571530198X>
- [72] T. Jagdhuber et al., "Physics-based modeling of active-passive microwave covariations for geophysical retrievals," in *2018 IEEE Int. Geosci. Remote Sens. Symp.*, Jul. 2018, pp. 250–253.
- [73] M. H. Cosh, J. Tao, T. J. Jackson, L. McKee, and P. E. O'Neill, "Vegetation water content mapping in a diverse agricultural landscape: National Airborne Field Experiment 2006," *J. Appl. Remote Sens.*, vol. 4, no. 1, 2010, Art. no. 043532. [Online]. Available: <https://handle.nal.usda.gov/10113/56319>
- [74] O. Erenstein, M. Jaleta, K. A. Mottaleb, K. Sonder, J. Donovan, and H.-J. Braun, "Global Trends in Wheat Production, Consumption and Trade," in *Wheat Improvement: Food Security in a Changing Climate*, Cham, Switzerland: Springer International Publishing, 2022, pp. 47–66.
- [75] L. Tao, G. Wang, X. Chen, J. Li, and Q. Cai, "Estimation of soil moisture using a vegetation scattering model in wheat fields," *J. Appl. Remote Sens.*, vol. 13, no. 4, Oct. 2019, Art. no. 044503.
- [76] D. Mengen, T. Jagdhuber, A. Balenzano, F. Mattia, H. Vereecken, and C. Montzka, "High spatial and temporal soil moisture retrieval in agricultural areas using multi-orbit and vegetation adapted Sentinel-1 SAR time series," *Remote Sens.*, vol. 15, no. 9, Jan. 2023, Art. no. 2282. [Online]. Available: <https://www.mdpi.com/2072-4292/15/9/2282>
- [77] S.-B. Kim and T.-H. Liao, "Robust retrieval of soil moisture at field scale across wide-ranging SAR incidence angles for soybean, wheat, forage, oat and grass," *Remote Sens. Environ.*, vol. 266, Dec. 2021, Art. no. 112712. [Online]. Available: <https://www.sciencedirect.com/science/article/pii/S0034425721004326>
- [78] T. Ramsauer and P. Marzahn, "Global soil moisture estimation based on GPM IMERG data using a site specific adjusted antecedent precipitation index," *Int. J. Remote Sens.*, vol. 44, no. 2, pp. 542–566, Jan. 2023, doi: [10.1080/01431161.2022.2162351](https://doi.org/10.1080/01431161.2022.2162351).
- [79] G. Portal et al., "Assessment of multi-scale SMOS and SMAP soil moisture products across the iberian peninsula," *Remote Sens.*, vol. 12, no. 3, Jan. 2020, Art. no. 570. [Online]. Available: <https://www.mdpi.com/2072-4292/12/3/570>
- [80] J. Szturek, K. Osródko, A. Jurczyk, and L. Jelonek, "Concept of dealing with uncertainty in radar-based data for hydrological purpose," *Natural Hazards Earth Syst. Sci.*, vol. 8, no. 2, pp. 267–279, Mar. 2008. [Online]. Available: <https://hal.archives-ouvertes.fr/hal-00299505>
- [81] Y. Barton, I. V. Sideris, T. H. Raupach, M. Gabella, U. Germann, and O. Martius, "A multi-year assessment of sub-hourly gridded precipitation for Switzerland based on a blended radar–rain-gauge dataset," *Int. J. Climatol.*, vol. 40, no. 12, pp. 5208–5222, 2020. [Online]. Available: <https://onlinelibrary.wiley.com/doi/abs/10.1002/joc.6514>
- [82] G. Schoener and M. C. Stone, "Monitoring soil moisture at the catchment scale—A novel approach combining antecedent precipitation index and radar-derived rainfall data," *J. Hydrol.*, vol. 589, Oct. 2020, Art. no. 125155. [Online]. Available: <https://www.sciencedirect.com/science/article/pii/S0022169420306156>
- [83] O. Erenstein, J. Chamberlin, and K. Sonder, "Estimating the global number and distribution of maize and wheat farms," *Glob. Food Secur.*, vol. 30, Sep. 2021, Art. no. 100558. [Online]. Available: <https://www.sciencedirect.com/science/article/pii/S2211912421000675>
- [84] T. Jagdhuber, "Soil parameter retrieval under vegetation cover using SAR polarimetry," PhD Thesis, Fac. Math. Nat. Sci., Univ. Potsdam, Potsdam, Germany, 2012.

- [85] H.S. Srivastava, P. Patel, and R. R. Navalgund, "How far SAR has fulfilled its expectation for soil moisture retrieval," in *Microwave Remote Sensing of the Atmosphere and Environment V*, vol. 6410. Bellingham, WA, USA: SPIE, Dec. 2006, Art. no. 641001. [Online]. Available: <https://www.spiedigitallibrary.org/conference-proceedings-of-spie/6410/641001/How-far-SAR-has-fulfilled-its-expectation-for-soil-moisture/10.1117/12.693946.full>
- [86] J. Bouchat, E. Tronquo, A. Orban, X. Neyt, N. E. C. Verhoest, and P. Defourny, "Green area index and soil moisture retrieval in maize fields using multi-polarized C- and L-band SAR data and the water cloud model," *Remote Sens.*, vol. 14, no. 10, Jan. 2022, Art. no. 2496. [Online]. Available: <https://www.mdpi.com/2072-4292/14/10/2496>
- [87] A. T. Joseph, R. van der Velde, P. E. O'Neill, R. Lang, and T. Gish, "Effects of corn on c- and l-band radar backscatter: A correction method for soil moisture retrieval," *Remote Sens. Environ.*, vol. 114, no. 11, pp. 2417–2430, Nov. 2010. [Online]. Available: <https://www.sciencedirect.com/science/article/pii/S0034425710001641>
- [88] L. He, L. Tong, Y. Li, Y. Chen, L. Tan, and C. Guo, "Polarimetric analysis of radar backscatter from ground-based scatterometers and wheat biomass monitoring with advanced synthetic aperture radar images," *J. Appl. Remote Sens.*, vol. 10, no. 2, Apr. 2016, Art. no. 026008.
- [89] F. Mattia et al., "Multitemporal C-band radar measurements on wheat fields," *IEEE Trans. Geosci. Remote Sens.*, vol. 41, no. 7, pp. 1551–1560, Jul. 2003.
- [90] M. Zribi et al., "Analysis of L-band SAR data for soil moisture estimations over agricultural areas in the tropics," *Remote Sens.*, vol. 11, no. 9, Jan. 2019, Art. no. 1122. [Online]. Available: <https://www.mdpi.com/2072-4292/11/9/1122>
- [91] K. Kellogg et al., "NASA-ISRO synthetic aperture radar (NISAR) mission," in *IEEE Aerosp. Conf.*, Mar. 2020, pp. 1–21.
- [92] J. Inglada, A. Vincent, M. Arias, B. Tardy, D. Morin, and I. Rodes, "Operational high resolution land cover map production at the country scale using satellite image time series," *Remote Sens.*, vol. 9, no. 1, Jan. 2017, Art. no. 95. [Online]. Available: <https://www.mdpi.com/2072-4292/9/1/95>
- [93] A. Orynbaikyzy, U. Gessner, B. Mack, and C. Conrad, "Crop type classification using fusion of Sentinel-1 and Sentinel-2 data: Assessing the impact of feature selection, optical data availability, and parcel sizes on the accuracies," *Remote Sens.*, vol. 12, no. 17, Jan. 2020, Art. no. 2779. [Online]. Available: <https://www.mdpi.com/2072-4292/12/17/2779>
- [94] S. Ofori-Ampofo, C. Pelletier, and S. Lang, "Crop type mapping from optical and radar time series using attention-based deep learning," *Remote Sens.*, vol. 13, no. 22, Jan. 2021, Art. no. 4668. [Online]. Available: <https://www.mdpi.com/2072-4292/13/22/4668>
- [95] L. Blickensdörfer, M. Schwieder, D. Pflugmacher, C. Nendel, S. Erasmí, and P. Hostert, "Mapping of crop types and crop sequences with combined time series of Sentinel-1, Sentinel-2 and Landsat 8 data for Germany," *Remote Sens. Environ.*, vol. 269, Feb. 2022, Art. no. 112831. [Online]. Available: <https://www.sciencedirect.com/science/article/pii/S00344257211005514>
- [96] W. W. Verstraeten et al., "Remotely sensed soil moisture integration in an ecosystem carbon flux model. The spatial implication," in *Greenhouse Gas Inventories: Dealing With Uncertainty*, Dordrecht: Netherlands: Springer, 2011, pp. 117–136.
- [97] J. Neupane and W. Guo, "Agronomic basis and strategies for precision water management: A review," *Agronomy*, vol. 9, no. 2, Feb. 2019, Art. no. 87. [Online]. Available: <https://www.mdpi.com/2073-4395/9/2/87>
- [98] P. P. Preetha and A. Z. Al-Hamdan, "Developing nitrate-nitrogen transport models using remotely-sensed geospatial data of soil moisture profiles and wet depositions," *J. Environ. Sci. Health, Part A*, vol. 55, no. 5, pp. 615–628, Apr. 2020, doi: [10.1080/10934529.2020.1724503](https://doi.org/10.1080/10934529.2020.1724503).

**Thomas Weiß** received the B.Sc. degree in geography and the M.Sc. degree in environmental systems and sustainability (physical geography) from Ludwig-Maximilians-Universität (LMU), Munich, Germany, in 2012 and 2015, respectively.

From 2016, he was a Scientific Staff Member with LMU and contributed to several international projects. In 2023, he joined the newly founded Department of Smart Farming, Fraunhofer Institute for Computer Graphics Research (IGD), Rostock, Germany. His main research interests include data assimilation of microwave and optical remote sensing data to derive and monitor bio- and geophysical parameters for agricultural purposes.



**Thomas Jagdhuber** (Senior Member, IEEE) received the Diploma degree in physical geography, physics, remote sensing, and geoinformatics from Ludwig-Maximilians-Universität (LMU), Munich, Germany, and the Technical University Munich (TUM), Munich, in 2006, and the Ph.D. degree in hydrology from the Faculty of Science, University of Potsdam, Potsdam, Germany, in 2012.

Since 2007, he has been with the Microwaves and Radar Institute (HR), German Aerospace Center (DLR), Weßling, Germany. From 2014 to 2023, he

was a Yearly Visiting Scientist with the Massachusetts Institute of Technology (MIT), Boston, MA, USA, contributing to the preparation and continuation of the Soil Moisture Active Passive (SMAP) and SMAP/Sentinel-1 missions. He is also a Lecturer with the University of Jena, Jena, Germany, and the University of Augsburg, Augsburg, Germany. His main research interests include physics-based multisensor data integration with a focus on active and passive microwave interaction theory and polarimetric techniques for hydrological, agricultural, ecological, and cryospheric parameter modeling and estimation.

Dr. Jagdhuber was the recipient of the DLR Science Award for his research on polarimetric SAR decomposition techniques in 2014, and together with Prof. Entekhabi (MIT), he was the co-recipient of the MIT-MISTI Grant for global water cycle and environmental monitoring using active and passive satellite-based microwave instruments. He also serves as a Reviewer for several international journals and conference boards.



**Thomas Ramsauer** received the M.Sc. degree in environmental systems and sustainability (physical geography) from Ludwig-Maximilians-Universität (LMU), Munich, Germany, in 2015.

Optical data streams of multi- and hyperspectral sensors and microwave imagery obtained from satellite or drone platforms, as well as in-situ monitoring and field campaigns, are sources for his monitoring efforts. He participated in several international and national funded remote sensing campaigns and projects. His research interests include the monitoring and interpretation through subsequent time series analysis of high-resolution land surface state variables derived from remotely sensed imagery.

**Alexander Löw** received the M.S. degree in geography and the Ph.D. degree in physical geography from Ludwig-Maximilians-Universität (LMU), Munich, Germany, in 2001 and 2004, respectively.

He was a Full Professor of physical geography and microwave remote sensing with LMU. His research interests included the derivation of quantitative land surface parameters from remote sensing data, the assimilation of remote sensing data into climate and land surface process models, and the evaluation of climate models using observational data.



**Philip Marzahn** received the Diploma degree from the Christian-Albrechts University of Kiel, Kiel, Germany, where he studied geography, soil science, hydrology, and landscape ecology, in 2007, the Ph.D. degree in physical geography from the Faculty of Geoscience, Ludwig-Maximilians-Universität (LMU), Munich, Germany, in 2013, and the Habilitation degree in physical geography, in 2021, respectively.

Since 2021, he is a Full Professor for geodesy and geoinformatics with the Department of Agricultural and Environmental Sciences. His research interests include the monitoring of bio- and geophysical parameters from multidimensional SAR and optical data., the uncertainty assessment of such variables, and the retrieval of parameters from remote sensing data across scales using spaceborne, airborne, and drone data in conjunction with wireless sensor networks.

Dr. Marzahn is a frequent Reviewer for international remote sensing journals. He has participated in several international and national funded remote sensing campaigns and projects.

## 3.6 Usage of Publication IV and V (Python software packages) within Publication I, II and III

Currently, various remote sensing data are publicly available free of charge. Nevertheless, before remote sensing data can be utilized in different applications and models, additional processing steps are often required. Within the Sentinel-1 C-band Level-1 SLC data provided by the ESA, geometric and radiometric distortions due to the specific imaging geometry of the radar system are still present. Thus, before the data can be employed by RT models, various preprocessing steps must be applied to make the data usable.

To address this, the Python code from Publication IV offers an automated preprocessing pipeline to correct for geometric and radiometric distortions, ultimately producing a time series of Sentinel-1 images with sigma naught backscatter values. These sigma naught backscatter values are subsequently utilized in Publications I, II, and III as input data for the analyzed RT models. The open-source Python package SenSARP (Publication IV) is available on GitHub, enabling other researchers to employ an automated pipeline for Sentinel-1 data processing. Furthermore, SenSARP is part of the MULTIPLY platform, which allows for the retrieval of biophysical parameters from microwave and optical remote sensing sensors for various agricultural areas. End users of the MULTIPLY platform do not need any expertise in preprocessing microwave or optical data but can instead focus on retrieving the desired biophysical parameters.

The open-source Python package SenSE (Publication V) is also available on GitHub. SenSE encompasses existing microwave RT models for surface and vegetation scattering. The main advantage of SenSE is its ability to easily combine different surface and vegetation models, allowing for various model combinations to be utilized, adjusted, and analyzed. Since RT models are crucial for retrieving biophysical parameters, the scientific community will benefit from an easy-to-use Python package like SenSE, where the primary RT models are implemented and ready for use. This enables researchers to concentrate on data analysis and improving retrieval results, rather than spending valuable time translating existing RT model equations into programming code. The scientific publications I, II, and III heavily rely on the RT models implemented in the open-source Python package SenSE.

Although the quality of individual researchers is primarily assessed by their contributions and the impact of scientific research papers such as Publications I, II, and III, the production and publication of the utilized software code may be equally important. Without the development of scientific software code, the research quality or even the fundamental conclusions of many scientific publications would not be feasible.

## 3.7 Publication IV: SenSARP - A pipeline to pre-process Sentinel-1 SLC data by using ESA SNAP Sentinel-1 Toolbox

**Reference:** Weiß, T., Fincke, T., 2022. SenSARP: A pipeline to pre-process Sentinel-1 SLC data by using ESA SNAP Sentinel-1 Toolbox. *Journal of Open Source Software* 7, 3337. doi:10.21105/joss.03337

**Status:** published

**Plain language summary:** Sentinel-1 satellites will provide continuous, freely available microwave remote sensing data of the entire globe at least until the end of 2030. Nevertheless, before Sentinel-1 Level-1 SLC data can be utilized in applications, preprocessing is required to address the geometric and radiometric distortions present in the data. Although Sentinel-1 satellite data and processing software are freely available, the usage of this data is primarily limited to expert users in the field of microwave remote sensing.

SenSARP was developed to offer a user-friendly, push-button option for applying a rigorous preprocessing pipeline with sensible defaults to Sentinel-1 Level-1 SLC time series data, as well as to individual Sentinel-1 Level-1 SLC images. This enables non-expert users to utilize radiometrically and geometrically corrected sigma naught backscatter data for their specific applications. Expert users can further extend the functionalities of SenSARP and customize their preprocessing pipeline to better suit their respective research purposes.

**Author contributions:** Conceptualization, T.W.; Methodology, T.W.; Software writing, T.W. and T.F.; Writing-original draft preparation, T.W.; Writing-review and editing, T.W. and T.F.

**Journal:** Journal of Open Source Software (JOSS)

**Repository:** <https://github.com/multiply-org/sar-pre-processing>

**Documentation:** <https://multiply-sar-pre-processing.readthedocs.io/en/latest/>

# SenSARP: A pipeline to pre-process Sentinel-1 SLC data by using ESA SNAP Sentinel-1 Toolbox

Thomas Weiß<sup>1</sup> and Tonio Fincke<sup>2</sup>

DOI: [10.21105/joss.03337](https://doi.org/10.21105/joss.03337)

## Software

- [Review](#) ↗
- [Repository](#) ↗
- [Archive](#) ↗

---

Editor: [Pierre de Buyl](#) ↗

## Reviewers:

- [@arthur-e](#)
- [@danclewley](#)

Submitted: 20 April 2021

Published: 29 January 2022

## License

Authors of papers retain copyright and release the work under a Creative Commons Attribution 4.0 International License ([CC BY 4.0](#)).

<sup>1</sup> Department of Geography, Ludwig-Maximilians-Universität München, 80333 Munich, Germany <sup>2</sup> Brockmann Consult GmbH, 21029 Hamburg, Germany;

## Summary

The Sentinel-1 mission consists of two polar-orbiting satellites acquiring Synthetic Aperture Radar data (SAR) at C-band (frequency of 5.405 GHz) with a revisit time of 6 days. The SAR data is distributed free of charge via the Copernicus Open Access Hub (<https://scihub.copernicus.eu/>) by European Space Agency (ESA) and the European Commission. Large archives are also provided by Data and Information Access Services (DIAS) which serve the purpose to facilitate the access and use of Sentinel Data. Due to the specific imaging geometry of the radar system, the acquired radar data contains different radiometric and geometric distortions. The radiometric quality is affected by spreading loss effect, the non-uniform antenna pattern, possible gain changes, saturation, and speckle noise. Geometric distortions such as foreshortening, layover or shadowing effects are based on the side looking radar acquisition system. To account for these radiometric and geometric distortions, the Sentinel-1 Level 1 data has to be corrected radiometrically and geometrically before the data can be used for further analysis or within third party applications. Therefore, either an automatic or manual pre-processing of Sentinel-1 images is needed.

## Statement of need

Sentinel-1 satellites will provide continuous free available microwave remote sensing data of the entire globe at least until the end of 2030. Furthermore, ESA is not only providing Sentinel satellite images (e.g., Sentinel-1, Sentinel-2, Sentinel-3) but they also developed free open source toolboxes (Sentinel-1, 2, 3 toolboxes) for scientific exploitation. The toolboxes can be accessed and used via the Sentinel Application Platform (SNAP). SNAP offers a graphical interface where expert users can develop different processing schemes and apply them on the satellite images. Although, Sentinel-1 satellite data and a processing software are freely available, the usage of the data is mainly limited to expert users in the field of microwave remote sensing as different pre-processing steps need to be applied before using Sentinel-1 images.

SenSARP was developed to provide a push-button option to easily apply a rigid pre-processing pipeline with sensible defaults to a Sentinel-1 Level 1 SLC time series data as well as single Sentinel-1 Level 1 SLC images. Thus, non-expert users in the field of pre-processing microwave data are able to use radiometric and geometric corrected sigma nought backscatter data for their specific applications. Beside a rigid pre-processing pipeline, SenSARP provides filter options to retrieve only images of a specific year or images that contain a specific area of interest from a stack of downloaded Sentinel-1 data. Furthermore, the default processing scheme of SenSARP can handle if an area of interest is contained in two tiles of the same swath (due to storage reasons data of one Sentinel-1 satellite swath is provided by ESA within different tiles). Additionally, SenSARP checks if within a stack of Sentinel-1 images, one specific image was multiple processed by ESA and uses the newest.

For expert users, SenSARP provides the possibility to automate their pre-processing on a

large scale by either modifying the default pre-processing scheme (modification of xml graph `pre_processing_step1.xml`) or create their own pre-processing scheme (create a new xml graph) with the graph builder of the SNAP software. They can benefit from the filter options, the default pre-processing step 2 (co-registration of images) and the SenSARP functions to stack all processed and co-registered images within a netCDF file with additional image information e.g., satellite name, relative orbit, and orbit direction.

## Method

This Python package generates a file list of to be processed Sentinel-1 images (already downloaded and stored in a specific folder) based on different user defined criteria (specific year, area of interest). Additionally, specific cases of repeatedly processed data are handled, as sometimes Sentinel-1 data were initially processed multiple times and stored under similar names on the Copernicus Open Access Hub. Also, cases where Sentinel-1 data within the user-defined area of interest might be stored in consecutive tiles are considered.

Based on the generated file list the default processing pipeline of the Python package applies a pre-processing chain to Sentinel-1 Single Look Complex (SLC) time series or single images to generate radiometrically and geometrically corrected sigma nought backscatter values. Furthermore, if a time series is processed the images are co-registered and additional output files of multi-temporal speckle filtered data are generated. In addition, a single speckle filter instead of a multi-temporal one is applied as well and the output will be stored as a separate layer. To pre-process the images, the Python package uses the GPT (Graph Processing Tool) of SNAP to execute different operators provided by the Sentinel-1 Toolbox. The Sentinel Toolbox is available for download at <http://step.esa.int/>, its source code is available in the `senbox-org` organization on GitHub. Each of these operators performs a pre-processing step. The operators can be chained together to form a graph, which is used by the Python package to run on the Sentinel-1 data using the Graph Processing Framework (GPF). The graphs are stored in xml-files. Users may change the graphs by modifying the files directly or via the Sentinel Toolbox. User Guides to show how the GPF can be used are provided here: <https://senbox.atlassian.net/wiki/spaces/SNAP/pages/70503053/Processing>.

After the pre-processing the resulting radiometrically and geometrically corrected images are stored for further usage within a NetCDF4 stack file. The processing workflow was developed and optimized to use a Sentinel-1 time series of pre-processed sigma nought backscatter values to retrieve biophysical land surface parameters by the use of radiative transfer models. The sigma nought backscatter values provided by the default workflow of SenSARP might be used in other applications like flood risk analysis, monitoring land cover changes or monitoring global food security but it has to be mentioned that different applications have different demands and therefore, slight adjustments of the default workflow might be required. In the future, many more new products and operational third party services based on consistent Sentinel-1 time series might be developed.

## Applications

This Python package was developed within the Horizon 2020 project called MULTIscale SENTINEL land surface information retrieval Platform (MULTIPLY) (<http://www.multiply-h2020.eu/>, <https://cordis.europa.eu/project/id/687320>, <https://multiply.obs-website.eu-de.otc.t-systems.com>). Furthermore, data processed by this package is used within Sentinel-Synergy-Study S3 project (<https://www.researchgate.net/project/Sentinel-Synergy-Study-S3>). In addition, the Python code was used to process Sentinel-1 time series images for the detection and analysis of temporary flooded vegetation (Tsyganskaya et al., 2018, 2019) and for the evaluation of different radiative transfer models for microwave backscatter estimation of wheat fields (Weiß et al., 2020).

## Other available Python software packages using ESA's SNAP software to pre-process SAR data

The ESA's SNAP toolbox has been written in Java. For Python users the developers provide a Python interface called Snappy. However, the Snappy interface is lacking in terms of installation, processing performance and usability. Hence, the remote sensing community developed different wrappers (e.g., SenSARP, snapista or pyroSAR) to use SNAP processing functionalities by utilizing the SNAP Graph Processing Tool (GPT).

### snapista

Snapista (<https://snap-contrib.github.io/snapista/index.html>) targets mainly experts remote sensing users with Python programming skills. It provides access to the processing operators of all toolboxes (e.g., Sentinel-1, Sentinel-2 or Sentinel-3) within SNAP. Expert users can generate processing graphs and execute their generated graphs in a pure Pythonic way. Guidelines about which processing steps are needed for different applications, or about which processing steps can or have to be combined, are not provided yet. Establishing guidelines about how to process different satellite data for different applications is not an easy task to do and would exceed the goal of snapista as a Python wrapper for the SNAP software. Summarizing, snapista provides access to all SNAP toolboxes (not just to Sentinel-1 Toolbox) via Python. But as it provides no default processing chains, snapista will be primarily usable by expert remote sensing users. The advantage of snapista is the accessibility of processing operators for SAR and optical data.

### pyroSAR

PyroSAR (<https://pyrosar.readthedocs.io/en/latest/index.html>) is a Python library which provides a Python wrapper to SAR pre-processing software SNAP and GAMMA (Wegnüller et al., 2016; Werner et al., 2000). The library provides utilities to read and store metadata information of downloaded satellite data within a database. Furthermore, pyroSAR provides access to processing operators of SNAP and GAMMA. A default workflow with different user options is provided to process single or time-series Sentinel-1 images. After executing the default processing workflow radiometric and geometric corrected gamma nought backscatter data are provided in Geotiff format (Truckenbrodt et al., 2019). The processed images can also be stored within an Open Data Cube. For expert users which might want to use a different processing workflow pyroSAR provides an option to create SNAP xml-workflows and execute them with the GPT. Summarizing, pyroSAR provides a similar push-button option to process Sentinel-1 data with a slightly different default workflow (pyroSAR: no temporal speckle filter, gamma nought backscatter output in Geotiff format) than SenSARP (SenSARP: temporal speckle filter, sigma nought backscatter output in netCDF format). PyroSAR, as a more complex library than SenSARP, provides on the one hand more changeable parameters within the processing workflow but on the other hand the usability for non-expert users might be narrowed compared to SenSARP. An advantage of SenSARP, especially for non-expert users, might be the provision of background information (theory/purpose) of the different pre-processing steps within the documentation.

## Acknowledgements

The project leading to this application has received funding from the European Union's Horizon 2020 research and innovation program under Grant Agreement No. 687320. We would like to thank Alexander Löw and Philip Marzahn for guiding discussions that lead to this publication. We also would like to thank Thomas Ramsauer for discussions and suggestions. The author also wishes to thank the reviewers and editors for their efforts and for their helpful comments to improve this paper and the software package.

## References

- Truckenbrodt, J., Cremer, F., Baris, I., Glaser, F., & Eberle, J. (2019). *pyroSAR - a Python Framework for Large-Scale SAR Satellite Data Processing*. <https://elib.dlr.de/133267/>
- Tsyganskaya, V., Martinis, S., & Marzahn, P. (2019). Flood Monitoring in Vegetated Areas Using Multitemporal Sentinel-1 Data: Impact of Time Series Features. *Water*, *11*(9), 1938. <https://doi.org/10.3390/w11091938>
- Tsyganskaya, V., Martinis, S., Marzahn, P., & Ludwig, R. (2018). Detection of Temporary Flooded Vegetation Using Sentinel-1 Time Series Data. *Remote Sensing*, *10*(8), 1286. <https://doi.org/10.3390/rs10081286>
- Wegnüller, U., Werner, C., Strozzi, T., Wiesmann, A., Frey, O., & Santoro, M. (2016). Sentinel-1 Support in the GAMMA Software. *Procedia Computer Science*, *100*, 1305–1312. <https://doi.org/10.1016/j.procs.2016.09.246>
- Weiß, T., Ramsauer, T., Löw, A., & Marzahn, P. (2020). Evaluation of Different Radiative Transfer Models for Microwave Backscatter Estimation of Wheat Fields. *Remote Sensing*, *12*(18), 3037. <https://doi.org/10.3390/rs12183037>
- Werner, C., Wegmüller, U., Strozzi, T., & Wiesmann, A. (2000). Gamma SAR and interferometric processing software. *Proceedings of the Ers-Envisat Symposium, Gothenburg, Sweden, 1620*, 9. [https://www.gamma-rs.ch/uploads/media/2000-1\\_GAMMA\\_Software.pdf](https://www.gamma-rs.ch/uploads/media/2000-1_GAMMA_Software.pdf)

## 3.8 Publication V: SenSE - Community SAR ScattEring model

**Reference:** Weiß, T., Löw A., 2024. SenSE: Community SAR ScattEring model. Journal of Open Source Software. (Manuscript submitted)

**Status:** submitted

**Plain language summary:** Over the past decades, various microwave RT models for retrieving biophysical parameters have been developed. The most commonly used empirical, semi-empirical, and physical microwave RT models have been consolidated into a single Python package called SenSE. Currently, the implemented surface models include Oh92 (Oh et al., 1992), Oh04 (Oh, 2004), Dubois95 (Dubois et al., 1995), IEM (Fung et al., 1992), and WCM (Attema and Ulaby, 1978), while the vegetation models consist of WCM (Attema and Ulaby, 1978) and SSRT (Ulaby and Long, 2014).

Each model can be utilized independently, or surface and vegetation models can be easily combined, allowing for the testing, analysis, and application of various model combinations for diverse research activities. The integration of different RT models within a single open-source software package enhances accessibility and facilitates comparative analysis. Consequently, researchers can concentrate on applying different RT models and generating research outputs in terms of usable and accurate biophysical parameters, rather than spending valuable time programming existing and frequently used RT models.

**Author contributions:** Conceptualization, T.W. and A.L.; Methodology, T.W. and A.L.; Software writing, T.W. and A.L.; Writing-original draft preparation, T.W.; Writing-review and editing, T.W.

**Journal:** Journal of Open Source Software (JOSS)

**Repository:** <https://github.com/McWhity/sense>

**Documentation:** <https://sense-community-sar-scattering-model.readthedocs.io/en/latest/>

# 1 SenSE: Community SAR ScattEring model

2 **Thomas Weiß** <sup>1,2,3</sup> and **Alexander Löw**<sup>1</sup>

3 **1** Department of Geography, Ludwig-Maximilians-Universität München, 80333 Munich, Germany **2**

4 Geodesy and Geoinformatics, University of Rostock, Justus-von-Liebig-Weg 6, 18059 Rostock, Germany

5 **3** Fraunhofer Institute for Computer Graphics Research IGD, Joachim-Junigus-Straße 11, 18059 Rostock,  
6 Germany

DOI: [10.xxxxxx/draft](https://doi.org/10.xxxxxx/draft)

## Software

- [Review](#) 
- [Repository](#) 
- [Archive](#) 

Editor: [Open Journals](#) 

## Reviewers:

- [@openjournals](#)

Submitted: 14 October 2024

Published: unpublished

## License

Authors of papers retain copyright  
and release the work under a  
Creative Commons Attribution 4.0  
International License ([CC BY 4.0](#)).

## 7 Summary

8 SenSE is a comprehensive community framework designed for radiative transfer (RT) modeling  
9 in the active microwave domain. It summarizes various RT models developed for synthetic  
10 aperture radar (SAR) to simulate backscatter responses from open soil and vegetated land  
11 surfaces, primarily in agricultural settings. This integration encompasses different models for  
12 scattering and emission across various surfaces, providing a cohesive operational structure.

13 One of the framework's most significant advantages is its modular design, which allows for  
14 the easy substitution and analysis of different surface and canopy scattering models within a  
15 single system. This flexibility facilitates seamless model exchange, enhancing the framework's  
16 adaptability and utility. The SenSE package currently includes several surface models such  
17 as Oh92 (Y. Oh et al., 1992), Oh04 (Yisok Oh, 2004), Dubois95 (Dubois et al., 1995), IEM  
18 (Fung et al., 1992), and the surface component of the Water Cloud Model (WCM) (Attema &  
19 Ulaby, 1978). For canopy modeling, it supports models like SSRT Ulaby & Long (2014) and  
20 WCM (Attema & Ulaby, 1978).

21 Additionally, the framework incorporates the dielectric mixing model by Dobson et al. (Dobson  
22 et al., 1985), available in various versions for converting soil moisture content to a dielectric  
23 constant. SenSE also includes essential utility functions, such as those for frequency-wavelength  
24 conversion and calculating Fresnel reflectivity coefficients, further enhancing its analytical  
25 capabilities.

26 For more detailed information, users are directed to the ReadtheDocs documentation and  
27 the original sources of each model, ensuring comprehensive access to technical details and  
28 operational guidelines.

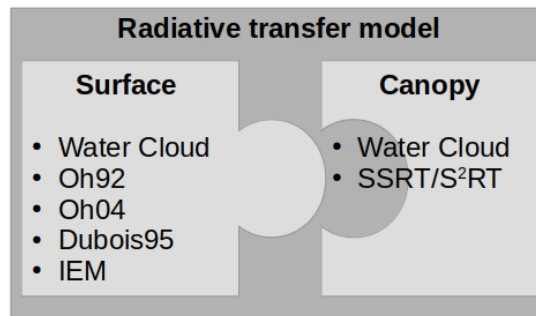


Figure 1: Implemented RT models within SenSE

## 29 Statement of need

30 Over the last several decades, various (empirical to physically based) RT models in the active  
31 microwave domain have been developed, tested, and further modified. However, an easy-to-  
32 use framework combining the most common microwave RT models (simulating backscatter  
33 responses of active microwave sensors) is lacking. Thus, every researcher must produce their  
34 own code implementation from the original source. This Python framework aims to serve  
35 as a first attempt to combine the most common active microwave-related RT models in a  
36 modular way. As a result, surface and volume scattering models can be easily exchanged with  
37 one another. Such a modular framework provides an opportunity to easily plug and play with  
38 different RT model combinations for various research questions and use cases. SenSE facilitates  
39 the application of RT models, especially for comparative analysis. Over time, the framework  
40 is expected to grow, incorporating more RT models (e.g., passive microwave domain) and  
41 supplementary functions (e.g., more dielectric mixing models).

## 42 Applications

43 The Python framework was employed within the EU-sponsored MULTIPLY Project  
44 (<https://cordis.europa.eu/project/id/687320>). Furthermore, the implementation of RT models  
45 in SenSE played a crucial role in the analysis conducted for several publications (Weiß et al.,  
46 2020, 2021, 2024). Additionally, the functionalities of SenSE are planned to be utilized in  
47 Project 2 - Remote Sensing of Vegetation Canopy Properties: States & Spatio-temporal  
48 Dynamics of the Land Atmosphere Feedback Initiative (LAFI) (<https://www.lafi-dfg.de/p-2>).  
49 Further collaboration with researchers in the field of vegetation optical depths in forest areas  
50 is ongoing. Consequently, the functionality of SenSE will continue to be used, and further  
51 extensions of SenSE are anticipated.

## 52 Other available software scripts (Ulaby and Long code library)

53 Ulaby and Long (Ulaby & Long, 2014) authored an extensive book on the fundamentals of  
54 microwave remote sensing, including a wealth of MATLAB codes for demonstration purposes.  
55 However, these MATLAB codes consist of individual snippets from different RT models, which  
56 makes it challenging to interchange combinations of RT models. While the interactive version  
57 of the MATLAB codes is effective for demonstration, it does not support processing large  
58 datasets. SenSE addresses the limitations of the MATLAB approach through practical examples  
59 provided in various Jupyter notebooks.

## 60 Acknowledgements

61 In memory of Alexander Löw († 2 July 2017) who started this library.

## 62 References

- 63 Attema, E. P. W., & Ulaby, F. T. (1978). Vegetation modeled as a water cloud. *Radio Science*,  
64 13(2), 357–364. <https://doi.org/10.1029/RS013i002p00357>
- 65 Dobson, M. C., Ulaby, F. T., Hallikainen, M. T., & El-rayes, M. A. (1985). Microwave Dielectric  
66 Behavior of Wet Soil-Part II: Dielectric Mixing Models. *IEEE Transactions on Geoscience  
67 and Remote Sensing*, GE-23(1), 35–46. <https://doi.org/10.1109/TGRS.1985.289498>
- 68 Dubois, P. C., Zyl, J. van, & Engman, T. (1995). Measuring soil moisture with imaging  
69 radars. *IEEE Transactions on Geoscience and Remote Sensing*, 33(4), 915–926. <https://doi.org/10.1109/36.406677>

- 71 Fung, A. K., Li, Z., & Chen, K. S. (1992). Backscattering from a randomly rough dielectric  
72 surface. *IEEE Transactions on Geoscience and Remote Sensing*, 30(2), 356–369. <https://doi.org/10.1109/36.134085>  
73
- 74 Oh, Yisok. (2004). Quantitative retrieval of soil moisture content and surface roughness from  
75 multipolarized radar observations of bare soil surfaces. *IEEE Transactions on Geoscience*  
76 *and Remote Sensing*, 42(3), 596–601. <https://doi.org/10.1109/TGRS.2003.821065>
- 77 Oh, Y., Sarabandi, K., & Ulaby, F. T. (1992). An empirical model and an inversion technique  
78 for radar scattering from bare soil surfaces. *IEEE Transactions on Geoscience and Remote*  
79 *Sensing*, 30(2), 370–381. <https://doi.org/10.1109/36.134086>
- 80 Roo, R. D. de, Du, Y., Ulaby, F. T., & Dobson, M. C. (2001). A semi-empirical backscattering  
81 model at L-band and C-band for a soybean canopy with soil moisture inversion. *IEEE*  
82 *Transactions on Geoscience and Remote Sensing*, 39(4), 864–872. <https://doi.org/10.1109/36.917912>  
83
- 84 Ulaby, F. T., & Long, D. G. (2014). *Microwave radar and radiometric remote sensing*.  
85 University of Michigan press. ISBN: 978-0-472-11935-6
- 86 Weiß, T., Jagdhuber, T., Ramsauer, T., Löw, A., & Marzahn, P. (2024). RTM-Based  
87 Downscaling of Medium Resolution Soil Moisture Using Sentinel-1 Data Over Agricultural  
88 Fields. *IEEE Journal of Selected Topics in Applied Earth Observations and Remote Sensing*,  
89 17, 15463–15479. <https://doi.org/10.1109/JSTARS.2024.3448625>
- 90 Weiß, T., Ramsauer, T., Jagdhuber, T., Löw, A., & Marzahn, P. (2021). Sentinel-1 Backscatter  
91 Analysis and Radiative Transfer Modeling of Dense Winter Wheat Time Series. *Remote*  
92 *Sensing*, 13(12). <https://doi.org/10.3390/rs13122320>
- 93 Weiß, T., Ramsauer, T., Löw, A., & Marzahn, P. (2020). Evaluation of Different Radiative  
94 Transfer Models for Microwave Backscatter Estimation of Wheat Fields. *Remote Sensing*,  
95 12(18). <https://doi.org/10.3390/rs12183037>

# Chapter 4

## Conclusion

This thesis encompasses the complete scientific workflow for producing a new set of high spatio-temporal soil moisture estimates derived from remote sensing data. It spans ground truth data acquisition (self-acquisition of in-situ data used in Publications I, II, and III), preprocessing of remote sensing data (Publication IV), and an in-depth analysis of RT models concerning their remote sensing input requirements (Publications I, II, and V), culminating in the primary goal of producing high spatio-temporal soil moisture estimates for agriculturally utilized areas (Publication III).

In the following, the RQs outlined in Chapter 2 are summarized, and their key findings are addressed in relation to Publications I - V and additional literature. Finally, an outlook on research applications and potential uses is provided to conclude this thesis.

### 4.1 Answers of Research Questions

In the following RQs I, II, and VI are considered initial RQs, while RQs III, IV, and V are significantly influenced by observations made during the investigation of RQs I and II.

**RQ I: Can existing microwave radiative transfer RT models accurately simulate high spatio-temporal Sentinel-1 VV-polarized radar backscatter throughout the entire wheat growing season?**

The findings in Publication I indicate that a simplistic approach using soil moisture, LAI, and a static empirical parameter to describe the attenuation of the canopy is insufficient to simulate the observed Sentinel-1 VV-polarized backscatter response for the entire growing period of wheat fields. Although different RT model combinations can accurately simulate the first half of the vegetation growing period (phenological stages including tillering, stem elongation, booting, and heading until maximum vegetation height is reached), the observed increase in VV-polarized backscatter during the second half of the growing period (flowering, fruit development, and ripening) is not represented in the RT model results. An in-depth analysis of the model parameters related to canopy attenuation (Publication I) revealed that, during the second half of the growing period, a dominant contribution from the canopy model with almost no changes over time was estimated. The main physiological changes in wheat fields after reaching their maximum height (the second half of the growing period) include increases in grain and stem biomass, as well as loss of vegetation water content (Harfenmeister et al., 2019). Since microwaves are sensitive to changes in water content in the soil and plants, a decrease in plant moisture should affect the attenuation

of the radar signal by the canopy, rendering it more transparent to radar waves (He et al., 2016). Thus, an increase in the modeled attenuation parameter for the second half of the growing period is expected. However, the LAI appears to be an inadequate descriptor for vegetation water loss, as it shows almost no change throughout the second half of the vegetation growing period. Therefore, a model configuration using soil moisture, LAI, vegetation height, and a static empirical model parameter as input variables is only suitable for the first half of the vegetation growing period, but not for the entire period. To model the second half of the growing period, a more advanced approach involving changes in an empirical parameter that influence the attenuation of the canopy is needed. The results in Publication I demonstrate that by adjusting one empirical parameter to be non-static, the missing information about water loss during the second half of the vegetation growing period, as well as the observed backscatter increase, can be accurately modeled by all analyzed microwave RT models.

**RQ II: To what extent do the simulated Sentinel-1 VV-polarized radar backscatter results differ among empirical, semi-empirical, and physically-based RT models?**

The analyzed soil models, ranging from empirical to more physically-based, include WCM (Attema and Ulaby, 1978), Dubois95 (Dubois et al., 1995), Oh92 (Oh et al., 1992), Oh04 (Oh, 2004), and IEM\_B (Baghdadi et al., 2017). The analyzed canopy models, varying from empirical to more physically-based, are WCM (Attema and Ulaby, 1978) and SSRT (Ulaby and Long, 2014). The findings published in Publication I indicate that the most sophisticated model combination of IEM\_B + SSRT provides the best results, with an ubRMSE of 1.82 dB and an  $R^2$  of 0.64 in terms of modeled backscatter. Similar results regarding ubRMSE and  $R^2$  are observed when the most sophisticated soil model is combined with a purely empirical canopy model (IEM\_B + WCM; ubRMSE of 1.92 dB and  $R^2$  of 0.62) and when the most sophisticated canopy model is paired with a purely empirical soil model (WCM + SSRT; ubRMSE of 1.93 dB and  $R^2$  of 0.63). Other combinations of empirical and semi-empirical soil models (WCM, Oh92, Oh04, and Dubois95) yield slightly poorer values for ubRMSE (ranging from 2.08 dB to 2.22 dB) and  $R^2$  (ranging from 0.48 to 0.60) with both analyzed canopy models. Nevertheless, the choice of a specific model combination is highly dependent on the availability of the required model input parameters. Thus, although the best results (ubRMSE,  $R^2$ ) are achieved using more physically-based models, empirical-based model combinations serve as a good alternative due to their only slightly inferior performance. The popularity of the empirical WCM model, which benefits from low input parameter requirements, is further supported by a review of the literature (Kweon and Oh, 2015; Liu and Shi, 2016; Choker et al., 2017; Baghdadi et al., 2017; Tao et al., 2019). Despite the differences in input requirements and validation discrepancies in terms of ubRMSE and  $R^2$ , the time series results of all model combinations show a mismatch between the simulated RT model results and the observed Sentinel-1 backscatter across daily consecutive time steps. Therefore, a definitive conclusion regarding whether more physically-based RT models are better suited for simulating the high spatio-temporal

resolution of Sentinel-1 VV-polarized radar backscatter response in wheat cannot be drawn from the research results of Publication I.

**RQ III: What specific characteristics are observed in dense Sentinel-1 time series with varying acquisition geometries, and how do these geometries influence the simulated RT model outcomes?**

The constellation of the twin satellites Sentinel-1 A and B can provide images with the same acquisition geometries (same incidence and azimuth) every 6 days. However, due to the flight plan, some areas (e.g., large parts of Europe) are viewed by different overpasses (tracks), allowing for a much greater time series of Sentinel-1 images to be archived if images with different acquisition geometries are used (Geudtner et al., 2014). But, the unique acquisition technique of SAR images (e.g., side-looking acquisition) can result in different backscatter responses due to varying acquisition geometries, posing another challenge (Wegmuller et al., 2006; Mladenova et al., 2013; Arias et al., 2022). When analyzing a dense Sentinel-1 time series (revisit time of 1.5 days) for the MNI test site, acquisitions taken on consecutive days show backscatter variations of a few dB, even though in-situ measurements indicate no changes in vegetation or soil. Owing to the constellation of four different Sentinel-1 tracks with individual acquisition geometries regarding incidence and azimuth angles (two tracks with similar incidence but different azimuth angles; two tracks with similar azimuth angles but different incidence angles), the influences of azimuth and incidence angles on the radar backscatter response can be analyzed.

Publication II reveals that consecutive acquisition days with similar incidence angles (two tracks with incidence angles of  $35^\circ$  and  $36^\circ$ ; two tracks with incidence angles of  $43^\circ$  and  $45^\circ$ ) and different azimuth angles ( $-165^\circ$  and  $-15^\circ$  relative to north) show almost no changes in VV-polarized backscatter values when there are no changes in soil moisture or vegetation cover. A different picture emerges when analyzing the radar backscatter of consecutive days with the same azimuth angle but different incidence angles. Although in-situ data show no change in soil moisture and vegetation cover, different backscatter values are observed. Thus, Sentinel-1 VV-polarized backscatter variations in scenes with different acquisition geometries are primarily driven by changes in incidence angles, whereas the influence of azimuth angle changes is negligible. The findings in Publication II regarding the influence of incidence angle changes on radar backscatter align with research results from Balenzano et al. (2011); Molijn et al. (2019). Other studies on azimuth angle changes reveal that their influence varies with topographic slope orientation (Schaufler et al., 2018). Furthermore, in agricultural fields, the azimuthal effects on tilled soils depend heavily on the relationship between the row tillage direction and the viewing angle (Wegmuller et al., 2006; Mattia, 2011). Moreover, since agricultural fields are typically dynamic targets, the influence of incidence and azimuth angles on the backscatter response from vegetation might also depend on changes in scattering mechanisms as well as crop row orientation (Arias et al., 2022). The occurrence of different scattering mechanisms is further discussed in RQ IV.

In Publication I, a mismatch between retrieved (RT model) and observed (Sentinel-1)

VV-polarized backscatter data from consecutive days (change in observation geometry) was identified. Thus, understanding the influence of varying observation geometries of the Sentinel-1 time series on the simulated RT model results was the main objective of Publication II. Since different azimuth angles have a negligible influence on the dense Sentinel-1 time series and because azimuth angle changes are not considered in the RT models used, a detailed analysis of the azimuth angles was not feasible. On the other hand, the effects of incidence angle changes could be further investigated, as they result in deviations in Sentinel-1 backscatter and, in theory, are accounted for in the RT models. As the incidence angle is implemented as an input variable within the analyzed RT models, it was expected that these models should adequately consider Sentinel-1 backscatter differences due to incidence angle variations. However, the observed trend mismatch between the Sentinel-1 and RT model backscatter of daily consecutive images with different incidence angles reveals that simplistic model approaches fall short in addressing incidence angle variations within a dense time series. Even if the different incidence angles are normalized using a commonly employed cosine correction method (Kellndorfer et al., 1998), the analyzed RT models are unable to account for backscatter changes between images with differing incidence angles. These findings suggest that for accurate time series backscatter simulation with the analyzed RT models, only images with similar incidence angles should be used. Nevertheless, a modification of the RT model analyzing the possibility of utilizing a time series with varying observation geometries will be discussed in RQ V.

**RQ IV: How do different incidence and azimuth angles in Sentinel-1 images affect the emergence of distinct scattering mechanisms?**

With dual polarimetric eigen-decomposition, an analysis aimed at better understanding the physical differences in backscatter signals due to changes in incidence and azimuth angles was published in Publication II. Using VV-VH dual polarimetric decomposition, variations in scattering mechanisms are made apparent. Since changes in scattering mechanisms are heavily influenced by alterations in the canopy (e.g., height, biomass, or canopy water content), a change detection analysis was performed for different phenological stages. During the tillering stage (characterized by low vegetation cover), no significant deviations between different acquisition geometries are observed. This is expected, as the dominant scattering mechanism is direct backscatter from the soil when there is minimal vegetation cover. During the stem elongation stage, stronger changes in scattering mechanisms are evident at lower incidence angles ( $35^\circ$ ) compared to higher incidence angles ( $44^\circ$ ). Notably, differences due to varying azimuth angles are not distinguishable. For the flowering stage, the presence of different scattering mechanisms related to incidence angle variations remains visible, although not as clearly as during the stem elongation phase. By the end of the vegetation period (ripening stage), differences based on scattering mechanisms are nearly imperceptible. Unfortunately, further analyses in terms of scattering mechanism classification are challenging, as dual polarimetric eigen-decomposition is not as precise as four-component polarimetric methods when specifying the exact nature of scattering occurrences (Ji and Wu, 2015).

**RQ V: Can a modified RT model effectively simulate a dense Sentinel-1 time series comprising images with varying observation geometries?**

In RQs III and IV, the unique characteristics of a dense Sentinel-1 time series (varying acquisition geometries) and the associated challenges faced by RT models in accurately simulating this series were discussed. Although a more extensive time series could be available, due to the identified challenges, most studies (Baghdadi et al., 2017; El Hajj et al., 2017; Nativel et al., 2022) utilize only the 6 day Sentinel-1 repeat cycle (same observation geometry). However, since higher temporal resolution is particularly valuable for soil moisture assessment, a modified RT model approach, based on findings from RQs III and IV, was introduced in Publication II. The original RT model approach discussed in Publication I was enhanced by incorporating a time-variant model parameter. With this additional time-variant calibration coefficient, the transmissivity factor - based on varying incidence angles within the RT models - can be individually parameterized. The findings in Publication II demonstrate that this additional parameterization can partly compensate for the shortcomings of the RT model architecture in handling incidence angle variations. Nevertheless, a statistical comparison indicates that the best results are still achieved when only images with similar incidence angles are utilized. However, this approach would imply that, for the MNI test site, the average revisit time would decrease from 1.5 days to 6 days. In summary, the developed approach is suitable for using time series with changing observational geometries. However, depending on the specific application, the choice between greater temporal resolution or improved retrieval accuracy may lead to different selections of available Sentinel-1 time series.

**RQ VI: Can high-resolution soil moisture estimates over agricultural fields be derived using microwave and optical remote sensing data in conjunction with microwave RT models?**

The pre-analysis of RT models and the use of Sentinel-1 images with varying acquisition geometries, as discussed in Publications I and II, were essential steps in establishing a data assimilation process that ultimately enables the production of accurate high spatio-temporal soil moisture estimates. This addresses the initial goal and thus RQ VI. The findings in Publication III confirm that RQ VI can indeed be confirmed. An area-based retrieval of high spatio-temporal resolution (10 m; 1.5 days) for the MNI test site is achievable by driving an RT model retrieval using remote sensing information from Sentinel-1, Sentinel-2, and RADOLAN data. Validation results from several test fields demonstrate good overall agreement with in situ data for both wheat and maize fields. For the year 2017, the mean ubRMSE was  $0.045 \text{ m}^3/\text{m}^3$ , while for 2018, a mean ubRMSE of  $0.037 \text{ m}^3/\text{m}^3$  was achieved. Furthermore, with retrieval and in situ values ranging from  $0.05 \text{ m}^3/\text{m}^3$  to  $0.4 \text{ m}^3/\text{m}^3$ , the range of naturally occurring soil moisture values is adequately covered. Although other high-resolution approaches for soil moisture retrieval report similar ubRMSE values (Baghdadi et al., 2017; El Hajj et al., 2017; Nativel et al., 2022), they typically have a temporal resolution of 6 days (same acquisition geometry) rather than the

1.5 days achieved here. Another advantage of the approach utilized in Publication III is its enhanced transferability to other regions, as the retrieval methodology relies solely on input data that can be systematically obtained from freely available satellite sources.

## 4.2 Research Usage and Application

The research orientation of this thesis encompasses a comparative study on RT model composition (Publication I), fundamental research on satellite data (impacts of different acquisition geometries; Publication II), and applied research focusing on the retrieval of high spatio-temporal soil moisture maps (Publication III). Furthermore, the provision of research programming code through various Python packages (Publications IV and V) has significantly contributed to the scientific community. Publication IV not only facilitates the use of preprocessing steps within the remote sensing community but also enables both specialists and non-specialists to utilize microwave data with minimal knowledge of preprocessing techniques, thereby broadening the scope of applications. The compilation of the most common surface and canopy-based RT models in Publication V further supports the scientific community. With this freely available Python package, users can easily and efficiently analyze various combinations of RT models.

Although the research in Publications I-III is based on the MNI test site, the methods employed have significant potential for transferability to other regions due to the use of freely accessible remote sensing data. Moreover, the proposed approach (Publication III) minimizes the reliance on additional a priori data, such as soil properties or crop type information. First, no supplementary soil property information is required. Second, while land use (crop type) data is essential for accurate quantitative VWC estimates, the method demonstrated in Publication III shows that satisfactory soil moisture retrieval results can be achieved using a single equation for both wheat and maize, without differentiating based on land use. Unfortunately, validation for other crop types is not feasible due to a lack of in situ data. Nevertheless, wheat and maize collectively account for 65% of global cereal production (Erenstein et al., 2021).

The significance of the archived high spatio-temporal soil moisture information is highlighted by its diverse applications, ranging from improving crop yield estimates (Verstraeten et al., 2011) to providing comprehensive soil moisture assessments at the field scale (Peng et al., 2017). Additionally, timely soil moisture information can contribute to reducing water usage at local to regional scales, particularly in irrigation areas (Neupane and Guo, 2019). By minimizing fertilizer application (Peng et al., 2021b), spatially distributed soil moisture data also help mitigate the contamination of surface and groundwater resources (Preetha and Al-Hamdan, 2020). Moreover, since soil erosion is often influenced by local conditions, high spatio-temporal soil moisture data are essential for accurate soil erosion modeling and the development of agricultural adaptation strategies (Peng et al., 2021a).

Ultimately, the research presented in this thesis marks a significant advancement toward establishing a system for the operational provision of high spatio-temporal soil moisture information, thereby enhancing and facilitating precision farming applications.

# References

- Abbas, F., Afzaal, H., Farooque, A.A., Tang, S., 2020. Crop Yield Prediction through Proximal Sensing and Machine Learning Algorithms. *Agronomy* 10, 1046. doi:10.3390/agronomy10071046.
- Alexakis, D.D., Mexis, F.D.K., Vozinaki, A.E.K., Daliakopoulos, I.N., Tsanis, I.K., 2017. Soil Moisture Content Estimation Based on Sentinel-1 and Auxiliary Earth Observation Products. A Hydrological Approach. *Sensors* 17, 1455. doi:10.3390/s17061455.
- Arias, M., Campo-Bescós, M.A., Alvarez-Mozos, J., 2022. On the influence of acquisition geometry in backscatter time series over wheat. *International Journal of Applied Earth Observation and Geoinformation* 106, 102671. doi:10.1016/j.jag.2021.102671.
- Attema, E.P.W., Ulaby, F.T., 1978. Vegetation modeled as a water cloud. *Radio Science* 13, 357–364. doi:10.1029/RS013i002p00357.
- Baghdadi, N., El Hajj, M., Zribi, M., Bousbih, S., 2017. Calibration of the Water Cloud Model at C-Band for Winter Crop Fields and Grasslands. *Remote Sensing* 9. doi:10.3390/rs9090969.
- Balenzano, A., Mattia, F., Satalino, G., Davidson, M.W.J., 2011. Dense Temporal Series of C- and L-band SAR Data for Soil Moisture Retrieval Over Agricultural Crops. *IEEE Journal of Selected Topics in Applied Earth Observations and Remote Sensing* 4, 439–450. doi:10.1109/JSTARS.2010.2052916.
- Balenzano, A., Mattia, F., Satalino, G., Lovergine, F.P., Palmisano, D., Davidson, M.W.J., 2021. Dataset of Sentinel-1 surface soil moisture time series at 1 km resolution over Southern Italy. *Data in Brief* 38, 107345. doi:10.1016/j.dib.2021.107345.
- Balenzano, A., Mattia, F., Satalino, G., Pauwels, V., Snoeij, P., 2012. SMOSAR algorithm for soil moisture retrieval using Sentinel-1 data, in: 2012 IEEE International Geoscience and Remote Sensing Symposium, 1200–1203. doi:10.1109/IGARSS.2012.6351332.
- Bardi, U., 2011. *The limits to growth revisited*. Springer Publishing, France. URL: [https://www.socioeco.org/bdf\\_fiche-publication-685\\_en.html](https://www.socioeco.org/bdf_fiche-publication-685_en.html).
- Bartalis, Z., Wagner, W., Naeimi, V., Hasenauer, S., Scipal, K., Bonekamp, H., Figa, J., Anderson, C., 2007. Initial soil moisture retrievals from the METOP-A Advanced Scatterometer (ASCAT). *Geophysical Research Letters* 34. doi:10.1029/2007GL031088.
- Bauer-Marschallinger, B., Freeman, V., Cao, S., Paulik, C., Schaufler, S., Stachl, T., Modanesi, S., Massari, C., Ciabatta, L., Brocca, L., Wagner, W., 2019. Toward

- Global Soil Moisture Monitoring With Sentinel-1: Harnessing Assets and Overcoming Obstacles. *IEEE Transactions on Geoscience and Remote Sensing* 57, 520–539. doi:10.1109/TGRS.2018.2858004.
- Bauke, S.L., Amelung, W., Bol, R., Brandt, L., Brüggemann, N., Kandeler, E., Meyer, N., Or, D., Schnepf, A., Schloter, M., Schulz, S., Siebers, N., von Sperber, C., Vereecken, H., 2022. Soil water status shapes nutrient cycling in agroecosystems from micrometer to landscape scales. *Journal of Plant Nutrition and Soil Science* 185, 773–792. doi:10.1002/jpln.202200357.
- Baur, M., Jagdhuber, T., Link, M., Piles, M., Akbar, R., Entekhabi, D., 2018. Multi-Frequency Estimation of Canopy Penetration Depths from SMAP/AMSR2 Radiometer and Icesat Lidar Data, in: *IGARSS 2018 - 2018 IEEE International Geoscience and Remote Sensing Symposium*, 365–368. doi:10.1109/IGARSS.2018.8517438.
- Beale, J., Waine, T., Evans, J., Corstanje, R., 2021. A Method to Assess the Performance of SAR-Derived Surface Soil Moisture Products. *IEEE Journal of Selected Topics in Applied Earth Observations and Remote Sensing* 14, 4504–4516. doi:10.1109/JSTARS.2021.3071380.
- den Besten, N., Steele-Dunne, S., de Jeu, R., van der Zaag, P., 2021. Towards Monitoring Waterlogging with Remote Sensing for Sustainable Irrigated Agriculture. *Remote Sensing* 13, 2929. doi:10.3390/rs13152929.
- Bindlish, R., Jackson, T., Cosh, M., Zhao, T., O'Neill, P., 2015. Global Soil Moisture From the Aquarius/SAC-D Satellite: Description and Initial Assessment. *IEEE Geoscience and Remote Sensing Letters* 12, 923–927. doi:10.1109/LGRS.2014.2364151.
- Boretti, A., Rosa, L., 2019. Reassessing the projections of the World Water Development Report. *NPJ Clean Water* 2, 1–6. doi:10.1038/s41545-019-0039-9.
- Bousbih, S., Zribi, M., El Hajj, M., Baghdadi, N., Lili-Chabaane, Z., Gao, Q., Fanise, P., 2018. Soil Moisture and Irrigation Mapping in A Semi-Arid Region, Based on the Synergetic Use of Sentinel-1 and Sentinel-2 Data. *Remote Sensing* 10, 1953. doi:10.3390/rs10121953.
- Brocca, L., Crow, W.T., Ciabatta, L., Massari, C., de Rosnay, P., Enenkel, M., Hahn, S., Amarnath, G., Camici, S., Tarpanelli, A., Wagner, W., 2017. A Review of the Applications of ASCAT Soil Moisture Products. *IEEE Journal of Selected Topics in Applied Earth Observations and Remote Sensing* 10, 2285–2306. doi:10.1109/JSTARS.2017.2651140.
- Brocca, L., Tarpanelli, A., Filippucci, P., Dorigo, W., Zaussinger, F., Gruber, A., Fernández-Prieto, D., 2018. How much water is used for irrigation? A new approach exploiting coarse resolution satellite soil moisture products. *International Journal of Applied Earth Observation and Geoinformation* 73, 752–766. doi:10.1016/j.jag.2018.08.023.

- Brogi, C., Vereecken, H., Bogaen, H.R., Brocca, L., 2023. Soil processes in the hydrologic cycle, in: Goss, M.J., Oliver, M. (Eds.), *Encyclopedia of Soils in the Environment* (Second Edition). Academic Press, Oxford, 469–481. URL: <https://www.sciencedirect.com/science/article/pii/B9780128229743000793>.
- Burek, P., Satoh, Y., Fischer, G., Kahil, M.T., Scherzer, A., Tramberend, S., Nava, L.F., Wada, Y., Eisner, S., Flörke, M., Hanasaki, N., Magnuszewski, P., Cosgrove, B., Wiberg, D., 2016. *Water Futures and Solution - Fast Track Initiative (Final Report)*. Technical Report. WP-16-006. IIASA, Laxenburg, Austria. URL: <https://pure.iiasa.ac.at/id/eprint/13008/>.
- Campbell, B., Beare, D., Bennett, E., Hall-Spencer, J., Ingram, J., Jaramillo, F., Ortiz, R., Ramankutty, N., Sayer, J., Shindell, D., 2017. Agriculture production as a major driver of the Earth system exceeding planetary boundaries. *Ecology and Society* 22. doi:10.5751/ES-09595-220408.
- Carrière-Swallow, Y., Deb, P., Furceri, D., Jiménez, D., Ostry, J.D., 2023. Shipping costs and inflation. *Journal of International Money and Finance* 130, 102771. doi:10.1016/j.jimonfin.2022.102771.
- Champion, I., 1996. Simple modelling of radar backscattering coefficient over a bare soil: variation with incidence angle, frequency and polarization. *International Journal of Remote Sensing* doi:10.1080/01431169608949045.
- Chaparro, D., Vall-llossera, M., Piles, M., Camps, A., Rüdiger, C., Riera-Tatché, R., 2016. Predicting the Extent of Wildfires Using Remotely Sensed Soil Moisture and Temperature Trends. *IEEE Journal of Selected Topics in Applied Earth Observations and Remote Sensing* 9, 2818–2829. doi:10.1109/JSTARS.2016.2571838.
- Choker, M., Baghdadi, N., Zribi, M., El Hajj, M., Paloscia, S., Verhoest, N.E.C., Lievens, H., Mattia, F., 2017. Evaluation of the Oh, Dubois and IEM Backscatter Models Using a Large Dataset of SAR Data and Experimental Soil Measurements. *Water* 9, 38. doi:10.3390/w9010038.
- Cholet, C., Houle, D., Sylvain, J.D., Doyon, F., Maheu, A., 2022. Climate Change Increases the Severity and Duration of Soil Water Stress in the Temperate Forest of Eastern North America. *Frontiers in Forests and Global Change* 5. URL: <https://www.frontiersin.org/articles/10.3389/ffgc.2022.879382>.
- CloudFerro S.A., 2024. Copernicus Data Space Ecosystem - Case studies. URL: <https://cloudferro.com/cases/copernicus-data-space-ecosystem/>.
- Crapolicchio, R., Bigazzi, A., De Chiara, G., Neyt, X., Stoffelen, A., Belmonte, M., Wagner, W., Reimer, C., 2016. The scatterometer instrument competence centre (SCIRoCCo): Project's activities and first achievements, in: *Proc. Eur. Space Agency Living Planet Symp*, 9–13.

- Dai, A., Zhao, T., Chen, J., 2018. Climate Change and Drought: a Precipitation and Evaporation Perspective. *Current Climate Change Reports* 4, 301–312. doi:10.1007/s40641-018-0101-6.
- Das, K., Paul, P.K., 2015. Present status of soil moisture estimation by microwave remote sensing. *Cogent Geoscience* 1, 1084669. doi:10.1080/23312041.2015.1084669.
- Das, N.N., Entekhabi, D., Dunbar, R.S., Chaubell, M.J., Colliander, A., Yueh, S., Jagdhuber, T., Chen, F., Crow, W., O'Neill, P.E., Walker, J.P., Berg, A., Bosch, D.D., Caldwell, T., Cosh, M.H., Collins, C.H., Lopez-Baeza, E., Thibeault, M., 2019. The SMAP and Copernicus Sentinel 1A/B microwave active-passive high resolution surface soil moisture product. *Remote Sensing of Environment* 233. doi:10.1016/j.rse.2019.111380.
- Dingman, S.L., 2008. *Physical Hydrology*. 2 ed., Waveland Pr Inc, Long Grove, Ill.
- Dorigo, W., Wagner, W., Albergel, C., Albrecht, F., Balsamo, G., Brocca, L., Chung, D., Ertl, M., Forkel, M., Gruber, A., Haas, E., Hamer, P.D., Hirschi, M., Ikonen, J., de Jeu, R., Kidd, R., Lahoz, W., Liu, Y.Y., Miralles, D., Mistelbauer, T., Nicolai-Shaw, N., Parinussa, R., Pratola, C., Reimer, C., van der Schalie, R., Seneviratne, S.I., Smolander, T., Lecomte, P., 2017. ESA CCI Soil Moisture for improved Earth system understanding: State-of-the art and future directions. *Remote Sensing of Environment* 203, 185–215. doi:10.1016/j.rse.2017.07.001.
- Dubois, P., van Zyl, J., Engman, T., 1995. Measuring soil moisture with imaging radars. *IEEE Transactions on Geoscience and Remote Sensing* 33, 915–926. doi:10.1109/36.406677.
- Dwivedi, R.S., Rao, B.R., Kushwaha, S.P., 2000. The Utility of Day-and-Night Observation and Cloud-Penetration Capability of ERS-1 SAR Data for Detection of Wetlands. *Geocarto International* 15, 7–12. doi:10.1080/10106040008542134.
- El Hajj, M., Baghdadi, N., Zribi, M., Bazzi, H., 2017. Synergic Use of Sentinel-1 and Sentinel-2 Images for Operational Soil Moisture Mapping at High Spatial Resolution over Agricultural Areas. *Remote Sensing* 9. doi:10.3390/rs9121292.
- Engman, E.T., 1991. Applications of microwave remote sensing of soil moisture for water resources and agriculture. *Remote Sensing of Environment* 35, 213–226. doi:10.1016/0034-4257(91)90013-V.
- Entekhabi, D., Njoku, E.G., O'Neill, P.E., Kellogg, K.H., Crow, W.T., Edelstein, W.N., Entin, J.K., Goodman, S.D., Jackson, T.J., Johnson, J., Kimball, J., Piepmeier, J.R., Koster, R.D., Martin, N., McDonald, K.C., Moghaddam, M., Moran, S., Reichle, R., Shi, J.C., Spencer, M.W., Thurman, S.W., Tsang, L., Van Zyl, J., 2010. The Soil Moisture Active Passive (SMAP) Mission. *Proceedings of the IEEE* 98, 704–716. doi:10.1109/JPROC.2010.2043918.

- Erenstein, O., Chamberlin, J., Sonder, K., 2021. Estimating the global number and distribution of maize and wheat farms. *Global Food Security* 30. doi:10.1016/j.gfs.2021.100558.
- Fajgelbaum, P.D., Khandelwal, A.K., 2022. The Economic Impacts of the US–China Trade War. *Annual Review of Economics* 14, 205–228. doi:10.1146/annurev-economics-051420-110410.
- Finger, R., Swinton, S., El Benni, N., Walter, A., 2019. Precision Farming at the Nexus of Agricultural Production and the Environment. *Annual Review of Resource Economics* 11. doi:10.1146/annurev-resource-100518-093929.
- Fischer, G., Tubiello, F.N., van Velthuizen, H., Wiberg, D.A., 2007. Climate change impacts on irrigation water requirements: Effects of mitigation, 1990–2080. *Technological Forecasting and Social Change* 74, 1083–1107. doi:10.1016/j.techfore.2006.05.021.
- Fortune Business Insights, 2023. Satellite Imaging Market Growth, Size, Share & COVID-19 Impact Analysis, By Application (Geospatial Data Acquisition, Navigation & Mapping, Defense & Intelligence, Surveillance & Security, and Others), By End-user (Government, Defense, Commercial, and Others), and Regional Forecasts, 2023-2030. Technical Report. Fortune Business Insights. URL: <https://www.fortunebusinessinsights.com/satellite-imaging-market-103372>.
- Freud, E., Stajduhar, A., Rosenbaum, R.S., Avidan, G., Ganel, T., 2020. The COVID-19 pandemic masks the way people perceive faces. *Scientific Reports* 10, 22344. doi:10.1038/s41598-020-78986-9.
- Fung, A., Li, Z., Chen, K., 1992. Backscattering from a randomly rough dielectric surface. *IEEE Transactions on Geoscience and Remote Sensing* 30, 356–369. doi:10.1109/36.134085.
- Gao, Y., Cabrera Serrenho, A., 2023. Greenhouse gas emissions from nitrogen fertilizers could be reduced by up to one-fifth of current levels by 2050 with combined interventions. *Nature Food* 4, 170–178. doi:10.1038/s43016-023-00698-w.
- Geudtner, D., Torres, R., Snoeij, P., Davidson, M., Rommen, B., 2014. Sentinel-1 System capabilities and applications, in: 2014 IEEE Geoscience and Remote Sensing Symposium, 1457–1460. doi:10.1109/IGARSS.2014.6946711.
- Global Footprint Network, 2015. August 13th is Earth Overshoot Day this year. URL: [https://www.footprintnetwork.org/content/documents/EOD2015\\_PR\\_final.pdf](https://www.footprintnetwork.org/content/documents/EOD2015_PR_final.pdf).
- González-Zamora, A., Sánchez, N., Martínez-Fernández, J., Gumuzzio, A., Piles, M., Olmedo, E., 2015. Long-term SMOS soil moisture products: A comprehensive evaluation across scales and methods in the Duero Basin (Spain). *Physics and Chemistry of the Earth, Parts A/B/C* 83-84, 123–136. doi:10.1016/j.pce.2015.05.009.

- Gruber, A., Dorigo, W.A., Crow, W., Wagner, W., 2017. Triple Collocation-Based Merging of Satellite Soil Moisture Retrievals. *IEEE Transactions on Geoscience and Remote Sensing* 55, 6780–6792. doi:10.1109/TGRS.2017.2734070.
- Gruber, A., Peng, J., 2023. Remote sensing of soil moisture, in: Goss, M.J., Oliver, M. (Eds.), *Encyclopedia of Soils in the Environment* (Second Edition). Academic Press, Oxford, 618–630. URL: <https://www.sciencedirect.com/science/article/pii/B9780128229743000197>.
- Gruber, A., Scanlon, T., van der Schalie, R., Wagner, W., Dorigo, W., 2019. Evolution of the ESA CCI Soil Moisture climate data records and their underlying merging methodology. *Earth System Science Data* 11, 717–739. doi:10.5194/essd-11-717-2019.
- Hajnsek, I., Desnos, Y.L. (Eds.), 2021. *Polarimetric Synthetic Aperture Radar: Principles and Application*. Springer Nature. URL: <https://library.oapen.org/handle/20.500.12657/48227>.
- Harfenmeister, K., Spengler, D., Weltzien, C., 2019. Analyzing Temporal and Spatial Characteristics of Crop Parameters Using Sentinel-1 Backscatter Data. *Remote Sensing* 11, 1569. doi:10.3390/rs11131569.
- He, L., Tong, L., Li, Y., Chen, Y., Tan, L., Guo, C., 2016. Polarimetric analysis of radar backscatter from ground-based scatterometers and wheat biomass monitoring with advanced synthetic aperture radar images. *Journal of Applied Remote Sensing* 10. doi:10.1117/1.JRS.10.026008.
- Holmes, T.R.H., De Jeu, R.A.M., Owe, M., Dolman, A.J., 2009. Land surface temperature from Ka band (37 GHz) passive microwave observations. *Journal of Geophysical Research: Atmospheres* 114. doi:10.1029/2008JD010257.
- Holsten, A., Vetter, T., Vohland, K., Krysanova, V., 2009. Impact of climate change on soil moisture dynamics in Brandenburg with a focus on nature conservation areas. *Ecological Modelling* 220, 2076–2087. doi:10.1016/j.ecolmodel.2009.04.038.
- Hosseini, M., McNairn, H., 2017. Using multi-polarization C- and L-band synthetic aperture radar to estimate biomass and soil moisture of wheat fields. *International Journal of Applied Earth Observation and Geoinformation* 58, 50–64. doi:10.1016/j.jag.2017.01.006.
- Hou, D., Bi, J., Ma, L., Zhang, K., Li, D., Rehmani, M.I.A., Tan, J., Bi, Q., Wei, Y., Liu, G., Yu, X., Luo, L., 2022. Effects of Soil Moisture Content on Germination and Physiological Characteristics of Rice Seeds with Different Specific Gravity. *Agronomy* 12, 500. doi:10.3390/agronomy12020500.
- Hussain, A.A., Al-Turjman, F., 2021. Artificial intelligence and blockchain: A review. *Transactions on Emerging Telecommunications Technologies* 32, e4268. doi:10.1002/ett.4268.

- Iizumi, T., Shin, Y., Kim, W., Kim, M., Choi, J., 2018. Global crop yield forecasting using seasonal climate information from a multi-model ensemble. *Climate Services* 11, 13–23. doi:10.1016/j.cliser.2018.06.003.
- Intergovernmental Panel on Climate Change (IPCC), 2018. *Global Warming of 1.5°C: IPCC Special Report on Impacts of Global Warming of 1.5°C above Pre-industrial Levels in Context of Strengthening Response to Climate Change, Sustainable Development, and Efforts to Eradicate Poverty*. Cambridge University Press, Cambridge. URL: <https://www.cambridge.org/core/books/global-warming-of-15c/D7455D42B4C820E706A03A169B1893FA>.
- Intergovernmental Panel on Climate Change (IPCC), 2019. *Climate Change and Land: An IPCC special report on climate change, desertification, land degradation, sustainable land management, food security, and greenhouse gas fluxes in terrestrial ecosystems*. URL: <https://www.ipcc.ch/site/assets/uploads/2019/11/SRCCL-Full-Report-Compiled-191128.pdf>.
- Intergovernmental Panel on Climate Change (IPCC), 2021. *Climate Change 2021: The Physical Science Basis. Contribution of Working Group I to the Sixth Assessment Report of the Intergovernmental Panel on Climate Change*. URL: [https://report.ipcc.ch/ar6/wg1/IPCC\\_AR6\\_WGI\\_FullReport.pdf](https://report.ipcc.ch/ar6/wg1/IPCC_AR6_WGI_FullReport.pdf).
- Intergovernmental Panel on Climate Change (IPCC), 2022. *Climate Change 2022: Impacts, Adaptation and Vulnerability. Contribution of Working Group II to the Sixth Assessment Report of the Intergovernmental Panel on Climate Change*. URL: [https://report.ipcc.ch/ar6/wg2/IPCC\\_AR6\\_WGII\\_FullReport.pdf](https://report.ipcc.ch/ar6/wg2/IPCC_AR6_WGII_FullReport.pdf).
- Iqbal, R., Raza, M.A.S., Toleikiene, M., Ayaz, M., Hashemi, F., Habib-ur Rahman, M., Zaheer, M.S., Ahmad, S., Riaz, U., Ali, M., Aslam, M.U., Haider, I., 2020. Partial root-zone drying (PRD), its effects and agricultural significance: a review. *Bulletin of the National Research Centre* 44, 159. doi:10.1186/s42269-020-00413-w.
- Jacquette, E., Bitar, A.A., Mialon, A., Kerr, Y., Quesney, A., Cabot, F., Richaume, P., 2010. SMOS CATDS level 3 global products over land, in: *Remote Sensing for Agriculture, Ecosystems, and Hydrology XII*, SPIE. 137–142. doi:10.1117/12.865093.
- Ji, K., Wu, Y., 2015. Scattering Mechanism Extraction by a Modified Cloude-Pottier Decomposition for Dual Polarization SAR. *Remote Sensing* 7, 7447–7470. doi:10.3390/rs70607447.
- Kashyap, B., Kumar, R., 2021. Sensing Methodologies in Agriculture for Soil Moisture and Nutrient Monitoring. *IEEE Access* 9, 14095–14121. doi:10.1109/ACCESS.2021.3052478.
- Kellndorfer, J., Pierce, L., Dobson, M., Ulaby, F., 1998. Toward consistent regional-to-global-scale vegetation characterization using orbital SAR systems. *IEEE Transactions on Geoscience and Remote Sensing* 36, 1396–1411. doi:10.1109/36.718844.

- Khan, S.I., Adams, T.E. (Eds.), 2019. *Indus River Basin: Water Security and Sustainability*. Elsevier, Amsterdam, Netherlands.
- Kim, S., Liu, Y.Y., Johnson, F.M., Parinussa, R.M., Sharma, A., 2015. A global comparison of alternate AMSR2 soil moisture products: Why do they differ? *Remote Sensing of Environment* 161, 43–62. doi:10.1016/j.rse.2015.02.002.
- Kim, S., Zhang, R., Pham, H., Sharma, A., 2019. A Review of Satellite-Derived Soil Moisture and Its Usage for Flood Estimation. *Remote Sensing in Earth Systems Sciences* 2, 225–246. doi:10.1007/s41976-019-00025-7.
- Kong, X., Dorling, S.R., 2008. Near-surface soil moisture retrieval from ASAR Wide Swath imagery using a Principal Component Analysis. *International Journal of Remote Sensing* 29, 2925–2942. doi:10.1080/01431160701442088.
- Konings, A.G., Rao, K., Steele-Dunne, S.C., 2019. Macro to micro: microwave remote sensing of plant water content for physiology and ecology. *New Phytologist* 223, 1166–1172. doi:10.1111/nph.15808.
- Kornelsen, K.C., Coulibaly, P., 2013. Advances in soil moisture retrieval from synthetic aperture radar and hydrological applications. *Journal of Hydrology* 476, 460–489. doi:10.1016/j.jhydrol.2012.10.044.
- Kweon, S.K., Oh, Y., 2015. A Modified Water-Cloud Model With Leaf Angle Parameters for Microwave Backscattering From Agricultural Fields. *IEEE Transactions on Geoscience and Remote Sensing* 53, 2802–2809. doi:10.1109/TGRS.2014.2364914.
- Lakhankar, T., Krakauer, N., Khanbilvardi, R., 2009. Applications of microwave remote sensing of soil moisture for agricultural applications. *International Journal of Terraspace Science and Engineering* 2, 81–91.
- Larsen, C., Rand, S., Schmid, A., Dean, A., 2018. *Developing Skills in a Changing World of Work: Concepts, Measurement and Data Applied in Regional and Local Labour Market Monitoring Across Europe*. 1st ed., Rainer Hampp Verlag, München.
- Liang, G., 2022. Nitrogen fertilization mitigates global food insecurity by increasing cereal yield and its stability. *Global Food Security* 34, 100652. doi:10.1016/j.gfs.2022.100652.
- Lin, D., Wambersie, L., Wackernagel, M., 2022. Estimating the Date of Earth Overshoot Day 2022. URL: <https://www.overshootday.org/content/uploads/2021/06/Earth-Overshoot-Day-2021-Nowcast-Report.pdf>.
- Liu, C., Shi, J., 2016. Estimation of Vegetation Parameters of Water Cloud Model for Global Soil Moisture Retrieval Using Time-Series L-Band Aquarius Observations. *IEEE Journal of Selected Topics in Applied Earth Observations and Remote Sensing* 9, 5621–5633. doi:10.1109/JSTARS.2016.2596541.

- Liu, J., Zhan, X., Hain, C., Yin, J., Fang, L., Li, Z., Zhao, L., 2016. NOaa Soil Moisture Operational Product System (SMOPS) and its validations, in: 2016 IEEE International Geoscience and Remote Sensing Symposium (IGARSS), 3477–3480. doi:10.1109/IGARSS.2016.7729899.
- Liu, Y., Yang, Y., 2022. Advances in the Quality of Global Soil Moisture Products: A Review. *Remote Sensing* 14, 3741. doi:10.3390/rs14153741.
- Loboguerrero, A.M., Campbell, B.M., Cooper, P.J.M., Hansen, J.W., Rosenstock, T., Wollenberg, E., 2019. Food and Earth Systems: Priorities for Climate Change Adaptation and Mitigation for Agriculture and Food Systems. *Sustainability* 11, 1372. doi:10.3390/su11051372.
- Loew, A., Ludwig, R., Mauser, W., 2006. Derivation of surface soil moisture from ENVISAT ASAR wide swath and image mode data in agricultural areas. *IEEE Transactions on Geoscience and Remote Sensing* 44, 889–899. doi:10.1109/TGRS.2005.863858.
- Martill, B., 2023. Withdrawal symptoms: party factions, political change and British foreign policy post-Brexit. *Journal of European Public Policy* 0, 1–24. doi:10.1080/13501763.2023.2198578.
- Mattia, F., 2011. Coherent and incoherent scattering from tilled soil surfaces. *Waves in Random and Complex Media* 21, 278–300. doi:10.1080/17455030.2011.552533.
- Mattia, F., Le Toan, T., Picard, G., Posa, F., D'Alessio, A., Notarnicola, C., Gatti, A., Rinaldi, M., Satalino, G., Pasquariello, G., 2003. Multitemporal C-band radar measurements on wheat fields. *IEEE Transactions on Geoscience and Remote Sensing* 41, 1551–1560. doi:10.1109/TGRS.2003.813531.
- Meadows, D.H., Meadows, D., 2007. The history and conclusions of *The Limits to Growth*. *System Dynamics Review* 23, 191–197. doi:10.1002/sdr.371.
- Meadows, D.H., Meadows, D.H., Randers, J., Behrens III, W.W., 1972. *The Limits to Growth: A Report for the Club of Rome's Project on the Predicament of Mankind*. Universe Books, New York.
- Mekonnen, M.M., Hoekstra, A.Y., 2016. Four billion people facing severe water scarcity. *American Association for the Advancement of Science* 2, e1500323. doi:10.1126/sciadv.1500323.
- Mina, M., Messier, C., Duveneck, M.J., Fortin, M.J., Aquilué, N., 2022. Managing for the unexpected: Building resilient forest landscapes to cope with global change. *Global Change Biology* 28, 4323–4341. doi:10.1111/gcb.16197.
- Mishra, R.K., 2023. Fresh Water availability and Its Global challenge. *British Journal of Multidisciplinary and Advanced Studies* 4, 1–78. doi:10.37745/bjmas.2022.0208.

- Mitra, R., 2016. Sustainability and Sustainable Development, in: *The International Encyclopedia of Organizational Communication*. John Wiley & Sons, Ltd, 1–10. URL: <https://onlinelibrary.wiley.com/doi/abs/10.1002/9781118955567.wbieoc201>.
- Mladenova, I.E., Jackson, T.J., Bindlish, R., Hensley, S., 2013. Incidence Angle Normalization of Radar Backscatter Data. *IEEE Transactions on Geoscience and Remote Sensing* 51, 1791–1804. doi:10.1109/TGRS.2012.2205264.
- Molijn, R.A., Iannini, L., Vieira Rocha, J., Hanssen, R.F., 2019. Sugarcane Productivity Mapping through C-Band and L-Band SAR and Optical Satellite Imagery. *Remote Sensing* 11, 1109. doi:10.3390/rs11091109.
- Nativel, S., Ayari, E., Rodriguez-Fernandez, N., Baghdadi, N., Madelon, R., Albergel, C., Zribi, M., 2022. Hybrid Methodology Using Sentinel-1/Sentinel-2 for Soil Moisture Estimation. *Remote Sensing* 14. doi:10.3390/rs14102434.
- Nayak, H.P., Osuri, K.K., Sinha, P., Nadimpalli, R., Mohanty, U.C., Chen, F., Rajeevan, M., Niyogi, D., 2018. High-resolution gridded soil moisture and soil temperature datasets for the Indian monsoon region. *Nature Publishing Group* 5, 180264. doi:10.1038/sdata.2018.264.
- Neupane, J., Guo, W., 2019. Agronomic Basis and Strategies for Precision Water Management: A Review. *Agronomy* 9. doi:10.3390/agronomy9020087.
- O, S., Orth, R., Weber, U., Park, S.K., 2022. High-resolution European daily soil moisture derived with machine learning (2003–2020). *Scientific Data* 9, 701. doi:10.1038/s41597-022-01785-6.
- Oh, Y., 2004. Quantitative retrieval of soil moisture content and surface roughness from multipolarized radar observations of bare soil surfaces. *IEEE Transactions on Geoscience and Remote Sensing* 42, 596–601. doi:10.1109/TGRS.2003.821065.
- Oh, Y., Sarabandi, K., Ulaby, F., 1992. An empirical model and an inversion technique for radar scattering from bare soil surfaces. *IEEE Transactions on Geoscience and Remote Sensing* 30, 370–381. doi:10.1109/36.134086.
- Oni, D., 2024. Space economy revenue worldwide will increase at a CAGR of 9% from USD99 billion in 2022 to USD240 billion in 2032. Technical Report. Analysys Mason company. URL: <https://www.analysismason.com/research/content/reports/global-space-economy-4th-nsr/>.
- Osuri, K.K., Nadimpalli, R., Mohanty, U.C., Chen, F., Rajeevan, M., Niyogi, D., 2017. Improved prediction of severe thunderstorms over the Indian Monsoon region using high-resolution soil moisture and temperature initialization. *Nature Publishing Group* 7, 41377. doi:10.1038/srep41377.

- Owe, M., de Jeu, R., Holmes, T., 2008. Multisensor historical climatology of satellite-derived global land surface moisture. *Journal of Geophysical Research: Earth Surface* 113. doi:10.1029/2007JF000769.
- Owe, M., de Jeu, R., Walker, J., 2001. A methodology for surface soil moisture and vegetation optical depth retrieval using the microwave polarization difference index. *IEEE Transactions on Geoscience and Remote Sensing* 39, 1643–1654. doi:10.1109/36.942542.
- Pandey, D.K., Teja Noothi, S., M., S., Srivastava, P.K., Das, A., Pal, O., Rohilla, K., Prawasi, R., Sekh, N.H., Bisht, S., Putrevu, D., Misra, A., Kumar, R., 2021. Active-Passive Approach for NISAR High Resolution Soil Moisture Products: Retrieval and Accuracy Assessment over Indian Cropland, in: 2021 IEEE International India Geoscience and Remote Sensing Symposium (InGARSS), 281–284. doi:10.1109/InGARSS51564.2021.9791952.
- Peng, J., Albergel, C., Balenzano, A., Brocca, L., Cartus, O., Cosh, M.H., Crow, W.T., Dabrowska-Zielinska, K., Dadson, S., Davidson, M.W.J., de Rosnay, P., Dorigo, W., Gruber, A., Hagemann, S., Hirschi, M., Kerr, Y.H., Lovergine, F., Mahecha, M.D., Marzahn, P., Mattia, F., Musial, J.P., Preuschmann, S., Reichle, R.H., Satalino, G., Silgram, M., van Bodegom, P.M., Verhoest, N.E.C., Wagner, W., Walker, J.P., Wegmüller, U., Loew, A., 2021a. A roadmap for high-resolution satellite soil moisture applications – confronting product characteristics with user requirements. *Remote Sensing of Environment* 252. doi:10.1016/j.rse.2020.112162.
- Peng, J., Loew, A., Merlin, O., Verhoest, N.E.C., 2017. A review of spatial downscaling of satellite remotely sensed soil moisture. *Reviews of Geophysics* 55, 341–366. doi:10.1002/2016RG000543.
- Peng, J., Tanguy, M., Robinson, E.L., Pinnington, E., Evans, J., Ellis, R., Cooper, E., Hanaford, J., Blyth, E., Dadson, S., 2021b. Estimation and evaluation of high-resolution soil moisture from merged model and Earth observation data in the Great Britain. *Remote Sensing of Environment* 264. doi:10.1016/j.rse.2021.112610.
- Petropoulos, G.P., Ireland, G., Barrett, B., 2015. Surface soil moisture retrievals from remote sensing: Current status, products & future trends. *Physics and Chemistry of the Earth, Parts A/B/C* 83-84, 36–56. doi:10.1016/j.pce.2015.02.009.
- Phung, Q.A., Thompson, A.L., Baffaut, C., Costello, C., John Sadler, E., 2022. Assessing Future Water Allocation under Climate Variability and Land Management Change in an Agricultural Watershed. *Journal of the American Water Resources Association* 58, 1575–1591. doi:10.1111/1752-1688.13059.
- Preetha, P.P., Al-Hamdan, A.Z., 2020. Developing nitrate-nitrogen transport models using remotely-sensed geospatial data of soil moisture profiles and wet depositions. *Journal of Environmental Science and Health, Part A* 55, 615–628. doi:10.1080/10934529.2020.1724503.

- Ramsauer, T., Weiß, T., Löw, A., Marzahn, P., 2021. RADOLAN\_api: An Hourly Soil Moisture Data Set Based on Weather Radar, Soil Properties and Reanalysis Temperature Data. *Remote Sensing* 13. doi:10.3390/rs13091712.
- Rees, W.E., 1992. Ecological footprints and appropriated carrying capacity: what urban economics leaves out. *Environment and Urbanization* 4, 121–130. doi:10.1177/095624789200400212.
- Richards, J.A., 2009. *Remote Sensing with Imaging Radar. Signals and Communication Technology*, Springer, Berlin, Heidelberg. URL: <https://link.springer.com/10.1007/978-3-642-02020-9>.
- Rodríguez-Fernández, N.J., Kerr, Y.H., Van der Schalie, R., Al-Yaari, A., Wigneron, J.P., De Jeu, R., Richaume, P., Dutra, E., Mialon, A., Drusch, M., 2016. Long Term Global Surface Soil Moisture Fields Using an SMOS-Trained Neural Network Applied to AMSR-E Data. *Remote Sensing* 8, 959. doi:10.3390/rs8110959.
- Sabaghy, S., Walker, J.P., Renzullo, L.J., Jackson, T.J., 2018. Spatially enhanced passive microwave derived soil moisture: Capabilities and opportunities. *Remote Sensing of Environment* 209, 551–580. doi:10.1016/j.rse.2018.02.065.
- Sachs, J.D., Schmidt-Traub, G., Mazzucato, M., Messner, D., Nakicenovic, N., Rockström, J., 2019. Six Transformations to achieve the Sustainable Development Goals. *Nature Sustainability* 2, 805–814. doi:10.1038/s41893-019-0352-9.
- Saco, P.M., McDonough, K.R., Rodriguez, J.F., Rivera-Zayas, J., Sandi, S.G., 2021. The role of soils in the regulation of hazards and extreme events. *Philosophical Transactions of the Royal Society B: Biological Sciences* 376, 20200178. doi:10.1098/rstb.2020.0178.
- Salman, A.Z., Al-Karablieh, E.K., Fisher, F.M., 2001. An inter-seasonal agricultural water allocation system (SAWAS). *Agricultural Systems* 68, 233–252. doi:10.1016/S0308-521X(01)00010-5.
- Schaufler, S., Bauer-Marschallinger, B., Hochstöger, S., Wagner, W., 2018. Modelling and correcting azimuthal anisotropy in Sentinel-1 backscatter data. *Remote Sensing Letters* 9, 799–808. doi:10.1080/2150704X.2018.1480071.
- Scheierling, S.M., Treguer, D.O., 2016. Enhancing Water Productivity in Irrigated Agriculture in the Face of Water Scarcity. *Choices: The Magazine of Food, Farm, and Resource Issues* 31, 1–10. URL: <https://ideas.repec.org//a/ags/aaeach/242357.html>.
- Schulla, J., Jasper, K., 2015. *Model Description WaSiM*. Institute for Atmospheric and Climate Science, Swiss Federal Institute of Technology: Zurich, Switzerland .
- Seneviratne, S.I., Corti, T., Davin, E.L., Hirschi, M., Jaeger, E.B., Lehner, I., Orlowsky, B., Teuling, A.J., 2010. Investigating soil moisture–climate interactions in a changing climate: A review. *Earth-Science Reviews* 99, 125–161. doi:10.1016/j.earscirev.2010.02.004.

- Shannon, D.K., Clay, D.E., Kitchen, N.R., 2018. Precision agriculture basics. volume 176. John Wiley & Sons, Madison, Wisconsin.
- Shukla, A., Panchal, H., Mishra, M., Patel, P., Srivastava, H., Patel, P., 2014. Soil Moisture Estimation using Gravimetric Technique and FDR Probe Technique: A Comparative Analysis. *American International Journal of Research in Formal, Applied & Natural Sciences* 14, 89–92.
- Song, P., Zhang, Y., Guo, J., Shi, J., Zhao, T., Tong, B., 2022. A 1 km daily surface soil moisture dataset of enhanced coverage under all-weather conditions over China in 2003–2019. *Earth System Science Data* 14, 2613–2637. doi:10.5194/essd-14-2613-2022.
- Srivastava, H.S., Patel, P., Navalgund, R.R., 2006. How far SAR has fulfilled its expectation for soil moisture retrieval, in: *Microwave Remote Sensing of the Atmosphere and Environment V*, SPIE. doi:10.1117/12.693946.
- Sutanto, S.J., Paparrizos, S., Kranjac-Berisavljevic, G., Jamaldeen, B.M., Issahaku, A.K., Gandaa, B.Z., Supit, I., van Slobbe, E., 2022. The Role of Soil Moisture Information in Developing Robust Climate Services for Smallholder Farmers: Evidence from Ghana. *Agronomy* 12, 541. doi:10.3390/agronomy12020541.
- Tao, L., Wang, G., Chen, X., Li, J., Cai, Q., 2019. Estimation of soil moisture using a vegetation scattering model in wheat fields. *Journal of Applied Remote Sensing* 13. doi:10.1117/1.JRS.13.4.044503.
- Tebbs, E., Gerard, F., Petrie, A., De Witte, E., 2016. Chapter 19 - Emerging and Potential Future Applications of Satellite-Based Soil Moisture Products, in: Srivastava, P.K., Petropoulos, G.P., Kerr, Y.H. (Eds.), *Satellite Soil Moisture Retrieval*. Elsevier, 379–400. URL: <https://www.sciencedirect.com/science/article/pii/B978012803388300019X>.
- Thompson, R.B., Gallardo, M., Valdez, L.C., Fernández, M.D., 2007. Using plant water status to define threshold values for irrigation management of vegetable crops using soil moisture sensors. *Agricultural Water Management* 88, 147–158. doi:10.1016/j.agwat.2006.10.007.
- Trier, S.B., Chen, F., Manning, K.W., 2004. A Study of Convection Initiation in a Mesoscale Model Using High-Resolution Land Surface Initial Conditions. *Monthly Weather Review* 132, 2954–2976. doi:10.1175/MWR2839.1.
- Ulaby, F.T., Long, D.G., 2014. *Microwave radar and radiometric remote sensing*. University of Michigan press, Ann Arbor.
- United Nation General Assembly, 2015. Resolution adopted by the General Assembly on 25 September 2015. Transforming our world: the 2030 Agenda for Sustainable Development. New York URL: <https://upload.wikimedia.org/wikipedia/commons/d/d5/N1529189.pdf>.

- United Nations Department of Economic and Social Affairs, 2022. World Population Prospects 2022: Summary of results. UN DESA/POP/2022/TR/NO. 3. URL: [https://www.un.org/development/desa/pd/sites/www.un.org.development.desa.pd/files/wpp2022\\_summary\\_of\\_results.pdf](https://www.un.org/development/desa/pd/sites/www.un.org.development.desa.pd/files/wpp2022_summary_of_results.pdf).
- United Nations World Water Assessment Programme, 2018. The United Nations World Water Development Report 2018: Nature-Based Solutions for Water. Paris, UNESCO. URL: <https://www.unwater.org/publications/world-water-development-report-2018>.
- U.S. Global Change Research Program (USGCRP), 2017. Climate Science Special Report: Fourth National Climate Assessment, Volume I. Technical Report. U.S. Global Change Research Program. Washington, DC, USA.
- Vanino, S., Nino, P., De Michele, C., Falanga Bolognesi, S., D'Urso, G., Di Bene, C., Pennelli, B., Vuolo, F., Farina, R., Pulighe, G., Napoli, R., 2018. Capability of Sentinel-2 data for estimating maximum evapotranspiration and irrigation requirements for tomato crop in Central Italy. *Remote Sensing of Environment* 215, 452–470. doi:10.1016/j.rse.2018.06.035.
- Verstraeten, W.W., Veroustraete, F., Wagner, W., Van Roey, T., Heyns, W., Verbeiren, S., Feyen, J., 2011. Remotely sensed soil moisture integration in an ecosystem carbon flux model. The spatial implication, in: Jonas, M., Nahorski, Z., Nilsson, S., Whiter, T. (Eds.), *Greenhouse Gas Inventories: Dealing With Uncertainty*. Springer Netherlands, Dordrecht, 117–136.
- Vu, P., Huynh, N., Phan, H., Hoang, H., 2023. Financial Earthquakes and After-shocks: From Brexit to Russia-Ukraine Conflict and the Stability of European Banks. doi:10.2139/ssrn.4474469.
- Wackernagel, M., Beyers, B., 2019. *Ecological Footprint: Managing Our Biocapacity Budget*. New Society Publishers, Gabriola Island, BC, Canada.
- Wagner, W., Blöschl, G., Pampaloni, P., Calvet, J.C., Bizzarri, B., Wigneron, J.P., Kerr, Y., 2007. Operational readiness of microwave remote sensing of soil moisture for hydrologic applications. *Hydrology Research* 38, 1–20. doi:10.2166/nh.2007.029.
- Wagner, W., Hahn, S., Kidd, R., Melzer, T., Bartalis, Z., Hasenauer, S., Figa-Saldaña, J., Rosnay, P.d., Jann, A., Schneider, S., Komma, J., Kubu, G., Brugger, K., Aubrecht, C., Züger, J., Gangkofner, U., Kienberger, S., Brocca, L., Wang, Y., Blöschl, G., Eitzinger, J., Steinnocher, K., 2013. The ASCAT Soil Moisture Product: A Review of its Specifications, Validation Results, and Emerging Applications. *Meteorologische Zeitschrift* 22, 5. URL: [https://www.academia.edu/17452107/The\\_ASCAT\\_Soil\\_Moisture\\_Product\\_A\\_Review\\_of\\_its\\_Specifications\\_Validation\\_Results\\_and\\_Emerging\\_Applications](https://www.academia.edu/17452107/The_ASCAT_Soil_Moisture_Product_A_Review_of_its_Specifications_Validation_Results_and_Emerging_Applications).

- 
- Wagner, W., Lemoine, G., Borgeaud, M., Rott, H., 1999a. A study of vegetation cover effects on ERS scatterometer data. *IEEE Transactions on Geoscience and Remote Sensing* 37, 938–948. doi:10.1109/36.752212.
- Wagner, W., Lemoine, G., Rott, H., 1999b. A Method for Estimating Soil Moisture from ERS Scatterometer and Soil Data. *Remote Sensing of Environment* 70, 191–207. doi:10.1016/S0034-4257(99)00036-X.
- Wegmuller, U., Cordey, R., Werner, C., Meadows, P., 2006. “Flashing Fields” in Nearly Simultaneous ENVISAT and ERS-2 C-Band SAR Images. *IEEE Transactions on Geoscience and Remote Sensing* 44, 801–805. doi:10.1109/TGRS.2005.861479.
- Weiß, T., Ramsauer, T., Jagdhuber, T., Löw, A., Marzahn, P., 2021. Sentinel-1 Backscatter Analysis and Radiative Transfer Modeling of Dense Winter Wheat Time Series. *Remote Sensing* 13. doi:10.3390/rs13122320.
- Weng, Q. (Ed.), 2016. *Remote Sensing for Sustainability*. CRC Press, Boca Raton.
- Woodhouse, I.H., 2006. *Introduction to Microwave Remote Sensing*. CRC Press, Boca Raton.
- World Economic Forum, Deloitte, 2024. Amplifying the global value of earth observation. Technical Report. World Economic Forum. URL: <https://www.weforum.org/publications/amplifying-the-global-value-of-earth-observation/>.
- World Meteorological Organization, 2010. Implementation Plan for the Global Observing System for Climate in support of the UNFCCC: (2010 update). URL: [https://library.wmo.int/index.php?lvl=notice\\_display&id=449](https://library.wmo.int/index.php?lvl=notice_display&id=449).
- Zeng, J., Peng, J., Zhao, W., Ma, C., Ma, H., 2023. Microwave Remote Sensing of Soil Moisture. *Remote Sensing* 15, 4243. doi:10.3390/rs15174243.
- Zhang, C., Di, L., Yang, Z., Lin, L., Zhao, H., Yu, E.G., 2021. An Overview of Agriculture Cyberinformatics Tools to Support USDA NASS Decision Making, in: 2021 9th International Conference on Agro-Geoinformatics (Agro-Geoinformatics), 1–6. doi:10.1109/Agro-Geoinformatics50104.2021.9530327.
- Zhang, P., Xiao, P., Yao, W., Liu, G., Sun, W., 2020. Profile distribution of soil moisture response to precipitation on the Pisha sandstone hillslopes of China. *Scientific Reports* 10, 9136. doi:10.1038/s41598-020-65829-w.